DEVELOPMENT OF A CONTINUOUS-FLOW, AUTOMATED MICROFLUIDIC

DEVICE FOR SINGLE CELL LEVEL ELECTROPORATION

by

MINGDE ZHENG

A dissertation submitted to the

Graduate School-New Brunswick

Rutgers, The State University of New Jersey

and

The Graduate School of Biomedical Sciences

In partial fulfillment of the requirements

For the degree of

Doctor of Philosophy

Graduate Program in Biomedical Engineering

Written under the direction of

Jeffrey D. Zahn

And approved by

_____

_____

_____

_____

_____

New Brunswick, New Jersey

October, 2016

ABSTRACT OF THE DISSERTATION

Development of a Continuous-Flow, Automated Microfluidic Device for Single Cell

Level Electroporation

By MINGDE ZHENG

Dissertation Director:

Jeffrey D. Zahn

Electroporation is a powerful transfection technique that creates transient openings in the

cell membrane by applying an electric field, allowing for the intracellular delivery of

diagnostic and therapeutic substances. The ability to detect and control the degree of cell

membrane permeability plays a key role in determining the size of the delivery payload,

while safeguarding the overall cell viability. In order to create a universal electroporation

system, this dissertation describes the development of a continuous flow electroporation

microdevice that automatically detects, electroporates, and monitors individual cells for

changes in permeability and delivery. In contrast to devices that immobilize individual

cells for impedance analysis, this work demonstrates the capability to manipulate single

cells under flow and real-time analysis of membrane permeabilization before and after

electroporation, which dramatically increasing the number of cells which can be

electroporated and analyzed. Using an electric circuit model, and Multiphysics

computational tools, the key parameters for successful cell membrane permeabilization detection in a flow environment were determined. By varying the electric field parameters, we demonstrate the direct control of cell membrane permeabilization by electrically measuring the electroporation-induced cell membrane impedance change and by optically measuring the delivery of a fluorescent probe. Viability of the electroporated cells following collection also demonstrates a correlation with the applied pulse strength. By extending the device capability to include dynamic pulse adjustment according to the real-time feedback information on cell viability, an intelligent electroporation system capable of potentially maximizing delivery efficiency and cell viability can be thus realized.

ACKNOWLEDGEMENTS

First of all, I would like to extend my sincere gratitude to my primary academic advisor, Prof. Jeffrey Zahn for these years of guidance and mentorship. It has been a tremendously rewarding experience for me in the BioMEMS and Microfluidics laboratory. Not simply did I have the opportunity to perform my thesis work under his supervision, I was encouraged and supported to pursue other collaborative research projects with fellow graduate students. His experience, technical expertise, and enthusiasm in problem solving and product innovation have helped to guide my thinking as an engineer, and motivates me to seek for greater challenges.

In the same way, I extend my sincere thankfulness to Prof. David Shreiber for his guidance, advice, and words of wisdom over the years as one of my research advisors on this thesis work. He has been a valuable source of inspiration, direction and fresh prospective from the beginning.

I also would like to cordially acknowledge and thank Prof. Hao Lin for his years of academic discussion and feedback on the electroporation project. His insightful ideas and decisive approach to problem solving helped me overcame many challenges during my thesis work.

I would like to express my appreciation to Prof. Jerry Shan for being one of my advisors and making himself available for academic discussion and consultation. His input and feedback during my thesis research encouraged me to think critically and well-roundedly.

DEDICATIONS

To my family: Zheng Xinming, Liang Liquan, Zheng Chunli, and Zhou Xuyin

For their faith, love and unyielding support.

TABLE OF CONTENTS

LIST OF TABLES

LIST OF ILLUSTRATIONS

Chapter 1

Introduction

1.1 Significance of Transfection

A biological cell is the basic unit of all living organisms, bearing all essential genetic programming necessary to produce cell function and protein expressions. Our curiosity at this fundamental level of life has led to the development of many analytical tools for studying the genetic makeup and regulation of cells as well as cellular processes. The procedure commonly used in the deliberate introduction of genetic materials (DNA and RNA) into cells is known as transfection. This powerful technique has enabled the investigation and manipulation of gene functions and products, curing or improving symptoms of genetic diseases, and advancing research in both cell biology, drug discovery and target validation.[1] Transfection can be broadly categorized into three groups: viral, chemical and physical methods. Transfection through viral vectors is the most well-known approach. As a result of the potent viral integration, highly efficient transgene expressions can be obtained. However immunogenicity, cytotoxicity, limited space on a virus package, and potential mutagenesis/tumorigenesis from the use of viral vectors are some of the limiting drawbacks associated with this technique.[1,2] Transfection mediated by chemicals such as calcium phosphate, cationic lipids and cationic peptides is the oldest approach used in transfecting mammalian cells. Although this method is not limited by drawbacks found in virus-mediated approach, the transfection efficiency is generally low due to its sensitivity to factors such as solution pH, cell membrane conditions, etc.[3] Transfection can also be performed through a variety of physical means. Amongst a few are microinjection,[4]

biolistic particle delivery,[5] magnetofection,[6] sonoporation,[7] electroporation,[8] and laser irradiation-based transfection.[9] In particular, electroporation is a widely used, effective, high throughput transfection technique that is relatively low cost, easy to operate, safe, fast, and efficient in transfecting many cell types.[1,10]. The distinctive advantages of the electroporation technique were quickly revealed to surpass other physical transfection methods. Electroporation utilizes electric fields to increase the cell membrane permeability by creating reversible pores, permitting the transfer of exogenous materials such as nucleic acids and proteins into the cell. Removal of the electric field allows for resealing of the membrane to take place, ensuring the survival of the cells. Because of electroporation's reliability and reproducibility in transfecting many cell types using empirically-refined protocols, it has become a popular transfection choice for many life science applications such as the in-depth analysis of gene and protein expressions through DNA transfection and transformation, and clinical applications such as cancer treatment, gene therapy, transdermal drug delivery and stem cell research.[11]

1.2 Main Challenges behind Electroporation

Although electroporation has shown great promise among other non-viral physical transfection approaches, it is not without challenges and limitations. Despite extensive research in recent decades, electroporation still falls short of the desired molecular transport efficiency and cell viability in many applications. The delivery efficiency of typical commercial electroporators for transfecting primary cells is approximately 30% and are often accompanied by significant cell death. For example, Pepe et al.[12] reported the use of a Gene Pulser II Apparatus to transfect Jurkat lymphocytes in-vitro with an applied voltage of 250 V, and they observed a delivery efficiency of 15.83 ± 3.5%, and an average cell

viability of 65.8 ± 7.3%. The challenge is more significant in *in-vivo* electroporation applications. There exists an inherent trade-off between delivery efficiency and cell viability. Higher efficiency can be obtained by increasing the electroporation pulse strength. However if not controlled, the applied electric field irreversibly damages the cell membrane, resulting in cell death. The opposite is true when the electroporation pulse strength is decreased, cell viability improves at the cost of reduced delivery efficiency, since a smaller number of cell membrane pores are formed to permit intracellular passage of materials.

Furthermore, successful electroporation of cells currently depends solely on empirically derived protocols, and they must be adjusted specifically for each cell type and experimental condition. This is due to each cell type's distinct response to the applied electric fields. For instance, mammalian cells in general, and several specific cell types, including neural precursors, neurons, and neutrophils in particular have been reported to be especially difficult to transfect via electroporation.[13,14] Transfection using current empirical electroporation protocols are intrinsically variable processes where losses in cell viability are unavoidable and can only be improved through iterative practices. Due to the inherent variability amongst cells, there is a need to develop a universal electroporation system that recognizes the membrane permeabilization limit on an individual cell basis, and carries out electroporation without causing irreversible damage.

1.3 Motivation for Control

Despite extensive research and application in the field of electroporation, many efforts have been dedicated to derive new protocols for transfecting a specific cell type or minimizing variability in the electroporation-mediated transfection process. Previous research

conducted by our group has elucidated the physical principles behind electroporation-mediated intracellular molecular transport and put forth guidelines for improving both delivery efficiency and cell viability in macroscale electroporation of 3T3 fibroblasts. However, we realized that it is only by first ensuring cell survival during the electroporation process, that we can apply our molecular transport guidelines to achieve high delivery efficiency and extends them for different types of cells. The key to preserve cell viability lays in the control of the cell membrane permeabilization magnitude, a characteristic found amongst many cell types during electroporation, so that irreversible damage does not occur. We hypothesize that: (1) by manipulating and performing electroporation at the single cell level, delivery efficiency and cell viability can be investigated with higher accuracy and selectivity. (2) Degrees of cell membrane permeabilization induced from applying electroporation pulse can be electrically measured to allow cell viability assessment and control in real time. (3) The process of single cell electroporation treatment and cell membrane permeabilization tracking can be automated in a continuous-flow fashion. (4) Electroporation can be reliably extended to different types of cells without empirical derivation of protocols by including the dynamic pulse adjustment based on real-time feedback information on the cell. Hence, the motivation behind this dissertation research is to contribute to the field of electroporation by developing a high throughput, feedback-controlled electroporation microchip that combines our knowledge in intracellular molecular transport and microscale engineering with single cell impedance spectroscopy to potentially maximize delivery and cell viability in a fully automated and efficient manner.

1.4 Dissertation Overview

This dissertation thesis consists of two topic themes. The first theme demonstrates and explains the manipulation, electroporation and collection of single cells in a microfluidic channel using merely sheathing flows. The motivation was to control cells in a continuous flow microchannel while improving the intracellular molecular delivery profile by implementing microscale electroporation methods to effectively increasing the cell membrane permeabilization area. The approach involves controlling the cell orientation by fluidic 'pinching' of cells and applying multiple electroporation pulses to the rotating cells. The second theme of this thesis investigates the sensitive detection and measurement of single cells in microchannels and their membrane impedance response following electroporation treatments. We approach this aim by first identifying the necessary parameters to experimentally measure electroporation-induced membrane permeabilization with numerical and computational tools. Our preliminary investigation of such detection capability began by measuring the aggregated cell impedance responses following irreversible and reversible electroporation for both small and large cell population. The knowledge obtained from preliminary experiments allowed us to design, fabricate and evaluate a reliable single cell detection microchannel geometry to serve as the basis for single cell membrane level measurements. An automated electroporation microdevice capable of real time measurement and tracking of cell membrane impedance was then developed. The electrical measurements indicative of the membrane permeabilization were validated by optical observation and viability staining following cell collection.

In chapter one, the significance of transfection by electroporation was introduced. Despite extensive research and application in electroporation, there are still challenges remain which hinder the advancement and application of electroporation. This thesis sets out to investigate a potential approach in addressing these challenges through the development of an intelligent single cell level electroporation microchip.

The second chapter presents the background principles behind electroporation and electroporation-mediated molecular transport, and then provides an overview of the recent electroporation evolution from conventional macroscale into the microscale domain. Current cell membrane permeabilization approaches are also explored in this chapter.

Chapter three demonstrates a microfluidically-controlled cell orientation manipulation technique that aims to increase the intracellular delivery profile of molecules during microscale electroporation. Details regarding the microchannel design, fabrication and materials required to hydrodynamically control the single cell orientation and bring forth circumferentially elevated molecular delivery will be discussed. The correlation between single cell rotation angular velocity and sheathing stream flow rate will be characterized, and the capability to deliver molecules into cells either circumferentially or partially through the membrane are demonstrated.

In chapter four, an overview of the single cell impedance cytometry theories and numerical models of a cell in suspension will be presented. And microfluidic-based impedance cytometer with different channel designs are fabricated and tested. Experimental detection accuracy and sensitivity of single cells using these channel designs are compared to highlight the most reliable microchannel configuration, so it can be implemented to serve as a platform for developing dynamic electroporation and cell membrane permeabilization

detection and measurement. The implementation and application of the detection sensor based on the Lock-in Amplification technique will also be described for cell impedance signal extraction.

Chapter five focuses on the practical detection and measurement of cell membrane permeabilization signals. The approach consists of: (1) constructing a cell/electrolyte circuit model to identify parameters that affect the cell membrane permeabilization impedance magnitude. (2) Experimentally measuring the impedance of cell aggregates before and after applying irreversible electroporation to hone in on the magnitude of permeabilization for an individual cell and verify the detection capability. (3) Microfabricating channels to immobilize single cells and evaluate the membrane permeabilization dynamics on an individual cell during irreversible and reversible electroporation treatments.

In Chapter six, the dynamic measurement of single cell membrane impedance before and after electroporation is performed and analyzed to demonstrate the ability to control a cell's membrane permeabilization in a continuous-flow manner. Microchannel design, sensory configuration, and the integration of electronic sensing with electroporation is described and discussed in detail. Electrical data demonstrating cell membrane permeabilization control is presented, and validated with nucleic-acid binding fluorescent probes and live-dead staining of collected cells.

Chapter seven first describes the overall automation process for the ultimate development of an intelligent electroporation system. Then a working approach to enable cell impedance monitoring during electroporation is presented. This approach allows automated control of the cell membrane permeabilization so that only membrane pore density that ensures cell

survival will be created for intracellular molecular delivery. This is accomplished by implementing a solid state relay with a fast and reliable switching mechanism to continuously measure the cell impedance signal during electroporation, and an algorithm capable of increasing the pulse strength when there is no membrane pore formation or deactivating the pulse when a threshold indicative of irreversible cell damage is reached, hence ensuring the cell viability is not compromised due to over-electroporation.

Chapter eight provides a comprehensive summary for each chapter in this thesis. Ongoing investigation and future work will be discussed including next generation prototypes, prospects for improvement and applications of the developed device.

1.5 Chapter References

1   T. K. Kim and J. H. Eberwine, *Anal. Bioanal. Chem.*, 2010, **397**, 3173–8.

2   N. Woods, A. Muessig, M. Schmidt, J. Flygare, K. Olsson, P. Salmon, D. Trono, C. Von Kalle and S. Karlsson, 2003, **101**, 1284–1289.

3   V. V. Kumar, R. S. Singh and A. Chaudhuri, *Curr. Med. Chem.*, 2003, **10**, 1297–306.

4   I. Martinou, *J. Cell Biol.*, 1995, **128**, 201–208.

5   J. A. O'Brien and S. C. R. Lummis, *Nat. Protoc.*, 2006, **1**, 977–81.

6   J. Dobson, *Gene Ther.*, 2006, **13**, 283–7.

7   H. J. Kim, J. F. Greenleaf, R. R. Kinnick, J. T. Bronk and M. E. Bolander, *Hum. Gene Ther.*, 1996, **7**, 1339–46.

8   D. J. Wells, *Gene Ther.*, 2004, **11**, 1363–9.

9   C. P. Yao, Z. X. Zhang, R. Rahmanzadeh and G. Huettmann, *IEEE Trans. Nanobioscience*, 2008, **7**, 111–9.

10   A. Bolhassani, A. Khavari and Z. Orafa, 2014.

11   J. C. Weaver and Y. A. Chizmadzhev, *Bioelectrochemistry Bioenerg.*, 1996, **41**, 135–160.

12   J. Pepe, M. Rincón and J. Wu, *Acoust. Res. Lett. Online*, 2004, **5**, 62.

13   E. G. Guignet and T. Meyer, *Nat. Methods*, 2008, **5**, 393–5.

14   I. Richard, M. Ader, V. Sytnyk, A. Dityatev, G. Richard, M. Schachner and U. Bartsch, *Brain Res. Mol. Brain Res.*, 2005, **138**, 182–90.

Chapter 2

Electroporation Background

2.1 Electroporation Theories

Cell membrane electroporation is achieved when an applied electric field becomes sufficient to overcome the cell membrane voltage barrier required for reversible electrical breakdown (ΔV_m). The general mathematical expression for this value is shown in Equation 1 where E_{app} is the applied electric field, r is the radius of the cell, θ is the angle polar angle relative to the electric field vector. κ is a value determined by a number of influencing factors, which reported by many authors to be close to 1.5.[1] As a result, ΔV_m varies from cell to cell, and cell type to cell type, but it has a typical range from 0.2 to 1 volts.[2,3]

$$\Delta V_m = \kappa E_{app} r cos\theta \qquad (2.1)$$

This equation reveals that the smaller the cell radius, the higher the electric field required to initiate membrane permeabilization. By this rationale, an electric field strong enough to permeabilize the cell membrane is not able to penetrate intercellular organelles such as mitochondria, and mammalian cells would be easier to electroporate in comparison to smaller cells such as bacteria.[4] Overcoming this resting transmembrane potential is important in initiating the sequence of membrane permeabilization events. Permeabilization occurs at the polar regions of the cell facing the electrodes. However the process begins on the region facing the positive electrode due to the resting, negatively charged cellular interior (Figure 2.1). The extent and degree of permeabilization is attributed to the applied electric pulse amplitude and duration, respectively.[4]

The time scale of membrane pore formation is reported to be in the range of micro-seconds, however pore resealing is a more complex process and usually falls in the range of minutes.[5,6] This has been attributed to the electroporation pulse parameters used (extent of permeabilization), temperature (rate of resealing) and intactness of the cytoskeleton (resealing infrastructure) that assist pore closure. Studies on the resealing time have conventionally been performed in-vitro, and there have been many reports on this front when analyzing different types of cells. Since it is especially crucial in reversible electroporation applications to ensure high viability, methods utilizing surfactant such as *Poloxamer-188* has been demonstrated to aid in membrane resealing and to reduce the electrical trauma induced by the electroporation treatment.[7]
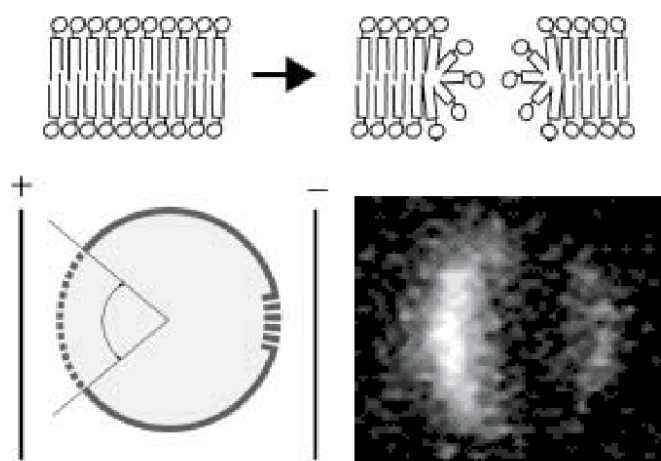
Figure 2.1. Graphical illustration showing the transition from intact cell membrane bilayers to the dielectric breakdown of the membrane causing hydrophilic pores to form. Pores form on the region facing the positive electrode prior to region facing negative electrode. And this is evidenced from the delivery of fluorescence dye into the cell where greater delivery can be seen from the side facing the positive electrode. Reprinted with permission from Gehl *et al.*[4]

Depending on the strength of the electric field, electroporation can either be reversible or irreversible. Both realms of electroporation have their own biotechnological and clinical implications, and thus have been a subject of rigorous investigation in recent years. Reversible electroporation has been in development since the early 1980s. By evoking transient pores to form in the cell membrane, reversible electroporation allows for the transfection of molecules (DNA, RNA, proteins, etc.) into the cell cytoplasm without killing the cell. Irreversible electroporation applies a lethal dose of electric field (typically above 1 kV/cm) to the cells so that the pores in the cell membrane do not reseal after the treatment, resulting in cell death. It has been a useful tool in performing cell lysis for DNA and/or protein extraction, tissue ablation for cancer tumor treatment, and de-cellularization of tissue constructs to create scaffolds.[3,8–10]

2.2 Macroscale Electroporation

The concept of cell membrane disruption with the application of an externally applied electric field was reported as early as the 1950s. It was also found that by tuning the electrical pulse duration alone, cells could recover from the electrical treatments.[11] These pioneering discoveries led the way to open up a brand new direction of research in molecular cell biology, genetics and biomedical engineering. Many electroporation setups, parameters, and treatment protocols have since been reported for a variety of different cell types. The iterative practice and application of these processes amounts to the development of general and diverse recipes for cell electroporation. Several factors have been isolated to account for the success of electroporation in gene transfection. The first important factor is the growth phase of the cells. Several reports have shown that the cells are most electro-competent when they are harvested during the mid-log phase compared to early or late

phases, with a two to five fold increase of transformation efficiency improvement.[12,13] The composition of the electroporation buffer determines not only its resistivity, cell suspension resistance and capacitance, but also strongly influences the cell viability following treatment. Therefore, the second important factor is the medium in which the cells are being electroporated. The medium should contain a non-ionic, osmotic stabilizing ingredient such as sucrose or sorbitol and millimolar concentrations of divalent cations such as Ca^{2+} and Mg^{2+} to tailor the buffer conductivity as well as to promote transformation efficiency and cell viability.[14] The pH of the electroporation buffer should resemble the pH of that cellular cytoplasm as well, 7.2 has been an accepted pH value for most cells. The temperature at the electroporation site has also been reported to affect the transfection efficiency. Temperatures from $0 - 4\degree C$ could slow down the metabolic reaction of the cells and the rapid resealing of the perforated membrane, maintaining the cell viability while facilitating intracellular uptake of molecules. A balanced osmotic environment is also an important factor in electroporation. Following treatment, electropermeabilized cells are exposed to the extracellular space, thus preventing them from swelling or shrinking by using osmotically balanced medium can promote a higher post-pulse viability.[14]

Conventionally, electroporation of cell populations are carried out in large chambers called cuvettes which consists of parallel electrode plates for cell volume ranges from $10 - 100$ µL.[15,16] A concentric electrode geometry with diameter larger than the electrode gap is used when the volume is in the mL range in order to supply a homogenous electric field. There are many commercially available electroporation units; they differ by their pulse configuration, waveforms, buffer conditions, and targeted cell types. Bio-Rad Gene Pulse, for instance, is a popular unit that utilizes exponentially decaying square pulse generators

to transfect a variety of cell populations with high efficiency.[17–19] The basic components of an electroporator consists of current limiting resistors, internal capacitors holding sufficient charge for sample current draw, DC power supply to charge the capacitors, mechanical or solid state relays for pulse triggering, and an oscilloscope for monitoring the pulse output. The applied electric field E is according to the total voltage V applied across the distance between the electrodes d, commonly expressed as $E = \dfrac{V}{d}$.

$$V_t = V_0(e^{-\left(\frac{t}{\tau}\right)}) \qquad (2.2)$$

When a DC pulse is discharged from the capacitor of the electroporator, it follows an exponential decay as shown in Figure 2.2 below. The initial voltage applied between the electrodes is the highest (V_0) and declines overtime following Equation 2.2, where V_t is the final voltage, t is the time, and τ is the time constant, a product of R and C dictates when the output pulse strength falls to 37% of the peak value.[20] Nearly perfect DC pulses can be generated by modern electronics to ensure a time constant in which the voltage drop-off is at the desired voltage level.
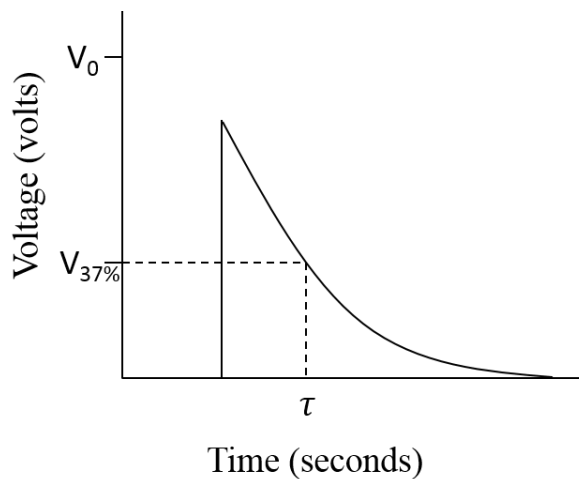
Figure 2.2. Exponential decay of an electroporation pulse from a capacitor.

The applications of electroporation are extensive, a few well-known examples are gene transfection, stem cell differentiation, electroinsertion, cancer therapies. In gene transfection, Wong and Neumann were among the first to demonstrate the delivery of thymidine kinase gene into *tk*-deficient mouse L-cells using electroporation.[21] Since then, it has become standard to transfect cells with nucleic acids and other factors to study various cell functions. An example of cell function investigation is the study of neural stem cell differentiation into murine astrocytes using a micro-capillary electroporation technique to transfect wild type astrocytes with plasmids. This study revealed the critical role of Pax6, is a vital transcription factor for promoting neurogenesis and gliogenesis.[22] Besides gene transfection, electroporation has also been used as a tissue ablation tool to treat cancer. Miller and Rubinsky demonstrated the complete removal of human hepacarcinoma cells (HepG2) by using a high electric field (1.5 kV/cm) and sub-millisecond pulses (300 µs) to irreversibly electro-permeabilize cell membranes.[8] They have identified this irreversible electroporation technique to be an effective and alternative tissue ablation approach to conventional surgical methods. Electro-insertion of proteins is another use of permeabilized cell membranes from applying a pulsed electric field. This technique has found clinical applications to treat serious disease such as HIV virus infection where full-length CD4 (RBC-CD4) is inserted into the human erythrocytes to specifically bind with immunodeficiency virus type-1 (HIV-1).[23]

2.3 Intracellular Molecular Transport

For a cell with permeabilized membrane, small molecules can enter into intracellular space via diffusion regardless of particle charge. However as the molecular size increases, the uptake of these macromolecules by the cell requires an effective driving force other than

diffusion.[24] Many in vivo studies have reported the importance of electrophoretic force necessary for the successful DNA transfection using electroporation.[24] However this mechanism of transport has not been widely studied and only a few speculative and modeling approaches were reported to elucidate this phenomenon. In recent years, investigation from our group has unraveled the mystery behind electroporation-mediated intracellular molecular transport, and offered both theoretical and experimental evidence to demonstrate that electrophoresis is the dominant mode of transport behind electroporation. Our group has also demonstrated that the accumulation of species inside the cell is explained by a phenomenon known as the field amplified sampling stacking (FASS) due to the intra- and outer cell membrane conductivity differences.
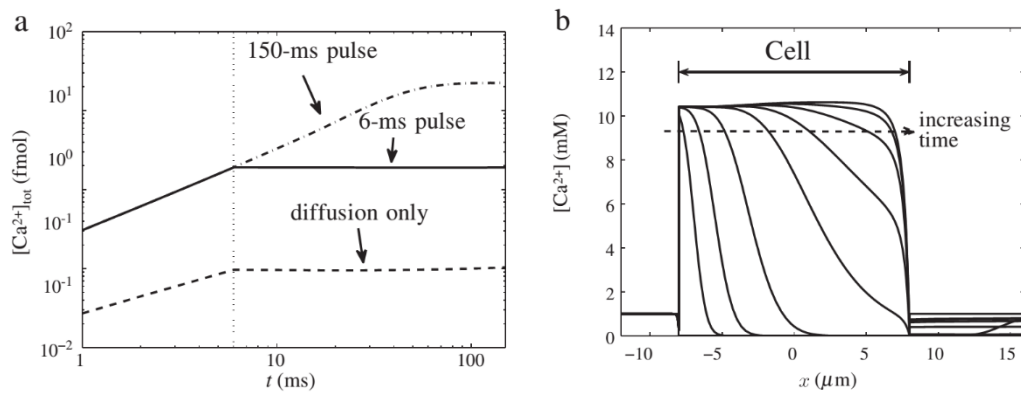
Figure 2.3. (a) Ca^{2+} concentration inside the cell by diffusion and electroporation. Vertical dashed line indicates a 6-ms pulse at 1 kV/cm field amplitude (b) Ca^{2+} concentration at the cell centerline with incremental pulse durations from (0 to 120 ms) while keeping the electric field constant at 1 kV/cm. Horizontal dashed arrow indicates the progression of Ca^{2+} concentration for pulse times of 0, 1.1 ms, 3.3 ms, 10 ms, 30 ms, 50 ms, 70 ms, 90 ms, and 120 m respectively. Reprinted with permission from Li *et al*. [25]

By solving the Nernst-Planck equations for intracellular molecular transport and an asymptotic Smoluchowski equation for cell membrane permeabilization, Li and Lin revealed the important role of electrophoresis in driving the transport of calcium ions into the Chinese Hamster Ovary cells.[25,26] This was performed to numerically explain a similarly observed phenomena by Gabriel and Teissié.[27] Shown in Figure 2.3a, diffusion alone contributes to a considerably lower amount of Ca^{2+} transport into the cell than delivery mediated by electroporation over the same 6-ms pulse time scale. A higher concentration of Ca^{2+} inside the cell was facilitated by using increasingly longer pulsing times from $0 - 120$ ms while keeping the electric field constant (Figure 2.3b). This work demonstrates that electrophoresis is the dominant driving force of molecular transport during electroporation, and the electrophoretic velocity, u, of the molecules is controlled by the applied electric field shown through Equation 2.3 where q is the particle charge, E is the electric field, μ is the dynamic viscosity, R_E is an effective radius of the particle. In comparison, diffusion-mediated delivery through the permeabilized cell membrane is a much slower process.

$$u = \frac{qE}{6\pi\mu R_E} \qquad (2.3)$$

Furthermore, Li *et al.*'s investigation on the effect of extracellular conductivity on electroporation-mediated molecular transport efficiency reported an inverse correlation between the concentration of small molecules such as Propidium Iodide (PI) inside the cell and the extracellular buffer conductivity.[28] As shown in Figure 2.4a-b, both the numerical model prediction and experimental results reported that as the extracellular buffer conductivity increased from $0.1 - 0.5$ S/m, the concentration of PI delivered within the cell decreased accordingly. Extracellular buffer conductivity influenced the distribution of the
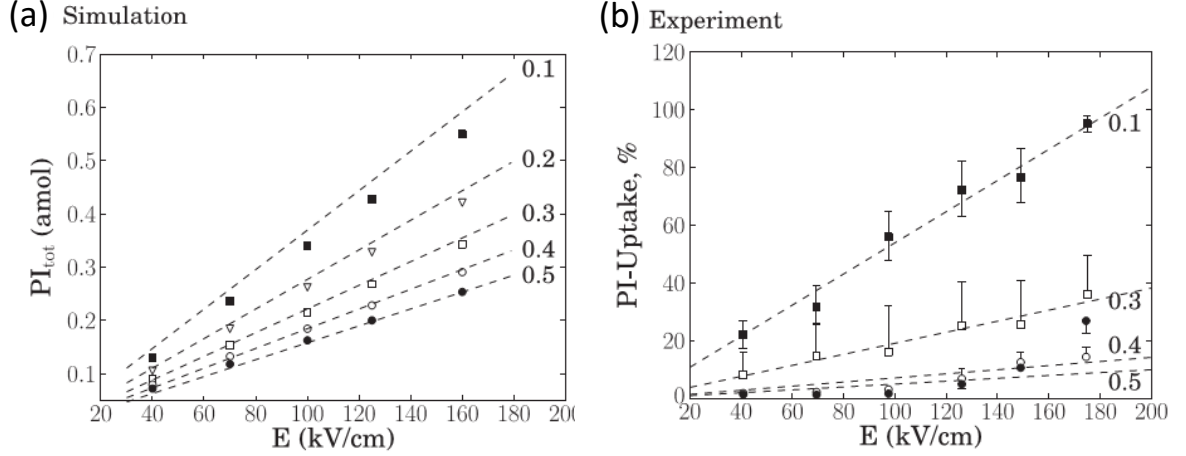
Figure 2.4. (a) Simulated (b) experimentally determined PI delivery into cell with extracellular buffer conductivities from $0.1 - 0.5$ S/cm as a function of electric field and a constant pulse duration at 95 ns. Reprinted with permission from Li *et al.*[28,43]

electric field strongly according to the Ohm's Law of electric current conservation shown in Equation 2.4 where σ the buffer conductivity, E is the electric field, J is the Ohmic current and the subscript *e* and *i* denotes outside and inside the cell, respectively.

$$J = \sigma_e E_e = \sigma_i E_i = Constant \qquad (2.4)$$

When there is conductivity gradient, as in the case of the cell boundary where inside the cell is significantly more conductive (5000 µS/cm) than outside the cell (i.e. 100 µS/cm), according to Equation 2.4, in order to maintain current continuity when $\sigma_e < \sigma_i$, E_e must be higher than E_i. As a result, the electrophoretic force must be higher in the low conductivity buffer. In the presence of an electric field, positively charged ions in the low conductivity buffer would for an instance, electro-migrate in the direction of the applied field, but because of the electrophoretic velocity is directly proportional to the applied electric field, the ions experience a sudden slow-down at the conductivity interface and accumulate. This explains why charged particles tend to accumulate at the cell membrane interface during

electroporation-mediated transport. These electrokinetic theories have also been validated experimentally by Sadik *et al.*[29] By suspending 3T3 fibroblasts in buffers with two different conductivities and tracking the temporal and spatial progression of PI into single cells during electroporation, there was a significantly lower concentration of PI within the cell in the high conductivity buffer (2000 µS/cm) than that of the low conductivity buffer (100 µS/cm), as seen in Figure 2.5.[29] Delivery during the 100 ms pulse application contributes the greatest to the total PI concentration inside the cell, in comparison to diffusion-driven transport.
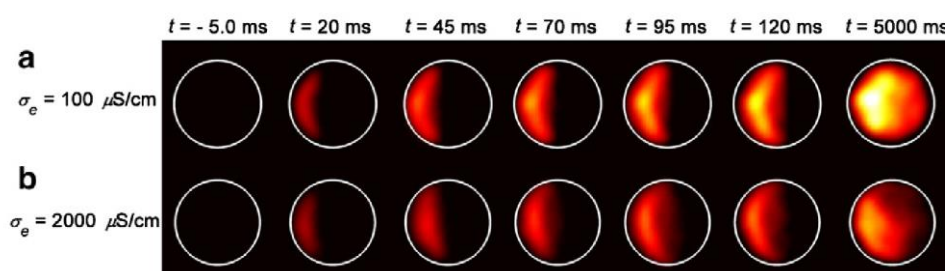
Figure 2.5. Spatial and temporal distribution of Propidium Iodide into a cell during electroporation at a field strength of 0.8 kV/cm for 100 ms for two buffer conductivities (a) 100 µS/cm and (b) 2000 µS/cm. Reprinted with permission from Sadik *et al.* [29]

2.4 Microscale Electroporation

Rapid advancements made in microscale technology in the past decades have re-shaped the landscape of our society, with both life sciences and biotechnology industries undergoing a technological transformation that aim toward system miniaturization. The motivation is to create small analytical and therapeutic tools that could: (1) significantly reduce chemical consumptions and material demands that lead to a lower overall cost, (2) enable faster reactions, quicker turn-around times and analysis, (3) improve productivity

with parallel operations, (4) increase functionality with integratible systems such as electronics to bring forth compact and versatile devices, and (5) provide safer, biocompatible, and controllable platforms for biological study.[30]

There are many advantages to miniaturizing electroporation platforms. Microscale electroporation carries out the electroporation process at the single cell level, and eliminates macroscale level issues such as pH variation, joule heating, non-uniformity of the electric field, extremely high fringing electric field near electrodes and sample contamination. Additionally, electroporation at the microscale also permits: (1) in situ visualization of the intracellular molecular transport process, (2) continuous tracking of cellular responses to stimuli in real time, (3) individual cell manipulation, isolation and
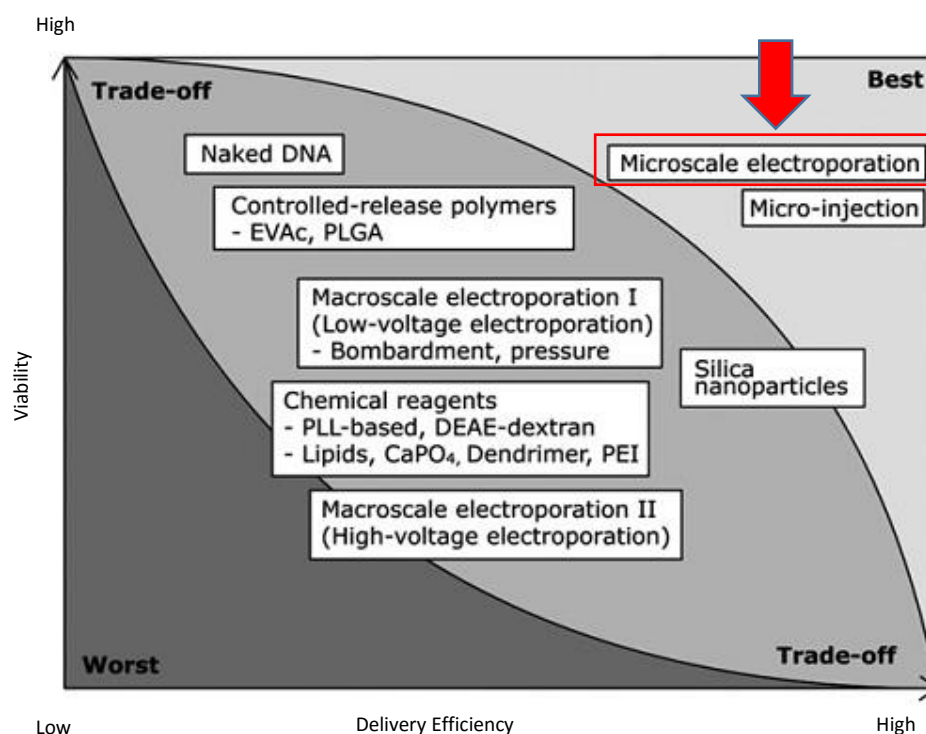
Figure 2.6. Chart showing trade-off between cell viability and delivery efficiency of different non-viral transfection approaches. Reprinted with permission from Lee *et al*. [44]

electroporation, (4) uniform application of electric fields, (5) a potentially automatable process that is simpler, faster and labor-free.[31–35] Because of the ability to manipulate, visualize and analyze single cells and their responses in-situ, researchers in the field such as Khadahussimi have projected that microscale electroporation can potentially maximize both intracellular molecular delivery and cell viability (Figure 2.6).[30]

There are two approaches to single cell electroporation, patch-clamping and patch-free electroporation. The former approach requires the immobilization of the targeted single cell at a prescribed electroporation location, which permits repeated investigation of the same cell (Figure 2.7a-c). Ryttsén *et al.* was among the first to demonstrate single cell electroporation by mechanically positioning a cell between two electrodes with a micropipette.[36] Khine *et al*. later demonstrated the use of a three-layered microchannel to immobilize single cells at a suction hole between two conducting electrode plates. She carried out electroporation and measured current traces indicative of cell membrane permeabilization.[37] In 2004, Lee *et al.* also reported the development of a 2-dimensional microchannel to trap and electroporate single cells. In addition, they also reported the
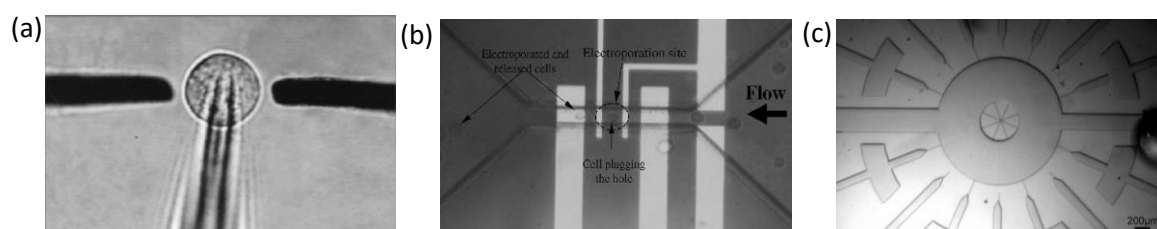
Figure 2.7. (a) Glass micropipette-based electroporation of a single cell. Reprinted with permission from Ryttsén *et al*. [36] (b) A flow-based sandwich microfluidic device for trapping, electroporating and monitoring single cells. Reprinted with permission from Huang *et al*.[45] (c) An array of microfluidic single cell traps for single cell electroporation and current monitoring. Reprinted with permission from Khine *et al*. [34]

measurement of cell membrane permeabilization and resealing signals.[38,39] These studies have provided the foundation for conducting electroporation measurement on single cells. However, one significant drawback associated with this mechanism of single cell study is the inherent low throughput of the devices, in which analysis is limited to only a few cells at once and the treated cells cannot be recovered for further downstream processing.

Rather than immobilizing single cells, there have also been reports on the electroporation of mobile single cells (Figure 2.8a-c). This approach permits the dynamic flow of single cells across a pair of planar electrodes (electroporation site) where a prescribed electric field is constantly applied to permeabilize the passing cells. In 2004, Lu *et al*. showed that with the implementation of saw tooth electrodes parallel to the cell flow direction, extremely high electric fields can be delivered to lyse the passing cells.[10] In a simpler design, Wang and Lu demonstrated that by incorporating an electric field amplifying micro-constriction to focus the cell stream, electric field applied across the constriction can be tuned to electroporate single cells and enable studies of cell swelling and rupture.[40] Recently, the use of acoustic wave in combination with electric field to electro- sonoporate
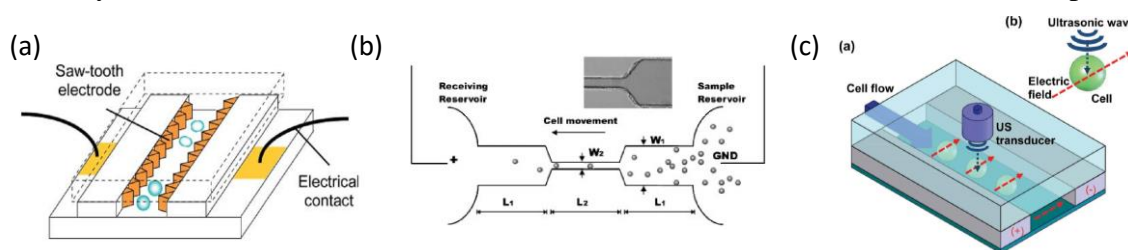
Figure 2.8. (a) Saw-tooth electrode-based electrical lysis of a stream of single cells. Reprinted with permission from Lu *et al*. [10] (b) A constriction-based micro-electroporation chamber for electroporating cells at a high throughput. Reprinted with permission from Wang *et al*.[40] (c) Electrosonoporation of a stream of single cells. Reprinted with permission from Longsine-Parker *et al*.[41]

cells at high efficiency and throughput was demonstrated by Longsine-Parker *et al*. They showed that by directing both electric field and ultrasonic wave to flowing single cells, greater density of transient pores can be created with lower field intensities thus maximizing delivery efficiency while minimizing cell death.[41] Although this is a high throughput electroporation process, little can be learned about the individual cell during the electroporation treatment process, and viability assessment is only feasible through final cell collection and live-dead staining. Additionally, different types of cells would require each of its own empirically-obtained protocols.

2.5 Cell Membrane Permeabilization

The dielectric breakdown of the cell membrane as a result of applied electric field has fascinated scientists as early as the 1970s. In order to detect and investigate this phenomena, Zimmermann and colleagues used a Coulter Counter to analyze the impedance changes among a cell population as electric field varies. They found that there exists a critical electric field threshold at which dielectric breakdown occurs and the cell membrane becomes permeabilized.[42] With the major technological breakthrough of a Patch Clamp amplifier invented in the early 1980s by Erwin Neher and Bert Sakmann, precise electrical analysis of the cell membrane and its ion channels significantly improved our understanding of fundamental cell processes. The Patch Clamp amplifier uses a glass micropipette as the recording electrode, and the size of the pipette tip determines the size of the cell membrane area measured. Suction is then applied to obtain a good seal on the cell membrane, typically in the Giga-ohm range in order to isolate the electrical current signal from the cell membrane from surrounding noise. A reference electrode outside the micropipette was kept at zero current level to compare with the current changes due to the

cell under test. The success of Patch clamping measurements has allowed it to become a standard laboratory tool for studying single cells. However it was not until 2000, when researchers such as Ryttsén *et al.* performed single cell electroporation using patch clamping method to determine the dielectric breakdown voltage for which cell membrane permeabilization occurs.[36] While a pair of electrode wires was placed near the cell to apply the electroporation pulse, an area of the cell membrane was patched to record cell membrane current (Figure 2.9a). As a greater electric field was applied to the cell, incremental changes in membrane current were measured that indicated the formation of larger membrane pores (Figure 2.9b). Many follow-up investigations have since been performed to further understand the electroporation-induced membrane pore formation phenomenon.
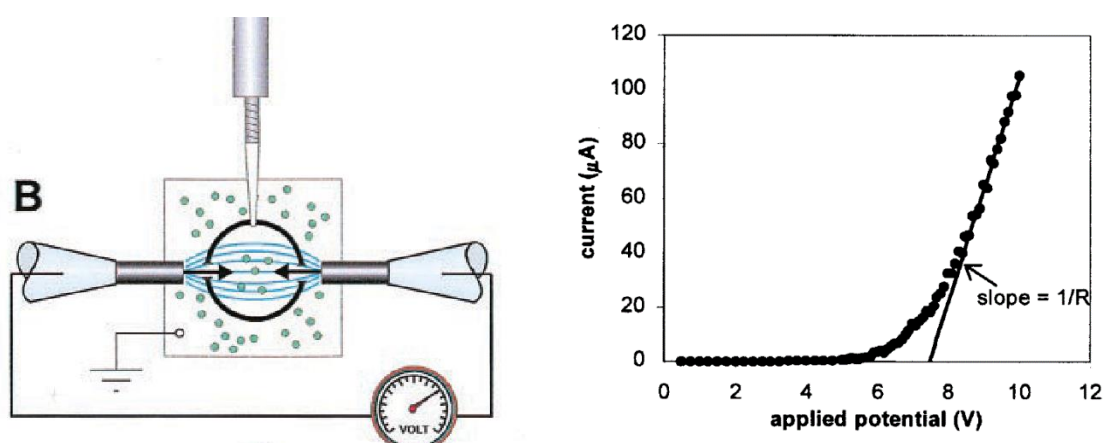
Figure 2.9. (a) Schematic showing glass micropipette-based electroporation setup with an individual cell in the center. (b) Patch clamp current measurement of an individual cell under electroporation with vamping voltages. Reprinted with permission from Ryttsén *et al.*[36]

Recently, advancements made in the field of microfluidics have facilitated an explosion of research in the development of well-controlled single cell manipulation and measurement platforms for cellular analysis. Rather than using a micropipette, Huang and Rubinsky microfabricated a suction hole in a three-layered microelectroporation chip (Figure 2.10a) to physically trap individual cells for electroporation treatment and measurement.[37] By applying a ramped voltage to the cell plugging the suction hole and monitoring the electric current, they showed that a sharp current 'jump' occurred when the voltage reached above 20 Volts, indicative of the dielectric breakdown of the cell membrane (Figure 2.10b).
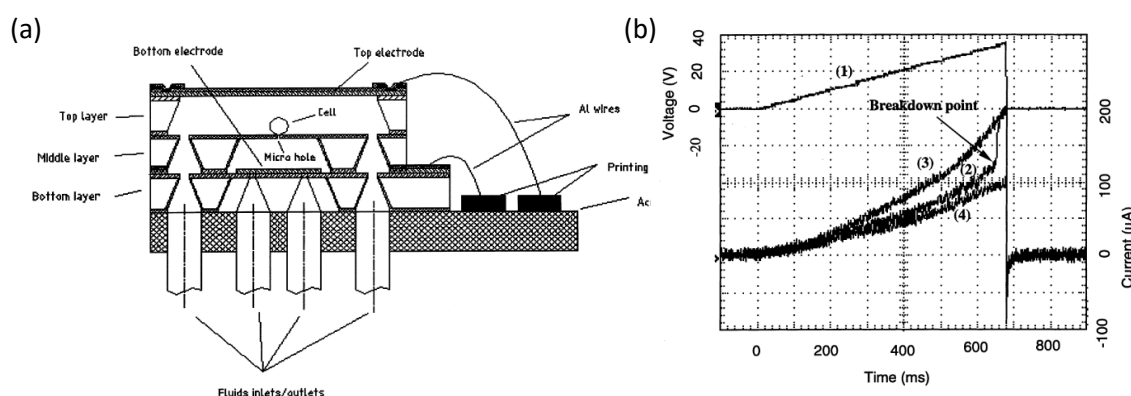
Figure 2.10. (a) Schematic showing a three-layered single cell trapped microdevice. (b) The electrical measurement of the trapped cell current as a vamping voltage was applied. Reprinted with permission from Huang *et al.*[37]

Similar cell membrane permeabilization phenomena were also observed when Khine *et al.* microfabricated a 2-dimensional cell trap device to electroporate single cells and record their permeabilization activities (Figure 2.11a).[34] Instead of a hole, a channel mimicking a rectangular micropipette immobilizes a cell, and two distal electrodes across the cell apply the electric field. Due to the better seal formed by suction, they were able to record a very clear current 'jump' during a voltage sweep, and with a much lower voltage required (0.8 volts) to initiate dielectric breakdown of cell membrane (Figure 2.11b). In addition,

repeated investigation on the same cell also allowed them to discover the occurrence and dynamics of the membrane resealing (Figure 2.11c).
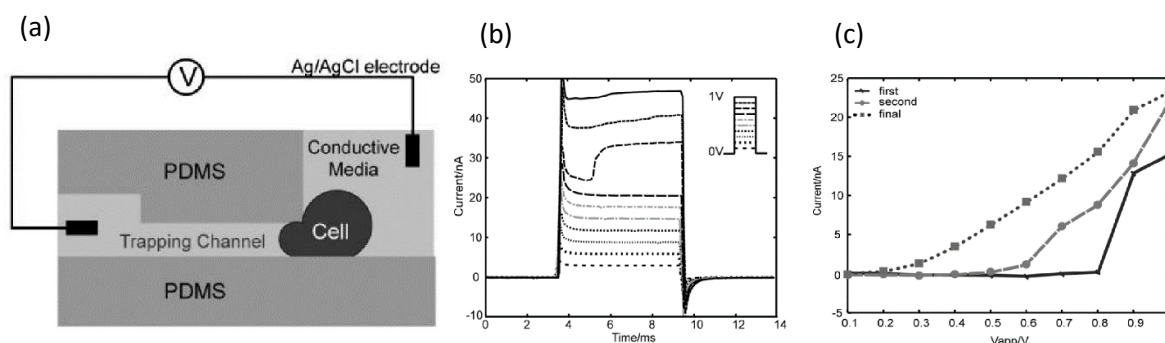
Figure 2.11. (a) Schematic showing a 2-dimensional microchannel for trapping individual cell in a conductive media. (b) Electrical current traces of a cell under 10 incremental voltage pulses. (c) Electrical current traces for three different runs of measurement with delay time in between to observe cell membrane resealing phenomena. Reprinted with permission from Khine *et al.*[39]

It is clear that electric field induced aqueous pore formation on the cell membrane is characterized by the dielectric breakdown of the whole cell membrane. Live cells with intact membranes have a high insulating resistance, intracellular transport of materials is only possible through gated channels. When the membrane of a live cell becomes permeabilized, pore formation lowers the cell membrane resistance, and such decrease in conductance has been repeatedly measured during single cell level electrical sweep. Following the same idea set forth by patch clamping, microfabricated devices have been serving as sensing platforms for recording single cell membrane dynamics.

2.6 Chapter References

1   T. Kotnik, F. Bobanovic and D. Miklavcic, 1997, **43**, 285–291.

2   Justin.Teissie and M.-P. Rols, *Biophys. J.*, 1993, **65**, 409–413.

3   T. Y. Tsong, *Biophys. J.*, 1991, **60**, 297–306.

4   J. Gehl, *Acta Physiol. Scand.*, 2003, **177**, 437–47.

5   M. P. Rols and J. Teissié, *Biophys. J.*, 1998, **75**, 1415–23.

6   R. C. Lee, L. P. River, F. Pan, L. Ji and R. L. Wollmannt, 1992, **89**, 4524–4528.

7   J. Gehl, *Acta Physiol. Scand.*, 2003, **177**, 437–47.

8   J. Lavee, G. Onik, P. Mikus and B. Rubinsky, *Heart Surg. Forum*, 2007, **10**, E162–7.

9   R. V. Davalos, B. Rubinsky and L. M. Mir, *Bioelectrochemistry*, 2003, **61**, 99–107.

10   H. Lu, M. a Schmidt and K. F. Jensen, *Lab Chip*, 2005, **5**, 23–9.

11   *Guide to Electroporation and Electrofusion*, Academic Press, 1991.

12   M. Grey and M. Brendel, *Curr. Genet.*, 1992, **22**, 335–336.

13   N. M. Calvin and P. C. Hanawalt, *J. Bacteriol.*, 1988, **170**, 2796–801.

14   G. L. Prasanna and T. Panda, *Bioprocess Eng.*, 1997, **16**, 261.

15   S. Fiedler and R. Wirth, *Anal. Biochem.*, 1988, **170**, 38–44.

16   E. Neumann, A. E. Sowers and C. A. Jordan, Eds., *Electroporation and Electrofusion in Cell Biology*, Springer US, Boston, MA, 1989.

17   *Proceedings of the 2012 International Conference on Applied Biotechnology (ICAB 2012), Volume 3*, Springer Science & Business Media, 2013, vol. 18.

18   T. Wang, E. S. Lander and D. M. Sabatini, *Cold Spring Harb. Protoc.*, 2016, **2016**, pdb.prot090803.

19   R. Y. Muller, M. C. Hammond, D. C. Rio and Y. J. Lee, *J. Biomol. Tech.*, 2015, **26**, 142–9.

20   E. Neumann, S. Kakorin and K. Toensing, *Methods Mol. Med.*, 2000, **37**, 1–35.

21   T.-K. Wong and E. Neumann, *Biochem. Biophys. Res. Commun.*, 1982, **107**, 584–587.

22   K. Sakurai and N. Osumi, *J. Neurosci.*, 2008, **28**, 4604–12.

23   B. P. Tosi, D. Schwartz, U. Sharma, Y. Mouneimne, J. Hannig, G. Li, G. Mckinley, M. Grieco, C. W. Flexner, J. Lazarte, D. Norse, C. Nicolau and D. J. Volsky, 2016, 4839–4845.

24   S. I. Sukharev, V. a Klenchin, S. M. Serov, L. V Chernomordik and Chizmadzhev YuA, *Biophys. J.*, 1992, **63**, 1320–7.

25   J. Li and H. Lin, *Bioelectrochemistry*, 2011, **82**, 10–21.

26   J. Li and H. Lin, *Biomicrofluidics*, 2010, **4**, 13206.

27   B. Gabriel and J. Teissie, 1997, **73**, 2630–2637.

28   J. Li, W. Tan, M. Yu and H. Lin, *Biochim. Biophys. Acta*, 2013, **1828**, 461–70.

29   M. M. Sadik, J. Li, J. W. Shan, D. I. Shreiber and H. Lin, *Biochim. Biophys. Acta*, 2013, **1828**, 1322–8.

30   W. G. Lee, U. Demirci and A. Khademhosseini, *Integr. Biol. (Camb).*, 2009, **1**, 242–51.

31   W. G. Lee, H. Bang, H. Yun, J. Min, C. Chung, J. K. Chang and D.-C. Han, *Lab Chip*, 2008, **8**, 224–6.

32   J. A. Kim, K. Cho, Y. S. Shin, N. Jung, C. Chung and J. K. Chang, *Biosens. Bioelectron.*, 2007, **22**, 3273–3277.

33   J. A. Kim, K. Cho, M. S. Shin, W. G. Lee, N. Jung, C. Chung and J. K. Chang, *Biosens. Bioelectron.*, 2008, **23**, 1353–60.

34   M. Khine, A. Lau, C. Ionescu-Zanetti, J. Seo and L. P. Lee, *Lab Chip*, 2005, **5**, 38–43.

35   M. Golzio, J. Teissie and M.-P. Rols, *Proc. Natl. Acad. Sci. U. S. A.*, 2002, **99**, 1292–7.

36   F. Ryttsén, C. Farre, C. Brennan, S. G. Weber, K. Nolkrantz, K. Jardemark, D. T. Chiu and O. Orwar, *Biophys. J.*, 2000, **79**, 1993–2001.

37   Y. Huang and B. Rubinsky, *Sensors Actuators A Phys.*, 2001, **89**, 242–249.

38   M. Khine, C. Ionescu-Zanetti, A. Blatz, L.-P. Wang and L. P. Lee, *Lab Chip*, 2007, **7**, 457–62.

39   M. Khine, A. Lau, C. Ionescu-Zanetti, J. Seo and L. P. Lee, *Lab Chip*, 2005, **5**, 38–43.

40   H.-Y. Wang and C. Lu, *Biotechnol. Bioeng.*, 2006, **95**, 1116–25.

41   W. Longsine-Parker, H. Wang, C. Koo, J. Kim, B. Kim, A. Jayaraman and A. Han, *Lab Chip*, 2013, **13**, 2144–52.

42   U. Zimmermann, G. Pilwat and F. Riemann, *Biophys. J.*, 1974, **14**, 881–99.

43   K. J. Müller, V. L. Sukhorukov and U. Zimmermann, *J. Membr. Biol.*, 2001, **184**, 161–170.

44   W. G. Lee, U. Demirci and A. Khademhosseini, *Integr. Biol. (Camb).*, 2009, **1**, 242–51.

45   Y. Huang and B. Rubinsky, *Sensors Actuators A Phys.*, 2003, **104**, 205–212.

Chapter 3

Single Cell Manipulation & Electroporation

Note: Excepts of this chapter was adapted from the following publication:

3.1 Single Cell Manipulation Background

The capability of controlling individual cells is of great interest in many areas of life sciences and biomedical engineering disciplines ranging from cell identification and isolation to gene therapy and cancer research. The growing need to develop adaptable microfluidic systems that match the length scale of biological single cells necessitates the miniaturization, reliability, integratibility, operation simplicity and cost-effectiveness of single cell manipulation platforms. Such a need has been one of the motivations for the advancement of microfuidics.[1] Many micro-scale manipulation techniques have surfaced over the past decades to physically transport, sort, trap, and fuse biological cells.[1–3] Particularly, optical manipulation techniques such as the optical tweezers[4,5] have garnered the reputation of precise control of single cells to move tens of nanometer to hundreds of micrometer distance by exploiting the forces exerted from a strong focused beam of light. Although properly sculpted wave fronts of light can be utilized to easily control motions and flows in micromechanics and microfluidics applications, the cost for such precision is high due to the requirements of high power laser systems and complex microscopic lens setup. Electrical manipulation using electrophoresis (EP) and dielectrophoresis (DEP) is another method to separate and position single cells at the micro-scale. Due to the intrinsic

charges on the cell surface, EP works by acting on the cells' charges under a DC electric field while DEP acts on their induced charges under a non-uniform AC electric field. Even though the electrical forces scale favorably with system size, and the ease of microelectrode fabrication had facilitated their application adaptation, their usage in controlling single cells is not without a toll on the cell such as potential cell damage caused by joule heating at the interfacial electrodes; imposed transmembrane potential; and limited specificity.[6,7] Magnetic forces have also been utilized to separate and sort cells, either by taking advantage of the magnetic property of the cell (iron-containing hemoglobin in erythrocytes) or cell-labeling magnetic nano-particles. The latter approach is the most commonly employed due to its versatility in targeting cells of interest via antibody-antigen labeling for selective cell migration, separation and sorting.[8] Although it is a promising means of cell manipulation, however it does require time-consuming and labor intensive preparation of expensive off-chip antigen-antibody conjugation reagents. Acoustic tweezers that utilize acoustic standing wave to dexterously manipulate single cells have also gained popularity in recent years. This approach uses the chirped interdigital transducers with wide resonance band to obtain real-time control of cells. Because the power density required is so much less than that of its optical counterpart, Acoustic-based techniques are more biocompatible and suitable for miniaturization.[9] However, it is nonetheless a complex operation and requires costly equipment and intensive labor. There has also been demonstration of deterministic cell manipulation through affinity between cell surface receptors and pre-coated microchannel surfaces. Taking advantage of the cell to ligand interactions, targeted cells rotating on the ligand-coated surface alters the flow streams for cell separation, and non-target cells which do not attach to the surface would not rotate.[10,11] This method is

highly efficient in cell identification and sorting, however complexity still exists in the microchannel preparation as well as high cost for the antibody labeling reagents.

The most commonly performed single cell manipulation is through hydrodynamic flows.[12,13] By simply controlling the cell and sheathing buffer stream flow rates in either a two-inlet or multi-inlet microchannel, the flowing single cells can be positioned anywhere along the width of the microfluidic channel and rotate at defined angular velocities as well. An example of hydrodynamically controlled single cell rotation in the microchannel was demonstrated by Daniel Chiu and his colleagues by creating microvortices.[14,15] In their work, a diamond-shaped chamber was constructed adjacent to a straight channel paralleling with fluid flow in order to take advantage of the flow detachment into the chamber to form re-circulating flows. In this chapter, we further explore the maneuverability of hydrodynamic flows to control single cell orientation without the use of micro vortices, rather by merely stratifying the flows in the microchannel and their respective flow ratio to rotate single cells along the channel side wall; and by investigating the correlation between cell angular rotation and flow stream velocity and shear rate to control the cell rotation. Because such rotation mechanism exposes a greater, changing cell surface area, we also demonstrate enhanced intracellular molecular delivery profile by combining the micro-scale electroporation technique with rotating cells. Due to the polar phenomena of electroporation, only the membrane surface perpendicular to the electric field becomes permeabilized after reaching a transmembrane potential threshold. Hence cell rotation allows larger membrane area to be permeabilized and more uniform distribution of the molecules into the cell.

3.2 Hydrodynamic Control of Single Cell Rotation

3.2.1 Hydrodynamic fluid shearing and cell rotation in a microchannel

Characterization of the microfluidic channel under fluid perfusion was carried out to better understand the effects of fluid flow on cell rotation. The schematic in Figure 3.1 illustrates the flow profile at the channel center plane perpendicular to the depth direction with cells experiencing different velocities across the streamlines near the wall. For notation purposes, the *x*-axis represents the flow direction, the *y*-axis extends across the channel width, and the *z*-axis extends in the direction of the channel depth.
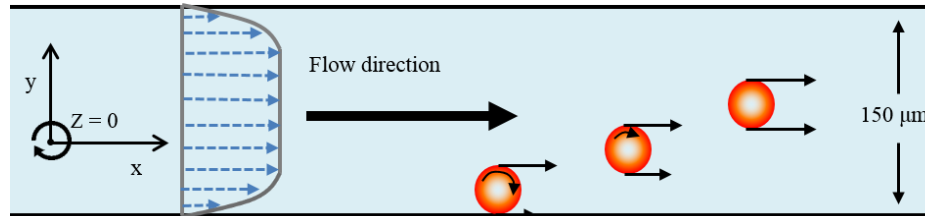
Figure 3.1 Schematic drawing of the velocity profile in a microfluidic channel with cells flowing at various distance away from the side wall. Shear is highest at the wall, while the cell experiences various degrees of rotation depending on its relative position from the wall.

In the idealized case of a spherical particle following a simple two dimensional shear flow (i.e., at a low Reynolds number with torque-free boundary condition at the particle surface), the particle will rotate around the flow vorticity axis (and the particle center) proportional to the local flow rotation rate. The rotation rate, ω, of the particle is directly proportional to the shear rate, $\dot{\gamma}$ as

$$\omega = \frac{\dot{\gamma}}{2}. \qquad (3.1)$$

The general situation with non-spherical, ellipsoidal particles at low Reynolds numbers was considered by Jeffery.[16] In this case, the particle rotation is periodic and will rotate about the particle's two polar axes producing Jeffery orbits. Bretherton has shown that by integrating the fluid motions equations described by Jeffery,[17] the rotation rate can be determined through the period of rotation that a particle revolves about the minor axis as[18]

$$\omega = \frac{2\pi}{T}, \qquad T = \frac{2\pi}{\dot{\gamma}}(r_e + \frac{1}{r_e}) \ . \qquad\qquad (3.2)$$

This relationship provides an angular frequency that takes into account the variability in cell shape represented mathematically by an effective axis ratio r_e of the particle, α/β where α and β are the semi-diameters measured parallel and perpendicular to the axis of rotation. For our considerations, the cell is assumed to be of a spheroid with an effective axis ratio of 1 since the degree of non-sphericity in cell shape is rather small (i.e., a 10% increase in r_e results in <1% increase in ω). With the assumption of r_e being 1, the angular frequency ω of Equation 3.2 reduces to the cell rotation rate determined in Equation 3.1.

The rotation rate depends on shear rate, which is a function of the infused fluid flow rate, the location of cells within the flow channel, as well as the particular channel geometry. For a single cell suspended in buffer under uniform shear rate, $\dot{\gamma}$, in a one dimensional flow, the fluid's rate of velocity change is normal to the direction of flow at a distance y away from the wall boundary.[18] The shear rate equals zero ($\dot{\gamma} = 0$) when all cells are flowing at the same velocity within parallel streamlines, and becomes non-zero in the presence of shear as the flow velocity varies across the streamlines.

We analytically calculate the one-dimensional flow profile within the channel as a function of distance across the channel and channel depth. The flow is expected to be parabolic in

the depth-wise (z) direction. Across the width (y) of the channel, the lateral walls will create a wall boundary layer with a uniform core velocity at any depth. Following similar microchannel characterization studies,[19] velocity and shear stress profiles of a Newtonian fluid of viscosity η flowing in a microfluidic channel with a known cross-sectional dimension of 150 µm × 20 µm was plotted at the depth-wise centerline ($z = 0$ plane) in Figure 3.2a according to the exact solutions to Stokes equation for the channel geometry.[20] The fully developed solutions for axial velocity, $u(y,z)$ and flow rate, Q can be represented in terms of the pressure gradient dP/dx, solution viscosity and channel geometry as shown in Equation 3.3 and 3.4:

$$u(y,z) = \frac{16a^2}{\eta\pi^3}\left(-\frac{dP}{dx}\right)\sum_{i=1,3,5..}^{\infty}(-1)^{\frac{i-1}{2}}\left[1 - \frac{\cosh\left(\frac{i\pi y}{2a}\right)}{\cosh\left(\frac{i\pi b}{2a}\right)}\right]\cos\left(\frac{i\pi z}{2a}\right)/i^3 , \quad (3.3)$$

$$Q = \left(\frac{4ba^3}{3\eta}\right)\left(-\frac{dp}{dx}\right)\left(\left[1 - \frac{192a}{\pi^5 b}\sum_{i=1,3,5..}^{\infty}\left[\frac{\tanh\left(\frac{i\pi b}{2a}\right)}{i^5}\right]\right]\right). \quad (3.4)$$
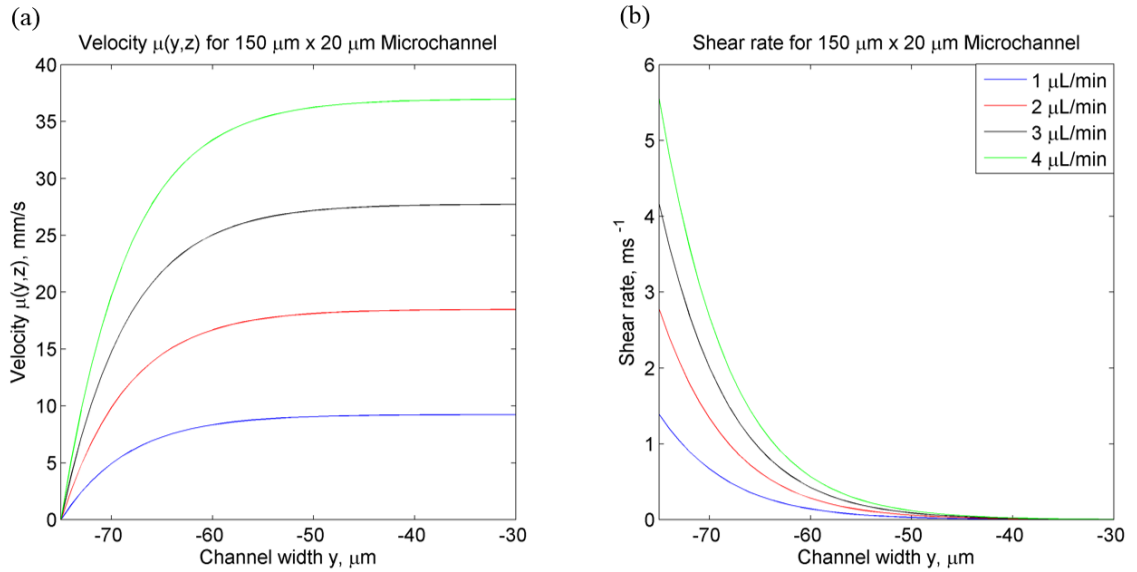
Figure 3.2. Fully developed (a) velocity and (b) shear rate profile in a rectangular microfluidic channel at the center plane ($z=0$), calculated from Equation 3.3 and 3.5.

Briefly, *i* is an odd integer for the series solution, the solution is valid over the bounds of *-b < y <b* and *–a < z < a* where b is the channel half-width and *a* is the channel half-depth. The shear rate *γ·* can be determined by taking the derivative of the axial velocity with respect to *y* assuming the cell is on the center plane (*z=0*),

$$\dot{\gamma} = \frac{\partial u(y,z)}{\partial y}\bigg|_{z=0} = \frac{16a^2}{\eta\pi^3}\left(-\frac{dP}{dx}\right)\sum_{i=1,3,5..}^{\infty}(-1)^{\frac{i-1}{2}}\left[-\left(\frac{i\pi}{2a}\right)\frac{\sinh\left(\frac{i\pi y}{2a}\right)}{\cosh\left(\frac{i\pi b}{2a}\right)}\right]\left(\frac{1}{i^3}\right). \quad (3.5)$$

The resultant plot is shown in Figure 3.2b. For the channel width of 150 µm, the highest velocity occurs in the center of the channel, and is constant across a 60 µm width extending both left and right. The flow profile is also parabolic in the depth-wise direction. For our analysis, the cells were assumed to travel on the depth-wise center plane due to the shallow channel depth (20 µm) so the rotation is exclusively due to vorticity in the *z*-direction. Experimentally, we found that the cells rotate about the *z*-axis without any forward tumbling from rotation about the *y*-axis, validating this assumption. The greatest shear rate occurs at the lateral sidewalls where the flow velocity decreases because of the influence of the bounding walls of the channel.

Closer examination of the fluid shearing motion acting on the cell can reveal how it translates into effective cell rotation. When a single cell flows close to the channel walls, in the presence of the velocity gradient, two different sides of the cell experience a different velocity depending on the diameter and position of the cell relative to the wall. The shear vorticity is maximal at the walls of the channel where the shear is the greatest so cells within this boundary layer experiences rotation due to the shear gradient. For instance, when the centroid of a 10 µm diameter cell is positioned 10 µm from the wall during a 4 µL/min fluid perfusion rate, the cell's edge closest to the wall (*y=5* µm) would experience

a velocity of 20 mm/s whereas the cell's edge furthest from the wall (y=15 µm) would experience a velocity of 34 mm/s; the velocity differential thereby rotates the cell in a counter clockwise direction. Based on the tendency of a suspended cell to rotate along its vorticity axis, we believe that perfusing the sheath stream can create controllable cell rotation by hydrodynamically pinching the cell stream at prescribed velocities against the channel wall in the x-y plane.

However, the analyses performed by Jeffery assumed an isolated particle within a linear shear flow. In our system, the flow shear rate determined by Equation 3.5 is not a linear shear flow. The cell can disrupt the flow profile as the fluid flows around the cell, and friction on the cell can adversely affect the translation of the fluidic shear into rotational torque due to the lateral bounds as well as top and bottom channel walls. We recognize that complex cell rotation behavior could arise when a cell rotates near the boundaries due to viscous interactions between the fluid, cell and walls; and these wall effects on the rotating cells are amplified by three bounding walls of the channel. The effect of channel boundaries on the rotation rate of rigid particle having a fixed radius has been studied in detail with varying particle-wall gaps in the low-Reynolds-number regime[21,22] where the rotation rate decreases logarithmically as the particle edge approaches a bounding wall. For cells that are pinched to the sidewall, a correction factor would need to be determined to account for the aggregating wall effects under hydrodynamic rotation.

3.2.2 Device Microfabrication

In order to experimentally rotate single cells under hydrodynamic flow, microfluidic channels with a two-inlet, two-outlet and a three-inlet, three-outlet geometry were designed in AutoCAD designer software (AutoCAD Autodesk 2015, San Rafael, CA) with a

dimension of 1 cm in length, 150 µm in width and 10 µm in depth. It was fabricated using standard soft lithography methods to create an SU-8-based master mold. Briefly, a ratio of 1:10 polydimethylsiloxane (PDMS) elastomer to curing agent was mixed then cast onto the master mold to obtain a negative replica of the features after overnight oven curing at 65 ℃. To ensure a closed microfluidic device, the surfaces of PDMS microfluidic device and a glass substrate were irreversibly bonded under oxygen plasma at 100 W power for 60 seconds.

3.2.3 Cell Culture & Harvest

NIH 3T3 mouse fibroblast cells were cultured in Dulbecco's modified eagle medium supplemented with 10% v/v fetal bovine serum, 1% v/v penicillin-streptomycin, and 1% L-glutamine (Sigma-Aldrich, St. Louis, MO). Cells were harvested for experiments when they reached a confluency at roughly 80%. Prior to each experiment, the cells were transferred into an electroporation buffer after 2 minutes of trypsinization, centrifugation and aspiration of the trypsinized media. The electroporation buffer is an osmotically balanced solution consisting of 250 mM sucrose, 10 mM HEPES, and 0.4 mM of $MgCl_2$ salt was added to provide a buffer conductivity of 100 µS/cm.[23] A Conductivity/TDS Meter (Oakton, Vernon Hills IL) was used to ensure the solution conductivity. A buffer solution pH of 7.4 is maintained and measured with a Beckman 340 pH/Temp Meter (Beckmann Coulter, Inc., Fullerton CA). The solution osmolarity was carefully adjusted to a suitable cell level of 310 mOsm/kg using the Advanced Osmometer 3D3 (Advanced Instrument, Norwood MA).

3.2.4 Generating Non-rotating Cells

In order to generate non-rotating cells flowing down the length of the microfluidic channel, hydrodynamic focusing technique was implemented for stable cell positioning and rotation balance (Figure 3.3a). The pulsing buffer served as sheath fluid to sandwich the cell stream in this setup was infused from two of the lateral inlets in a three-inlet, three-outlet microchannel at equal flow rate. While keeping the cell stream at a constant flow rate of 0.5 µL/min, flow rates of lateral sheath streams were increased from 0.5 to 4.5 µL/min at an increment of 0.5 µL/min in order to focus the cell stream to the channel center, pinching the cells into a single file.
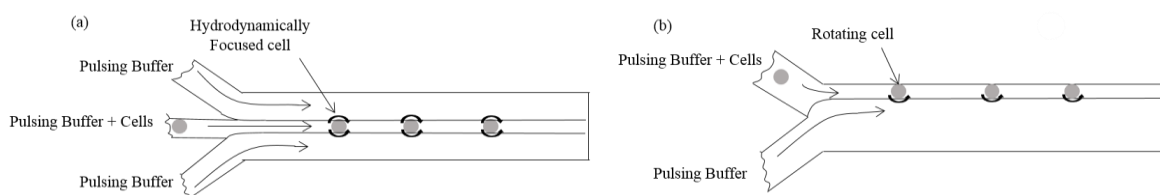
Figure 3.3. (a) Schematic of a three-inlet microchannel with cell carrier flow being hydrodynamically focused between two sheathing flows. (b) Schematic of a two-inlet microchannel with cell carrier buffer infused from the top inlet whereas the sheath pulsing buffer is infused from the bottom to pinch the cells into a single file along the side wall.

3.2.5 Generating Rotating Cells

Cell rotation was generated in a two-inlet, two-outlet microchannel using a differential flow-shearing technique (Figure 3.3b). The pulsing buffer was infused from one of the inlets to serve as sheath to define the width of the cell stream to the channel wall at a relatively higher flow rate; whereas the 3T3 mouse fibroblast cells suspended in the pulsing buffer was infused from the other inlet. To investigate how changing the flow rate ratio

between sheath and cell stream would affect cell angular velocity, an incremental ratio of 1, 2, 5, and 10 was used. Since we are also interested in determining the correlation between perfusion flow rate and cell angular velocity, flow rates from $1.0 - 4.5$ µL/min at 0.5 µL/min increment was employed for each ratio. We hypothesize that higher flow rate ratio between the two streams would yield larger degree of cell rotation, and faster flow rates would further enhance the rotation. In order to capture clear cell rotation, our CMOS camera was set at maximal capture rate of 2000 frames per second to properly acquire clear images of the fast flowing process, and 4.5 µL/min was the maximal tolerable flow rate prior to irresolvable image quality.

3.2.6 Cell Rotation Tracking

Bright field images of flowing single cells were captured using a CMOS multi-modal camera (PCO Inc., Baltimore MD) under the rolling shutter mode. Because cellular surface markers are crucial in the measurement of its rotational velocity, cell features such as shape and organelle linings need to be visibly identifiable. This was achieved geometrically by reducing the height of the microchannel to a minimal of 10 µm to prevent blurriness from vertical cell drift and optically by setting the microscope to a differential interference contrast (DIC) mode. DIC is an illumination technique that takes advantage of the differences in the light refraction by different parts of the specimen to enhance contrast in unstained samples. A total of 1000 images were individually collected for each cell along with their instantaneous time signature. All raw images and data were collected and analyzed using MATLAB (The Mathworks, Inc., Natick, MA).

3.2.7 Experimental cell rotation

Figure 3.4 demonstrates the hydrodynamic control of a cell stream width (top: clear solution with cells) via a sheath buffer (bottom: green dye labeled buffer). Depending on the flow rate ratio between the two streams, a tailorable cell-stream width between 13 and 72 µm was achieved as the cell-stream flow rate was varied from 0.1 – 1 µL/min while keeping the sheath-stream flow rate constant at 1 µL/min to produce a sheathing/cell-stream flow-rate ratio of 10:1 to 1:1. Cells are more efficiently pinched to the sidewall as the flow rate ratio increases. Representative longitudinal cell rotation in a counter-clockwise direction at different flow rates and flow rate ratios is demonstrated in Figure
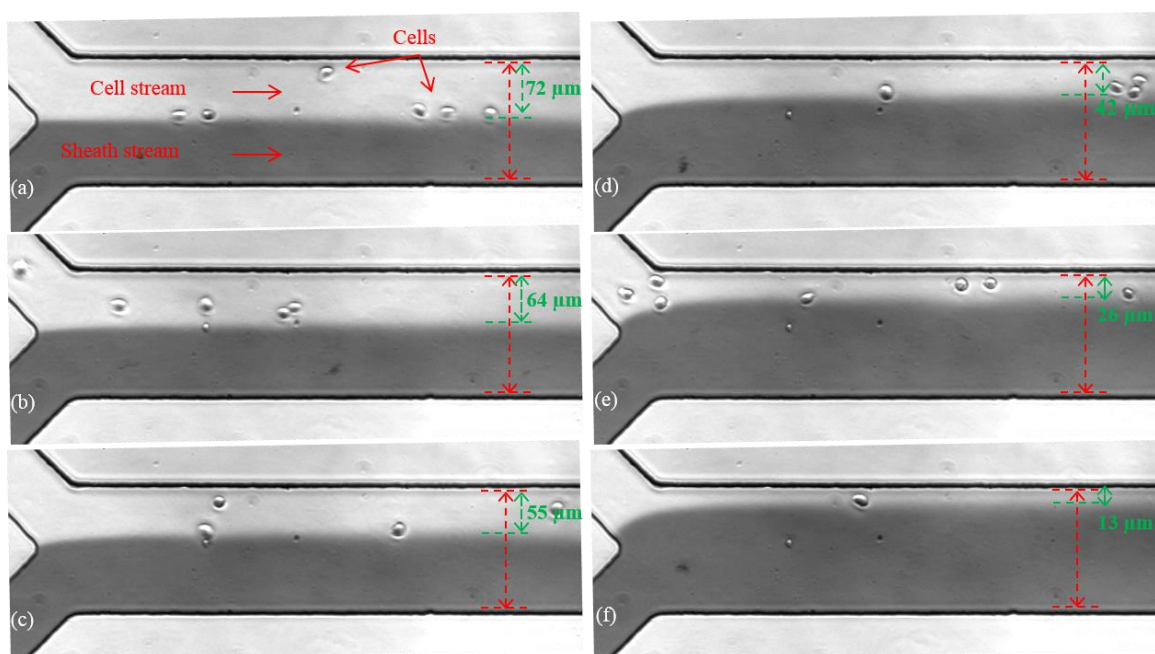
Figure 3.4. Hydrodynamic patterning of the cell stream by a sheathing stream labeled with green dye at 1 µL/min flow rate. The sheath stream increasingly pinches the width of the cell stream which is set to (a) 1 µL/min (b) 0.8 µL/min (c) 0.6 µL/min (d) 0.4 µL/min (e) 0.2 µL/min and (f) 0.1 µL/min. As a result, the measured width of cell-carrying buffer reduces from (1) 72 µm to (2) 64 µm (3) 55 µm (4) 42 µm (5) 25 µm (6) 13 µm.

3.5. The rotation rate was determined by tracking a constant cell feature from the acquired DIC images such as shape or cytoplasmic structure (marked by arrows) at the periphery of the cell over a period of 80 ms to ensure accuracy of the angular velocity measurement.

$\omega = 0.4\ °/ms$ $Q_{cell} = 0.1\ \mu L/min, Q_{sheath} = 0.2\ \mu L/min$

$\omega = 0.8\ °/ms$ $Q_{cell} = 0.1\ \mu L/min, Q_{sheath} = 0.5\ \mu L/min$

$\omega = 2.3\ °/ms$ $Q_{cell} = 0.2\ \mu L/min, Q_{sheath} = 2\ \mu L/min$

$\omega = 4.1\ °/ms$ $Q_{cell} = 0.4\ \mu L/min, Q_{sheath} = 4\ \mu L/min$

(a)

(b)

(c)

(d)

0 ms   20 ms   40 ms   60 ms   80 ms
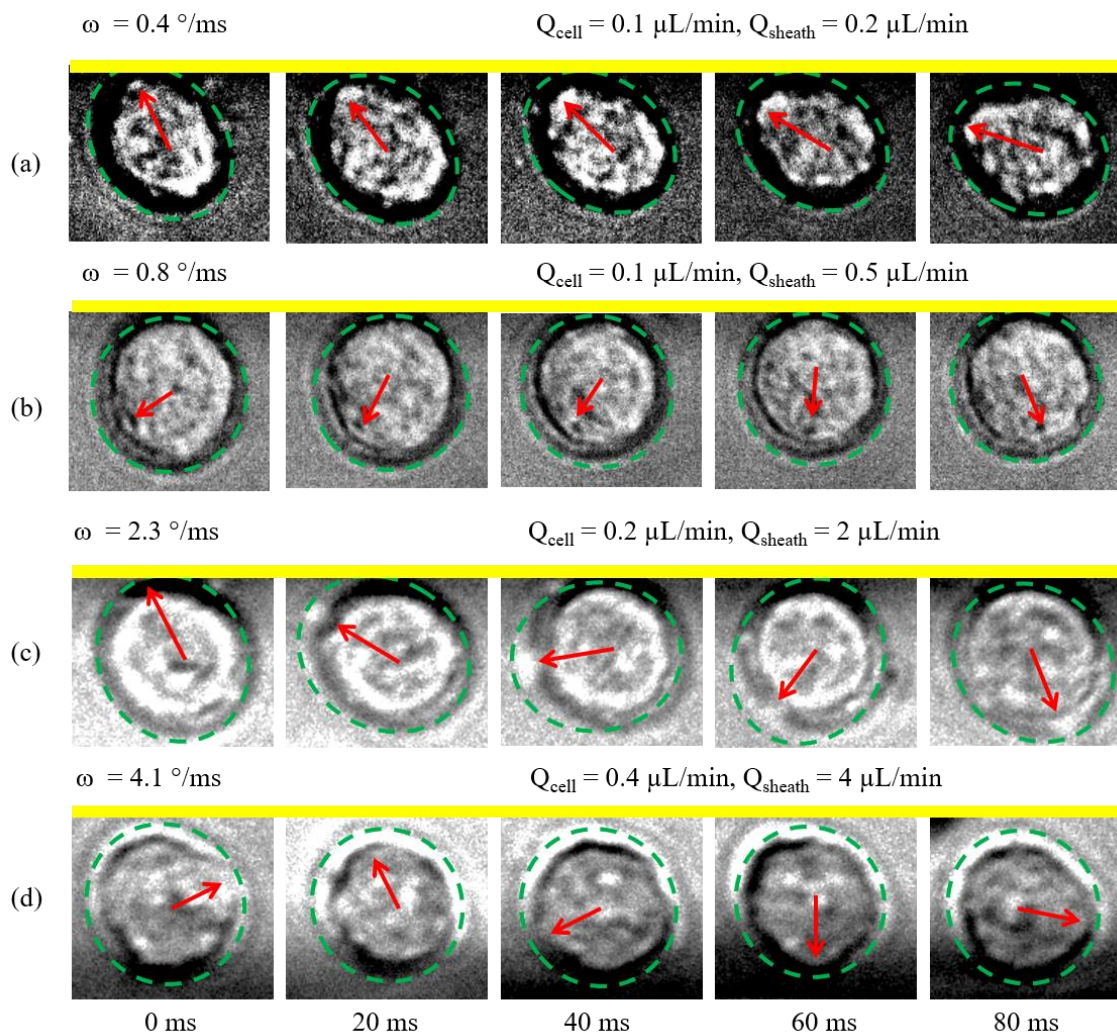
Figure 3.5. Differential Interference Contrast Microscopy (DICM) images showing four single cells perfused from left to right, rolling at 4 angular velocities using 4 sets of sheathing flow rates and flow rate ratios.

Cell angular velocity (ω) can be controlled by the flow-rate ratio between the cell (Q_{cell}) and the sheath stream flow rates (Q_{sheath}) and the total flow rate ($Q_{cell} + Q_{sheath}$). As demonstrated in Figure 3.5a-b, Q_{cell} was maintained at 0.1 µL/min while Q_{sheath} was varied from 0.2 to 0.5 µL/min to obtain an increase in flow-rate ratio from 2:1 to 5:1. This resulted in an increase in ω from 0.4°/ms to 0.8°/ms, respectively. Cell angular velocity can also vary with increasing flow rates while maintaining the same flow rate ratio between Q_{cell} and Q_{sheath}. Figure 3.5c-d demonstrate that at a flow-rate ratio of 10:1, doubling Q_{sheath} from 2 to 4 µL/min and Q_{cell} from 0.2 to 0.4 µL/min results in an increase in ω from 2.3 to 4.1°/ms, approximately doubling the rotation rate as well. These results indicate that both the flow rate ratio and flow rates affect the cell angular velocity.
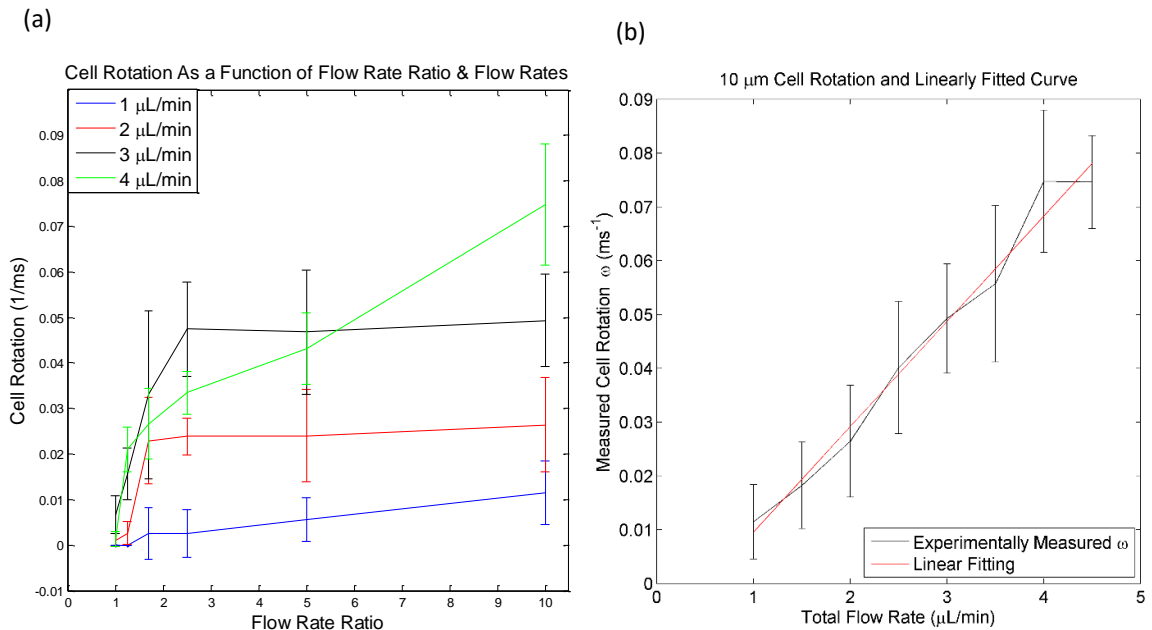
Figure 3.6. (a) Cell angular velocities changes as a function of sheath flow rate ratios and flow rates (b) Linearly fitted curve (red curve) on cell angular velocities experimentally measured at fixed flow rate ratio of 10 (black curve).

In order to compare the measured rotation rate to that predicted by Equation 3.1, experimental evaluations of 240 cells were carried out to measure the cell angular velocity as a function of both the flow-rate ratio and total flow rates (Figure 3.6). Figure 3.6a shows that even at the lowest flow rate (1 µL/min), increasingly greater cell rotation can be observed with increasing flow-rate ratio, albeit this dependence is small due to the small shear rate. The higher flow-rate ratios elicit a greater and more reliable angular rotation since all cells are pinched closer to the sidewall. However, at lower flow rate ratios (<10:1), cells in the cell stream are not completely pinched to the channel sidewall but are distributed across the stream width. As a result, cells further from the wall experience a lower average fluidic shear. In addition, cell margination at higher flow rates can further enhance the cell's movement away from the channel wall. A cell-free layer tends to form close to boundaries due to a cell's propensity to marginate towards an area of low shear.[24] In these cases, cells that migrate away from the channel wall will experience less rotation. As the sheath flow rate is increased, the degree of cell rotation can be greatly enhanced as a result of the increased shear rate. While maintaining a flow-rate ratio of 10:1 between the sheath and cell streams, the cell rotation rate was plotted as a function of increasing total flow rate (black curve) (Figure 3.6b). There was a linear dependence between the cell rotation rate (within error bars) and flow rate. Thus, the rotation rate can be easily adjusted simply by increasing the total flow rate while maintaining a constant flow-rate ratio of 10:1.

Since the angular velocity of cell rotation is directly proportional to the shear rate of the fluid, a direct link to control the cell rotation through the sheath-flow velocity (flow rate) can be established. The 3T3 fibroblasts used in the experiments have an average diameter of 10 µm, and since they were pinched hydrodynamically to the channel wall, the resultant

angular rotation was compared to the shear vorticity estimated within an 8–10 μm distance of boundary shearing layer. The measured rotation rate was 4.5% of the rotation rate predicted by Equation 1. This discrepancy was attributed to wall effects[21] and wall frictional forces from the boundaries acting on the cell. Vahidkhah and colleagues observed similar discrepancy in their simulation to quantify the tumbling frequency of platelets in the presence and absence of whole blood. For isolated platelets tumbling close to the channel side wall under linear shear flow in a single-bounding wall, its tumbling frequency is 10% compared to the platelets far away from the wall in a cell-free layer.[25] Additionally, in our experiments, not all cells were perfectly pinched to the channel side wall due to an irregular cell shape or natural cell drift. Thus, since shear rate decreases rapidly with distance from the wall, the rotation rate of cells located away from the wall would be expected to decrease as well.

3.3 Intracellular Transport of Small Molecules into Stationary Single Cells

An example application of controlled cell rotation via hydrodynamic 'pinching' in the microchannel is the enhancement of intracellular delivery profile when the technique is integrated with single cell level electroporation. We hypothesize that by rotating the cell in a uniform electric field, larger cell surface area can be electroporated to allow greater and more uniform transport of molecules into the cells. This section describes the real time, spatial and temporal tracking of fluorescent probes being delivered into stationary single cells and performs fluorescence analysis to confirm electrokinetic-driven transport phenomena. Partial and circumferential cell membrane permeabilization is demonstrated through the optical tracking of fluorescent probes into rotating single cells in the

microfluidic channel in the next section. The extension of this cell rotation-mediated circumferential electroporation platform to include the transport of large molecules is also demonstrated in the last section of this chapter.

3.3.1 Single Cell Electroporation

The ability to track fast molecular uptake events during electroporation-mediated delivery was first demonstrated with stationary 3T3 fibroblasts. A microfluidic channel identical to that used for hydrodynamic cell rotation study was used here. It has a channel dimension of 1 cm in length, 150 µm in width and 10 µm in depth. A pair of metal electrodes 50 µm in width with a center-to-center distance of 410 µm was designed to deliver the electroporation pulses without generating electrolysis and provide a large optical window for capturing molecular transport events (Figure 3.7). The planar electrodes were fabricated using a physical vapor deposition machine (Kurt J. Lesker PVD 75, Jefferson Hills PA) to sputter titanium and platinum onto lithographically patterned, and buffered hydrofluoric acid (BHF) etched glass slides. Immediately after surface activation using the oxygen
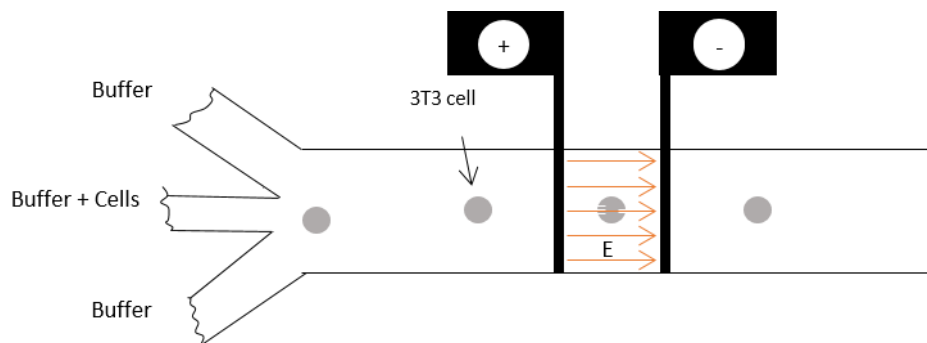
Figure 3.7. Schematic of a three-inlet microchannel with a pair of planar electrodes that intersects the cell carrier flow. Electroporation pulse is applied to the 3T3 cells that came to a natural stop in between the electrodes when the flow is stopped. Orange arrows indicate the direction of the electric field.

plasma machine, the electrode-patterned glass substrate was aligned then bonded with the PDMS microfluidic channel under a stereo microscope (Olympus SZ61, Center Valley PA) to create a vertical intersect of the microfluidic channel. Conductive epoxy (Circuit Works, Inc., Somerville NJ) was applied to fuse the exposed planar electrode pads with single threaded copper wires, allowing connections with peripheral electronics.

3T3 mouse fibroblasts harvested at 80% confluency were perfused into the microfluidic channel through any of the inlets at an initial, arbitrary albeit sufficiently high flow rate to establish cell passage between the electrodes. This region is hereby denoted as the electroporation zone. The cell flow was then turned off to allow the cells to come to a natural stop. For a cell density of 2 million/ml measured in our experiments, approximately three cells are typically settled in the middle of the electroporation zone. To enable fluorescence-based delivery monitoring during electroporation experiments, Propidium iodide (PI) was included in the pulsing buffer at a final solution concentration of 100 μM. PI (FD, Life Technologies, Grand Island, NY) is a nucleic-acid binding dye that is used as a fluorescence reporter, it has a 536 nm excitation wavelength and a 617 nm emission wavelength. A custom-designed electroporator was used to conduct the electroporation procedures in this chapter.[79] It comprises of a DC power supply (KiKsui Pan70-5A, Yokohama Japan) capable of reaching a high voltage of 350 volts, electrolytic capacitors (capitol scientific, Austin TX) at high capacitance (2100 microfarad) for storing sufficient electric charge, and a control module for adjusting input and output voltages, external triggering connections and multiple-pulse application mechanisms. The pulse duration, delay and frequency of application was controlled by a BNC model 555 pulse delay generator (Berkeley Nucleonics Corporation, San Rafael CA).

Three electroporation pulse durations (10, 20, and 50 ms) were separately applied to different cells while keeping the electric field strength constant at 0.6 kV/cm. The fluorescence intensity of the PI was continuously tracked before, during and after pulse initiation. In order to optically track the rapid uptake events during electroporation-mediated molecular delivery, the same CMOS camera was used to capture fluorescence images at 2000 frames per second under a 0.5 ms exposure time. A fluorescent lamp (Nikon Intense C-FGHI, Nikon, MA) was used to excite the fluorescent dye molecules. The camera was synchronized with the electroporator timing module and the pulse output generator so that instant activation of optical recording and electroporation with negligible delay (<1 ns) can be obtained when the pulse is initiated. This synchronization is essential in obtaining precise temporal information on the acquired fluorescence images. The output of the pulse generator was connected to a 54600B model oscilloscope (Hewlett Packard, Palo Alto, CA) for visual verify the applied electric field parameters such as pulse strength, duration, frequency and shape. All raw images and data were collected and analyzed using MATLAB (The Mathworks, Inc., Natick, MA). To account for background noise, four corners of each image with a dimension of 20 x 20 pixels where continuous changes were not observed was first averaged then subtracted from each image. The total fluorescence intensity of each cell was calculated by summing the signal over the entire cell volume for each image frame.

3.3.2 Intracellular Molecular Delivery Analysis

Optical tracking of PI delivery into the stationary cell via the CMOS camera allows us to visually identify the fluorescence intensity differences when longer pulse duration was applied. Figure 3.8 demonstrates the temporal and spatial progression of PI inside three different cells under three different electroporation pulse durations (10, 20, and 50 ms). At the 10 ms time mark, the cell that received the 10 ms-pulse yielded a smaller amount of PI delivery compared to the cells electroporated for 20 and 50 ms, as indicated by their fluorescence intensity. Subsequent measurements at different time points also show significant fluorescence intensity increases for the latter two pulse conditions. This observation suggests that at 0.6 kV/cm field strength, a 10 ms pulse is sufficient to overcome the transmembrane potential and permeabilized the cell membrane, however
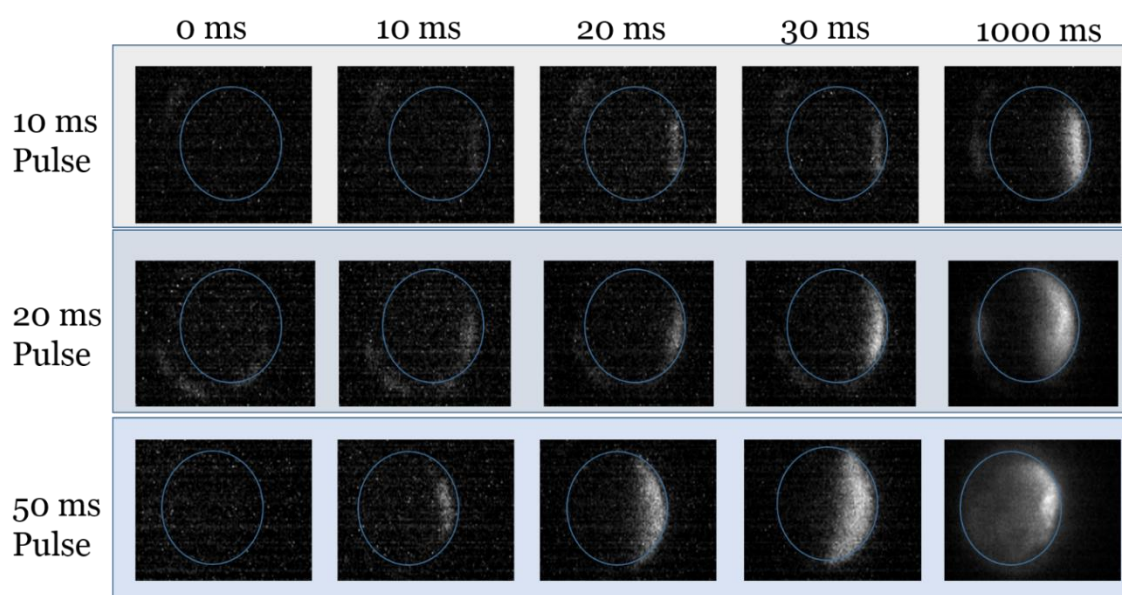
Figure 3.8. Temporal and spatial progression of Propidium iodide during electroporation for three different stationary cells (labeled by blue circle). Each cell received the same pulse strength of 0.6 kV/cm but different duration: 10 ms, 20 ms, and 50 ms.

longer electric field exposure is required to drive the transport of PI into the permeabilized cell membrane.

To quantify delivery, PI fluorescence intensity was summed over the cell image area for every frame captured. Plotted as a function time in Figure 3.9, the progression of PI before, during and after the electroporation pulse application reveals the dynamic transport process. A delay of 10 ms prior to the application of the first pulse marks the initial fluorescence baseline for post-pulse comparison. When a 20 ms pulse was applied to the cell, the electric field permeabilized the cell membrane in approximately 10 ms as showed by the graduate increase in fluorescence intensity (Figure 3.9). The sharp change in slope indicates electrophoresis driven transport, since the migration of positively charged PI into the cell occurs over a very short period of time. As mentioned in the previous chapter, this is due
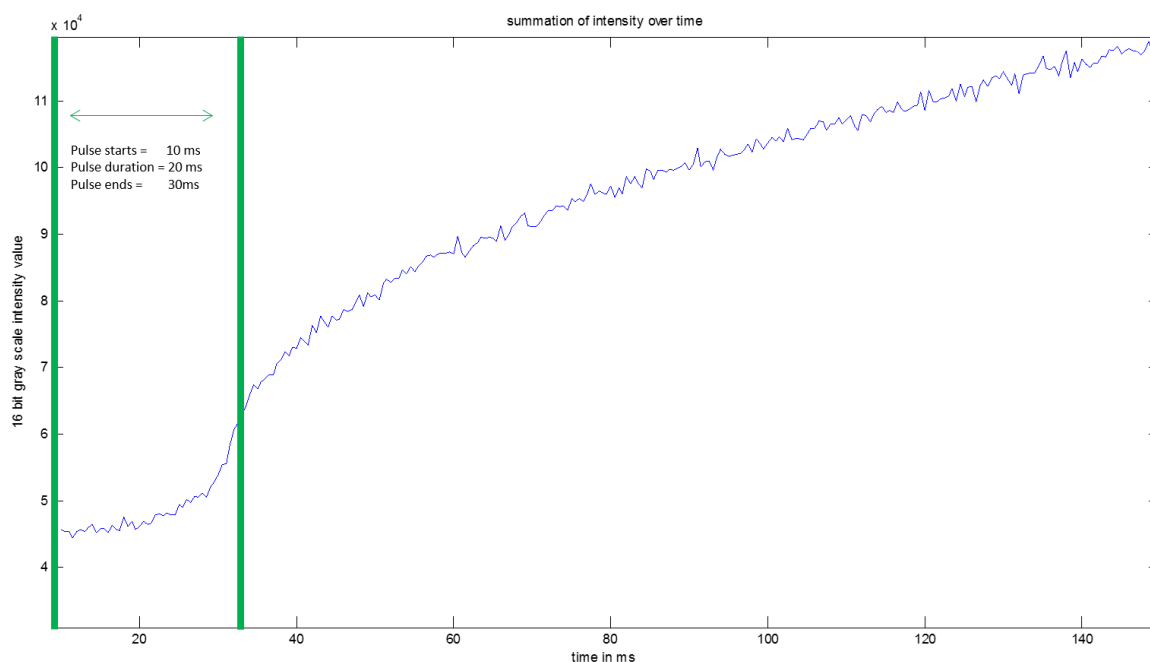
Figure 3.9. The summation of PI fluorescence intensity inside a cell underwent a 0.6 kV/cm electric field for 20 ms (plotted in blue curve). Green vertical lines marks the interval of 20 ms pulse applied to the cell.

to the expected FASS phenomena. Because of the conductivity gradient between inside (~5000 µS/cm) and outside the cell (100 µS/cm), a sudden slow-down of PI at the cell membrane interface contributes to an accumulation inside the cell, resulting in elevated PI fluorescence intensity. Diffusion-attributed transport through the electropermeabilized cell membrane can be observed following the end of the pulse, in which the slope of PI concentration increase is shallower over time, suggesting a passive transport of PI into the cell. Because the fluorescence intensity continues to increase, this suggests a compromised cell membrane integrity from the applied electric field strength.

The electrokinetic contribution to PI accumulation can be better observed and confirmed by plotting the fluorescence intensity as a function of finite difference between data points. This allows us to investigate the temporal rate of PI delivery as shown in Figure 3.10. A
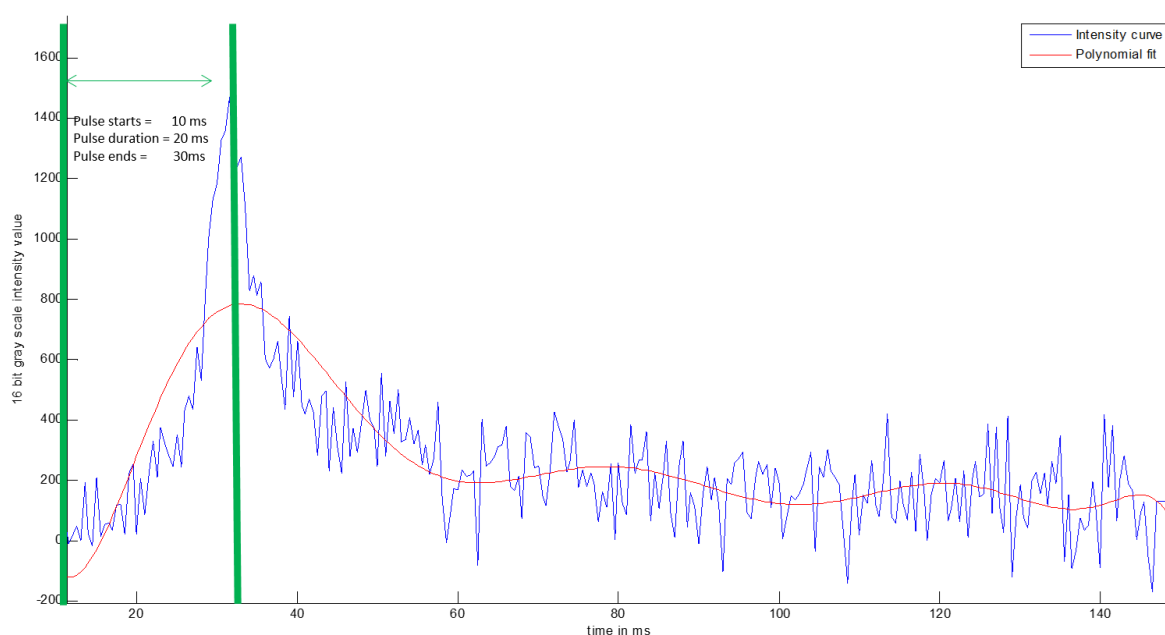
Figure 3.10. Temporal rate of PI fluorescence intensity delivery calculated based on the fluorescence intensity in Figure 3.9. Green vertical lines marks the interval of a 20 ms pulse, and the red trace shows the polynomial fit of the rate of change.

drastic change in the rate of fluorescence intensity can be clearly distinguished during the application of the 20-ms pulse, supporting an electrophoretic transport phenomena, and the rate of fluorescence intensity found elsewhere supports diffusion-based delivery. Additional fluorescence intensity analysis was also performed for single cells undergoing multiple electroporation pulses and various inter-pulse delays. This study can be found in Appendix E.

3.4 Intracellular Transport of Small Molecules to Rotating Single Cells

3.4.1 Cell Rotation in Electric Fields

Combining the hydrodynamic fluid shearing technique to rotate single cells within the electroporation zone of a 2-inlet, 2-outlet microchannel, and this section demonstrates the visualization of intracellular PI transport through selectively permeabilized cell membrane areas as a result of controlling cell rotational velocity. An initial 20-ms duration DC pulse was applied to the cells at 0.6 kV/cm electric field strength to sufficiently permeabilize the cell membrane.[26] Immediately following a 10 ms delay, another 20-ms DC pulse was applied to demonstrate the cell rotation-mediated permeabilization of (1) the entire circumference of the cell membrane; (2) two distinct membrane locations and (3) a single location for non-rotating cells. All three conditions were achieved for single cells rotating at a fast (8°/ms), slow (5°/ms), and zero angular velocity. The electroporation was activated manually once stable stratified flows had been established. A low density cell suspension (2 million/ml) was used in the hydrodynamically focused flow stream to ensure each cell flowed individually between the electrodes and received the applied electric field. A triggering signal instantly initiated the pulse generator and the camera recorder, allowing all events during and after electroporation to be recorded. The acquired fluorescence

images were stored only for cells that remained between the electrodes for the entire duration of the electroporation pulses.

Two rotating conditions were carried out to demonstrate a difference in PI-delivery profiles into rotating cells under the same two-pulse electroporation protocol. When single cells reach the electroporation zone, the first of the two electroporation pulses permeabilizes the cell membrane region perpendicular to the direction of the electric field. The positively charged nucleic acid-binding PI molecules are electrophoretically transported into the cell. Once the PI enters the cytoplasm, it binds to cytosolic nucleic acids and fluoresces. Keeping the pulsing parameters constant (two 20 ms duration pulses at 0.6 kV/cm electric field strength with a 10 ms delay in between), the first rotating condition was generated by a larger Q_{sheath}-to-Q_{cell} ratio, to yield an angular rotation of about 8 °/ms (Figure 3.11a). At
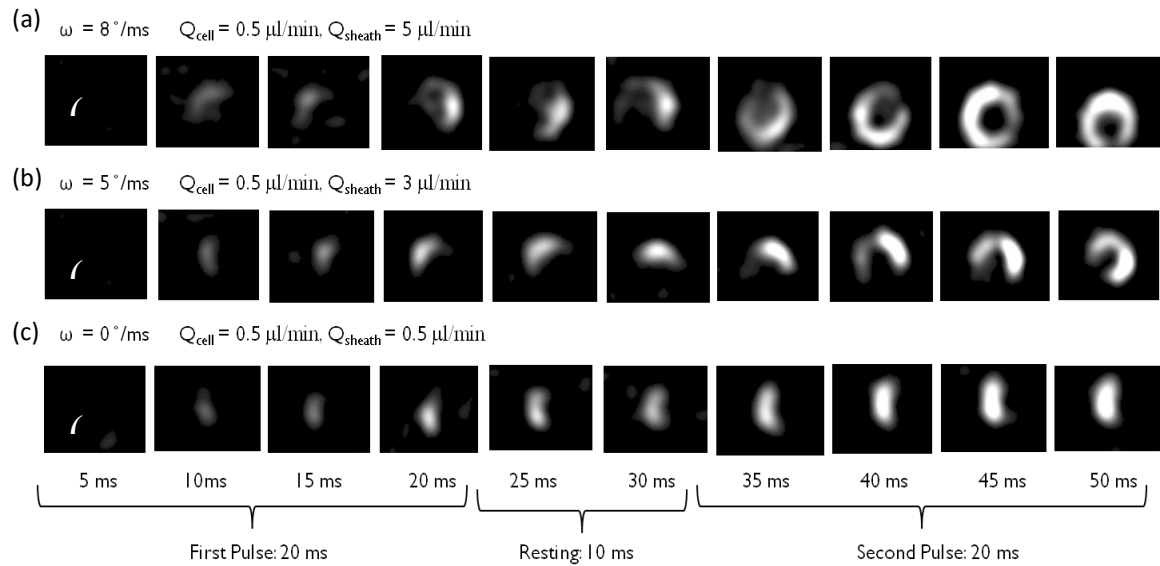
Figure 3.11. Spatial and temporal progression of PI delivery into rolling single cell during two pulse electroporation. The cells flow from left to right with a clockwise rolling velocity of (a) 8°/ms, (b) 5°/ms and (c) 0°/ms. The first pulse was applied in the first 20 ms. After a 10 ms delay, a 20 ms second pulse was applied from 30 to 50 ms.

this rotational velocity, a total of 50 ms pulse time would render a 400 ° cell rotation, which is sufficient to electroporate the entire circumference of the cell. A slight un-electroporated region towards the end of the second pulse was due to the fact that during the initial pulse field it takes some time to permeabilize the cell membrane prior to the observation of PI delivery. The second condition utilized a lower flow rate and smaller Q_{sheath} to Q_{cell} ratio to demonstrate a smaller cell angular velocity that would result in incomplete circumferential delivery of PI. At 5 °/ms, a total pulse time of 50 ms would render a 250 ° cell rotation. Figure 3.11b shows the incomplete circumferential delivery of PI into single cell.

In the non-rotating condition, hydrodynamic focusing was used to balance the cell stream with two sheathing buffer streams so cells flow through the device without rotation. In this condition, the cells reach the electroporation zone and the first pulse permeabilizes the cell membrane and delivers PI into the cell. Then the second pulse was applied which will further deliver PI at the same membrane location. Due to the saturation of PI during the first delivery pulse, the additional pulse application provides limited increase in intracellular delivery compared to the rolling cells. Figure 3.11c shows the spatial and temporal delivery of PI into single cells permeabilized by electroporation under the non-rotating condition, with both sheath and cell streams perfused at a constant flow rate of 0.5 μL/min.

3.4.2 Intracellular Molecular Delivery Quantification

To further quantify delivery, the fluorescence intensity was summed and compared over the cell image area for both rotation and non-rotation-mediated PI delivery (Figure 3.12). An averaged (n=21 cells) summation of PI delivery intensity with standard error is plotted as a function of time for both rotating (blue curve) and non-rotating (red curve) cells. The

gray shading in Figure 3.12a indicates the application of the electric field. The intensity of both curves remains similar during the first 20 ms pulse application. After a 10 ms time delay, the application of a second 20 ms pulse yielded a higher fluorescence intensity for rotating cells than for non-rotating cells. A two-sample t-test showed that the difference between the two curves after 35 ms are significant ($p < 0.05$). The temporal rate of PI delivery was estimated using the finite difference of the intensity between 3 successive images (Figure 3.12b) for both rotating, (8 °/ms, blue curve) and non-rotating (red curve) cells. A higher PI delivery rate is apparent for rotation-mediated electroporation during the application of the second pulse when rotation of the cell results in circumferential exposure of the cell membrane to the electric field. As a result, this rotation technique not only
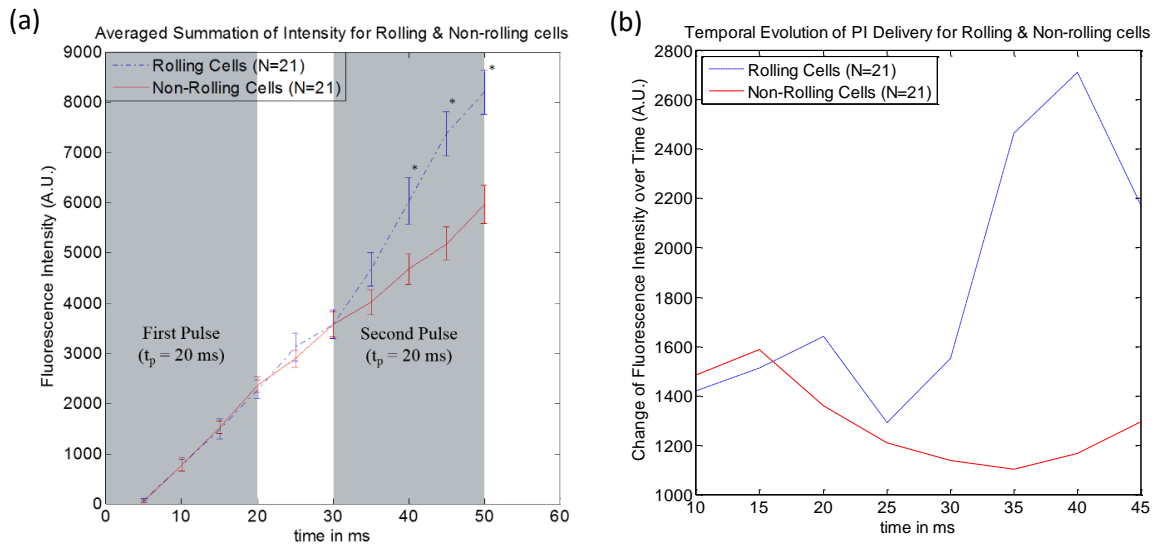
Fig. 3.12 (a) Total delivered PI intensity with standard error is plotted as a function of time for both rotating & non-rotating cells. (b) The finite difference of the intensity between 3 images at different times were used to estimate the temporal rate of PI delivery plotted according to data in Fig. 3.12a for both rotating and non-rotating cells.

increases the rate and amount of delivery but also the delivery profile so that a greater PI delivery payload is obtained throughout the cell volume.

3.5 Intracellular Transport of Large Molecules to Rotating Single Cells

A continuous pulsing scheme[27] was devised to allow continuous cell membrane permeabilization followed by delivery of macromolecules into rotating and non-rotating single cells. By collecting the electroporated single cells at the channel outlet, cell viability and delivered payload could be characterized. 100 µM Fluorecinated Dextran (FD) with a molecular weight of 10 kilo-Dalton (FD, Life Technologies, Grand Island, NY) was used for intracellular delivery of large molecules. FD, which has an excitation and emission wavelength of 494 nm and 524 nm respectively, was added to both the sheath and cell pulsing buffer, and infused into a two-inlet, two-outlet channel. A flow ratio of 10:1 between the sheath and cell streams, at a 4 µL/min sheath flow rate, was used to establish a cell rotation of 4°/ms. A three-inlet, three-outlet channel with the same flow condition was used to establish the non-rotating cell state. In order to electroporate the rotating and non-rotating cells at the prescribed channel location continuously without generating electrolysis gas bubbles, a high frequency pulse sequence at a sufficient amplitude was used to prevent electrolytic reaction build-up.

3.5.1 Continuous Electroporation Pulse Configuration

Figure 3.13 shows a typical schematic of the pulse sequence. Each pulsing cycle is a continuously operating pulse sequence at 8 ms delay interval, each sequence composes of two high frequency DC pulses of 50% duty cycle with the first pulse lasting 1 ms and providing an electric field of 1 kV/cm at 500 kHz with a 50% duty cycle and second pulse

First pulse: 1 kV/cm, 500 kHz, 1 ms

Second pulse: 0.6 kV/cm, 500 kHz, 10 ms

8 ms time delay
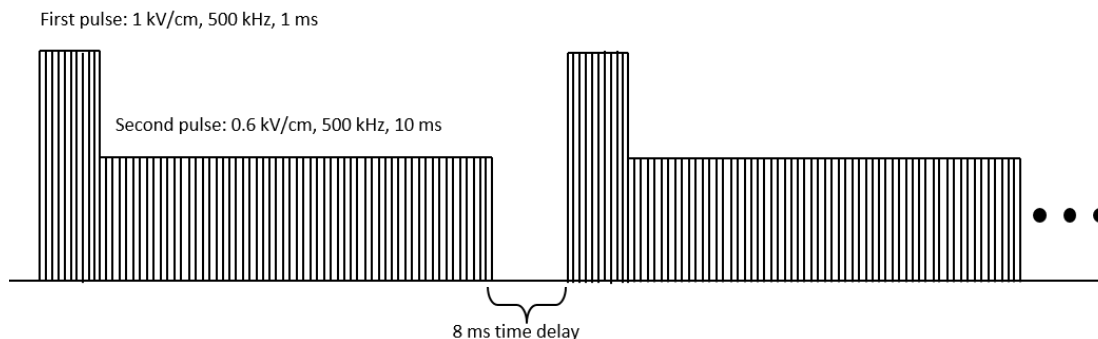
Figure 3.13. Continuous pulse sequence consists of a short (1ms), high amplitude (1 kV/cm) and high frequency (500 kHz) cell membrane permeabilizing pulse and a long (10ms), low amplitude (0.6 kV/cm), and high frequency (500 kHz) delivery pulse. This sequence is continuously applied with 8 ms delay in between.

at 10 ms providing an electric field of 0.6 kV/cm at 500 kHz with a 50% duty cycle. This two pulse scheme was modeled after the results of Sadik *et al.*'s finding that a first pulse that is high in intensity but short in duration permeabilizes the cell membrane while a second pulse that is lower in intensity but long in duration drives the delivery.[28] This pulsing pattern was applied in between the electroporation electrodes once a stable stream of rotating cells was established. It is worth noting that although our pulsing scheme permits the application of DC pulses at a high frequency, a delicate balance must be carefully maintained between pulse frequency, amplitude, duration, conductivity of local cell buffer, and the combined flow rate in order to avoid formation of electrolysis bubbles. At optimized experimental conditions, we have been able to perform on average a minimum of 15 minutes operation and collection given a consistent suspended cell density and a maximal total flow rate of 4.4 µL/min, permitting the analysis of roughly 200 cells per experiment. Three conditions were performed for each condition: rotating, non-rotating and control cells. Control cells underwent the same perfusion protocol as that of the rotating condition but without electroporation. All cells were collected at the channel outlet and

allow 45 minutes for resealing in the cell media, then the cells were washed twice with $1\times$ PBS buffer.

3.5.2 Image Processing

An interactive algorithm was written in MATLAB to correctly identify all cells and measure the PI fluorescence intensity in each cell. Briefly, bright-field and epi-fluorescence images of the target cells was captured by the CMOS camera and processed jointly by the MATLAB detection algorithm. Bright-field images allow accurate scanning and labeling of each cell due to the high edge contrast under the DIC imaging mode while epi-fluorescent images overlaid beneath the bright-field images were used for intensity analysis. The location of each identified cell was directly transcribed onto the epi-fluorescent images to ensure accurate measurement of the intensity for each cell volume only. During each single cell analysis operation, users maintain control over the algorithm's detection outcome in order to prevent false positive identification from similar sized debris or cell fragments.

3.5.3 Cell Collection Results & Analysis

To confirm our findings with a larger molecule, we investigated the continuous electroporation of single cells inside the microfluidic channel with predefined pulse parameters to transport FD inside the cells under both rotating and non-rotating conditions. The delivery concentration of FD was quantified based on the fluorescence intensity of the cells collected after perfusion through the microchannel.

Delivery of FD into rotating and non-rotating cells follows a similar perfusion scheme as that of the PI experiments. A different pulsing scheme was used to continuously

permeabilize and drive molecules into every passing cell. Under such pulsing scheme where high frequency DC pulses were in constant application in the direction parallel to single cell flow, the residence time of the traveling cells which is controlled by the channel dimension and fluid flow rate needs to be determined so that sufficient molecules enter the permeabilized cell membrane. For instance, based on the channel volume in between the electrodes, a traveling single cell at a flow rate of 4 μL/min will experience the electric field for a total of 18.5 ms; and under the same flow rate and a flow rate ratio of 10:1, it is estimated that the cell rotates at ~4 °/ms, therefore a total of 72 degrees permeabilization can be obtained. Larger electrode gaps can be fabricated to permit a longer residence time if greater membrane permeabilization is desired to allow a higher influx of dextran into each cell. However to preserve cell viability, the membrane permeabilization region needs to be limited.
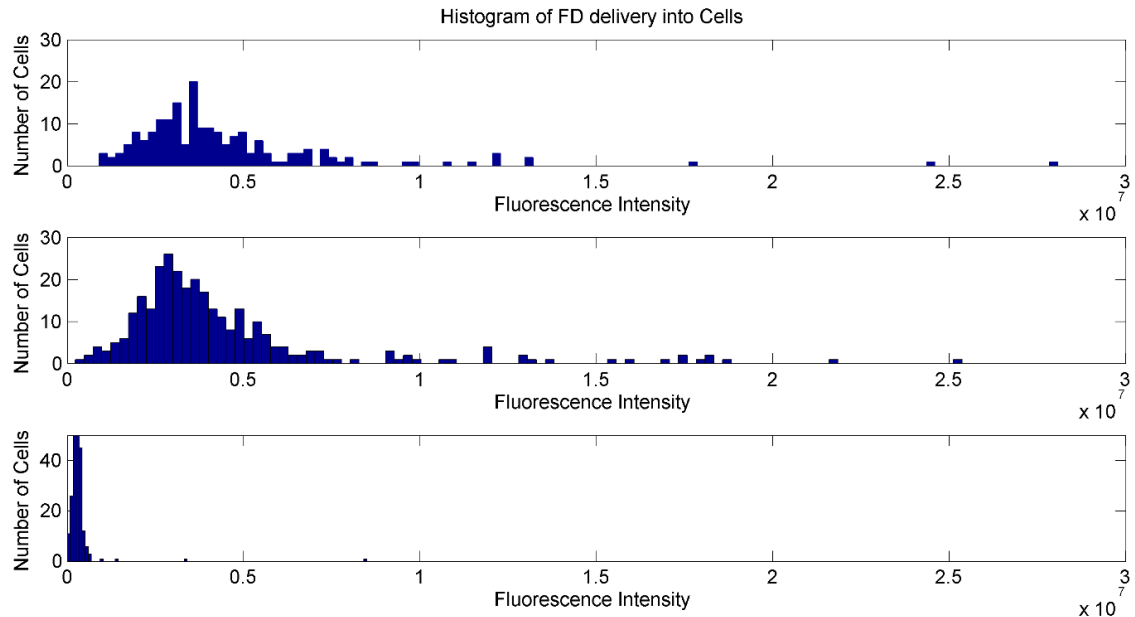
Figure 3.14 Histograms of rotating (top), non-rotating (mid), and control cell fluorescence distribution (bottom). A $p < 0.05$ value of confidence is present between rotating and non-rotating cell.

A histogram of the FD delivery into single cells was plotted for both rotating, non-rotating and control conditions to show their relative intensity distribution as well as their statistical significance from each other (p<0.05) (Figure 3.14). 200 cells were counted based on the bright-field imaging cell detection algorithm, and an average fluorescence intensity of $5.9 \times 10^6 \pm 8.4 \times 10^5$ A.U. was quantified for rotating cells, which is a 31.25% increase from the non-rotating condition case which has a cell count of 300 with an average intensity of $4.5 \times 10^6 \pm 2.0 \times 10^5$ A.U. (Figure 3.15). Since no electric field was applied to the control cells, a very low fluorescence intensity was detected. This demonstrates that dextran was indeed delivered into the single cells, and rotating could facilitate the delivery payload.
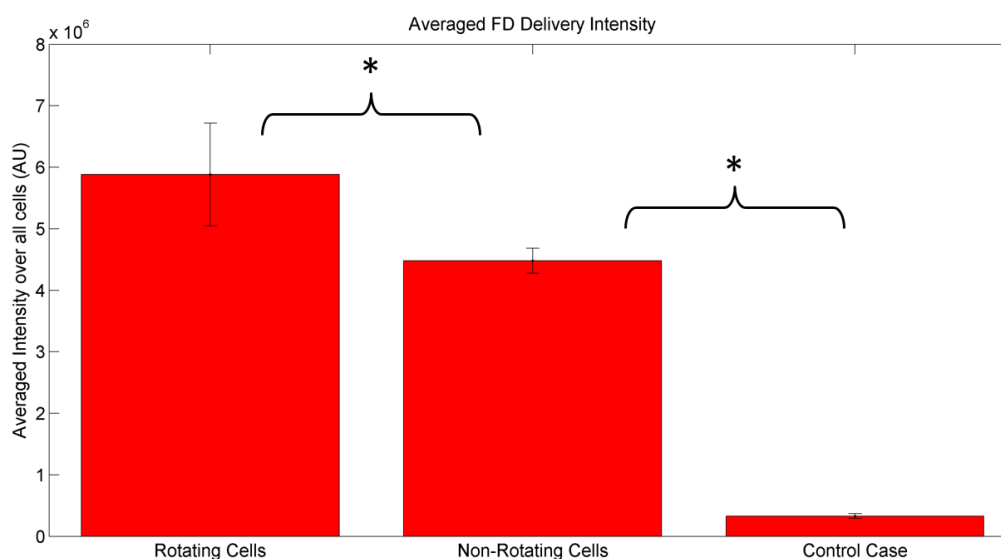
Figure 3.15 Average FD fluorescent intensity with standard errors for rotating, non-rotating, and control conditions. A $p < 0.05$ value of confidence is present between each of the conditions.

3.6 Chapter References:

1   H. Yun, K. Kim and W. G. Lee, *Biofabrication*, 2013, **5**, 022001.

2   H. Andersson and A. van den Berg, *Sensors Actuators B Chem.*, 2003, **92**, 315–325.

3   P. S. Dittrich and A. Manz, *Nat. Rev. Drug Discov.*, 2006, **5**, 210–8.

4   D. G. Grier, 2003, **424**.

5   P. E. Boukany, A. Morss, W.-C. Liao, B. Henslee, H. Jung, X. Zhang, B. Yu, X. Wang, Y. Wu, L. Li, K. Gao, X. Hu, X. Zhao, O. Hemminger, W. Lu, G. P. Lafyatis and L. J. Lee, *Nat. Nanotechnol.*, 2011, **6**, 747–54.

6   J. Voldman, *Annu. Rev. Biomed. Eng.*, 2006, **8**, 425–54.

7   M. Bocchi, M. Lombardini, a Faenza, L. Rambelli, L. Giulianelli, N. Pecorari and R. Guerrieri, *Biosens. Bioelectron.*, 2009, **24**, 1177–83.

8   Y. Pan, X. Du, F. Zhao and B. Xu, *Chem. Soc. Rev.*, 2012, **41**, 2912–42.

9   M. Yu, W. Tan and H. Lin, *Biochim. Biophys. Acta*, 2012, **1818**, 2494–501.

10   S. Nagrath, L. V Sequist, S. Maheswaran, D. W. Bell, D. Irimia, L. Ulkus, M. R. Smith, E. L. Kwak, S. Digumarthy, A. Muzikansky, P. Ryan, U. J. Balis, R. G. Tompkins, D. A. Haber and M. Toner, *Nature*, 2007, **450**, 1235–9.

11   S.-O. Choi, Y.-C. Kim, J. W. Lee, J.-H. Park, M. R. Prausnitz and M. G. Allen, *Small*, 2012, **8**, 1081–91.

12   D. Di Carlo, D. Irimia, R. G. Tompkins and M. Toner, *Proc. Natl. Acad. Sci. U. S. A.*, 2007, **104**, 18892–7.

13   S. C. Hur, N. K. Henderson-MacLennan, E. R. B. McCabe and D. Di Carlo, *Lab Chip*, 2011, **11**, 912–20.

14   J. P. Shelby and D. T. Chiu, *Lab Chip*, 2004, **4**, 168–170.

15   D. T. Chiu, *Anal. Bioanal. Chem.*, 2007, **387**, 17–20.

16   G. B. Jeffery, *Proc. R. Soc. A Math. Phys. Eng. Sci.*, 1922, **102**, 161–179.

17   F. P. Bretherton, *J. Fluid Mech.*, 1962, **14**, 284–304.

18   L. G. Leal and E. J. Hinch, *J. Fluid Mech.*, 1971, **46**, 685.

19   P. J. Shrewsbury, S. J. Muller and D. Liepmann, *Biomed. Microdevices*, 2001, **3**, 225–238.

20   F. White, *Viscous Fluid Flow*, Second., 1974.

21   A. J. Goldman, R. G. Cox and H. Brenner, *Chem. Eng. Sci.*, 1967, **22**, 637–651.

22   Q. Liu and A. Prosperetti, *J. Fluid Mech.*, 2010, **657**, 1–21.

23   M. M. Sadik, J. Li, J. W. Shan, D. I. Shreiber and H. Lin, *Biochim. Biophys. Acta*, 2013, **1828**, 1322–8.

24   R. Fahraeus and T. Lindqvist, *Am. J. Physiol.*, 1931, **8**, 562–568.

25   K. Vahidkhah, S. L. Diamond and P. Bagchi, *Biophys. J.*, 2014, **106**, 2529–40.

26   M. M. Sadik, J. Li, J. W. Shan, D. I. Shreiber and H. Lin, *Biochim. Biophys. Acta*, 2013, **1828**, 1322–8.

27   M. C. Morales, H. Lin and J. D. Zahn, *Lab Chip*, 2012, **12**, 99–108.

28   M. M. Sadik, M. Yu, M. Zheng, J. D. Zahn, J. W. Shan, D. I. Shreiber and H. Lin, *Biophys. J.*, 2014, **106**, 801–12.

Chapter 4

Single Cell Impedance Cytometry

The impedance of an individual cell suspended in an electrolytic buffer is an important electrical parameter that enables label-free detection of the cell in a continuous-flow microfluidic channel. By understanding the governing principles behind impedance-based flow cytometry, this section explores the sensory and microfluidic parameters that will enhance the cell detection accuracy, sensitivity and reliability. These parameters establish an operating basis for measuring cell membrane impedances in the later chapters, and building a crucial first step in the development of an automated, continuous-flow single cell electroporation system.

4.1 Single Cell Impedance Theory

The development of an automated electroporation system starts with the ability to count, identify, and monitor single cells at a high speed. A well-known example of this capability is the flow cytometer, which analyzes a large number of cells through fluorescence-activated cell sorting. However these machines are expensive, cumbersome, complex in operation, and unsuitable for small sample volumes. A Coulter Counter on the other hand is an electrical resistance-based detection apparatus that counts and sizes particles suspended in an electrolytic buffer at a high rate. Compared to flow cytometers, a Coulter Counter is relatively cheaper and label-free, and it has been widely adapted at the microscale for detection of sub-micron particles. In recent years, microscale technologies have offered new approaches in high throughput single cell analysis based on electrical impedance spectroscopy. This is a non-invasive and label-free technique that measures the

AC electrical properties unique to each cell/particle in suspension. The study of bio-impedances can be traced back to the 1910s when Höber[1] first experimentally measured the permeability of erythrocytes using low and high frequencies to investigate transport of molecules through the cell membrane. Since then, many research has emerged that aims to characterize the cell electrical behaviors with predictive models such as Maxwell's mixture theory, and experiments that measure cell properties such as impedance, conductance, capacitance, and dielectric parameters. Impedance is a well-established concept that offers an alternative approach to count, identify, and analyze single cells in suspension at high speed. By understanding the underlying principles behind this electrical measurement mechanism, cell membrane impedance characterization during and following electroporation can be better understood, and integrated to accomplish real-time detection, tracking, and control of the cell membrane permeabilization.

4.1.1 Coulter Counter

A Coulter Counter is one of the most widely used impedance measurement methods to date.[2] It consists of two chambers connected via an aperture. A pair of parallel electrodes in each chamber establishes a constant DC electric current through the aperture. When a particle passes through the aperture from one chamber into another, an increase in electrical resistance is produced, resulting in a decrease in current. This electric current disturbance is typically measured in voltage pulse amplitude, and correspond linearly to the volume displacement of the particle traversing through the aperture (Figure 4.1). With the rapid development of microscale technologies, this classic impedance measurement method has been implemented at the microscale. Planar microelectrodes are fabricated to replace electrode wires/rods in supplying the current, and microfabrication of orifice is tailored to

detect sub-micron particles, creating an extremely sensitive and accurate detection mechanism capable of interfacing with biological cells and diagnostic particles such as quantum dots and drug-bearing nanoparticles.
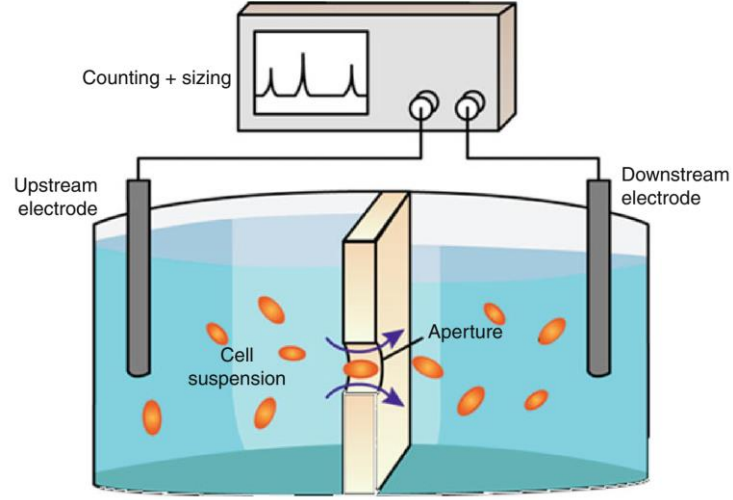
Figure 4.1. Graphical illustration of a classic Coulter Counter. Reprinted with permission from Sun *et al*.[13]

The detection principle of the Coulter Counter is based on the well-known resistive pulse method,[3] in which the change in impedance ΔR as a result of a cell presence with radius R_p across the aperture cross section area A_c can be calculated using Equation 4.1.

$$\Delta R = \left\{ \frac{\text{atan}\left(\frac{R_p}{\sqrt{\frac{A_c}{\pi} - R_p{}^2}}\right)}{\pi\sqrt{\frac{A_c}{\pi} - R_p{}^2}} - \frac{R_p}{A_c} \right\} \qquad (4.1)$$

This equation suggests that when large change in impedance ΔR is desired such as in particle detection-based applications, increasing the resistivity of the solution and the particle radius or decrease the cross-sectional area of the aperture increases ΔR, leading to a higher detection signal-to-noise ratio.

4.1.2 Impedance Spectroscopy

For a volume of buffer solution in between two electrodes, the electrical impedance of this system is typically determined by applying an excitatory AC voltage and analyzing the system response as a function of frequency. This relationship can be illustrated through Equation 4.2, where $Z(j\omega)$ is the system impedance, which can be re-written as its real Z_R and imaginary Z_{Im} components. $V(j\omega)$ is the AC voltage applied with amplitude typically ranges from 0.1 to 1 volts and over a range of frequencies. $I(j\omega)$ is the measured current response for the system under test.

$$Z(j\omega) = Z_R + Z_{Im} = \frac{V(j\omega)}{I(j\omega)} \tag{4.2}$$

When the excitation source is DC, the imaginary component of the system becomes zero, and the overall impedance is its real component, commonly known as the resistance of the system. When Z_{Im} is non-zero as a result of inductance or capacitance's influence, it is called the system's reactance. The overall magnitude and phase angle of the system $|Z(j\omega)|$ can be determined according to Equation 4.3 and 4.4, respectively.

$$|Z(j\omega)| = \sqrt{\left(Z_R{}^2 + Z_{Im}{}^2\right)} \tag{4.3} \qquad \angle Z(j\omega) = \arctan\left(\frac{Z_R}{Z_{Im}}\right) \tag{4.4}$$

The impedance of a system that involves dilute particles suspended in buffer solution has been well described by Maxwell's mixture theories (MMT).[4] The complex permittivity ε_{mix} of this system which describes the frequency dependent responses of the dielectric medium to the electric field is given by Equation 4.5, where ε_p and ε_m are the complex permittivity of the suspending particle and medium, respectively, β is the volume fraction ratio between the cell and the detection volume, and f_{CM} is the Clausius-Mossotti factor

given by Equation 4.6, which indicates the relative particle polarizability with respect to the suspension medium (effective dipole moment).

$$\varepsilon_{mix} = \varepsilon_m \left(\frac{1+2\beta f_{CM}}{1-\beta f_{CM}}\right) \qquad (4.5) \qquad f_{CM} = \frac{\varepsilon_p - \varepsilon_m}{\varepsilon_p + 2\varepsilon_m}$$

$$(4.6)$$

To obtain a more accurate mixture system to better characterize the dielectric components for a biological cell, MMT is integrated with a single shelled cell model, which treats the cell as a homogenous particle with a thin membrane and takes into account the permittivity of the cell cytoplasm (ε_i) and the membrane (ε_{mem}), and the normalized cell radius $\gamma = \frac{R}{R-d}$, with R being the cell radius and d is the membrane thickness. The resultant complex permittivity of the cell is illustrated by Equation 4.7.

$$\varepsilon_p = \varepsilon_{mem} \left(\frac{\gamma^3 + 2(\frac{\varepsilon_i - \varepsilon_{mem}}{\varepsilon_i + 2\varepsilon_{mem}})}{\gamma^3 - (\frac{\varepsilon_i - \varepsilon_{mem}}{\varepsilon_i + 2\varepsilon_{mem}})}\right) \qquad (4.7)$$

MMT is well suited for device geometry with a small cell volume fraction (<10%) in a uniform electric field. However since the distribution of electric field in an impedance cytometer is not uniform, the geometry makes it difficult to estimate the cell volume fraction. Previous work done by Morgan *et al.*[5] have provided a corrected cell volume fraction β equation (Equation 4.8) to account for the field variance using the cell constant of the flow cytometer, derived from Schwartz-Christoffel mapping.

$$\beta = \frac{4}{3}\pi R^3 \frac{1}{\nu wlh}, \quad \text{with } \nu = \frac{K(k)}{K'(k)} \text{ and } k = \tanh(\frac{\pi w}{2h}). \qquad (4.8)$$

v is the cell constant that changes with the parameters of the cytometric geometry, l, w, and h are the length, width and height of the cytometer channel, respectively. $K(k)$ is the elliptic integral of the first kind whereas $K'(k)$ is the complementary integral. k represents the elliptic function modulus. The final complex impedance of the mixture with the corrected cell volume fraction is therefore represented as

$$Z_{mix} = \frac{1}{j\omega\varepsilon_{mix}lv}. \tag{4.9}$$

4.1.3 Electrical Circuit Model

For a single cell suspended in buffer between two planar electrodes, a simplified electric circuit model can be used to represent this system to better understand the electrical dynamics under a frequency-driven excitation. Shown in Figure 4.2, the electrical double layer between the electrode and the buffer is represented by C_{DL}. R_M and C_M are the resistance and capacitance of the buffer surrounding the cell, respectively. The cell is represented by the membrane capacitance C_{mem} in series with the cytoplasmic resistance R_i, assuming an infinite membrane resistance R_{mem}.
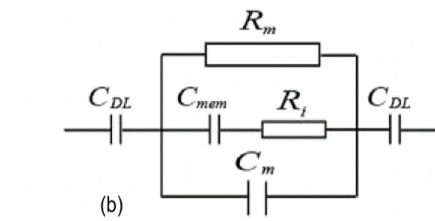
Figure 4.2. Schematic of an electrical circuit equivalent to an individual cell suspended in buffer with known solution conductivity. Reprinted with permission from Morgan *et al.*[14]

Electrical circuit analysis of this model shows that at very low frequencies ($\sim$ 1 Hz), the double layer capacitance C_{DL} acts as an open circuit to block the flow of current; as the frequency increases, the double layer capacitor gradually becomes short-circuited, and starts charging the extracellular buffer (R_M and C_M); when the excitatory frequency becomes sufficiently high (> 100 kHz), current passes through the cell membrane (C_{mem}) and cytoplasm with little resistance. Frequency-based excitation provides a means for isolating the targeted component in this cell-suspension system.

Therefore, by representing the system in this manner, Morgan and colleagues have shown that the MMT can be integrated with the electrical circuit model to provide a more elaborate representation of the cell/buffer system components. Formulas for computing the individual electrical components are as shown from Equations 4.10 – 4.15.[6]

$$R_m = \frac{1}{\sigma_m\left(1-\frac{3\beta}{2}\right)lv} \tag{4.10}$$

$$C_m = \varepsilon_\infty lv \tag{4.11}$$

$$C_{mem} = \frac{9\beta R C_{mem,0}}{4} \, lv \tag{4.12}$$

$$R_i = \frac{4\left(\frac{1}{2\sigma_m}+\frac{1}{\sigma_i}\right)}{9\beta lv} \tag{4.13}$$

$$C_{mem,0} = \frac{\varepsilon_{mem}}{d} \tag{4.14}$$

$$\varepsilon_\infty = \varepsilon_m \frac{2\varepsilon_m+\varepsilon_i-2\beta(\varepsilon_m-\varepsilon_i)}{2\varepsilon_m+\varepsilon_i+\beta(\varepsilon_m-\varepsilon_i)} \tag{4.15}$$

The new complex impedance of the cell-in-suspension system in terms of the electrical circuit components without accounting for the double layer effect is therefore:

$$Z = \frac{R_m(1+j\omega R_i C_{mem})}{j\omega R_m C_{mem}+(1+j\omega R_i C_{mem})(1+j\omega R_m C_m)}$$ (4.16)

And with the double layer effect, the impedance equation becomes:

$$Z = \frac{1}{j\omega C_{DL}} + \frac{R_m(1+j\omega R_i C_{mem})}{j\omega R_m C_{mem}+(1+j\omega R_i C_{mem})(1+j\omega R_m C_m)}$$ (4.17)

These equations provide a numerical approach to investigate the cell/buffer mixture system, allowing us to graphically analyze the impedance response as a function of system properties expressed as electrical components. For instance, these equations will allow us to demonstrate in the next chapter how varying the conductivity of the extracellular buffer and cell volume fraction alters the overall system impedance. A PSpice electrical circuit
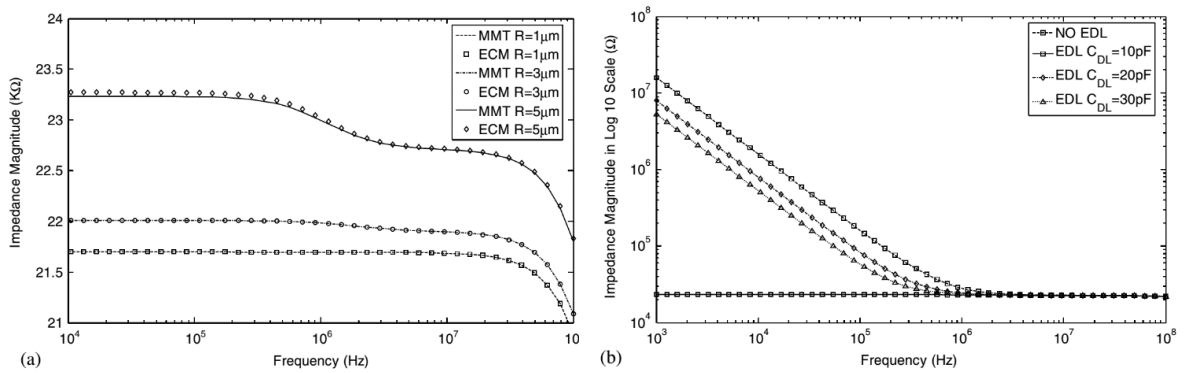
Figure 4.3. Impedance magnitude of a suspended single cell calculated using Maxwell's Mixture Theory and Electrical Circuit Model. (Left) Impedance magnitude without accounting for the electrical double layer effect. (Right) Impedance magnitude accounts for the double layer effect, in which cell level information is overwhelmed by the strong interfacial capacitive effect. Reprinted with permission from Morgan *et al.*[14]

simulation software has also been used by Morgan *et al*. to validate the results of their calculation. By simulating the aforementioned circuit model in PSpice, they plotted the results from the PSpice simulation with their MMT calculation of each electrical component. This is demonstrated in Figure 4.3. For any given cell size, the impedance generated using the electrical model matches the results from the MMT model perfectly, validating the accuracy of their approximation and enabling an alternative approach to represent the cell suspension impedance in a flow cytometer. These results also reveal two distinct changes in impedance between frequency 1 and 100 MHz, known as the dielectric dispersions. These phenomena has been previously theorized by Schwan,[7] the dominant dispersion at the intermediate frequency (1 - 10 MHz) is called the β dispersion which represents the polarization of the cell membrane. This region is characterized by the gradual downward sloping of the impedance magnitude as incremental frequencies overcome the resistance and reactance of the cell membrane, resulting in greater current crossing the cell membrane. As the frequency increases above 30 MHz, the cell membrane is gradually short-circuited to allow the current to pass through the cytoplasmic space, giving rise to the γ-dispersion which governs the polarization of the cytoplasmic space.

4.1.4 Effect of Buffer Conductivity on Dielectric Dispersions

The equations for calculating the complex cell/buffer impedance can also be modified to predict the impedance magnitude as a result of varying parameters. Such flexibility permits the in-depth analysis of the mixture system for conditions other than specified by Morgan and colleagues. One subject of investigation is the cell radius as shown in Figure 4.3a. In an impedance cytometer, a large cell radius (5 µm) produces an enhanced impedance magnitude curve with clear frequency regions demonstrating dielectric dispersion. These

dispersions become less obvious as the cell gets smaller. The observation of sensitivity to parametric variations is a clear indication that the impedance magnitude may also be dependent upon other parameters such as buffer conductivity. As a result, the single cell impedance magnitude for their device was replotted in Matlab Simulink software to demonstrate reproducibility. Shown in Figure 4.4 is the reproduced impedance magnitude plot for a suspended single cell with and without accounting for the double layer effect.
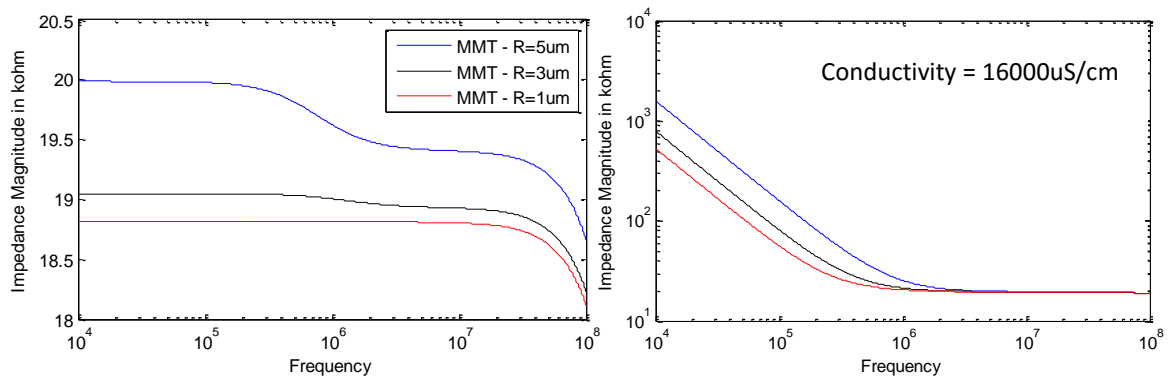
Figure 4.4. Reproduced Impedance magnitude of a suspended single cell simulated in Matlab Simulink software with equations from Maxwell's Mixture Theory and Equivalent Circuit Model.

After establishing all the equations for calculating the overall impedance, three different buffer conductivities (100, 500, and 1000 µS/cm) commonly used in our laboratory were examined for the impedance calculation while keeping all other parameters constant. Figure 4.5 shows the resultant impedance magnitude for a 5 µm radius cell without accounting for the double layer effect. In the case in which a 100 µS/cm buffer conductivity was used, the β-dispersion region characteristic of the cell membrane level response has clearly shifted towards the lower frequency spectrum from 100 to 10 kHz. Compared to the impedance plot in Figure 4.3, where the β dispersion was found between the ranges of 1 to 10 MHz under a buffer conductivity of 16000 µS/cm, a three-order of magnitude

difference in impedance. This shifting in frequency can also be observed for the other two buffer conductivities, in which the dominant β-dispersion lays between 100 and 500 kHz for 500 µS/cm buffer and 500 kHz and 1 MHz for 1000 µS/cm buffer.
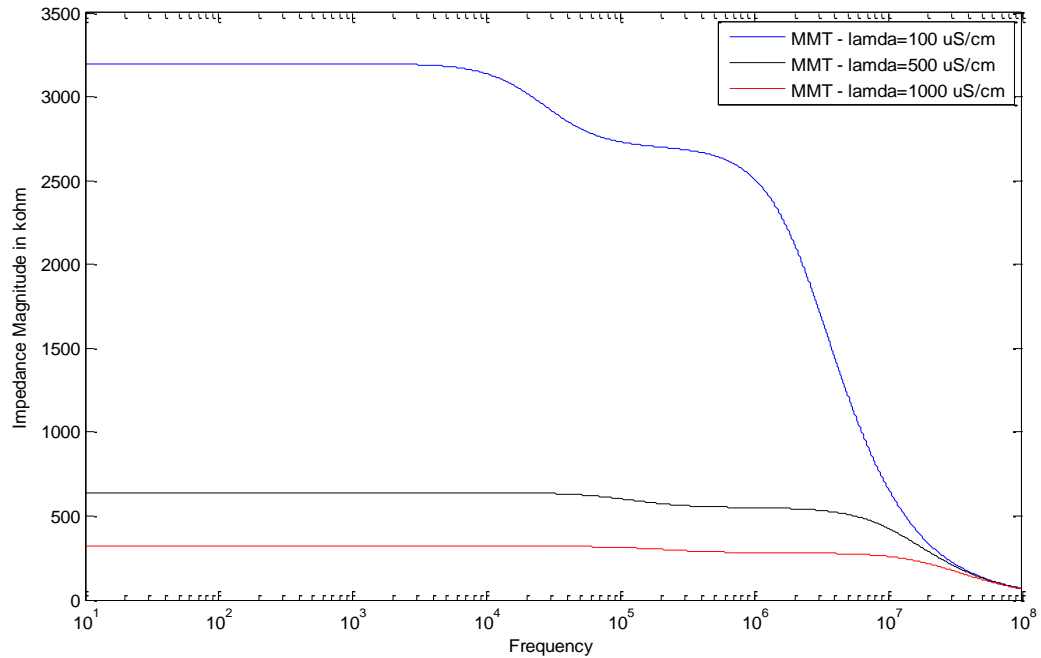
Figure 4.5. Impedance magnitude of a suspended single cell simulated in Matlab. Buffer conductivity is varied from $100 - 1000$ μS/cm to reflect the overall impedance changing dynamics. All other parameters are kept constant as reported by Morgan *et al*.

This is clear evidence that buffer conductivity is a strong determinant for the frequency band in which membrane characteristic dispersion occurs. This information is vital for the detection of cell membrane permeabilization using a frequency-based excitation source and signal acquisition. Together, the resultant impedance model (MMT), electrical circuit model (electrical) and their collective analysis of the frequency-dependent cell properties will establish a theoretical basis for the investigation of a cell undergoing electroporation in the next chapter.

4.2 Single Cell Impedance Measurement

The ability to reliably detect and measure single cell impedance in a continuous flow manner is a crucial first step for the development of an intelligent electroporation system. This section describes three microfluidic designs fabricated in conjunction with a pair of planar electrodes to create a sensing element that detects the presence of flowing individual cells while obtaining the corresponding signal-to-noise ratio. The goal is to select a microfluidic channel design that provides the greatest stability for continuous single cell flow, and preserve the highest detection sensitivity and accuracy. The implementation of a phase sensitive signal extraction approach using the Lock-in amplifier is described for the cell detection in all three microfluidic channels with identical sensory parameters. The fabrication of these micro-devices follows the same photolithography and soft lithography protocols described in the previous Chapter (Chapter 3.2.1). The preparation and harvest of NIH 3T3 mouse fibroblasts for single cell detection experiments is also described previously (Chapter 3.2.1). The reliable detection of continuous flowing single cells in a microfluidic channel will serves as the operating basis for the implementation of controlled electroporation and cell membrane impedance measurement.

4.2.1 Single Cell Detection Sensor

In order to measure the impedance of flowing cells in a microfluidic channel, a sinusoidal AC excitatory waveform with an amplitude of 1 V_{p-p} at a frequency of 15 kHz was generated from a function generator (33220AA Waveform Generator, Agilent). This waveform was then split in two via a T-connector in which one signal serves as the excitation source to the device (connected to one of the two electrodes), and the other identical signal sends to the oscilloscope for visual validation. The current flow in the

channel as a result of the excitation voltage is passed into the input receiver of an impedance sensor (Impedance sensor, A-M Technologies) through the second electrode on the device, hence completing a closed loop measurement. This is the basic setup for measuring current using a general impedance sensor, however because of the magnitude of ambient noise (an aggregate of high frequency power line noise, shot noise, thermal noise, Flicker noise, etc.) is significantly larger than the signal of a cell (15 µm in diameter in a 300 µm wide channel), detection at the single cell level is not possible. Therefore an additional approach has been incorporated at the analog and digital level to block the ambient noise and isolate the signal of interest.

At the analog level, raw signals from the device can be conditioned prior to digital processing, and this analog operation is termed the head-stage of signal measurement. A variety of signal conditioning systems are available in the market today, with functions varying based on application requirements. Understanding of the main composition of this head-stage ensures the reliability of the detection system for obtaining accurate sensitivity. The analog conditioning discussed in this setup consists of a series of instrumentation amplifiers, frequency filters, and transimpedance amplifiers. An important element in the
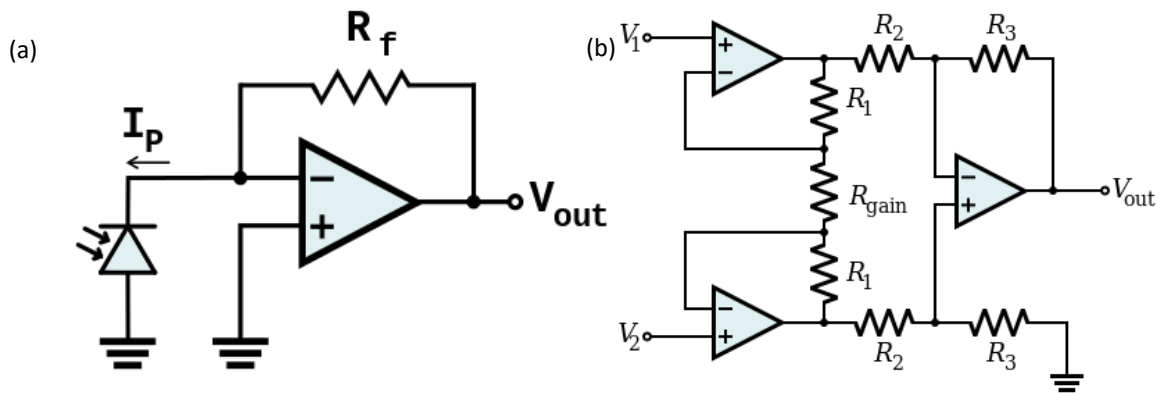
Figure 4.6. Schematic circuit diagram of (a) a general transimpedance amplifier and (b) an instrumentation amplifier.

head-stage is the transimpedance amplifier. This element is commonly known as the "current-to-voltage converter". As this term indicates, it converts the current into a voltage signal to enable digitization and processing. Its operation is simplistic as illustrated by the Figure 4.6 (a), the feedback resistor between the input and the output acts as gain stage to provide an adjustable conversion. The output can be calculated using Equation 4.18. Many models of transimpedance amplifiers are available commercially, the one used for this detection experiment is the OPA4277PA made by Texas Instruments.

The second most important element in the head-stage is the instrumentation amplifiers, they are essentially differential amplifiers with high common mode rejection ratio and input impedances that augment the input signal compared to the referenced ground. They have been known for their ability to offer (1) long term stability, (2) impedance matching, (3) low DC offset, low input noise and drift. Shown in Figure 4.6b is a circuit schematic of an instrumentation amplifier, where V_1 represents the input signal and V_2 is the system ground. From this schematic, it can also be shown that another advantage of having this instrumentation amplifier is the operational simplicity in changing the system gain, which is controlled by one resistor. Equation 4.19 is used for calculating the gain of the circuit based on the selected R_{gain} value:

$$V_{out} = -(I_{in} x R_F), \qquad (4.18) \qquad \frac{V_{out}}{V_2 - V_1} = \left(1 + \frac{2R_1}{R_{gain}}\right)\frac{R_3}{R_2}. \qquad (4.19)$$

Instrumentation amplifiers are also widely available commercially, and the one used in our experiment is the AD620AN made by One Technology Way. A gain factor of 1 million was implemented to detect the cell signal embedded in the electrical noises. An 8-Channel Dynamic Signal Acquisition PCI-board (NI PCI-4472, National Instruments, TX) with a

high sampling rate of 100 kS/s was used to convert the differential sensor output to digital signal.

The head-stage effectively suppressed the ambient signals, however noise sources at the device level (periodic signal from solution flows, electronic noises, etc.) can still render the input signal incomprehensible. Basic signal filtering techniques such as Gaussian smoothing improves signal quality by applying an averaging operation to both the signal and the accompanying noise, so that the signal can be better distinguished from the noise. However this operation only works well for signals with relatively high signal-to-noise ratio. A more accurate detection approach is required to isolate and amplify the weak signals. Phase sensitive Lock-in Amplification technique is a revolutionary sensing approach that has gained popularity in recent years due to its ability to 'lock' onto weak signals. This technique has found many applications where extracting low amplitude signals (in nV to µV range) from high amplitude background noises (> mV) is crucial for enabling new technology research and development.[8-10] Through the process of synchronized demodulation, this approach identifies weak signals from a known carrier reference signal, and rejects other signals (i.e. noises) that aren't synchronized with the reference. A basic Lock-in system consists of four main sections: a signal channel, a reference channel, a phase sensitive detector or commonly known as the mixer, and a low-pass filter (Figure 4.7a). The signal channel includes the head-stage described previously, a series of tunable lowpass, bandpass, notch, and highpass filters that conditions the input signal while suppresses ambient noises. A post-amplifier further increase the amplitude of the conditioned signal for next stage processing. The reference channel is a unique feature of the Lock-in measurement system that transforms the externally/internally supplied
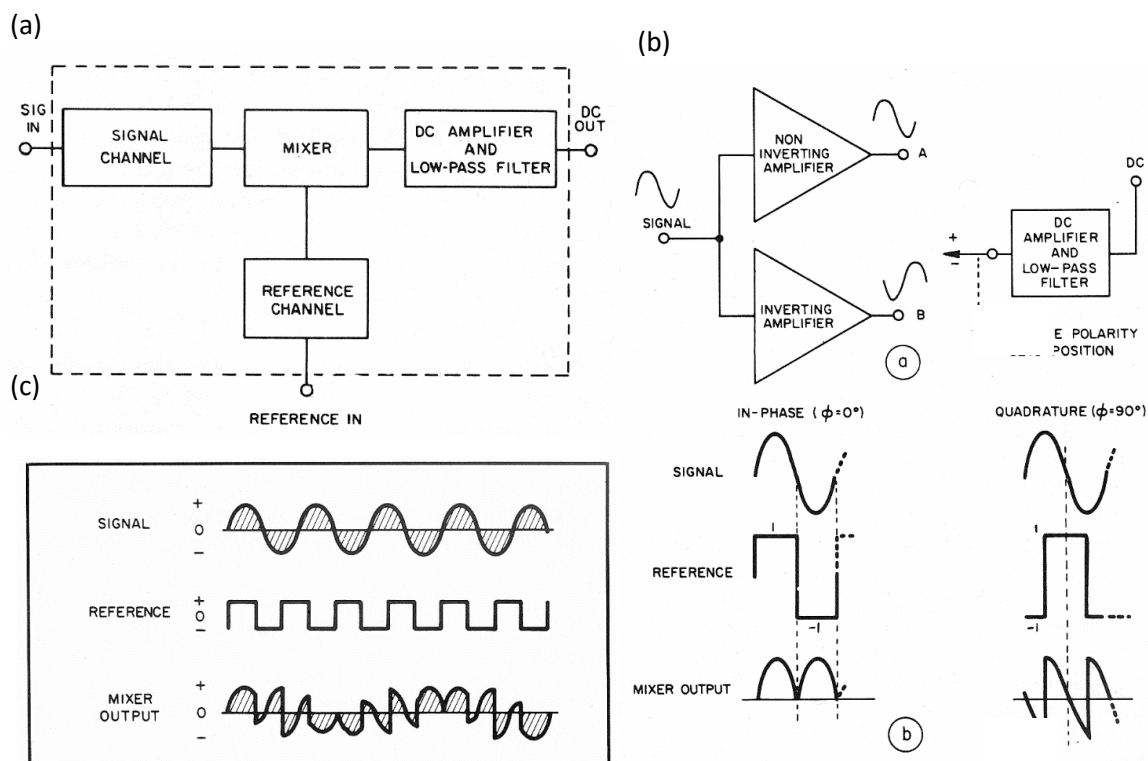
Figure 4.7. (a) Schematic illustration of the main sections of the Lock-in amplifier (b) Graphical illustration of the Lock-in amplifier's Mixer stage and (c) the Mixer output produced by the matching of the reference signal with the input signal containing out-of-phase components.

reference signal (typically a duplicate of the input signal) to the appropriate square waveform in order to drive the mixer. The reference signal amplitude does not contribute to the final system output, but it is crucial for the mixer to recognize and 'lock' onto the desired signal phase. The mixer channel is the heart of the Lock-in amplifier system. Because of its unique operational functionality, this component has many variations of the same name such as the phase-sensitive detector or synchronous demodulator in many modern commercial Lock-in machines. There are two ways to understand the operation of this mixer stage: graphically or mathematically. Figure 4.7b provides a graphical

illustration of the process. Signal passed down from the signal channel is partitioned into two sinusoids that are equal in amplitude but with one signal in-phase while the other one is out-of-phase with the reference signal. The mixer at this point acts as a phase sensitive switch such that when the first half of the reference signal is positive, the switch moves to position A in Figure 4.7b. As a result, the resultant mixer output is a positive, half-wave sinusoid. The switch moves to position B when the second half of the reference becomes negative, and the mixer output produces the same sinusoid as before. Therefore when the signal and the reference are in-phase, the mixer outcome is a full-wave, rectified sinusoid with a DC component proportional to the signal and twice the frequency as that of the reference. However, when the signal is 90 degrees out of phase (quadrature) with the reference signal as shown in Figure 4.7b-c, the DC component becomes zero. For instance, electrical noises which aren't in-phase (synchronous) with the reference signal are rejected by the low-pass filter.

Figure 4.8 provides a simplified mathematical illustration of the Lock-in amplification operation. A Fast Fourier transform was performed on the source signal according to the frequency and phase of the reference signal to suppress noises at all levels. The internal processing of the Lock-in amplifier then applies a narrow band-pass filter operation on the reference signal and calculates the signal magnitude with the built-in phase-locking loop algorithm. In short, two output components are produced by multiplying the input signal with the reference signal. The first component is characterized by a frequency that is the difference between the signal (W_S) and the internal reference (W_R) component (W_R - W_S). The second component has a frequency that is the sum of the two frequencies (W_R + W_S). For instance, when ($W_R = W_S$), a DC signal is produced from the first component whereas
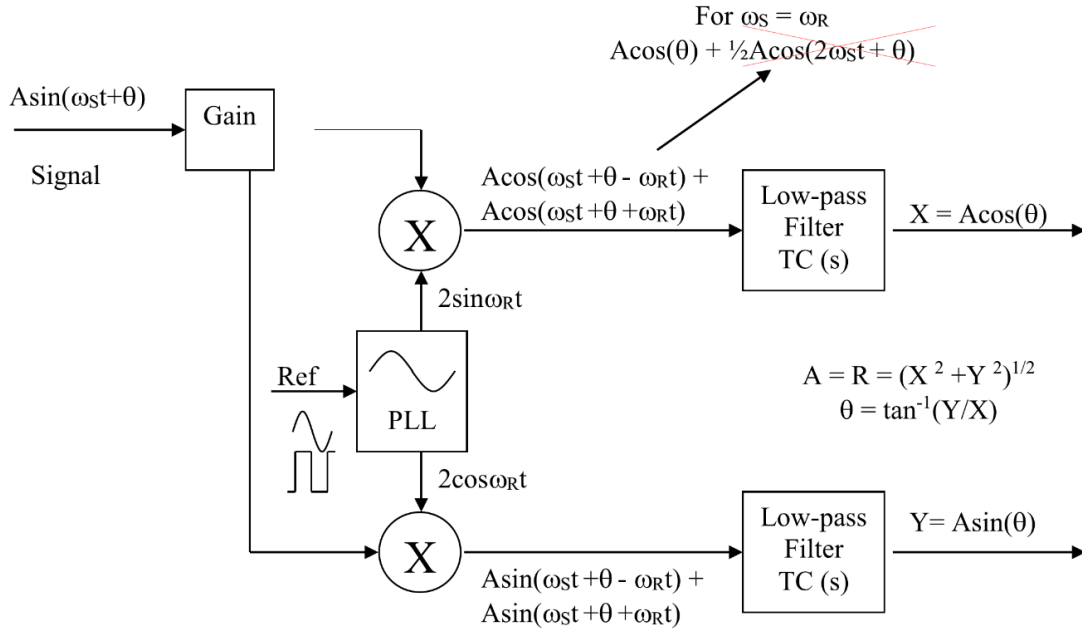
Figure 4.8. Mathematical illustration of the operating principle of the Mixer stage. The input signal is duplicated into two identical signals after a pre-conditioning gain stage. The Phase-Locking Loop (PLL) performs the necessary calculation prior to the lowpass filtering stage. The outcome of this operation consists of the real (X) and quadrature (Y) value of the calculation and their magnitude is the resultant impedance being monitored.

the second component has twice the reference frequency ($2W_R$). A DC component is retained by using a low-pass filter to reject everything else. The input signal was independently multiplied by a separate reference sine and cosine waveform to enable the calculation of the phase information and the amplitude of the final signal.

4.2.2 Single Cell Detection in a Straight Microchannel

In the simplest design, a single cell impedance detection micro-device was created using a 3-inlet, 1-outlet, straight microfluidic channel. This channel has a width of 50 µm and a height of 10 µm, the channel length is kept flexible, however with a minimal length greater

than the electrode gap, which in this design has a 300 µm separation distance. The schematic of this design is shown in Figure 4.9.
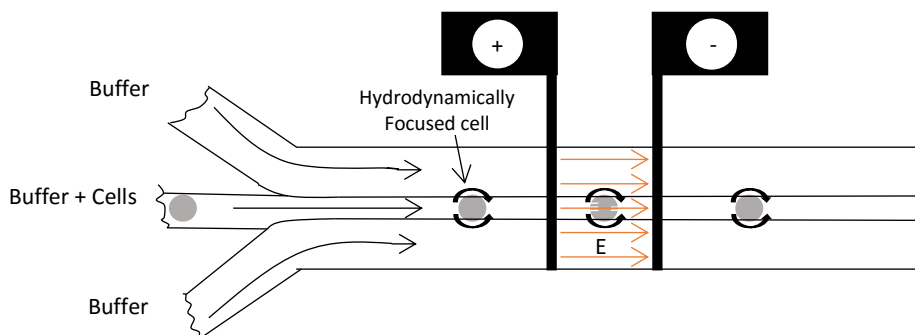
Figure 4.9. Schematic illustrating operation principle of the single cell impedance cytometry in a 3-inlet, 1-outlet microfluidic channel. Two vertically-intersecting planar electrodes create a sensing zone for measuring the current displacement produced by the hydrodynamically-focused single cells.

3T3 cells at a density of approximately 3000/µL were suspended in a pulsing buffer described in the previous chapter (chapter 3.2.1) and infused to the microchannel from the middle inlet at 0.4 µL/min flow rate, and two sheath flows consisting of only the pulsing buffer were introduced into the lateral side inlets at 0.6 µL/min total flow rate, to hydrodynamically pinch the cell stream to the channel center. The cell stream path produced from the pinching of fluid resulted in the alignment of single cells passing between the parallel sensing electrodes. The stability of these three stratified flows ensure the continuous cell transit across the electrodes. The low conductivity buffer used here (100 µS/cm) has an intrinsically low noise level, and it is therefore advantageous in single cell detection with a large channel, since the level of baseline noise is directly correlated with the detection volume (approximately 150 pL in this device calculated using microchannel width × distance between electrodes × microchannel depth) and the electrode area exposed

to the buffer (approximately 2500 µm² calculated using electrode width × channel width). The greater the detection volume, higher the concentration of conductive ions that results in a greater current density, hence higher ambient noise at a given excitation voltage. The greater the sensing area, greater amount of signals (signal of interest and noise) are acquired.

After establishing the analog preconditioning head-stage and the digital signal processing by phase sensitive Lock-in amplifier, the detection and measurement of single cells flowing in a microfluidic channel can thus be demonstrated. Figure 4.10 illustrates single cell detection in terms of current as a function of time, the stable current baseline demonstrates the establishment of stable flow rate at 1 µL/min, and each downward dip in current
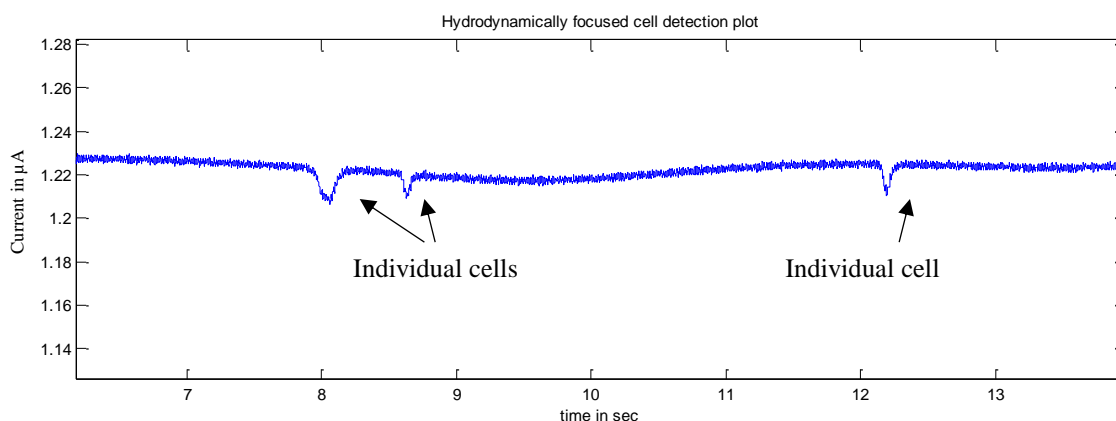
Figure 4.10. Single cell detection in a hydrodynamically focused microfluidic channel.

indicates the presence of an individual cell traversing between the parallel electrodes. The duration of each dip indicates the cell transit time, and the height of the dip represents volume displacement corresponding to the cell volume. This level of sensitivity would not have been possible without the Lock-in amplifier, since the detection volume (1.5^{-13} m³) is nearly 100 times greater than the volume of a 20 µm diameter cell (approximately

4.2^{-15}m^3, assuming a spherical cell), the extraction of this signal from this noise magnitude is evident of Lock-in amplifier's potential in realizing single cell level impedance sensing.

Despite a 15 dB signal-to-noise ratio produced from this straightforward microfluidic channel design, additional microfluidic channel designs were sought to further improve the signal quality.

4.2.3 Single Cell Detection in a Coulter Counter Microchannel

Mimicking the operating principle of a Coulter Counter, a microfluidic channel with a constriction region in the cell flow path has been fabricated to increase the cell-volume fraction, and ultimately increasing the signal-to-noise ratio in the lower frequency band. A constriction with a dimension of 250 µm long, 25 µm wide, and 12 µm deep was chosen to sufficiently allow the passage of single 3T3 cells based on the observed average cell diameter ranging from 10 to 17 µm. A pair of planar electrodes separated by a distance of 300 µm apart was fabricated to encompass the constriction region of the channel as shown in Figure 4.11 below. 3T3 cells were perfused from the channel upstream inlet at a flow
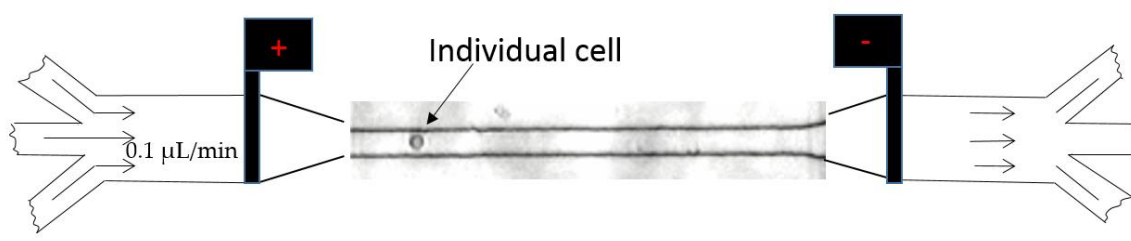
Figure 4.11. Schematic illustration of the constriction-based microfluidic channel used in the measurement of single cell flow cytometry. The constriction section shows a bright field image of an individual 3T3 cell traversing across the microchannel constriction along its flow path.

rate of 0.5 µL/min. An estimated cell volume fraction of 5% was obtained in this case. An identical detection setup and mechanism was used for the detection of passing single cells.

Figure 4.12 demonstrates the detection sensitivity and accuracy using this microfluidic device. An improved signal-to-noise ratio of 37 dB was obtained, compared to the SNR from the use of a straight microfluidic channel (15 dB). The constriction reduced the detection volume, thereby significantly increasing the cell volume fraction from 3% to 6%, leading to a greater signal pulse amplitude.
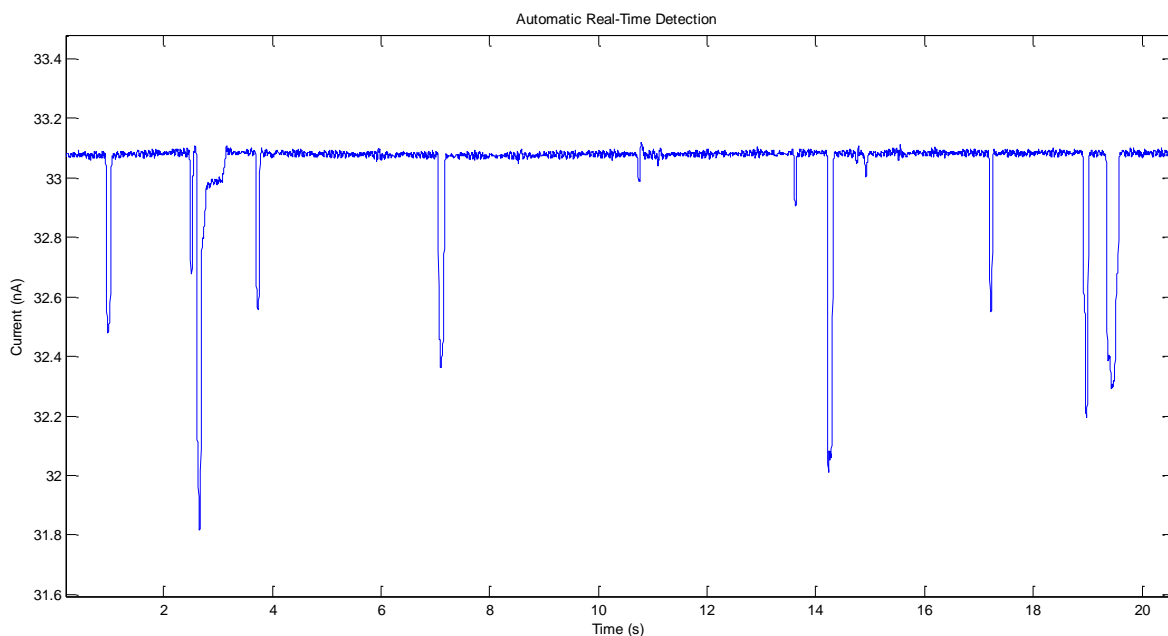
Figure 4.12. The demonstration of single cell detection using the constriction-based microfluidic channel. The detection current is plotted as a function of time, each dip in current represents the current displacement of an individual cell traversing across the

4.2.4 Single Cell Detection in a Compressed Microchannel

Microfluidic channel with a critically compressed constriction width has also been fabricated to further enhance the cell detection signal. This device design resembles a microfluidic cell trapping mechanism, in which single cells are temporarily immobilized by the constricting notch, permitting extended analysis of the same cell (Figure 4.13). The dimension of the previously fabricated Coulter Counter microfluidic device was reduced further to create a critically compressed constriction dimension of 25 µm in length, 15 µm in width and 12 µm in depth. This reduction forces the flowing single cells to squeeze through the constriction without being permanently trapped, and each cell creates a large current displacement as a result. This displacement is so significant that a 75 dB signal-to-noise was measured. Another advantage of this design is that as the single cell squeezes through the constriction, a temporal window is created for extended analysis on the cell.
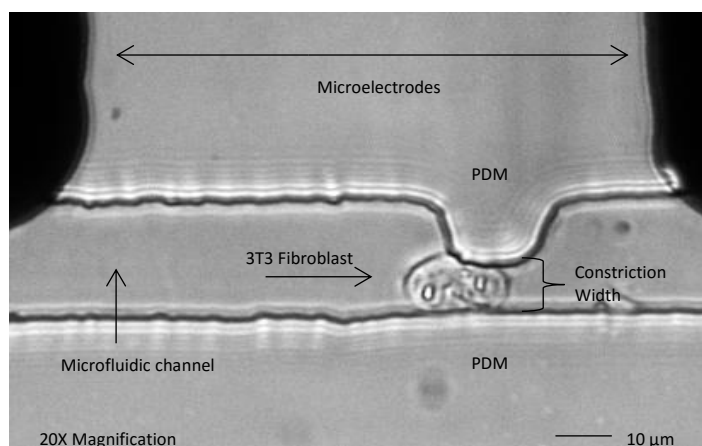
Figure 4.13. A bright field image of an individual cell squeezing through the microchannel constriction that has a width narrower than the diameter of the cell. A pair of planar electrodes enclose this constriction region in order to record the electrical impedance.

Depending on the cell size, the cell remains in the constriction for up to 500 ms to 1 second in duration. This window of opportunity is ideal for observing the cell response in a 'slow shutter mode', such as cell membrane permeabilization events following the application of an electroporation pulse to the cell. Figure 4.14 demonstrates the temporary immobilization of a single cell at the critically compressed channel constriction, a period of 700 ms was measured for the cell to squeeze through the constriction and resume its previous course of flow. Figure 4.14 also shows the current displacement signals produced by other cells with various transit times through the constriction.
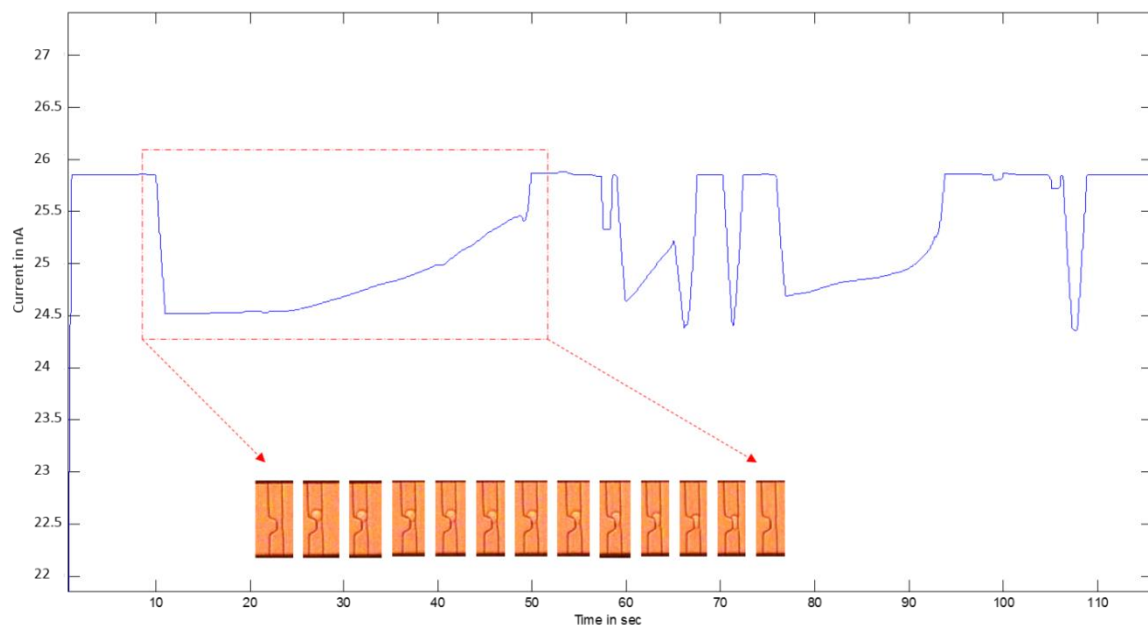
Figure 4.14. Electrical measurement of single cell current displacement from a narrowed channel constriction. The electrical current trace represented by the blue curve over time. The dashed inset shows the current displacement by a single cell and its corresponding bright field images in chronological order from left to right, from the cell entering to exit.

Although this channel design provides the obvious advantage of high signal-to-noise ratio and a way to temporarily immobilize a cell for extended analysis, the drawback is that many researchers in the field have documented the mechanical injury imposed upon the cell by this technique.[11,12] Additionally, this channel geometry does not permit continuous cell flow operation, and it is extremely unstable. Thus, cell conglomeration at the constriction occurs frequently that renders the device inoperable (Figure 4.15). Mechanical trauma further increases the likelihood of cell death at the constriction, resulting in more severe channel clogging. Therefore, since continuous flow of single cells is required for a high throughput operation system, this design was not implemented.
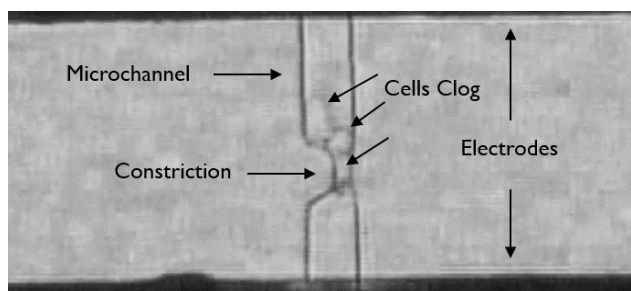
Figure 4.15. Bright field image showing multiple cells stuck in the microchannel constriction, preventing the smooth passage of incoming cells. Microchannel of this design is prone to cell clog since the smooth passage of each cell through the constriction is guaranteed.

In conclusion, the second microfluidic device employing a larger-than-cell-diameter constriction is selected as the optimal choice for successive electroporation device implementation. The microfluidic channel with improved cell-volume fraction combining with the low conductivity buffer provides a low-noise environment for the single cell impedance cytometry. As demonstrated above, the use of two planar electrodes is sufficient to capture single cell impedance information while retaining the simplicity of the physical

detection mechanism. The task of the detection sensitivity is fulfilled by the use of a signal Lock-in Amplification technique which extracts small signals from large magnitude of electrical noise.

4.3 Chapter References:

1   R. Höber, *Annu. Rev. Biochem.*, 1932, **1**, 1–20.

2   M. GRAHAM, *J. Assoc. Lab. Autom.*, 2003, **8**, 72–81.

3   R. W. DeBlois, *Rev. Sci. Instrum.*, 1970, **41**, 909.

4   M. Pavlin, T. Slivnik and D. Miklavcic, *IEEE Trans. Biomed. Eng.*, 2002, **49**, 77–80.

5   T. Sun, S. Gawad, N. Green and H. Morgan, *J. Phys. D-Applied Phys.*, 2007, **40**, 1–8.

6   H. Morgan, T. Sun, D. Holmes, S. Gawad and N. G. Green, *J. Phys. D. Appl. Phys.*, 2007, **40**, 61–70.

7   H. P. Schwan, in *Proceedings of 16th Annual International Conference of the IEEE Engineering in Medicine and Biology Society*, IEEE, 1994, pp. A70–A71.

8   M. Stachel, *http://www.lockin.de/)*.

9   D. Malchow, *Lock-inApplications Anthology*, 1985.

10   D. W. P. and E. R. Dietz, *The Art of Experimental Physics*, 1991.

11   I. L. Ahmad and M. R. Ahmad, *Micro Nano Syst. Lett.*, 2014, **2**, 8.

12   A. Sharei, J. Zoldan, A. Adamo, W. Y. Sim, N. Cho, E. Jackson, S. Mao, S. Schneider, M.-J. Han, A. Lytton-Jean, P. A. Basto, S. Jhunjhunwala, J. Lee, D. A. Heller, J. W. Kang, G. C. Hartoularos, K.-S. Kim, D. G. Anderson, R. Langer and K. F. Jensen, *Proc. Natl. Acad. Sci. U. S. A.*, 2013, **110**, 2082–7.

13   T. Sun and H. Morgan, *Microfluid. Nanofluidics*, 2010, **8**, 423–443.

14   H. Morgan, T. Sun, D. Holmes, S. Gawad and N. G. Green, *J. Phys. D-Applied Phys.*, 2007, **40**, 61–70.

Chapter 5

Cell Membrane Permeabilization Measurement for Static Single Cells

Cell membrane electropermeabilization can be used to directly monitor the electroporation process, and assess the cell susceptibility to the applied electric fields. The ability to extract this information enables the study of fundamental biophysics of cell membrane electrical behavior, allowing control of the cell viability through careful selection of applied electric field parameters while maximizing the transport of exogenous materials into cells. We began the cell membrane permeabilization investigation by modifying the cell/electrolyte circuit model described in chapter 4.1.3 to explore the controllable parameters which strongly influence the impedance magnitude of an individual cell before and after electroporation treatment. A parametric map was subsequently generated to predict the frequency range where the largest change in cell membrane permeabilization can be found in terms of buffer conductivity and cell volume fraction. The goal is to obtain a set of initial experimental parameters from the simulation model to aid in the experimental detection of predicted cell impedance events. We then demonstrated the experimental detection of electroporation-mediated cell membrane permeabilization from stationary cell aggregates in a microfluidic channel. By evaluating the cell aggregates' impedance differences following the application of a lethal electroporation pulse, we seek to confirm the frequency band in which the largest change in the β-dispersion of the impedance is found, since this region is indicative of cell membrane-specific responses. Lastly, various microfluidic channel designs for single cell level electropermeabilization measurement will be discussed. Such scale of detection will serve as the basis for developing the capability to monitor and control the permeability of a cell undergoing electroporation. A

trapping mechanism similar to the 2-dimensional microfluidic channel used by Khine *et al*. was adapted in conjunction with the phase sensitive Lock-in detection method to measure the impedance magnitude of a reversibly and irreversibly electroporated cell. Measurement performed at this single cell level allow us to establish a set of Lock-in amplifier sensory parameters and experimental procedures for advancing to a flow-based cell membrane permeabilization detection system.

5.1 Numerical Simulation of a Membrane Permeabilized Cell

In the previous chapter, single cell electrical impedance spectroscopy in a microfabricated flow cytometer was demonstrated using a cell/electrolyte circuit model. This well-established modeling approach is adapted here with slight modification to demonstrate the effect of electroporation on the cell impedance. In a similar manner, a cell suspended in buffer between a pair of electrodes was modeled as an electrical circuit. In order to reflect the overall impedance change as a result of cell membrane permeabilization by
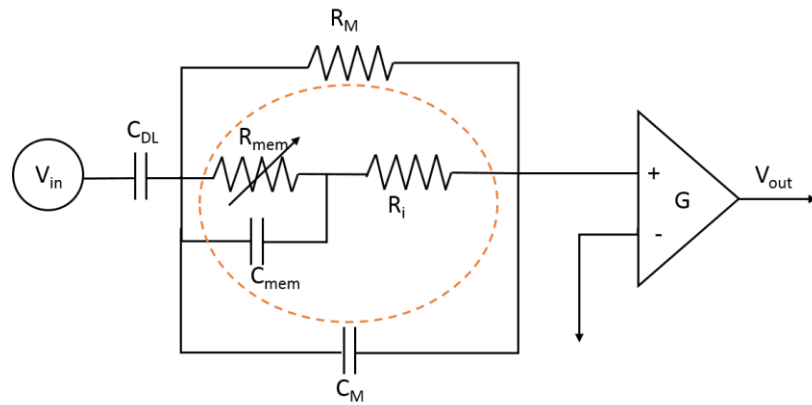
Figure 5.1. A cell (dashed circle) is modeled as a as a resistor R_i (cytoplasmic resistance) in series with a resistor variable R_{mem} (membrane resistance) in parallel with a capacitor C_{mem} (membrane capacitance). G represents a pre-amplifier that converts current into voltage for digital processing.

electroporation, a variable R_{mem} was implemented in parallel to C_{mem}. The new cell circuit is shown in Figure 5.1 with a pre-amplifier (G) that converts current into voltage for digital processing. The resultant impedance magnitude $|Z|$ for the suspended cell before and after applying electroporation allowed us to determine an optimal frequency range in which the largest change in impedance magnitude, $\Delta|Z|$ can be found.

The resultant overall impedance equation is shown in Equation 5.1. ω is the angular frequency, and the formula for calculating the values of the individual electrical components, except for R_{mem}, can be found in the previous chapter (Chapter 4.1.3). R_{mem} is based on the resistance of a typical patch of membrane $R_M = 10000$ Ω/cm^2,[1] and assuming a spherical cell with radius r can be calculated as follows: $R_{mem} = \frac{R_M}{4\pi r^2}$. Electro-permeabilized cell membrane resistance $R_{porated\_mem}$ is conservatively approximated based on our previously published numerical model,[2] assuming only 0.1% of the cell membrane is porated, $G_{mem} = 0.001\sigma_m(\frac{\pi r^2}{2d})$ where d is the membrane thickness of 5 nm and σ_m is the buffer conductivity at 100 µS/cm.

$$|Z| = \frac{1}{j\omega C_{DL}} + \frac{\left(R_m\left(1 + R_i\left(j\omega C_{mem} + \frac{1}{R_{mem}}\right)\right)\right)}{\left(R_m\left(j\omega C_{mem} + \frac{1}{R_{mem}}\right) + \left(1 + R_i\left(j\omega C_{mem} + \frac{1}{R_{mem}}\right)\right)(1 + j\omega R_m C_m)\right)}$$

(5.1)

Figure 5.2 shows the transition of impedance magnitude for a healthy cell from a un-electroporated state (plotted in black) to the electroporated state (plotted in red) as a function of frequency from 1 Hz to 10 MHz. This simulation ignores the double layer
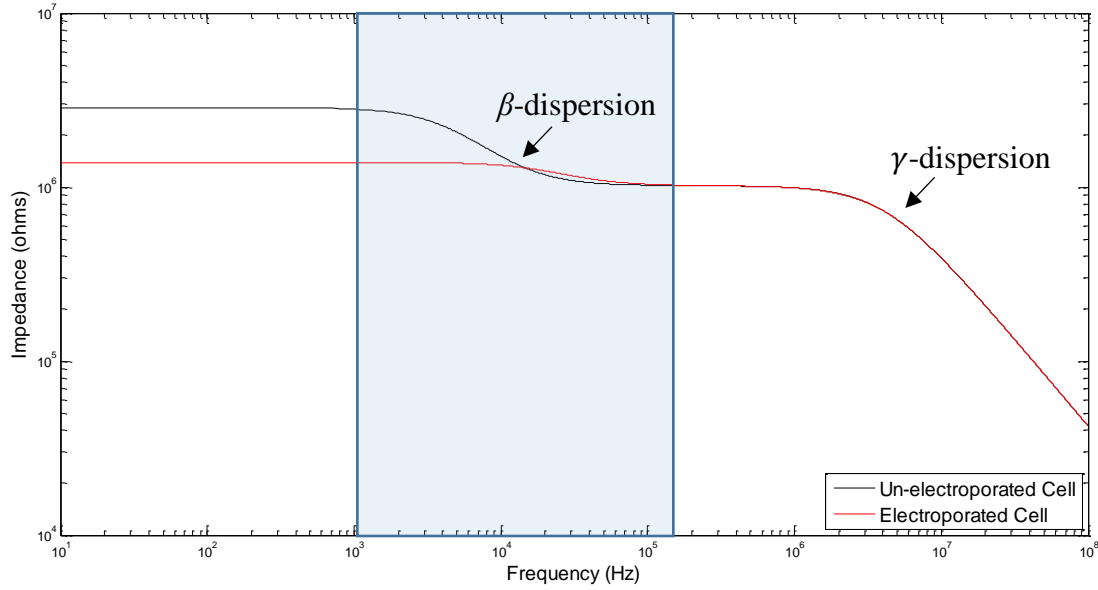
Figure 5.2. Numerical simulation of impedance magnitude as a function of sweeping frequency for an individual cell in suspension before (black curve) and after (red) electroporation-mediated membrane permeabilization, ignoring the double layer effect. Blue label highlights the β dispersion frequency range where largest change in membrane impedance can be found.

effect at the electrode and buffer interface, and investigates the electroporation-mediated cell membrane impedance changes of a single cell with a 5 µm radius suspending in 100 µS/cm conductivity buffer, while positioned in a constriction microchannel that produces a 5% cell-volume-fraction. Analysis on the cell circuit reveals that at low frequencies (1 – 5 kHz), the reactance of the extracellular buffer capacitance is high, therefore the impedance of the mixture system is the equivalent resistance of the resistive elements, giving rise to a constant value. At transitional frequencies (6 – 100 kHz), the reactance of the capacitors (C_M and C_{mem}) starts to decrease due to the increasing frequencies that lower the charging potential in the capacitors. In a non-electroporated cell, because the cell membrane resistance is very high, more current passes through C_{mem} at high frequencies,

resulting in a reduction in the overall impedance characterized by the β-dispersion. At high frequencies (above 100 kHz), reactance of C_{mem} decreases rapidly, and the current eventually 'short-circuited' through R_i, resulting in the characteristic γ-dispersion. When the cell is electroporated, assuming a 0.1% membrane permeabilization, the overall impedance is reduced as R_{mem} decreases at low frequencies since the total resistance is reduced due to the increase in membrane conductance. At transition frequencies, C_{mem} is no longer the only path where current passes through, the lowering of the membrane reactance leads to more current passing through the R_{mem}. Because of this current increase from an electropermeabilized cell membrane, membrane-sensitive β-dispersion is no longer visible in this frequency band. Since no changes occur at the cytoplasmic level, current passes through R_i to ground at high frequencies.

The effect of double layer capacitance can significantly alters the impedance curves of a cell undergoing electroporation. Including the C_{DL} in the circuit diagram, Figure 5.3 shows a region where the largest change in cell membrane impedance can be found over a range of frequencies. Due to the large reactance of the double layer capacitor, current is effectively blocked at very low frequency (i.e. DC). As frequency increases, more current passes through the cell. As a result, low frequencies produces identifiable impedance differences for a single cell before and after electropermeabilization. The blue label in Figure 5.3 highlights a frequency range between 300 Hz and 11 kHz to be the region where noticeable changes in overall impedance can be found, with the greatest change occurring at approximately 3 kHz. C_{DL} has less effect after frequencies increase beyond the cell membrane sensitive range (i.e.1 kHz).
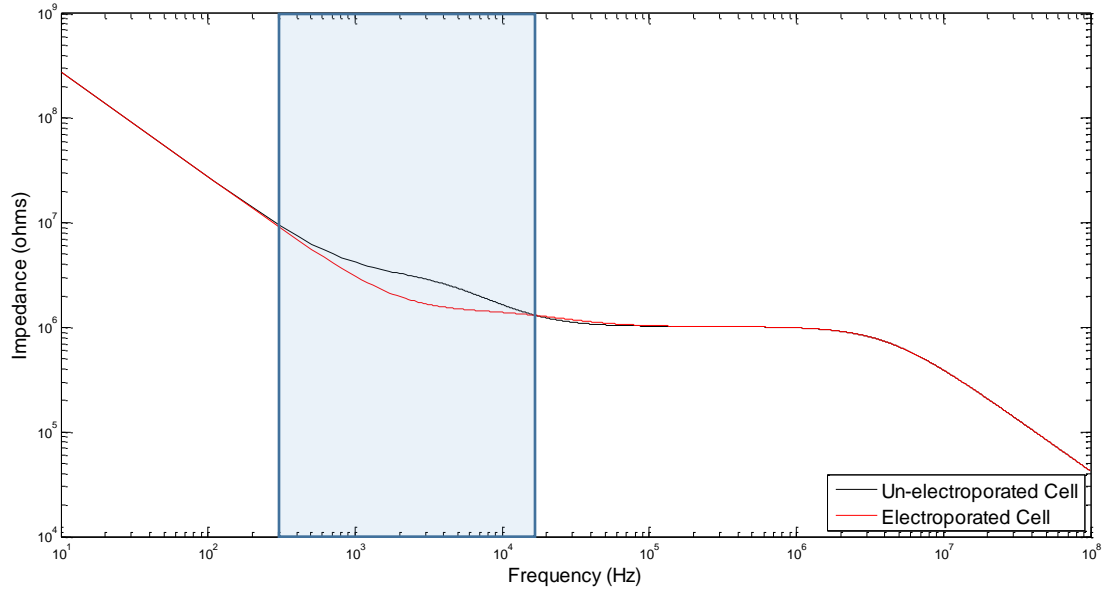
Figure 5.3. Numerical simulation of impedance magnitude as a function of sweeping frequency for an individual cell in suspending before (black curve) and after (red) electroporation-mediated membrane permeabilization, including the double layer effect. Blue label highlights the β dispersion frequency range where largest change in membrane impedance can be found.

Impedance spectroscopy demonstrating the effect of varying R_{mem} from a non-permeabilized (high R_{mem}) to permeabilized cell membrane state (low R_{mem}) allows the initial selection of a sensing frequency to be used experimentally for measuring cell membrane impedance changes.

In order to determine other factors influencing $\Delta|Z|$ following electroporation, we systematically varied the cell volume fraction from 5% to 25% and extracellular buffer conductivity from 0 to 1000 µS/cm as a function of frequency. The simulated results are shown as three dimensional contour maps (Figure 5.4). $\Delta|Z|$ is scaled as color intensity ranges from 0 to 120 kΩ of impedance difference. When buffer conductivity is plotted as a function of frequency in Figure 5.4a, a 5% cell volume fraction was held constant. The

(a)

(b)
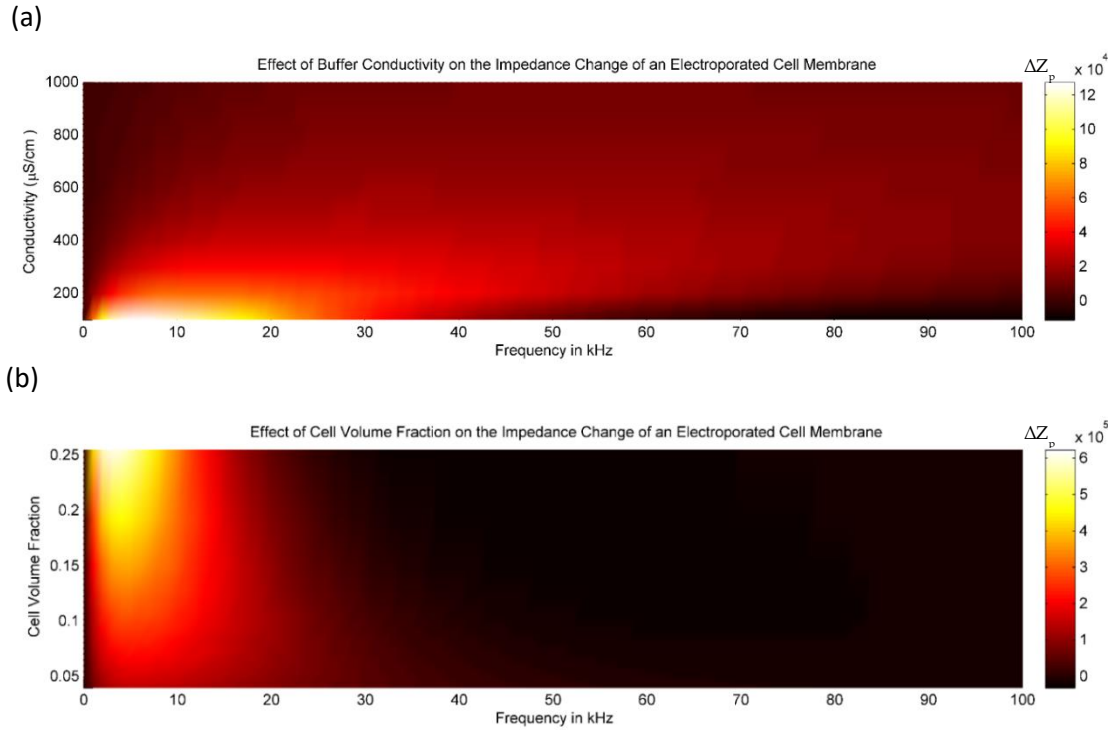
Figure 5.4. Numerical simulation of the change in impedance magnitude $\Delta|Z|$ as (a) a range of extracellular buffer conductivity is plotted against sweeping frequency and (b) a range of cell volume fraction is plotted against frequency. The color intensity represents the $\Delta|Z|$, whiter the color, greater the $\Delta|Z|$.

mapping indicates that $\Delta|Z|$ is the greatest at the lower frequency spectrum between 1 and 10 kHz in low conductivity buffer suspension. An inverse correlation can be found between the buffer conductivity and $\Delta|Z|$ in which increasing the buffer conductivity decreases $\Delta|Z|$. This inverse relationship is also true between $\Delta|Z|$ and frequency. The magnitude of impedance change for a single cell following membrane permeabilization is greatly dependent on the extracellular buffer conductivity. On the other hand, the effect of cell volume fraction on $\Delta|Z|$ is shown across the frequency spectrum in Figure 5.4b while using a constant buffer conductivity of 100 µS/cm. Significant changes in $\Delta|Z|$ are observed in the lower frequency band (1 and 10 kHz) with a high cell volume fraction of 25%, however

they are not strongly dependent on frequency. For instance, $\Delta|Z|$ at a 25% cell volume fraction is twice as large compared to that of cell volume fraction at 15% under 5 kHz frequency sweep, however there is little to no change in $\Delta|Z|$ for frequencies above 30 kHz.

By analyzing the 3D contour map, we determined that a large cell volume fraction (i.e. 25%) and low buffer conductivity (i.e. 100 µS/cm) at a low sensing frequency spectrum (1-10 kHz) produces the largest $\Delta|Z|$ following electroporation. This map thus provided a set of initial parameters to implement the permeabilization detection system. In our preliminary investigation of stationary cell membrane permeabilization, various microfluidic channels were designed to increase the cell volume fraction (up to 25%) in order to detect $\Delta|Z|$ after the application of electroporation pulses. In flow-based measurement systems, the micro-constriction channel geometry described in the previous chapter provides a cell-volume-fraction of 5%, a value that generates sufficiently high $\Delta|Z|$ while permitting continuous flow operation and adequate cell transit time for cell impedance dynamic analysis. A low extracellular buffer conductivity at 100 µS/cm provides two distinct advantages: (1) it produces the greatest $\Delta|Z|$ at lower frequency spectrum and (2) it is a parameter we previously reported to be capable of enhancing electrophoretic transport of molecules into cell.[3]

5.2 Cell Population Measurement in Time Domain

The parameters obtained from the numerical simulation of an electropermeabilized cell membrane allowed us to experimentally validate the detection feasibility of this cellular event. We hypothesize that by applying lethal electroporation pulses to lyse the cell membrane, large membrane disruption and pore formation will enable detection by the Lock-in amplifier sensor. An irreversible electroporation treatment with electric field

strengths at 2 kV/cm and durations above 10 ms will be applied to a large number of cells so that an aggregated permeabilization current measurement can be obtained. This is accomplished using microfluidic channels having a small or large sensing/electroporation region comprised of a pair of electrodes where a fixed number of stationary cells are isolated. The detection sensitivity down to the single cell level will be demonstrated through the use of microfluidic cell traps, creating a detection scale similar to that used in the cell/electrolyte circuit model for cell membrane permeabilization detection.

5.2.1 Channel Design & Fabrication

A microfluidic channel that is 1 cm in length, 300 µm in width, and 10 µm in depth was irreversibly bonded with a pair of titanium/platinum electrodes to form an intersecting configuration as shown in Figure 5.5a-b. This device fabrication follows the same photolithographic and soft lithographic procedures described in chapter 3. The electrodes were designed to be 410 µm apart from each other, forming a large detection/electroporation zone within the microchannel to collect aggregated current signal from a large number of cells. This region was made sufficiently large to accommodate up
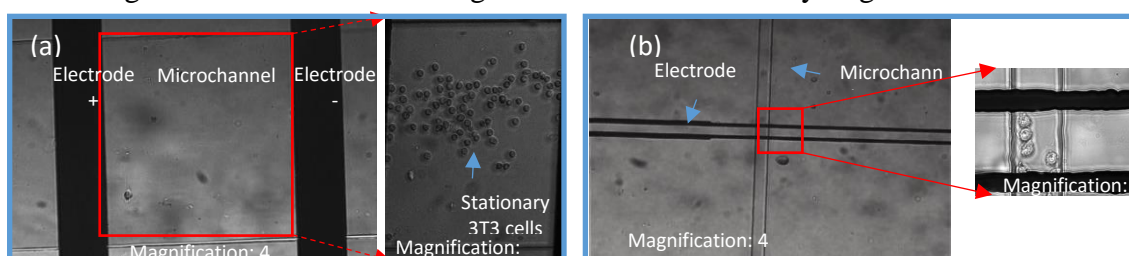
Figure 5.5. Bright field images of (a) a relatively large microfluidic channel with a dimension of 1 cm long by 300 µm wide by 10 µm deep compared to (b) a smaller microfluidic channel with a dimension of 1 cm long by 50 µm wide and by 10 µm deep is used to contain stationary cells for measurement. The inset of each images shows an enlarge area in the microchannel with 3T3 cells.

to ~300 cells, and the actual number of cells that can be placed here depends upon the harvesting density. A close-up view of the channel in Figure 5.5a shows the presence of approximately 100 stationary cells suspended in 100 µS/cm conductivity buffer in between the electrodes. In order to assess the cell current amplitude from a smaller population of cells (< 10 cells), a microfluidic channel with a dimension of 1 cm in length, 50 µm in width, and 10 µm in depth was fabricated (Figure 5.5b). The detection region of this device has an electrode separation distance of 100 µm. A close-up image in Figure 5.5b demonstrates the presence of 5 cells in the detection region of this device.

5.2.2 Experimental Operation

NIH 3T3 fibroblasts at 80% confluency was harvested and suspended in 100 µS/cm conductivity buffer. Propidium Iodide (PI), a nucleic acid binding fluorescent dye was added to the buffer at a total molar concentration of 100 µM. Since permeabilized cell membranes allow the entry of PI into the cell cytosolic space, intercellular fluorescence intensity of PI is indicative of the degree of permeabilization. Cells were perfused through the microfluidic channels at an arbitrary flow rate until the entirety of the detection region was filled with cells. Since a constant measurement baseline is desired to establish a reference of comparison, the cell carrier flow pressure was turned off and the cells were allowed to come to rest naturally. To perform electrical current measurement, the Lock-in amplifier waveform output was connected to one of the electrodes on the microchannel to supply an excitation voltage of 100 mV$_{p-p}$ at a frequency of 15 kHz. The current through the detection region was recorded by the Lock-in amplifier's sensor input which connected to the microchannel's second electrode. When the electroporation leads were connected on the micro-device electrodes, the Lock-in amplifier sensor input leads were temporarily

unplugged to prevent power surges that overloads the detection circuit. The Lock-in amplifier's senor input leads were reconnected for current measurement when the pulse is terminated. Cells in the electroporation zone of the channel were electroporated by the application of a lethal electric field at 2 kV/cm amplitude for 30 ms. The electroporation pulse was generated using a function generator and a DC amplifier as described in chapter 3.

5.2.3 Results & Discussions

Prior to cell population current response measurement following electroporation, a control study was performed using pure electroporation buffer without cells. The rationale is to calibrate the current measurements, and ensuring subsequent recording of current changes are the result of cell membrane permeabilization rather than artifacts or impulse responses from either the buffer or the device. Because current disturbances such as electrolysis have
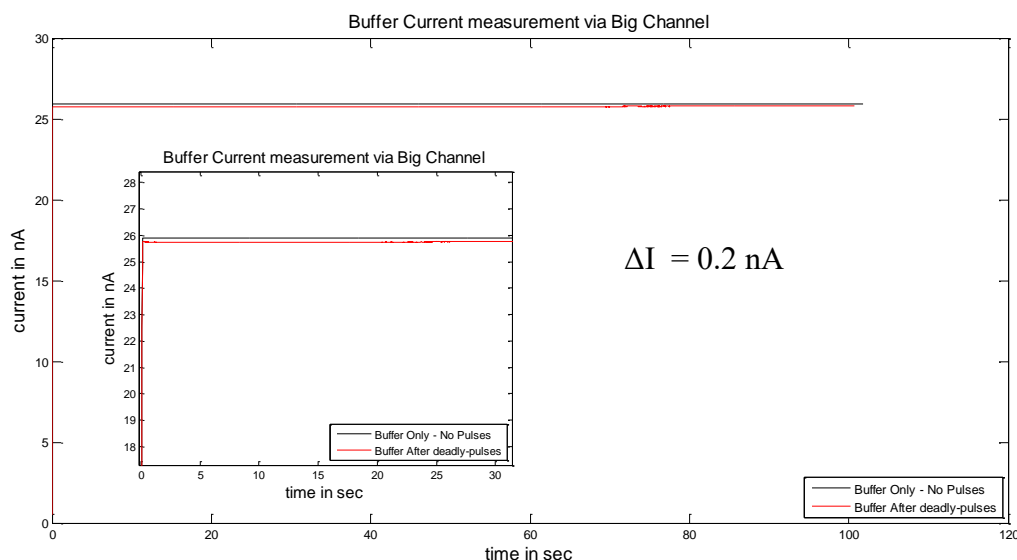
Figure 5.6. Electrical measurement of the electroporation buffer current in the large microfluidic channel without cells before (black curve) and after (red curve) applying lethal pulses to the buffer.

been known to occur at the interface between the electrodes and the buffer, pulsing the buffer establishes a baseline for comparison with the cell population current response.

Figure 5.6 demonstrates the current trace of the large microfluidic channel filled with 100 µS/cm conductivity buffer before and after applying lethal electroporation pulses. A difference of 0.2 nA was measured between these two current traces for a duration of 30 seconds. This current difference serves as the baseline difference for to the pulse applied. This control study was also performed on the smaller microfluidic channel with the same lethal electroporation pulses applied across the electrodes, and recorded by the Lock-in amplifier sensor. Figure 5.7 shows a current difference of 0.02 nA between un-treated buffer and buffer treated with lethal pulses. No current aberration was observed in the
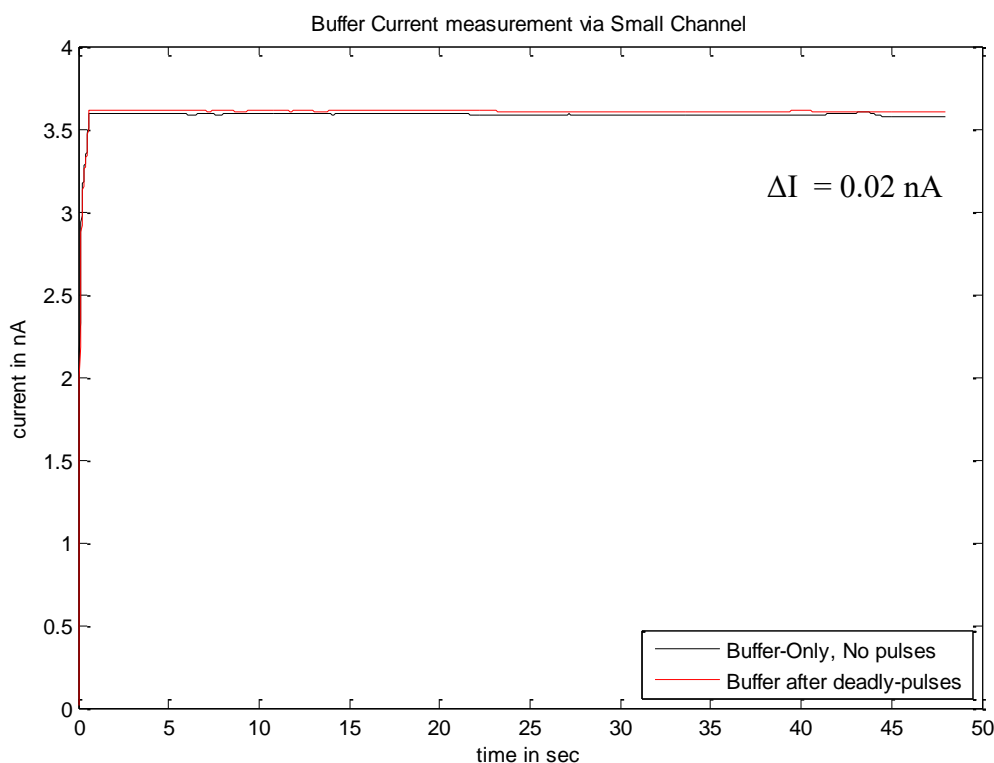
Figure 5.7. Electrical measurement of the electroporation buffer current in the small microfluidic channel without cells before (black curve) and after (red curve) applying lethal pulses to the buffer.

electroporation buffer, which prepares the device for the measurement of cell population current.

The measurement on the cell population was carried out after they were perfused into the microfluidic channels and remained stationary for the duration of the experiment. The bright field image in Figure 5.8a shows the presence of cells distributed randomly in the electroporation zone. The cells' membrane permeabilization state before electroporation is indicated by the fluorescence intensity of PI. The fluorescence image suggests a total number of 21 cells' membranes have already been permeabilized, therefore are not counted toward the total current measurement. This number will be subtracted from the total cell population as non-viable cells for cell current measurement following electroporation treatment. A small percentage of dead cells is inevitable in these experiments since the cells were subjected to a number of factors such as ambient temperature, pH fluctuation, joule heating, and mechanical trauma from handling the cells. A majority of the cells remain alive, indicated by the lack of viability staining from the PI dye.
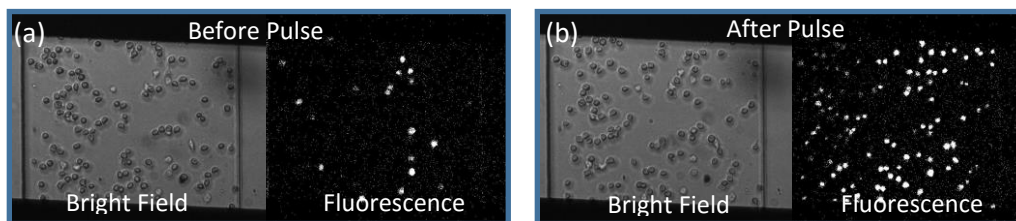
Figure 5.8. Microfluidic channel with large cell numbers in between the measurement electrodes under bright field and epifluorescence imaging mode (a) before and (b) after applying lethal electroporation pulses.

During the application of lethal electroporation pulses to these cells, no current recording was obtained. However, recording resumed immediately following the pulse termination (~ 3 seconds). The black curve in Figure 5.9 shows a baseline current of 25.4 nA from

approximately 108 stationary cells in the buffer solution measured between the electrodes. The current measurement performed after the electroporation treatment is displayed as the red trace in Figure 5.9, directly compared to the current from before the treatment. A distinctive steady current increase can be observed for over a minute which was measured to be 28.5 nA, compared to the control current of 25.4 nA before the pulse application. This current 'jump' is a clear indication of a compromised cell membrane. Cell membrane permeabilization for these treated cells can also be verified optically. As shown in Figure 5.8b's fluorescence images, PI was transported into the permeabilized cell membrane and fluoresced upon binding to the cytoplasmic nucleic acids after the lethal pulse application.
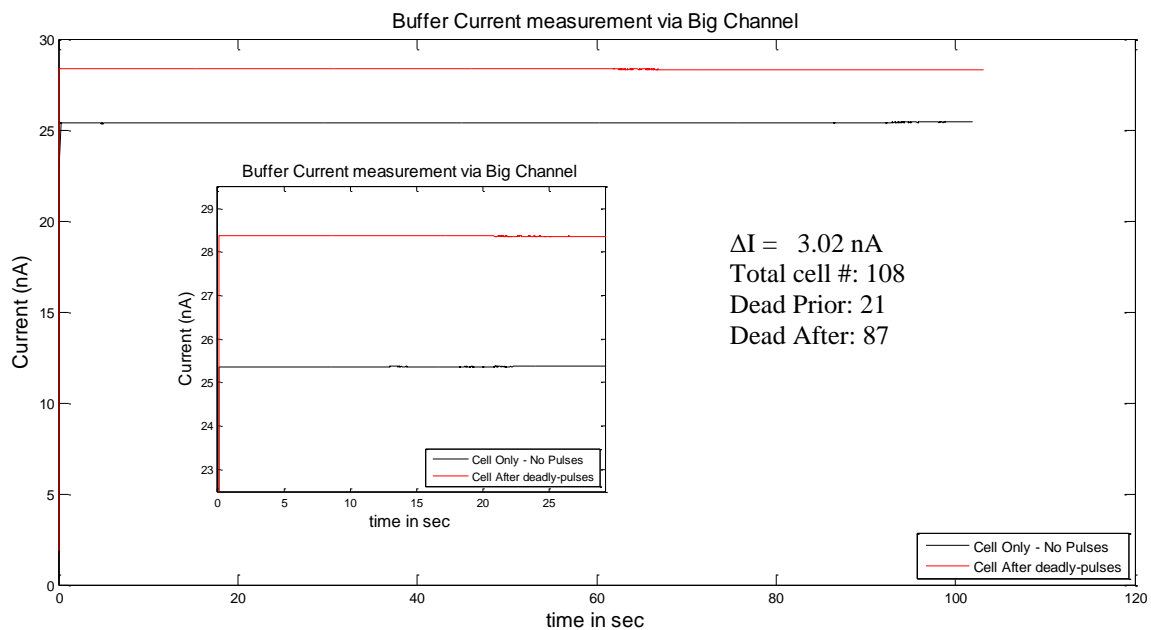
Figure 5.9. Electrical measurement of the stationary cell population (approximately 108 cells) in the microchannel measurement zone before (black curve) and after (red curve) applying lethal pulses to the cells. The elevated current reading after electroporation is indicative of cell membrane permeabilization.

Accounting for the initial cell death, this current reading was contributed by a total of 87 cells and was measured to be 3.02 nA.

The detection and measurement of a cell population current change from the irreversible electroporation was an encouraging first step. However, due to the large current contribution from the bulk solution in the large microfluidic channel, detection of current changes from fewer cells was difficult. This was a strong motivation for us to move toward microfluidic channel-based platforms with smaller detection volumes, and ultimately performing permeabilization measurements at the single cell level. In order to determine the feasibility of current measurement for small cell numbers, a narrower microfluidic channel was fabricated. Following the same operation as that used to measure large cell populations, the confining channel permitted only a few cells to be in between the electrodes, as shown in the bright field image of Figure 5.10a, six cells settled in the detection region for the electroporation treatment. The fluorescence intensity image disqualified one cell near the edge of the electrode, and the remaining five contributed to the resultant cell current reading.
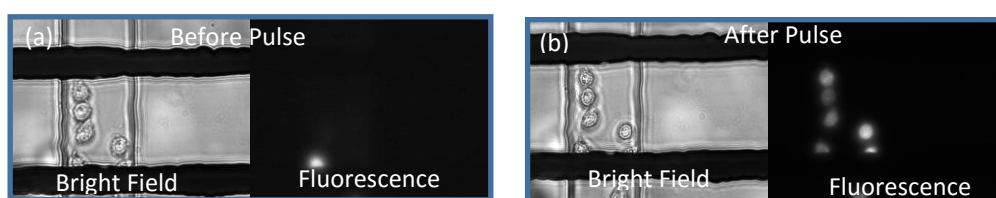
Figure 5.10. Microfluidic channel with small cell numbers in between the measurement electrodes under bright field and epifluorescence imaging mode (a) before and (b) after applying lethal electroporation pulses.

Identical lethal electrical pulses were delivered to these cells. Figure 5.11 shows the current traces before and after the pulse application, represented by the black and red curve,
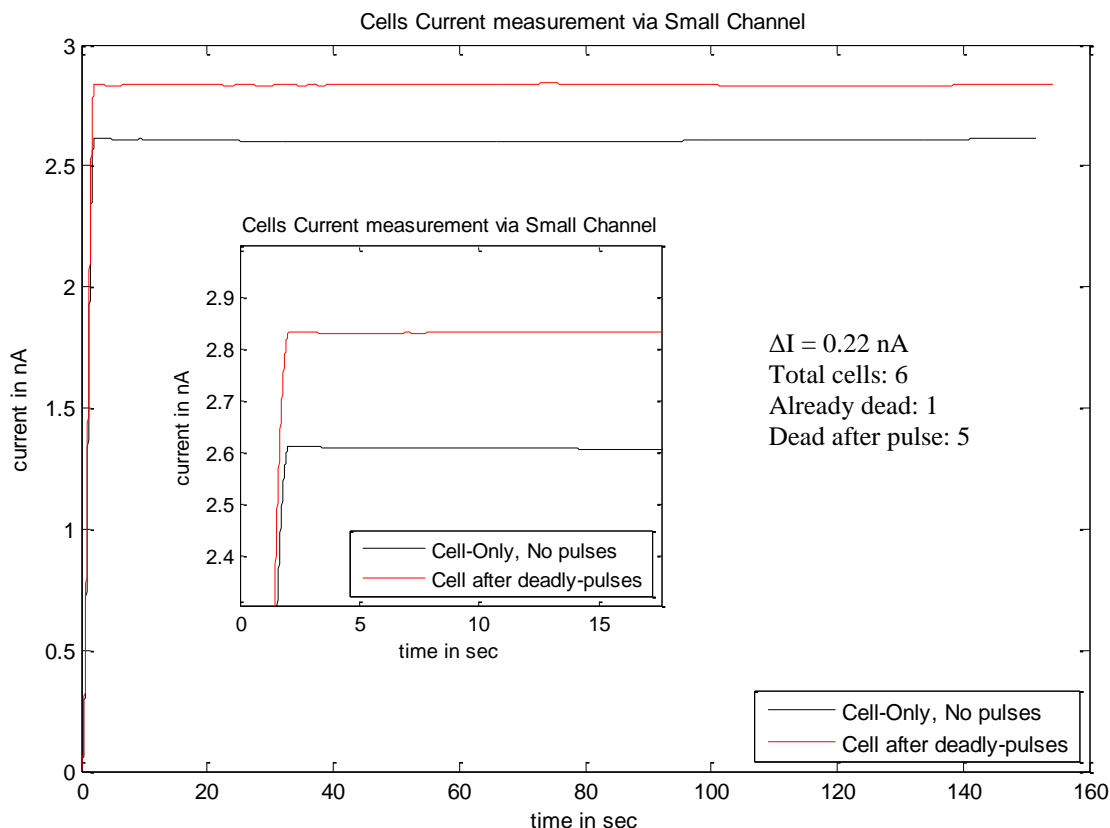
Figure 5.11. Electrical measurement of five stationary cells in the microchannel measurement zone before (black curve) and after (red curve) applying lethal pulses to the cells. The elevated current reading after electroporation is indicative of an aggregated cell membrane permeabilization.

respectively. A significant buffer baseline current reduction was measured as the direct result of a reduction in detection volume between the electrodes. A current difference of 0.22 nA was measured for these five cells. A fluorescence image of PI inside the cells is shown in Figure 5.10b, the elevated fluorescence intensity confirms the delivery of PI from a permeabilized cell membrane.

The number of cells in between the electrodes of the microchannel can be correlated to the current magnitude changes following the lethal electroporation treatment. Combining

multiple cell current measurement results from cell numbers ranging from 5 to 300 in both small and large microfluidic channels, Figure 5.12 presents a scatter plot of the change in current according to the number of cells in the channel. A linear curve fit was applied to the data set, and ± 1 σ confidence intervals were calculated along the mean. This linear trend of data suggests that the observed cell current increase is the result of an aggregated cell membrane permeabilization response after lethal pulse application, and it is therefore proportional to the number of cells in the channel.
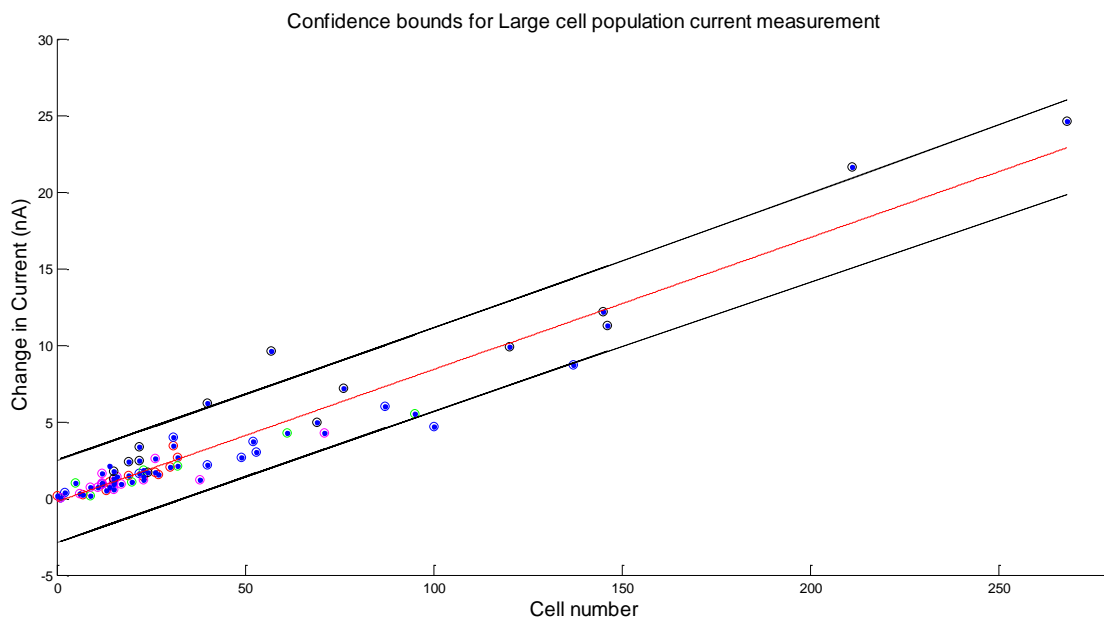
Figure 5.12. Change in current between un-electroporated and electroporate cell state as a function of cell number. A linear fitting was applied to the data set with ±1σ confidence intervals to demonstrate the dependency of current increment on number of cells being irreversibly electroporated.

5.3 Single Cell Immobilization and Membrane Permeabilization Measurement

Although the microfluidic channels described above are able to provide aggregated cell permeabilization current measurements, measurement at the single cell level was not feasible due to the small cell volume fraction, and large double layer capacitance at the electrode-buffer interface. The ability to detect and measure cell membrane permeabilization on an individual basis enhances the detection accuracy and enables an alternative approach other than optical imaging to assess the electroporation and cell viability state. It is also crucial in establishing a functional and sensitive microelectroporation device, paving the way for the development of a flow-based single cell membrane permeabilization control chamber. There are two main contributions of noise in this system that needs to be minimized for improving cell current-to-noise ratio. The first one is the amount of buffer solution in the measurement region, which both numerical simulation and experiments have suggested a high cell volume fraction is necessary for maximizing SNR. Another source of noise is the area of exposed electrode surface to the buffer. Although a large electrode surface has better sensitivity to input signal, it also generates a large amount of electrical noise. Since our input signal of interest (cell membrane pores) is extremely small, it is easily masked by surrounding electrical noise.

5.3.1 Single Cell Trapping Device Design

A microfluidic channel have been designed, fabricated and tested for improving static single cell level SNR (Figure 5.13). This is a "bowl" shaped single cell trapping design with two vertical planar electrodes separated by a distance of 70 µm directed at the center of the 'bowl'. 3T3 fibroblast cells at a low density were perfused into the channel from the left inlet, they flowed pass the center of the 'bowl' structure which is a small opening with
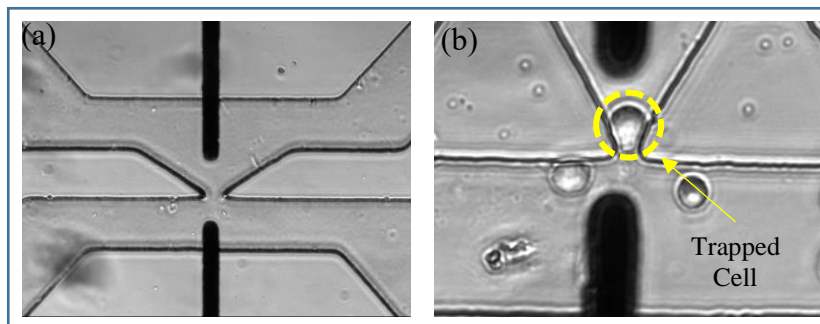
Figure 5.13. (a) A Microfluidic channel without a trapped cell is shown. (b) A 3T3 fibroblast cell is immobilized for electroporation treatment and membrane permeabilization measurement study, indicated by the yellow dash line.

a dimension of 10 µm in both width and depth, and they exited from either the right outlet, or through the center of the 'bowl' structure into two flow-pressure relieving outlets. This channel configuration allows the continuous flow of buffer and small cells over or through the 'bowl', rather than clogging the small opening. This architecture was specifically designed so that single cells with large radii (> 10 µm in diameter) could become passively immobilized at the small opening. After receiving electroporation treatment and permeabilization measurement, pulsatile fluidic flow pressure can be applied to dislodge the trapped cell to exit any one of the three channel outlets. In terms of fabrication, cell immobilization and measurement reliability and reproducibility, this design was selected to carry out the subsequent single cell membrane permeabilization investigation.

5.3.2 Single Cell Permeabilization Measurement in Frequency Domain

Prior to the measurement of single cell trapping and permeabilization measurement, the channel was filled with pure electroporation buffer at a conductivity of 100 µS/cm. A voltage sweep ranging from 1 to 10 V_{P-P} (an equivalent of 0.1 to 1.5 kV/cm electric field)

was applied to observe the change in impedance before and after pulse application. By performing a frequency sweep at each voltage, we can directly compare the experimental impedance magnitude on a single cell to numerically predicted value in the beginning of this chapter. The goal is to experimentally validate the numerical model and fine-tune the frequency band in which largest change in cell impedance occur after irreversible electroporation. Demonstrated in Figure 5.14, the application of electroporation pulses with the applied electric field strength does not cause significant rise in the buffer impedance reading or any other signal aberration. Although considerable noise is presented at the lower frequency band (<1 kHz), it is not a major concern since our predicted
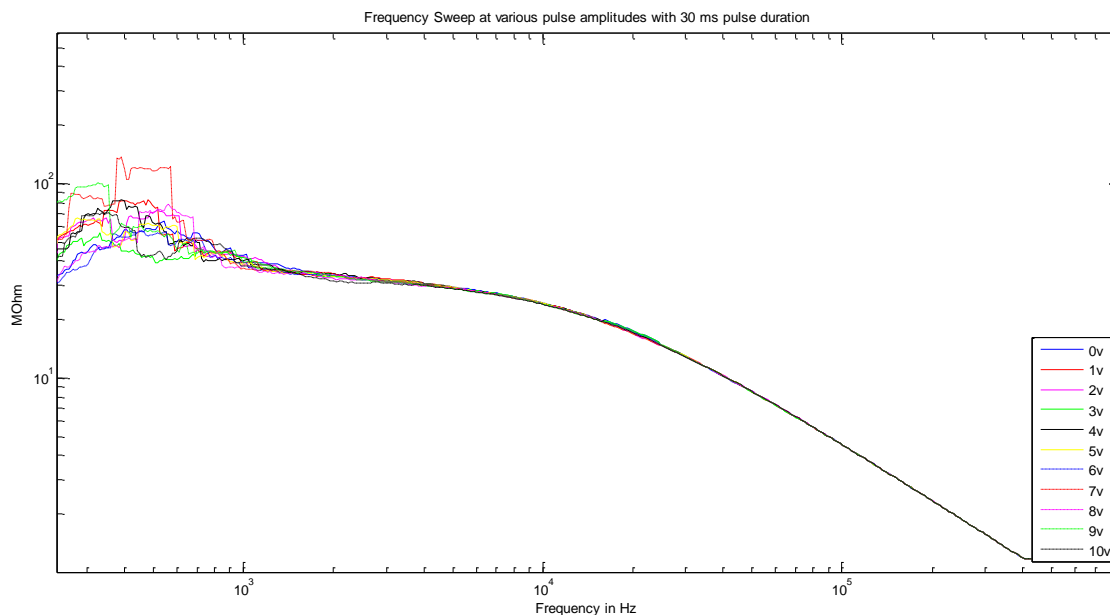
Figure 5.14. Voltage sweep of electroporation buffer impedance in the single cell trap microchannel, plotted as a function of frequency. A range of 0 to 10 volts peak-to-peak was applied to the buffer with 30 ms duration each. No significant impedance variation can be found in impedance beyond 1 kHz.

frequency range for which membrane permeabilization has the most impedance change is beyond 1 kHz, and there is less than 1 kΩ of impedance variation above this frequency.

When a live cell was successfully immobilized in the channel, a frequency sweep with an amplitude of 100 mV$_{p-p}$ was applied to record the cell impedance response from 1 Hz to 1 MHz. Then a lethal 30 ms long electroporation pulse at 2 kV/cm electric field strength was applied to the cell through the vertical electrodes to irreversibly electroporate the cell. The insets in Figure 5.15 consist of a bright field image of the trapped cell and two fluorescence images showing PI intensity before and after the irreversible electroporation treatment. A yellow dashed circle highlights the location of the cell. The cell remained non-fluorescent
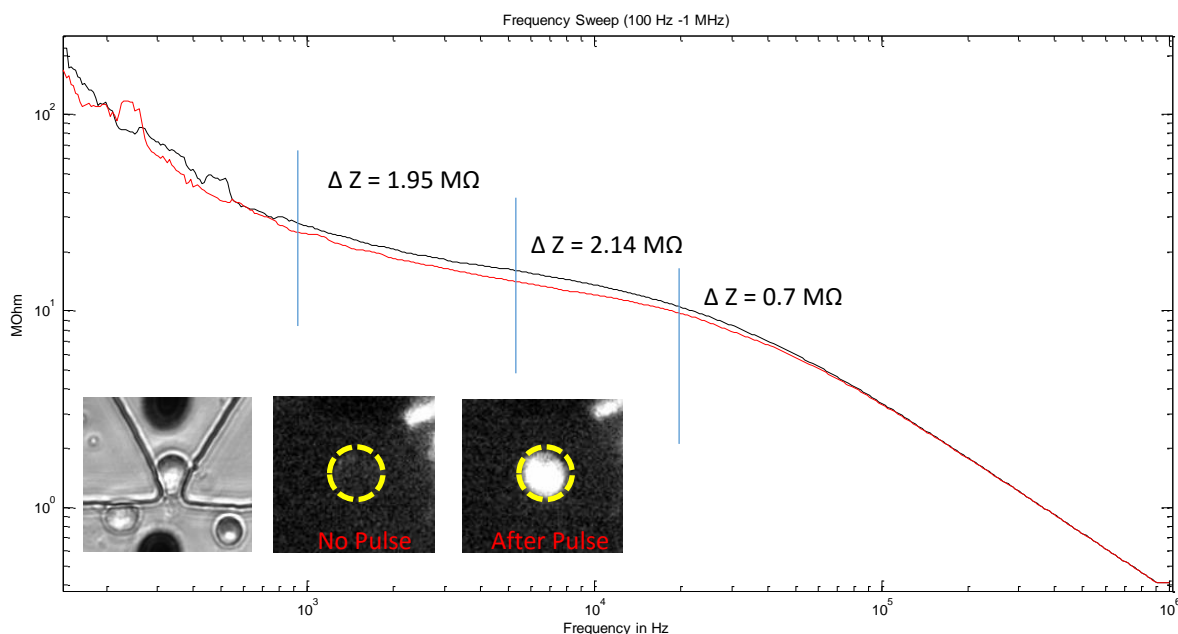
Figure 5.15. Impedance measurement of an immobilized cell as a function frequency before and after applying irreversible electroporation pulses. The vertical lines mark the impedance difference at 1, 5, and 20 kHz frequency to show regions of largest impedance change. The inset shows a bright field image of the trapped cell and two fluorescence images of the cell before and after the treatment.

until the pulses were applied, and the entire cell became saturated with the PI fluorescent dye, indicating the complete permeabilization of the cell membrane and transport of PI throughout the cytoplasmic space. The electrical signal of cell membrane permeabilization after the pulse application was captured by performing another frequency sweep with the same frequency range. Figure 5.15 illustrates the impedance difference between the black curve which is the impedance of a healthy cell and red curve, the impedance of the same cell with permeabilized membrane. The cell impedance closely resembles that predicted by the numerical simulation of a cell in suspension with the effect of double layer capacitance. A distinctive difference in cell membrane impedance can be determined from frequencies 1 to 20 kHz. Three vertical lines were placed at 1, 5, and 20 kHz to highlight an impedance difference of 1.95, 2.14 and 0.7 MΩ, respectively in Figure 5.15.

5.3.3 Single Cell Permeabilization Measurement in Time Domain

Impedance analysis via frequency sweep performed in the previous section confirms the frequency range necessary for detecting drastic impedance changes indicative of cell membrane permeabilization. As an additional analysis, we also demonstrate the tracking of this cell membrane event in the time domain to enable repeated electroporation and long term measurement on the same cell. We achieved this by adjusting the Lock-in amplifier sensor to 'lock' onto a single excitatory frequency. Based on the impedance analysis data from the previous section, a frequency of 5 kHz which elicited the highest impedance change was selected. After a new cell has been trapped in the microchannel, a lethal electroporation pulse was once again applied to the cell. Shown in Figure 5.16, the steady cell-buffer current was measured for one minute to ensure stability over time prior to the pulse application, then immediately after the pulse was applied, a nearly 2 nA sharp current
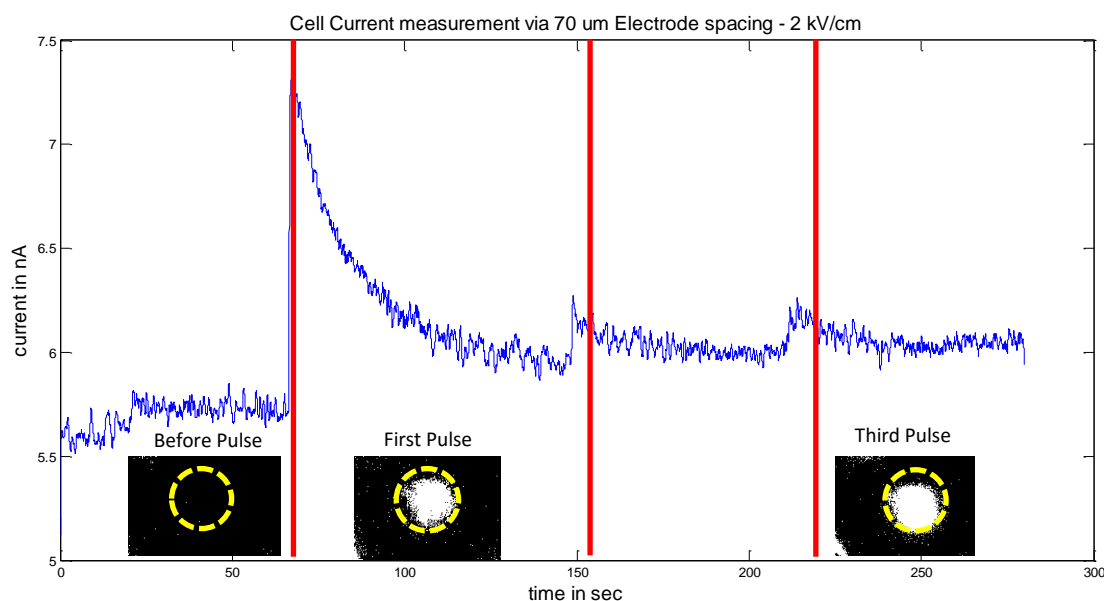
Figure 5.16. Current measurement of an immobilized cell over time with excitation voltage of 1 V_{p-p} at 15 kHz frequency. The vertical red lines mark the application of a 30 ms electroporation pulse with an amplitude of 2 kV/cm. Fluorescent images of the cell is highlighted by the yellow dashed circle before pulse application (left), after first pulse (middle) and at the end of last pulse (right). The cell is fully permeabilized and saturated with PI from the electrophoretic transport during electroporation.

"jump" was observed for this cell. This event was also captured by the epifluorescence camera, and shown in the inset of Figure 5.16 where a huge burst in PI fluorescence intensity can be observed after the pulse, compared to cell before the pulse. Such a sharp increase in cell permeability is likely attributed to the lysing of cell membrane from the lethal electroporation treatment. The gradual reduction in current over time to an elevated baseline of 6 nA in comparison with the pre-pulse current of 5.55 nA suggests a severe disruption in the cell membrane has occurred, allowing the highly conductive cytoplasmic content to leak out of the cell. The local current eventually reaches an equilibrium with the

surrounding buffer, establishing a higher current baseline than before. A compromised cell viability was confirmed by reapplying the lethal pulse to the same cell. A small current "jump", approximately 0.2 nA in amplitude was measured, which is likely due to the current rise from permeabilizing the cellular organelles. Fluorescence images of this cell after a final pulse application shows slight increase in fluorescence intensity, suggesting the complete saturation of the inner cell with PI.

5.3.4 Single Cell Measurement – Reversible Electroporation

Since the lethal electroporation pulses bring forth the analysis of irreversible cell membrane permeabilization, an electric field with sub-lethal amplitude and durations was applied to investigate the cell membrane resealing responses. Figure 5.17 demonstrates the representative responses of an individual cell underwent reversible electroporation treatment at an electric field strength of 0.9 kV/cm for 1 ms per pulse. The administration of first pulse elicited a moderate 0.2 nA of current increase, followed by its gradual return back to the original baseline current. Because cell membrane resealing after electropermeabilization is a slow process, with a time scale ranging from seconds to minutes, the observed current return from the peak amplitude suggests that a percentage of the membrane pores may have resealed, albeit not completely. The hypothesis of incomplete cell membrane resealing is supported by the application of another electroporation pulse of the same magnitude and duration. This second pulse elicited a drastic current 'jump', with an increase of 0.7 nA in current similar to the permeabilization signal measured for cells underwent lethal electroporation treatment in Figure 5.16. The measurement of this cell current increase from the second pulse application suggests the membrane was not completely resealed and it has a lowered transmembrane potential

threshold for the next pulse to overcome. Optical confirmation of the cell's membrane poration can be seen in the insets of Figure 5.17 where the first pulse yielded slightly elevated PI fluorescence intensity compared to the cell before pulse application. PI fluorescent intensity significantly increased following the second pulse application. The confirmation of this cell's compromised membrane integrity is shown through the administration of the following three additional pulses. Each successive pulse elicited smaller current 'jump', suggesting that the cell membrane has now fully permeabilized with no chance to reseal despite a prolonged waiting time. The fluorescence intensity inside the cell also suggests a fully saturated intercellular space as a result of unhindered delivery of PI from each pulse.
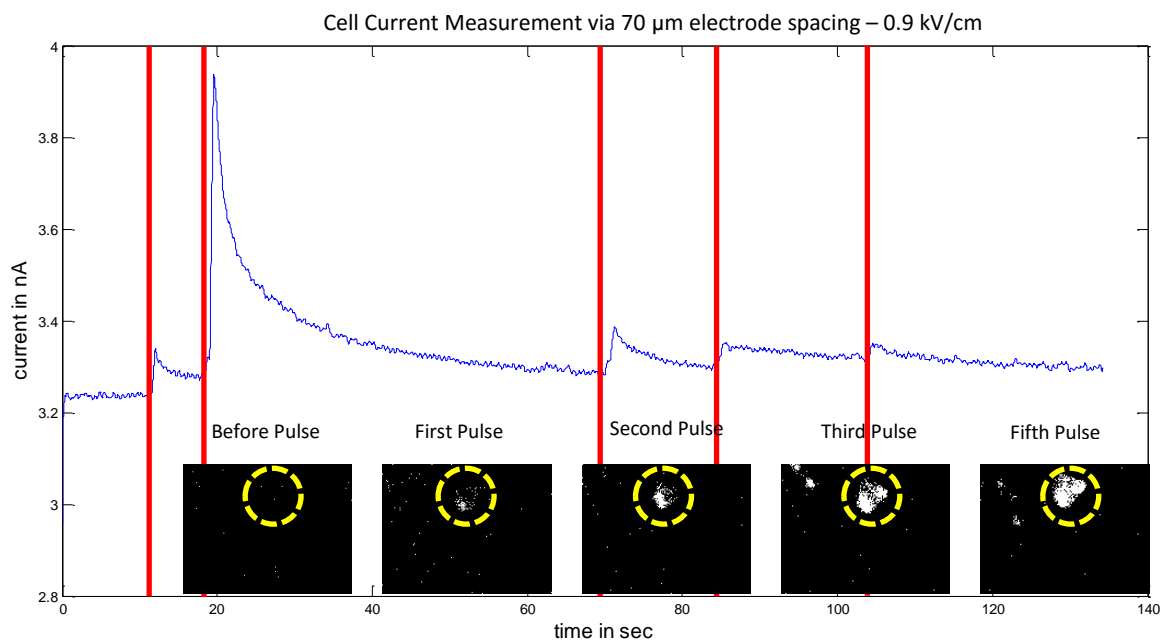
Figure 5.17. Current measurement of an immobilized cell over time with reversible electroporation pulse parameters (0.9 kV/cm for 1 ms) using a sensing excitation voltage of 1 V_{p-p} at 15 kHz frequency. The vertical red lines mark the application of a 1 ms pulse. Fluorescent images of the cell is highlighted by the yellow dashed circle to indicate location of the cell.

The successful detection and measurement of cell membrane permeabilization and resealing dynamics in an individual immobilizing microfluidic channel is encouraging for the translation and implementation of this platform to a continuous-flow based environment, where similar single cell level membrane behavior will be measured in a high throughput manner.

5.4 Chapter References:

1   L. J. Gentet, G. J. Stuart and J. D. Clements, *Biophys. J.*, 2000, **79**, 314–20.

2   J. Li, W. Tan, M. Yu and H. Lin, *Biochim. Biophys. Acta - Biomembr.*, 2013, **1828**, 461–470.

3   M. M. Sadik, J. Li, J. W. Shan, D. I. Shreiber and H. Lin, *Biochim. Biophys. Acta - Biomembr.*, 2013, **1828**, 1322–1328.

4   Y. Huang and B. Rubinsky, *Sensors Actuators A Phys.*, 2001, **89**, 242–249.

5   M. Khine, A. Lau, C. Ionescu-Zanetti, J. Seo and L. P. Lee, *Lab Chip*, 2005, **5**, 38–43.

Chapter 6

Cell Membrane Permeabilization Measurement for Flowing Single Cells

Note: Excepts of this chapter was adapted from the following publication:

6.1 Systems Integration

The demonstration of high SNR detection of flowing single cells in chapter 4, and the sensitive electrical measurements of immobilized single cells with and without electroporation treatments in chapter 5 established the foundation for the development of a novel high throughput single cell electroporation and impedance monitoring system. Taking advantage of the continuous-flow environment in high throughput electroporation microdevices, and cell membrane impedance sensing in patch-clamping-based microchannels, this chapter describes the development of a continuous-flow, automated microfluidic device for electroporation of individual cells and control of cell membrane permeabilization magnitude. This device operates autonomously to detect the entrance of an individual cell into the electroporation zone with a high SNR, and subsequently apply an electroporation pulse to the cell in transit. Cell membrane impedance is continuously monitored, and both optical and electrical measurements are conducted before and after pulse application. A collection reservoir at the outlet of the channel allows the retention and harvest of treated cells for viability assessments. The ability to electrically record and monitor the degree of cell membrane permeabilization enables real-time assessment of cell viability. By correlating the electroporation pulse parameters with cell impedance changes and viability, we demonstrate the device's ability to measure and control cell

membrane permeabilization in a continuous-flow fashion, and enable intracellular transport of small molecules. The ultimate goal of this work is to develop a 'smart' electroporation platform where a feedback controlled electric pulse is automatically applied to permeabilize each individual cell prior to a critical viability threshold while enabling maximal intracellular molecular delivery without sacrificing viability. This electroporation system has the potential to bridge the gap between single cell analyses via immobilization and continuous flow single cell electroporation devices, to drastically improve cell viability for different cell types without empirically-derived electroporation protocols.

6.2 Materials & Methodology

6.2.1 Principle of Operation

The operation of our automatic electroporation system starts with the perfusion of single cells through a microfluidic channel constriction, an active region consisting of both sensing and electroporation electrodes (hereby referred to as the electroporation zone) (Figure 6.1a). Upon user initiation of the electroporation process, the sensor continuously monitors each cell's passage across the electroporation zone. Cell entry into the electroporation zone produces a sharp current drop in comparison to the buffer baseline due to the well-known resistive pulse sensing technique.[1–3] A first-derivative peak detection algorithm monitors for this sudden change in current to determine the presence of a cell. The derivative based peak detection algorithm was implemented due to a faster computation speed in the sensor's real time processing unit compared to an integral algorithm. Once a cell has been identified, an electroporation pulse with predefined electric
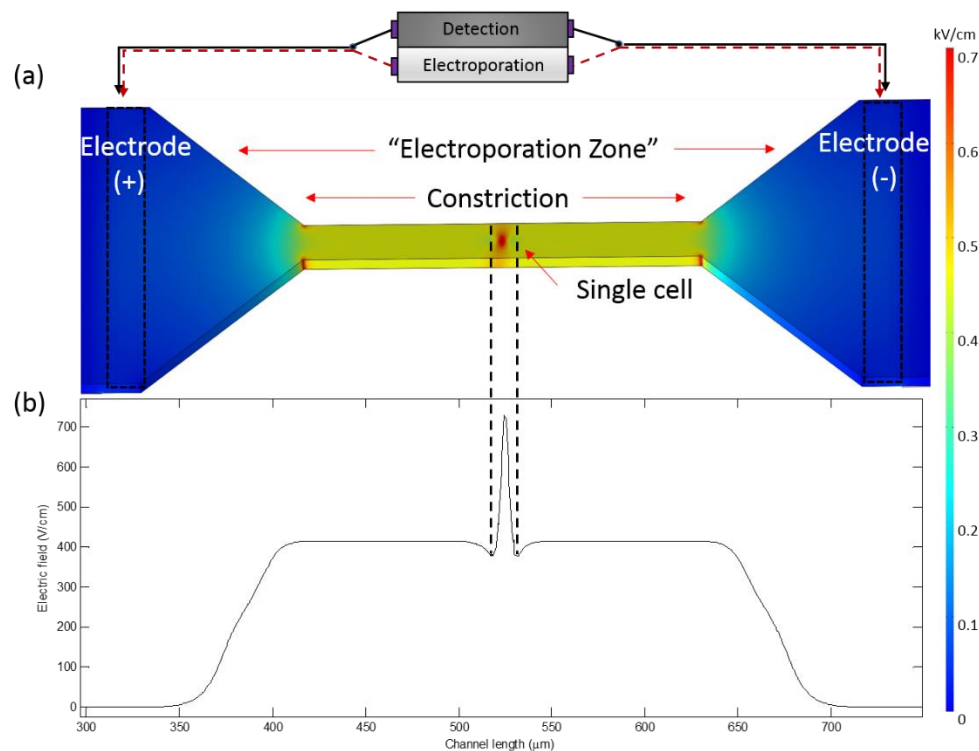
Figure 6.1. COMSOL simulation showing the electric field distribution in the microfluidic channel with a cell moving across the constriction region of the channel (electroporation zone). (a) This microfluidic channel consists of a 250 (L) × 25 (W) × 12 (D) µm constriction between a pair of planar electrodes that are 300 µm apart. Under detection mode, an AC sine wave monitors the single cell presence and cell membrane permeabilization. When an electroporation pulse is applied, detection is temporarily halted until the end of the pulse application (b) Applied electric field is amplified by the constriction of the channel. The addition of a cell adds to the channel resistance and further amplifies the applied electric field by 1.75×.

field strength and duration instantly outputs from the pulsing unit. This pulsing unit consists of a signal processing and rerouting program written in LabVIEW (LabVIEW Professional Edition 2015, National Instruments) and connected to the external electroporation and sensing apparatus. Immediately following the pulse application, the

sensor records any post-pulse impedance changes from the cell prior to its departure from the electroporation zone. The optimal sensing frequency required to detect single cell membrane permeabilization magnitude was obtained from the cell/electrolyte circuit model and immobilized cell impedance measurements described in the chapter 5.1 and 5.2.

An electroporation zone was designed as a microchannel constriction based geometry.[4] The constriction-based microchannel design provides three distinctive advantages: (1) a large current displacement signal for single cell presence detection (2) a high cell-volume fraction which increases the impedance change SNR during permeabilization (3) geometric amplification of the electroporation pulse to lower the input voltage requirement, thus avoiding unwanted effects such as joule heating, electrolysis, and extreme fringing electric fields near the electrodes. COMSOL simulation (COMSOL Multiphysics 4.2a, COMSOL) of the microchannel in Figure 6.1b shows the amplification of the electric field as a function of channel length. When a 0.4 kV/cm electric field is applied to the electrodes, 0.5 kV/cm electric field is measured at the constriction. The presence of a cell within the constriction further increases the local resistance, amplifying the electric field to a value of 0.7 kV/cm around the cell.

6.2.2 Device Fabrication

The device consists of a pair of planar electrodes on a glass substrate and a polydimethylsiloxane (PDMS) microchannel fabricated via soft lithography process described previously.[5] The silicon master mold with the device feature was fabricated using standard photolithographic procedures. The device main channel is 1 mm long, 150 µm wide, and 10 µm deep, incorporating a constriction with a dimension of 250 µm (L) × 25 µm (W) × 10 µm (D). Briefly, a 10:1 mixture of PDMS polymer and hardening agent were

poured onto the mold to create a negative replica following 65 °C curing overnight. A 0.5 mm diameter hole-punch was used to create a fluidic access to the channel inlet. Likewise, a 1.5 mm hole-punch creates an outlet collection reservoir. Titanium/Platinum (Ti/Pt) electrodes were fabricated via a metal 'lift-off' process. Traces for the planar electrodes were lithographically patterned on glass substrates and recesses were hydrofluoric acid etched with 10:1 BHF for 1 minute to a depth of ~ 2000 A. The metals were deposited via physical vapor deposition of titanium (Ti) and platinum (Pt) (KJL PVD75, Kurt J Lesker Co.) followed by dissolution of the photoresist in acetone leaving behind the electrode traces. The resultant Ti/Pt electrodes are 50 µm in width, with a 300 µm center-to-center separation. This distance provides sufficient cell resident time for electrical and optical analysis without compromising SNR quality. PDMS microchannel and the glass substrate surfaces were treated with oxygen plasma at 100 W power, 250 sccm O_2 at 700 mTorr for 60 s (PX-250, March Instruments). The activated substrates were aligned and irreversibly bonded using a stereo-microscope (SZ61 Binocular Stereo Zoom, Olympus). Copper wires were bonded to the planar electrode pads via conductive epoxy.

6.2.3 Experiment Setup & Preparation

Prior to each experiment, the microchannel was pre-treated with a 10% BSA solution incubated at room temperature for one hour to prevent unwanted cell adhesion to the channel surfaces. The microchannel was then drained, and excess BSA solution was removed from the outlet reservoir and replaced with 10 µL of Dulbecco's modified Eagle's medium (DMEM) media. NIH 3T3 mouse fibroblasts were cultured in DMEM with 10 % v/v fetal bovine serum (FBS), 1 % v/v penicillin–streptomycin (P/S) and 1 % l-glutamine (Sigma-Aldrich, St. Louis, MO). Cells were cultured to ~70 % confluency before being

harvested. The harvested cells were suspended in a 100 µS/cm conductivity pulsing buffer.[5–8] A microfluidic syringe pump (PicoPlus, Harvard Apparatus) was erected vertically to perfuse the cells across the microchannel constriction at 0.1 µL/min flow rate, resulting in an average cell transit time of 250 ms. The vertical alignment prevents cell settling at the bottom of the syringe. Once a stable flow with single cell transit across the electroporation zone was established, the electroporation system was initiated upon user command. Five electric fields (0.4, 0.6, 0.7, 0.9, 1 kV/cm) were investigated at five pulse durations each (0.2, 0.8, 1, 3, 5 ms) to demonstrate control of cell membrane permeabilization via the electroporation system. Two cell assays were carried out in our experiments to validate the electroporation system. During the first assay, Propidium iodide (PI) (P3566, Life Technologies), a cell membrane impermeant dye which fluoresces upon binding to cytosolic nucleic acids, was added to the pulsing buffer at 100 µM total concentration to optically signal membrane permeabilization. The electrical signal from the Lock-in amplifier and the fluorescence intensity of PI delivery were recorded on an individual cell basis. In a second assay, single cells underwent the same electroporation treatments without PI addition. Following each prescribed pulse treatment for 20 minutes, approximately 2000 cells were collected from the outlet reservoir for viability assessment. The collected cells were washed in 1× PBS buffer via centrifugation at 2000 RPM for 2 minutes, then incubated with 2 µM of 7-Aminoactinomycin D (7AAD) (7-AAD, ThermoFisher Scientific) on ice for 20 minutes to allow cell viability staining. The cells were then washed again in 1× PBS buffer prior to imaging under a fluorescence microscope. A semi-automated cell scanning and processing algorithm written in MATLAB (MATLAB R2012b, Mathworks) was used to process the fluorescence intensity of the collected cells.

Details regarding the assays, their image capture, and processing have been described in chapter 3.5.

The dynamic signal extraction and electroporation pulsing systems were implemented via a commercial Lock-in amplifier (HF2LI Lock-in Amplifier, Zurich Instruments). The system's detection and electroporation operation is programmed in a custom-built LabVIEW control algorithm and loaded onto the Lock-in amplifier's embedded system for real-time processing. One of the two device electrodes was connected with the Lock-in amplifier output to deliver a sensing excitation signal of 1 V_{p-p} while the other electrode was connected to a low noise current preamplifier input (HF2CA Current Preamplifier, Zurich Instruments) prior to passing the signal to the Lock-in amplifier sensor input. A frequency of 1.224 kHz was selected to provide optimal cell detection via the derivative based peak detection algorithm and cell membrane permeabilization sensitivity with the highest signal-to-noise ratio. Upon detection of a cell within the electroporation zone, the electroporation pulse is digitally triggered by the Lock-in amplifier output following a LabVIEW command. The digital output that carries the pulse initiation command was sent to the external trigger of a function generator (33220AA Waveform Generator, Agilent) to trigger the output of a pulse. The electroporation pulse was programmed in the function generator and the pulse signal was fed to a high voltage amplifier (Model 2350, TEGAM) to supply electric field pulses ranging from 0.4 to 1.0 kV/cm with a duration between 0.2 and 5 ms. A CMOS switch (DF419D)J+ Analog Switch, Maxim Integrated) synchronized with the function generator was added in series with the Lock-in amplifier's preamplifier input to prevent electronic artifacts from the electroporation pulse.[9] The pulse trigger signal was also split to the external trigger input of a microscope mounted CMOS camera

(PowerView 1.4MP, TSI) to simultaneously capture images of PI entry into cells after each pulse.

6.3 Automated Cell Detection & Electroporation

Automated detection of single cells and immediate pulse application to each cell is demonstrated in Figure 6.2 at a throughput of 1.3 cell/s. Cell transit across the constriction length yields a stable baseline due to the constant volume displacement in the channel. An estimated cell transit time of 250 ms provided an ample temporal window for electroporation and post-pulse impedance measurement. In this representative plot, the
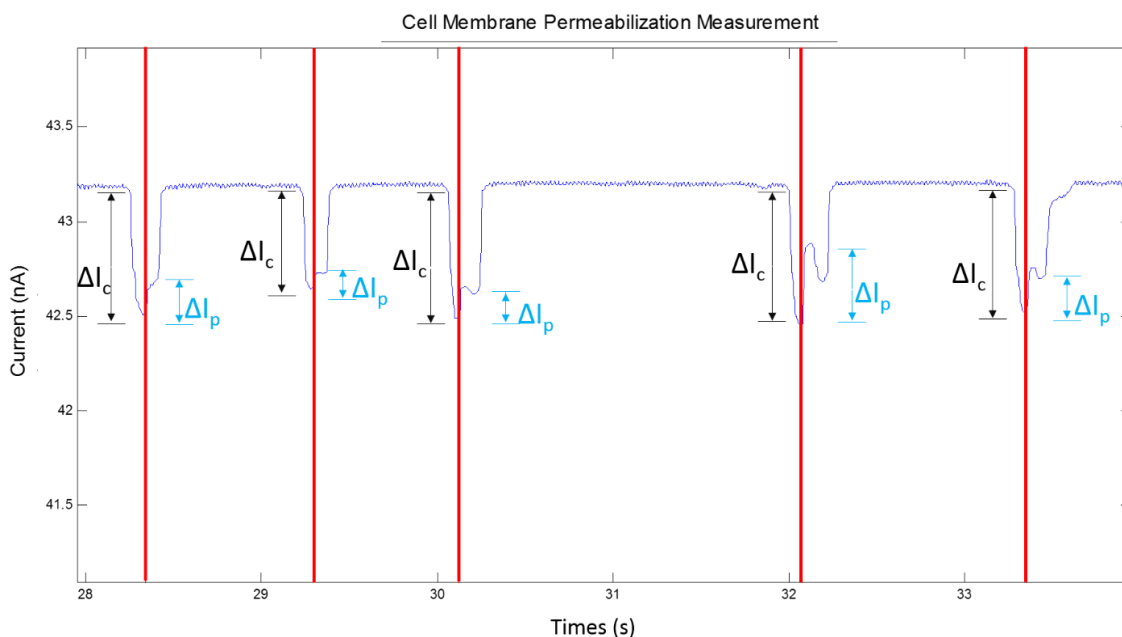
Figure 6.2. Resistive pulse-based detection of flowing single cells across the channel constriction. Current displacement of each cell entering the pulsing zone is measured as ΔI_c from the baseline current. The red curve indicates the administration of an electroporation pulse. The current "jump", following the pulse, is measured as ΔI_p. A flow rate of 0.1 µL/min was used to obtain a sufficient cell transit window for observing post-pulse cell responses.

vertical red line depicts the application of a prescribed electroporation pulse, in this case a 1.05 kV/cm electric field strength for 5.0 ms. A sharp rise in current is immediately observed after administering the pulse. This 'current jump' is a strong indication of an increase in cell membrane conductance and characteristic of the formation of pores as a result of electroporation-induced cell membrane permeabilization. This phenomena closely resembles the observed cell membrane dynamics in the chapter 5.3.3 and published reports by other researchers using microfluidic-based patch-clamping methods.[10,11] As the cell departs from the channel constriction, the electrical signal returns to the buffer solution baseline. This process repeats for each cell traversing through the electroporation zone. An SNR of 37 dB was measured for the single cell detection, and a 93.7% accuracy was determined for detecting and pulsing each cell. Error can be attributed to the occasional tailgating of single cells, leading to multiple pulse application to both cells in transit, and pulse misfire due to unexpected inconsistency in flow rates.

6.4 Dynamic Cell Membrane Permeabilization Control

In addition to detecting the cell membrane permeabilization event, we also demonstrate the ability to control the degree of permeabilization. As shown in Figure 6.3, the cell current responses for five representative cells are superimposed at the time of pulse application. By keeping the electric field constant at 1.05 kV/cm while altering the pulse durations from 0 to 5.0 ms, it was determined that a longer pulse duration results in a greater cell current 'jump', indicating a higher degree of membrane permeabilization, since a longer pulse duration provides a greater amount of electric charge buildup needed to overcome the transmembrane potential.
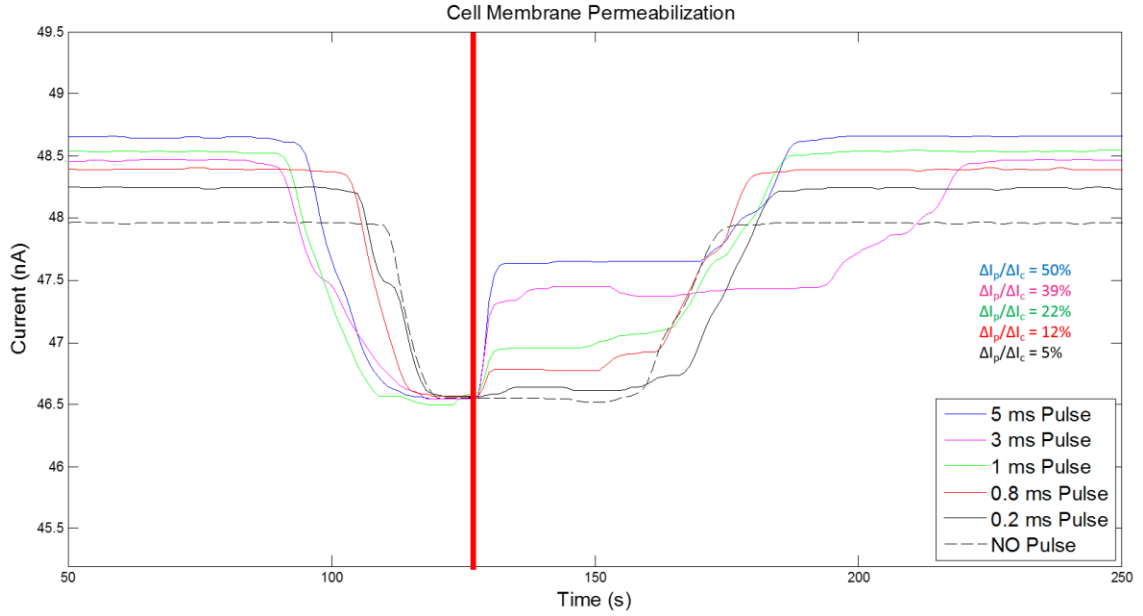
Figure 6.3. Electrical measurements of single cells that underwent electroporation treatment at 1 kV/cm electric field strength for 5 ms (blue trace), 3 ms (purple trace), 1 ms (green trace), 0.8 ms (red trace), 0.2 ms (black trace), compared with a single cell without electroporation treatment (dotted back trace). Cell membrane permeabilization, ΔI_p, is normalized by its corresponding cell current displacement, ΔI_c, and expressed according to their color-code.

A full characterization of the cell membrane response as a function of both electric field strength and duration is shown in Figure 6.4.

To ensure there are no cell-to-cell variations due to size differences, the change in the permeabilization current from the cell baseline (ΔI_p) was first normalized by the total cell current displacement (ΔI_c). This is expressed as a percentage increase from the detected cell current baseline. When plotted as a function of pulse duration, a dependency was found between the permeabilization magnitude ($\Delta I_p / \Delta I_c$) and the pulse duration (distinguished by symbol color used in the plot), for a given electric field strength (distinguished by the
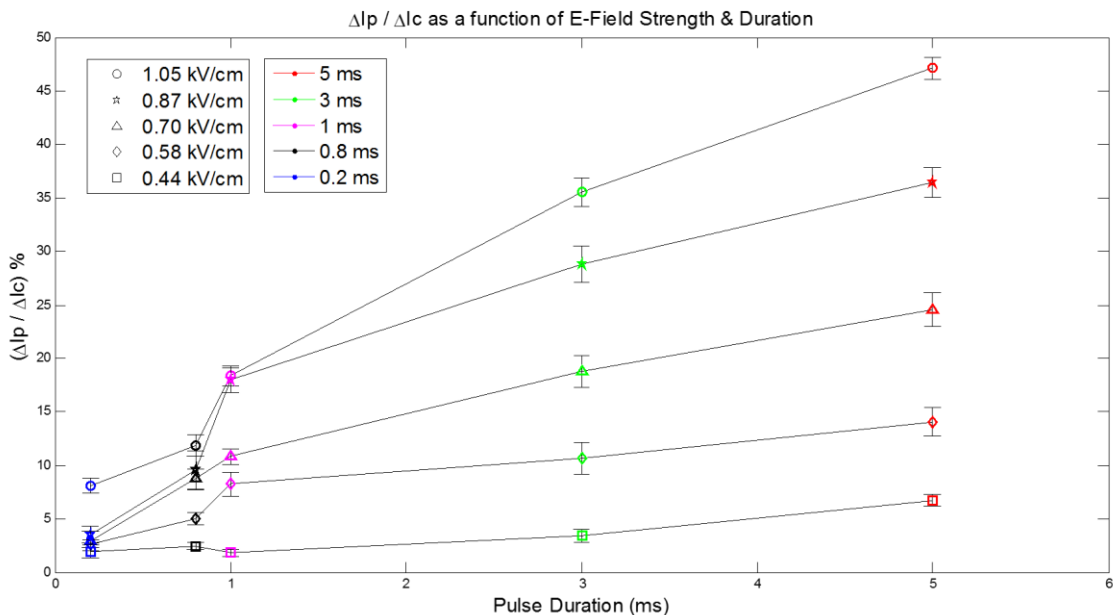
Figure 6.4. Normalized cell membrane permeabilization $\Delta I_p/\Delta I_c$ for single cells that underwent electroporation treatment with varying electric field strengths (0.4 – 1 kV/cm) and pulse duration (0.2 – 5 ms). Electric fields are symbolically coded whereas pulse duration is color-coded.

symbols used in the plot). A dependency was also observed when the dependent variable is changed to the electric field strength for a given pulse duration. For electric fields ranging from 0.58 to 1.05 kV/cm, we observed a rapid transition in the permeabilization signal occurring when the pulse duration reaches and exceeds 1.0 ms. This electrical threshold for creating the large, sustainable pores necessary for the intracellular delivery of therapeutic agents is consistent with numerous other observations during electroporation.[7,12–17] Unlike the patch-clamping based measurement methods, our system allows for a large number of cell responses to be dynamically measured. In our experiments, at least 200 cells were measured for each pulse condition, amounting to an analysis of 5,000 individual cells.

6.5 Cell Membrane Permeabilization Validation – PI tracking

Electrically observed cell membrane permeabilization was also verified optically using PI as a fluorescent probe. A cell viability staining dye, PI, is membrane impermeant and remains non-fluorescent until binding with nucleic acids within the cell cytosol. This property makes PI an excellent candidate to track the cell membrane permeabilization state during electroporation. When the cell membrane is permeabilized, entry and binding of PI in the cell emits a strong fluorescence signal which can be optically recorded. An optical camera was synchronized with the Lock-in amplifier sensor to capture a sequence of images of the pulsed cell following each pulse application. These images were then evaluated for fluorescence intensity on an individual cell basis. Figure 6.5 plots the fluorescence intensity of PI in a cell as a function of both electric field strength and pulse duration (using the same color and symbol coding used for the electrical characterization in Figure 6.4). The larger the pulse strength or duration leads to greater cell membrane permeabilization, which in term permits more PI entry through the porated cell membrane to bind with the nucleic acids in the cytoplasmic space, resulting in elevated fluorescence intensity.

Unlike the electrical measurement of the cell membrane permeabilization, a higher pulsing threshold is needed for distinguishable fluorescence quantification due to the lower sensitivity of our camera. However, using a pulse duration longer than 1.0 ms, we can determine with certainty that the fluorescence intensity indicative of the degree of cell membrane permeabilization correlates with the electrical parameters seen in Figure 6.4. This is especially apparent for 0.87 and 1.05 kV/cm field strengths. A significant jump in fluorescence intensity can be identified after the 0.8 ms pulse duration consistent with the
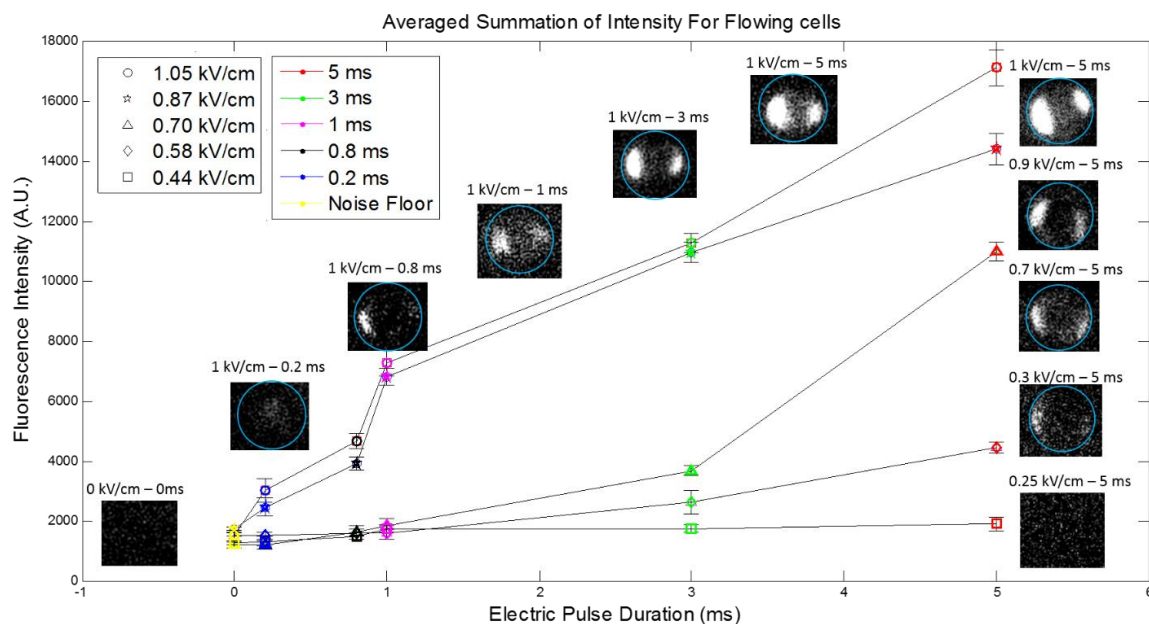
Figure 6.5. Optical measurement of Propidium iodide fluorescence intensity in single cells after prescribed electroporation treatments with varying electric fields (0.44 – 1.05 kV/cm) and pulse duration (0.2 – 5 ms). Representative images of individual cells that underwent 1 kV/cm with varying pulse duration is plotted along the top curve; cells that underwent 5 ms pulse duration with varying electric field strength is shown on the right.

electrical measurements of the permeabilization signal (Figure 6.4). A direct causal relationship can be drawn between the cell membrane permeabilization and intracellular PI delivery. By integrating the electrical and optical data onto one plot, such a link can be established to reveal the interdependent relationship between the two. Figure 6.6 shows a scatter plot of points with the normalized membrane permeabilization magnitude along the y-axis and the corresponding fluorescence intensity for cells at that permeabilization state along the x-axis. Identical symbols and colors were used to differentiate the five groups of electric field strengths (symbols) and its pulse duration (colors). Linear curve fitting was applied for each of the five electric field strengths and marked by labeled dashed lines.
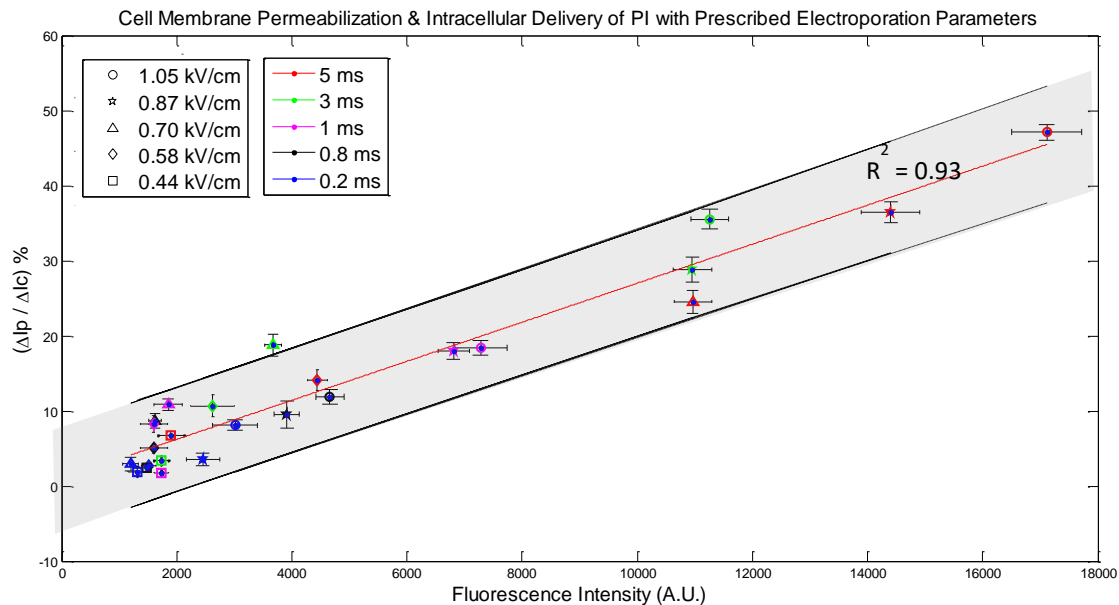
Figure 6.6. Electrically-measured cell membrane permeabilization magnitudes *(ΔI$_p$/ΔI$_c$)* plotted as a function of PI fluorescence intensity in single cells following electroporation treatment with varying pulse strengths and duration. A linear curve fit applied to the ensemble data shows a positive correlation between the electrical and optical characterization of the cell membrane permeabilization with a shaded region indicating ± 1σ intervals.

The fitted curves demonstrate that a linear and dependent relationship exists between the electrical response to the membrane pore opening and the amount of PI delivered inside the cell. The greater amount of pores are marked by a higher *ΔI$_p$/ΔI$_c$* value, which corresponds to a greater extent of PI fluorescence intensity measured inside the treated cells.

6.6 Cell Viability Study – Collection

 The viability of single cells undergoing a prescribed electroporation treatment were also correlated with the electroporation pulse parameters through 7AAD staining. Cells were recovered 20 minutes after being exposed to the electroporation pulse so that viable cells had time for membrane resealing following reversible electrical breakdown of the cell membrane. Following incubation of cells with 7AAD, histograms of 7AAD fluorescence intensity within cells exposed to 0.70, 0.87 and 1.05 kV/cm electric field strengths are shown (Figure 6.7a-c). Within each histogram, the distribution of cells treated with three different pulse durations (0.5, 1.0, and 5.0 ms) were compared with live cells perfused
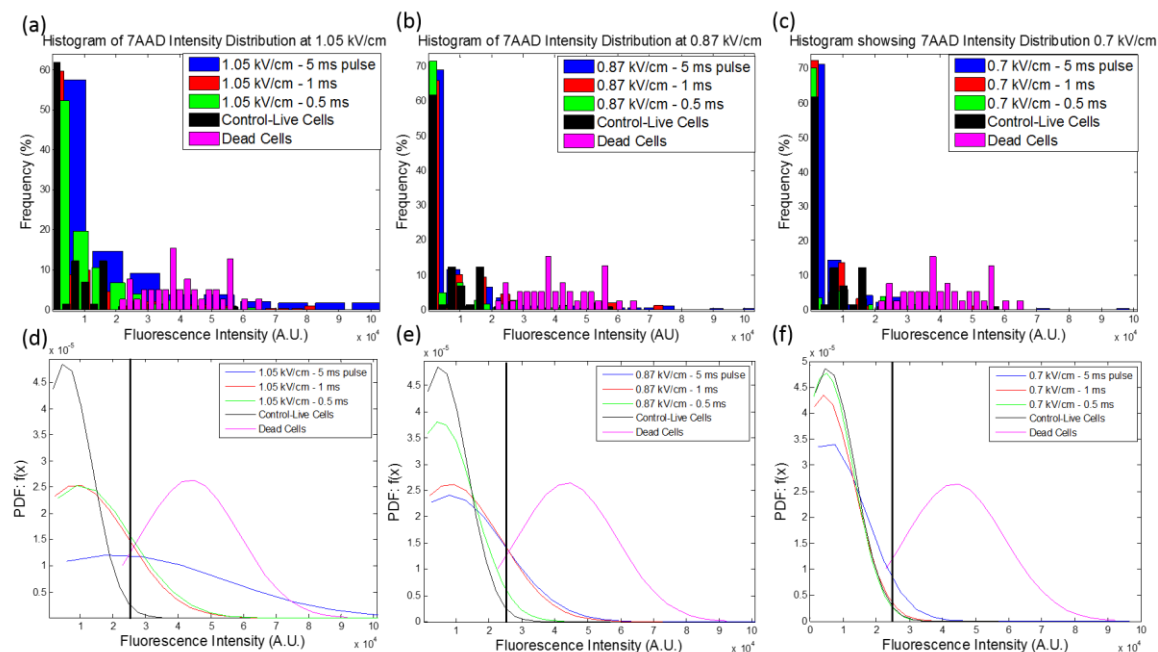
Figure 6.7. Histograms of cell populations treated with electroporation pulse at (a) 1.05 (b) 0.87 (c) 0.7 kV/cm from 0.5 to 5 ms pulse duration and (d-f) their respective normal curve fitting of the cell population histogram. Black vertical line in (d-f) marks the 95% lower confidence bound from the mean of the dead cell population fluorescence intensity.

through the microchannel but receiving no pulse treatment (black curve on left) and dead cells with 'leaky' membranes (purple curve on right). Normal curve fitting was applied to these cell populations and extracted to clearly observe population shifts as the electrical parameter varies. We found that single cells underwent electroporation with the highest electric field strength (1.05 kV/cm) and pulse duration (5ms) causes the greatest shift in fluorescence intensity towards the dead cells' fluorescence distribution curve. This is expected since the strong electroporation treatment was more likely to irreversibly damage the cell membrane, hindering resealing. The progression of shifts is reduced either when the pulse strength (i.e. blue curves in Figure 6.7d-f) or duration (i.e. blue and red curves in Figure 6.7d) is reduced. Cells that underwent electroporation treatment at 0.7 kV/cm all retained a comparable fluorescence to that of control live cells, suggesting that the membranes of the treated cells resealed preventing the uptake of 7AAD dye. Furthermore, by calculating the 95% confidence lower bound of the mean fluorescence intensity for the dead cell population, a viability threshold (black vertical line in Figure 6.7d-f) was determined for each of the cell populations. Figure 6.8 shows the viability of cells for each electroporation condition. The overall cell viability is dependent on both the electric field strength and pulse duration. A stronger pulsing condition was more likely to cause irreversible cell membrane damage leading to cell death, whereas cells treated with moderate conditions (0.7 kV/cm) likely recovered, showing a higher population viability.

The effectiveness of a continuous-flow-based electroporation microchip that automatically detects and electroporates single cells has been demonstrated in this chapter. Each passing cell was detected with high accuracy, and its membranes characteristic permeabilization signal after electroporation was measured electrically, and validated optically and via

viability assessment. This electroporation system allows direct control of single cell membrane permeabilization in a continuous-flow environment, while permitting the collection and downstream processing of the treated cells. Such controllable electroporation of individual cells carries the promise to maximize cell viability across different cell types, providing an improved approach to the conventional empirical approach.
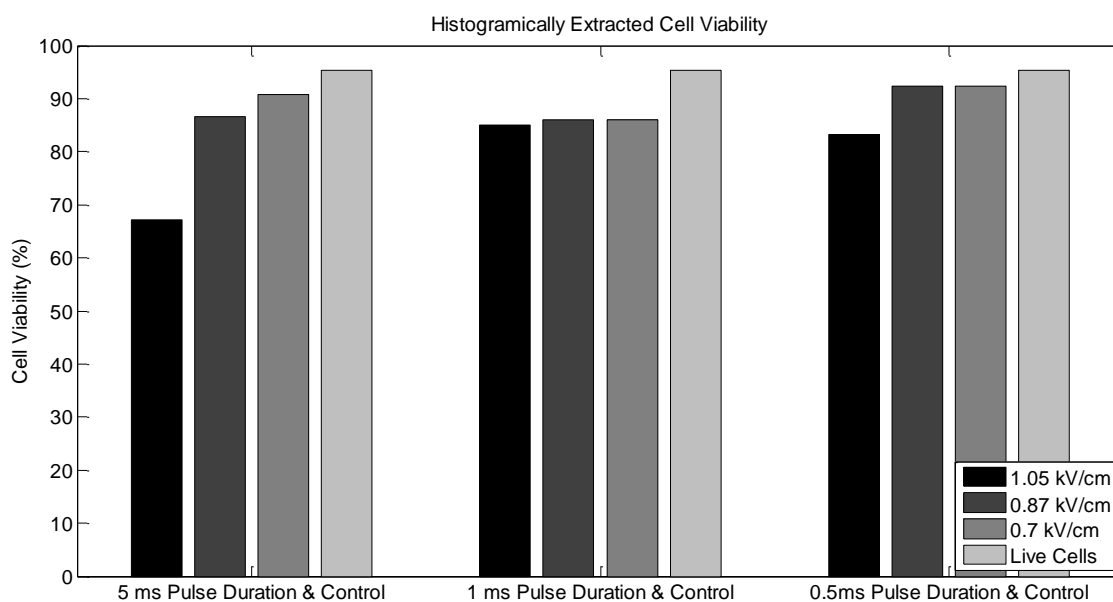
Figure 6.8. Cell viability in percentage determined by plotting the 95% confidence intervals in statistically significant cell population histograms ($p \ll 0.01$). Three groups of electroporation pulse duration are displayed on the x-axis (5, 1, and 0.5 ms). And each group contains the live cell control group for comparison. The applied electric fiend strength is color-coded in each group.

6.7 Further Investigations

6.7.1 System Throughput

Current throughput of the automatic electroporation system (1.3 cells/s) is determined by the cell perfusion flow rate through the microchannel constriction. This flow rate (0.1 µL/min) was chosen to provide sufficient transit time (~250 ms) for each cell to pass through the electroporation zone while obtaining a reliable measurement of cell membrane response after the pulse application. Due to the delays originating from the digital signal processing, digital-to-analog equipment communication and intrinsic delay within the computer processor which executes the main LabVIEW control program, an average lag time of approximately 50 – 80 ms was observed between the detection of a cell presence and the administration of the electroporation pulse. Time delay variation can be attributed to the processing state of the computer. Depending on the pulse duration applied to the cell, a post-electroporation recording period of 50 ms has been experimentally observed to obtain a confirmatory cell membrane permeabilization magnitude prior to cell exit. A longer recording time is required for cell membrane resealing investigations. This necessitates the cell transit time to be at a minimum of 150 ms per cell, or roughly 7 cells/s. The throughput of the system can be improved by increasing the flow rate or shortening the distance between the electrodes to reach the 150 ms transit time limit. An alternative approach that drastically improves the system throughput is by transferring the entire LabVIEW control algorithm to the Zurich Lock-in amplifier's programmable 32-bit RISC processor, which is internally connected to the core processor (Digital Signal Processor). The capability of minimal execution lag time is made possible through the implementation of a real-time module in the RISC processor to potentially enable a sub-millisecond delay

between digital-and-analog processors, since no external communications is necessary for signal acquisition and processing. However, such implementation requires the manual conversion of the LabVIEW program to the C language in order to interface directly with the Lock-in amplifier's embedded processors. Technical support staff from Zurich Instruments has offered startup assistance for this translation effort, which includes C programming examples and general setup guidance.

6.7.2 Cell Membrane Resealing Characterization

Cell membrane resealing has also been electrically observed in the course of the investigation. However due to the cell's varying sensitivity to electrical stimulus and the complexity of the membrane resealing response as a result of electroporation-induced permeabilization, cell membrane resealing dynamics are a difficult phenomenon to characterize.[18] In addition, membrane resealing has been reported by many researchers[19–21] in the field to be a slow process that takes seconds to minutes to complete, therefore the dynamic measurement window offered by our electroporation device may only provide transient membrane resealing information, and cannot offer a complete report of membrane resealing. However by establishing the relationship between transient membrane resealing magnitudes due to the applied electroporation treatment and cell viability, a pulse threshold may potentially be found that prevents irreversible cell damage and improve viability. Figure 6.9 demonstrates the membrane resealing current ΔI_R following the permeabilization current 'jump' ΔI_p as a result of the administration of a 1.05 kV/cm electroporation pulse for 5 ms to an individual cell. For this particular cell, a ΔI_R of 0.2 nA was measured for a ΔI_p of 0.43 nA, which suggests that the total opening area of membranes pores decreased to allow only half the electric current to pass through. The cell membrane
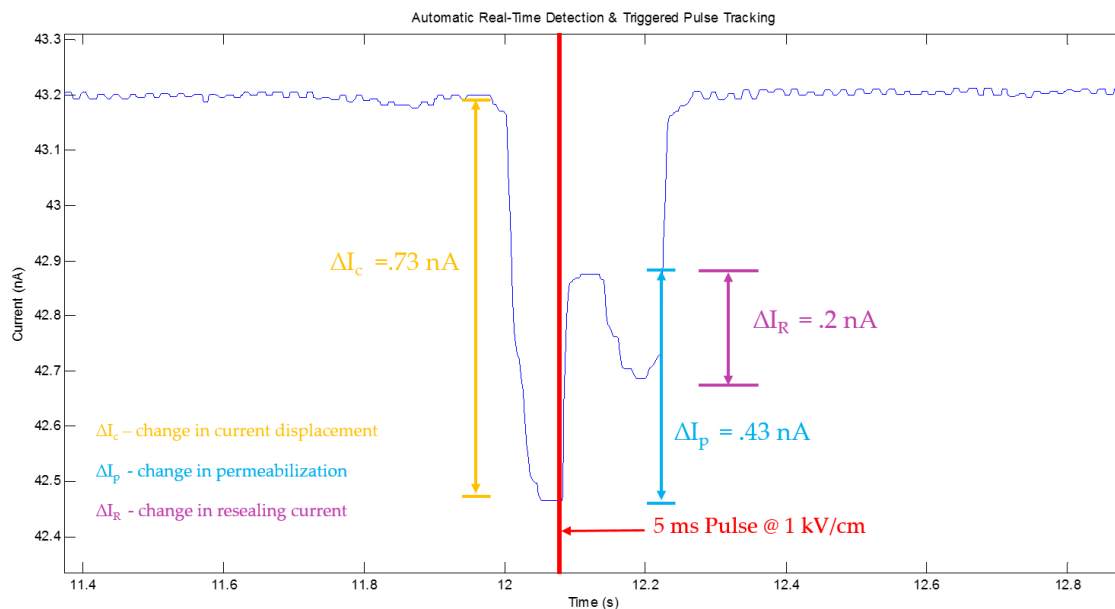
Figure 6.9. Close-up view of the electrical measurements of a cell transiting the electroporation zone and receiving a 1.05 kV/cm electroporation pulse for 5 ms (vertical red line). Total cell current displacement (ΔI_c), cell membrane permeabilization magnitude (ΔI_p), and membrane resealing current (ΔI_R) is shown.

may continue to reseal after exiting the electroporation zone given the environment (pH, temperature, osmolality, etc.) is favorable for the cells to recover from the electrical shock.

Since cell viability is directly linked to how well cell membrane reseals following electroporation, continuing efforts are focusing on the characterization of this resealing phenomenon which can lead to the development of reliable means to control and enhance the cell viability. Our preliminary investigation on cell membrane resealing using the automatic electroporation system has provided some insights regarding this complex behavior. Under the same electroporation pulse parameters that were applied to characterize cell membrane permeabilization, cell membrane resealing current normalized by the magnitude of its permeabilization ($\Delta I_R/\Delta I_p$) was measured for each flowing single

cells after the pulse treatments to reflect the membrane resealing responses (Figure 6.10).
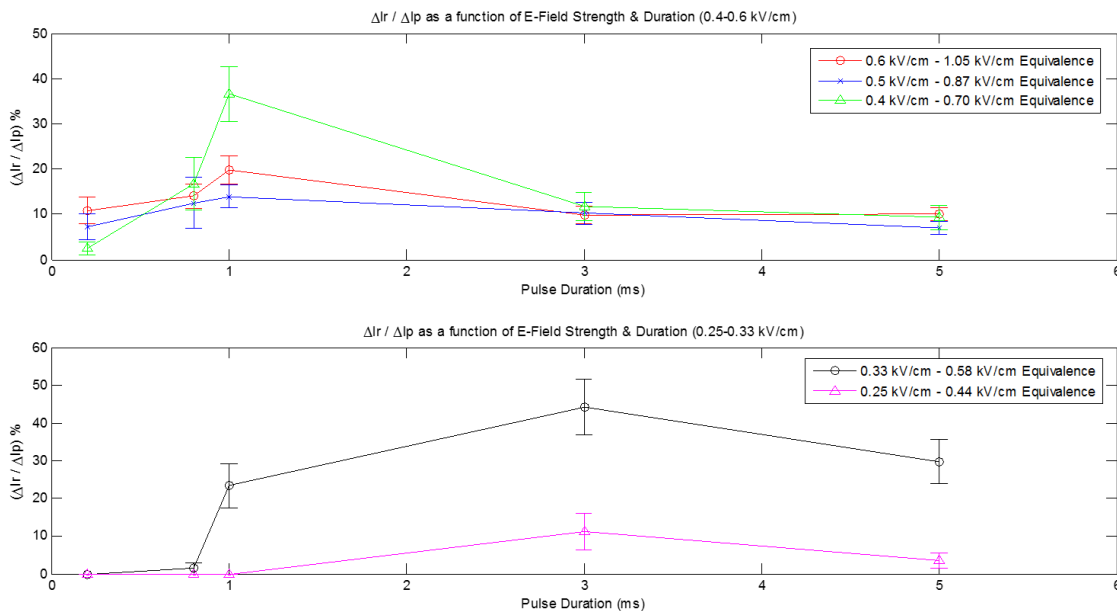
Figure 6.10. Normalized cell membrane resealing current $\Delta I_R/\Delta I_p$ for single cells that underwent electroporation treatment with varying electric field strengths (0.4 – 1 kV/cm) and pulse duration (0.2 – 5 ms). Electric fields are symbolically coded whereas pulse duration is color-coded.

The normalization of ΔI_R by its ΔI_p was based on the assumption that ΔI_P directly effects the magnitude of ΔI_R since a high permeabilization magnitude (large pore) leads to a higher resealing magnitude (small to no pore), given the cell has not suffered irreversible membrane damage. The normalized resealing current in Figure 6.10 is separated into two groups based on the applied electric field strength: (High EP group: 0.70, 0.87, and 1.05 kV/cm) and (Low EP group: 0.44 and 0.58 kV/cm) for better analysis. Because of the cell membrane permeabilization magnitudes below 1 ms duration for all electric fields are small (lower than 10% according to Figure 6.4), they can be unreliable when analyzing membrane resealing currents. Therefore only data after 1 ms pulse duration is considered

here. In the High EP group, a linear progressive trend can be observed where higher the electric field and duration leads to lower resealing current. The highest resealing (40%) occurs when 0.7 kV/cm electric field strength was applied for 1 ms. This may potentially be a pulse threshold for which cells experienced sufficiently large membrane permeabilization but aren't irreversibly damaged. The viability data in Figure 6.8 suggests that under this field strength and 1 ms duration, 85% of the treated cells remained viable. In the Low EP group, because the applied electric field is low, the degree of cell membrane permeabilization under 0.44 kV/cm electric field strength is small (Figure 6.4), as a result, smaller resealing currents are measured. Greater increase in resealing magnitude was measured when long pulse duration was applied, shown in the lower plot in Figure 6.10, a 3 ms pulse duration at an electric field strength of 0.58 kV/cm produced a 40% increase in resealing magnitude. A potential pulse threshold for generating improved cell viability. Future work on this study can include cell collection after electroporation treatment at this electric field parameters to validate this threshold for optimized cell viability.

6.8 Chapter References

1   T. Sun and H. Morgan, *Microfluid. Nanofluidics*, 2010, **8**, 423–443.

2   O. a. Saleh and L. L. Sohn, *Rev. Sci. Instrum.*, 2001, **72**, 4449.

3   a Carbonaro and L. L. Sohn, *Lab Chip*, 2005, **5**, 1155–60.

4   H.-Y. Wang and C. Lu, *Biotechnol. Bioeng.*, 2006, **95**, 1116–25.

5   M. Zheng, J. W. Shan, H. Lin, D. I. Shreiber and J. D. Zahn, *Microfluid. Nanofluidics*, 2016, **20**, 16.

6   M. M. Sadik, J. Li, J. W. Shan, D. I. Shreiber and H. Lin, *Biochim. Biophys. Acta - Biomembr.*, 2013, **1828**, 1322–1328.

7   M. M. Sadik, M. Yu, M. Zheng, J. D. Zahn, J. W. Shan, D. I. Shreiber and H. Lin, *Biophys. J.*, 2014, **106**, 801–12.

8   Y. Demiryurek, M. Nickaeen, M. Zheng, M. Yu, J. D. Zahn, D. I. Shreiber, H. Lin

and J. W. Shan, *Biochim. Biophys. Acta - Biomembr.*, 2015, **1848**, 1706–14.

9   R. H. Whittington, L. Giovangrandi and G. T. A. Kovacs, *IEEE Trans. Biomed. Eng.*, 2005, **52**, 1261–1270.

10   M. Khine, A. Lau, C. Ionescu-Zanetti, J. Seo and L. P. Lee, *Lab Chip*, 2005, **5**, 38–43.

11   Y. Huang and B. Rubinsky, *Sensors Actuators A Phys.*, 2001, **89**, 242–249.

12   B. Gabriel and J. Teissié, *Biophys. J.*, 1999, **76**, 2158–2165.

13   K. C. Smith, J. C. Neu and W. Krassowska, *Biophys. J.*, 2004, **86**, 2813–26.

14   M. Puc, T. Kotnik, L. M. Mir and D. Miklavcic, *Bioelectrochemistry*, 2003, **60**, 1–10.

15   S. J. Beebe, P. M. Fox, L. J. Rec, E. L. K. Willis and K. H. Schoenbach, *FASEB J.*, 2003, **17**, 1493–5.

16   J. Teissié, J. M. Escoffre, M. P. Rols and M. Golzio, *Radiol Oncol*, 2008, **42**, 196–206.

17   M. P. Rols and J. Teissié, *Biophys. J.*, 1998, **75**, 1415–1423.

18   Y. Demiryurek, M. Nickaeen, M. Zheng, M. Yu, J. D. Zahn, D. I. Shreiber, H. Lin and J. W. Shan, *Biochim. Biophys. Acta*, 2015, **1850**, 1706–14.

19   H. He, D. C. Chang and Y.-K. Lee, *Bioelectrochemistry*, 2007, **70**, 363–8.

20   M. Hibino, H. Itoh and K. Kinosita, *Biophys. J.*, 1993, **64**, 1789–800.

21   M. Khine, C. Ionescu-Zanetti, A. Blatz, L.-P. Wang and L. P. Lee, *Lab Chip*, 2007, **7**, 457–62.

Chapter 7

Towards Intelligent Electroporation

7.1 Overall System Automation

Extending beyond the ability to control cell membrane permeabilization on an individual cell basis in a continuous flow microchannel, the ultimate goal of this project aims to develop a fully automated electroporation system that permeabilizes and maximally transports molecules into cells according to their critical viability thresholds to prevent over-electroporation. This electroporation system is operated without user interventions throughout the entire process. Additionally, since cell viability is maintained via membrane permeabilization control at the single cell level, a universal electroporation system independent of cell types and experimental variations found in all empirically-derived electroporation protocols can thus be realized. The overall anticipated intelligent system is described schematically in Figure 7.1. The process starts with the automatic detection of hydrodynamically focused individual cells through the electroporation region of the microchannel. Upon cell detection, an electroporation pulse with an initial strength and duration is automatically administer to the cell while in transit across the electroporation zone. Changes in cell membrane impedance indicative of permeabilization is continuously tracked during the pulse application and measured against a predetermined permeabilization threshold. This impedance threshold serves as an indicator for predicting the percentage of viability according to the cell type, chapter 6.6 provided an example of such correlation between degrees of cell membrane permeabilization and cell viability using 3T3 fibroblasts. Transient pore opening on the cell membrane from electroporation also permits biomolecules such as nucleic acids and drugs or fluorescent probes in the
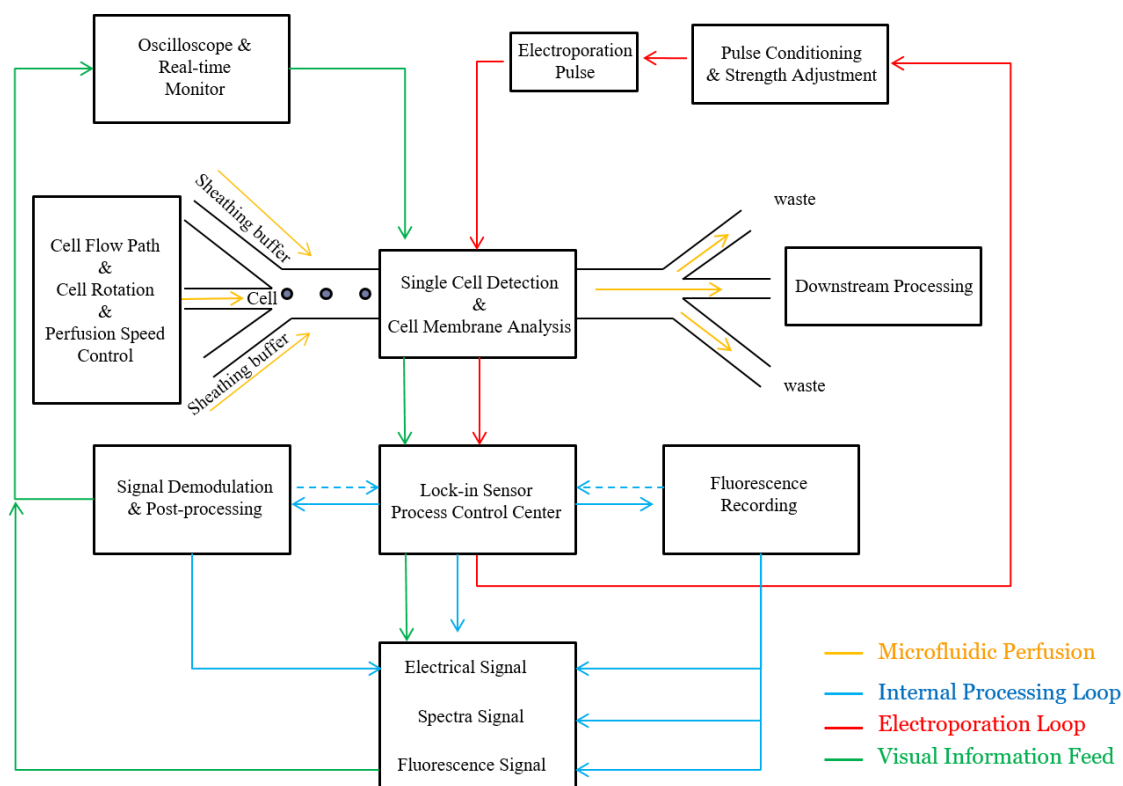
Figure 7.1. Schematic illustrating microfluidic (yellow lines), internal processing of electrical and optical data (blue lines), electroporation (red lines), and real-time user feedback (green lines) operation loops. These closed loop systems were integrated to form a synchronized, automatic cell detection, electroporation measurement, monitoring and control platform.

extracellular buffer to be electrophoretically transported into the cell. Once the cell membrane impedance reaches the threshold, electroporation pulse is turned off and the treated cell exits the channel into an outlet reservoir for collection or further downstream processing. This automated electroporation process repeats for each cell and takes approximately 200 ms per cell. Longer time can be achieved with slower cell perfusion rate to acquire more in-depth electrical and optical analysis. All electrical, optical, and digital signals are processed in real time, forming a closed-loop feedback system that

allows the application of an electroporation pulse tailored according to the cell's maximal tolerability, hence maximizing both intracellular molecular delivery as well as cell viability. However, this system's envisioned ability to reliably detect the cell presence, electroporate the cell while continuously tracking the cell membrane impedance, automatically increasing the pulse strength or terminate the pulse when the critical viability threshold, and repeating the process for every single cell in a high throughput setting has not yet been met and it is the topic of future investigation.

7.2 System Requirement & Development

A major challenge presented in the development of this intelligent system is the ability to perform simultaneous cell membrane permeabilization measurement and high frequency electroporation pulses application. This ability allows for the identification, characterization and real-time tracking of initial cell membrane permeabilization signal without interruption to produce a complete electrical representation of the cell membrane poration dynamics. Our current measurement electronics setup is not configured to perform this task, since each pulse application to the device is shunted by a switch at the sensor input to prevent electronic artifacts. As a result, a temporal absent of impedance information results for the duration of the electroporation pulse.

The schematic in Figure 7.2 demonstrates the existing setup for the electroporation and measurement of cell impedance between a pair of electrodes. By default, all impedance information from this detection region of the channel passes from the device electrode through lead I of the switch to the input of the Lock-in sensor input (Lead II), creating a closed sensing circuit loop. When an electroporation pulse is applied, the switch instantaneously connects Lead I to Lead III, completing a closed electroporation circuit
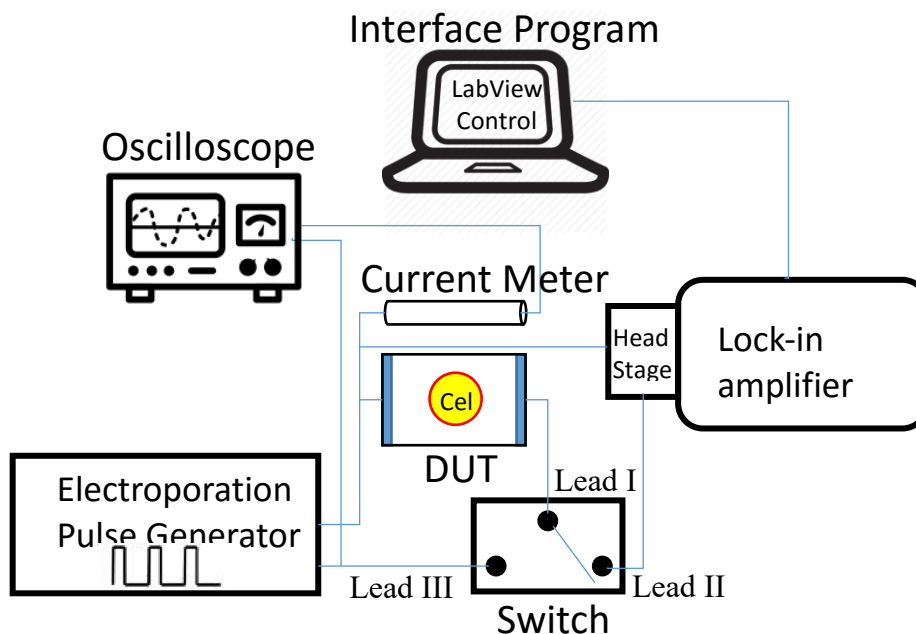
Figure 7.2. Schematic illustrating the mechanical switching between the signal detection measurement waveform and the electroporation pulse train. The switch is consists of 3 leads. Lead I is permanently connected to one of the electrodes of the device; Lead II is the positive output of the high voltage pulse generator, and lead III is the positive input of the Lock-in amplifier sensor. Excitation voltage is delivered to the other electrode on the device by the internal waveform generator in the Lock-in amplifier.

loop without causing sensor input artifacts. Based on this operating principle, we hypothesize that a pseudo-simultaneous sensing and pulsing mechanism can be established by enabling very high frequency switching connections from Lead II to Lead III, toggling between impedance measurement and pulse application. This is analogous to the sampling action of a DAQ (data acquisition analog-to-digital converter) which samples analog signal at above the Nyquist frequency to 'recreate' a high resolution digital signal. Unlike the DAQ, complete signal transduction from the device at Lead I to either Lead II or Lead III

confronts several challenges that result in signal degradation or loss during the leads' switching motion. These challenges are attributed to factors such as: (1) the incomplete mechanical contact of leads during high frequency switch motion; (2) high contact resistance between the leads; (3) wear and tear of the leads due to over-usage; (4) high voltage induced fusion of electrode leads; (5) extremely high voltage requirement for sub-millisecond switching. Many of these can be resolved with the adaptation of solid state switches or relays instead of conventional mechanical switches. A solid state switch bypasses the mechanical constraints and offers switching speeds up to the gigahertz range. Despite the advantages over mechanical counterparts, the vast variety of solid state switches each having distinct design, functionality, and configuration tailored for either general or very specific applications makes the task of selection very difficult for our specific need. By comparing and contrasting switch specification while narrowing down features we believe are necessary for carrying out the complete transduction of signal at high frequencies ($>$ MHz), a table of features and their corresponding parameters have been compiled to serve as a guide for the selection, testing and evaluation of solid state switch candidates capable of accomplishing simultaneous sensing and pulsing (Table 7.1).

An ADG 419 CMOS solid state switch that fulfills many of the requirements listed in Table 1 was selected for signal transduction testing at high switching rate, despite having a moderate switching time of 175 ns (max) and an off-solation rejection ratio of 68 dB. The experimental evaluation setup and operation process build for testing this switch establishes an evaluation framework for which all other switches will be tested. Each evaluation brings us closer in finding the right combination of parameters to permit high frequency relay of sensing and pulsing signals.

Features	Requirement
On-Resistance Matching	< 3 Ω
Charge Injection	< 10 pC
Off-leakage Current	< 5 nA
Configuration	SPDT Only
Switch time	< 1 ns (t_{on}) and (t_{off})
Power operation	Bipolar (± 4.5 V to ± 20)
Continuous passing current	> 30 mA
Lead temperature max	> 300 ℃
Analog signal range	± 15 V
Break-before-Make Interval	$V_{2-1} = V_{1-2} = \pm 10$ V
Off-Isolation Rejection Ratio	> 68 dB (R_L = 500 Ω, C_L = 5 pF, f = 1 MHz)
Cross-talk	< 85 dB

Table 7.1. Table of solid state switch features required for the flawless transduction of signals from the electroporation pulse output terminal to the Lock-in amplifier sensor input terminal.

7.3 Simultaneous Signal Processing & Pulsing

Without the use of switch, the superposition of the detection sine wave and electroporation pulse sequence is implemented and visualized in Figure 7.3. A DC pulse train mounts on top of a sine wave is clearly distinguishable. The power spectrum analysis shows a 10 kHz pulse train frequency with an amplitude of 1 V_{p-p} 'riding' on top of a 1 kHz detection sine wave with an amplitude of 1 V_{p-p}. This superimposed waveform is free of any signal transduction deficiency and abnormalities since they are both generated digitally and

converted to analog signals via an addition process. Although superpositioned waveform generated through this signal summation approach cannot be fed into the Lock-in sensor due to potential damage to the sensor and electronic artifacts produced from the DC pulses, it serves as a reference for quality comparison when different solid state switches are being evaluated.
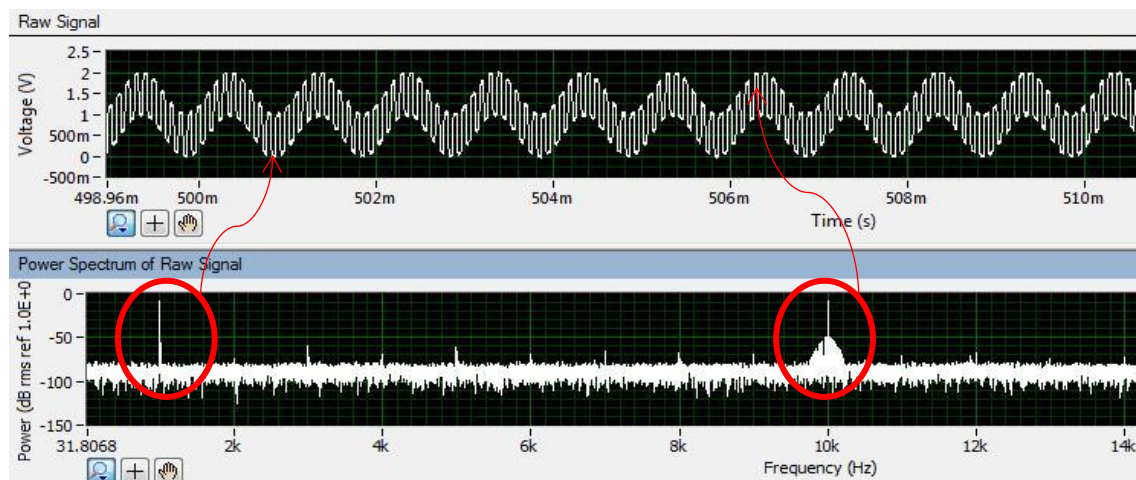
Figure 7.3. Superposition of the detection sine wave (1 V_{p-p} amplitude and 1 kHz frequency) with the electroporation pulse train (1 V_{p-p} and 10 kHz frequency). Each waveform is generated via a separate function generator and added together without the use of a switch to demonstrate the ideal combined waveform outcome.

As an example to demonstrate the experimental evaluation of a solid state switch for enabling transduction of sensing and pulse signals, we set the ADG 419 CMOS solid state switch to operate at the same frequency as that of the electroporation pulse sequence, and monitors the overlaid outputs on a digital oscilloscope. The setup is similar to Figure 7.2 except the oscilloscope was connected in place of the Lock-in amplifier sensor, and the switch is connected to the oscilloscope input by default. Figure 7.4 shows a 1 ms electroporation pulse with an amplitude of 1.5 V_{p-p} (plotted in red) was applied during the

continuous running of a sine wave at 1 kHz frequency with a 1 V_{p-p} amplitude (plotted in blue). During the period when the pulse was applied, ADG 419 switched from the sensing lead to the pulsing lead in 1 ms pulse duration before returning back to the sensing lead. About 80% of the sine wave during that 1 ms period is suppressed, however the remaining 20% can be seen as gradually deteriorating residue signal at the first 0.2 ms of the pulse. This is likely due to the delayed start of the switching t_{on}.
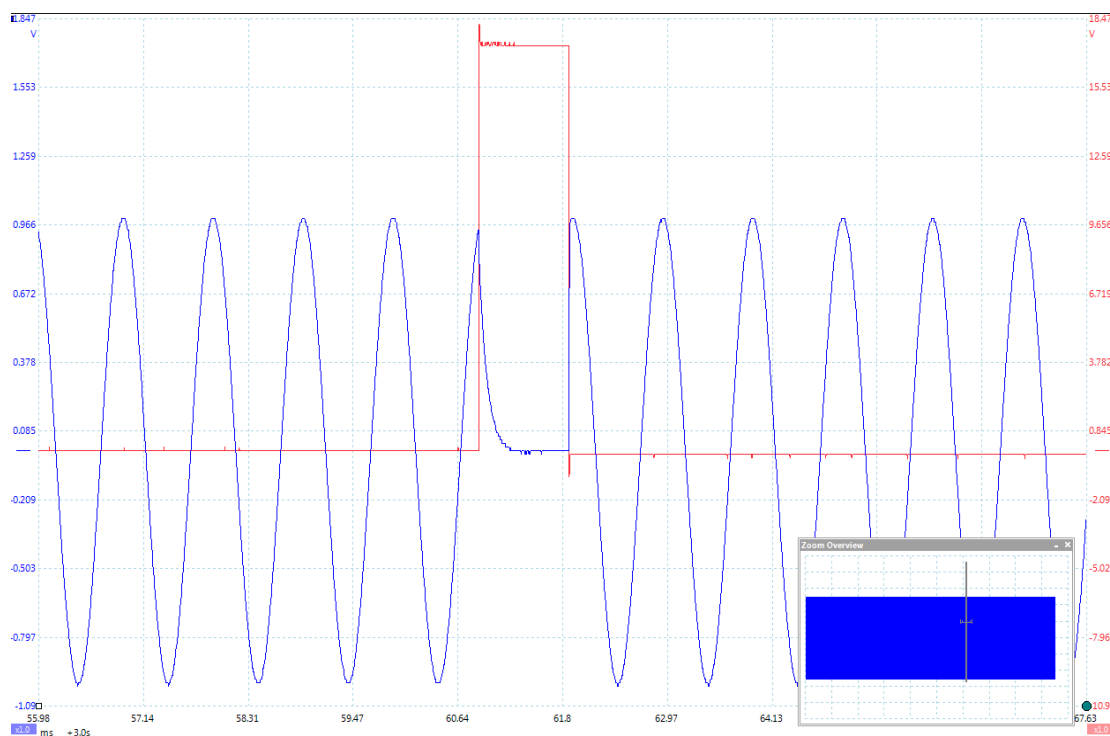
Figure 7.4. Superposition of the detection sine wave (1 V_{p-p} amplitude and 1 kHz frequency blue current trace) with a 1 ms electroporation pulse (red trace) using a solid state switch (ADG 419). One microsecond of DC level is expected in the detection sine wave when the pulse was applied as a result of the switching motion.

In order to test the switch's ability in handling high frequency pulses, 100 cycles of 5 μs electroporation pulses at an amplitude of 2 V_{p-p} were applied to the 1 kHz sine wave. A switching rate of 5 MHz is demanded from the ADG 419 switch to toggle between these two waveforms as shown in Figure 7.5, both the administration of electroporation pulses and switching efficiency of ADG 419 at this rate encounters significant challenges. Demonstrated in Figure 7.5 is a poorly superimposed waveform with the 5 MHz pulse train 'riding' on the 1 kHz sine wave. It is far from the ideal waveform shown in Figure 7.3. A major challenge is associated with the DC amplifier used for augmenting the amplitude of
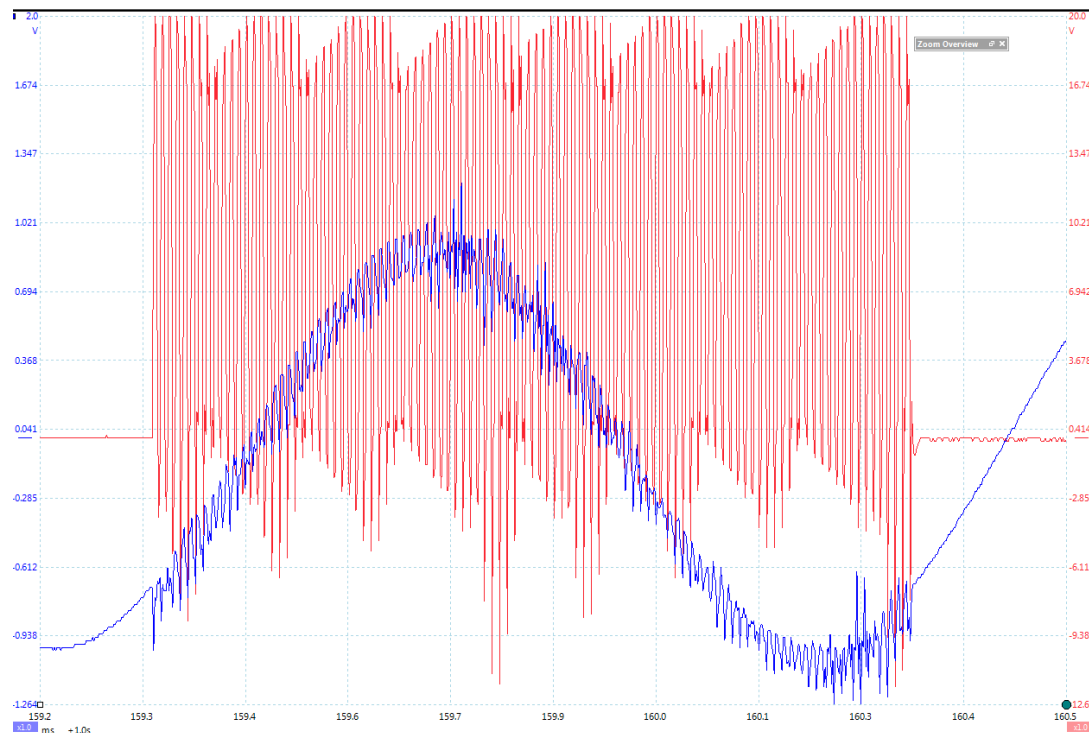
Figure 7.5. Superposition of the detection sine wave (1 V_{p-p} amplitude and 1 MHz frequency, blue trace) with an electroporation pule train (1 V_{p-p} amplitude and 5 MHz frequency for 100 cycles, red trace) using a solid state switch (ADG 419). 100 cycles of 10 microsecond DC level is expected in the detection sine wave when the pulse was applied as a result of the switching motion.

the electroporation pulse, the amplifier starts to experience a -13 dB cut-off at an input frequency above 1 MHz, and this translates to the incomplete amplification of the pulses which appeared as a non-square like DC pulse trains at the output. There is a limitation associated with the switching speed of the ADG 419 CMOS solid state switch. The switch cannot effectively complete each switching movement due to the high frequency request. As a result, it created a switch 'limbo' where the switching lead (Lead I of switch in Figure 7.2) makes incomplete connections with the sensor and electroporator inputs. Because of insufficient off-isolation rejection ratio of the switch, this 'limbo' state also created semi-permeable passages for high voltage electroporation pulse signal to get through to the sensor input, creating signal spikes on the sine wave. An evaluation platform has been built to continue the effort to select the appropriate solid state switches capable of high switching rate, off-isolation rejection ratio and other parameters necessary for the successful relay of sensing and pulsing signals. Several promising switch candidates have been found, and they will be acquired and evaluated.

7.4 Cell Viability Feedback-based Electroporation Algorithm

Successful automation and electroporation of single cells according to cell viability requires a set of algorithms to control the process. The intelligence of our electroporation system has been partially implemented to demonstrate the automatic detection and pulsing of cells using the overall cell displacement feedback information. With the completion of simultaneous sensing and pulsing mechanism, current algorithmic instructions can be further extended in LabVIEW to include the real-time cell viability feedback algorithm. Figure 7.6 shows a state diagram depicting the possible states of the electroporation process, potential outcomes and resolutions of those outcomes. The default state of the system is at

A = Baseline buffer impedance
N = Baseline buffer noise amplitude
B = Cell impedance
M = Cell impedance baseline noise amplitude
T_1 = Time difference from electrode to constriction
T_2 = ~ 50 ms minimal cell transit time from electrode to constriction
C_i = Percentage impedance drop from detected cell impedance baseline
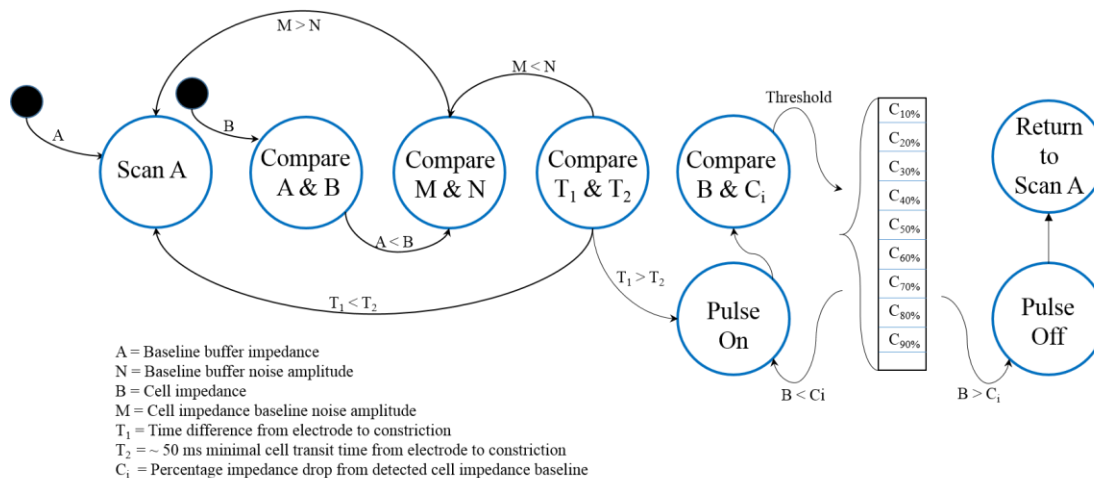
Figure 7.6. State diagram depicting the automated single cell detection, electroporation, and cell viability feedback-controlled pulse control. Majority of this functional state has been implemented in LabVIEW control algorithm in use for automatic single cell detection and electroporation. Automated pulse control is currently under development.

Scan A in which all systems (microfluidic, detection, electroporation, Lock-in sensor) are on stand-by and only the sensor is active in scanning the buffer solution impedance 'A'. Following the perfusion of single cells across the electroporation zone, each cell is registered to the sensor by its impedance value 'B'. This progression initiates the comparator operation between A & B in order to determine validity of a cell presence. Due to possibility of false detection from debris and particles in the cell solution, an impedance-gated threshold is used to increase the selectivity of the system to detect only cells. In our experiments, an impedance amplitude 10% above buffer baseline was found to provide reliable cell detection. If debris is found, the system forfeits current detection process and returns to the default stage (Scan A). When a cell is recognized, the detected cell impedance baseline noise (M) within the electroporation zone is compared with the buffer impedance

baseline noise (N) to ensure signal quality. Irregular cell movement can sometimes lead to noisy baseline, masking the permeabilization signal, and rendering false measurements. Therefore detected cells that failed to produce high SNR across the electroporation zone will be discarded, and the system returns to the default state (Scan A) to await for the next cell. However, a majority of the detected cells have been observed to produce either the same or higher baseline SNR in comparison with N. Thus initiating the next stage of comparator which ensures only cells with sufficient transit time for electroporation and permeabilization measurement are counted. Occasional flow rate instability in the microchannel can result in fast flowing single cells traversing across the electroporation zone with transit time less than required (200 ms) for accurate pulsing and measurement. By evaluating the time when a cell passes from the electrode to the channel constriction opening (T_1), an estimated cell transit time through the constriction can be anticipated. For instance, under a 0.1 µL/min flow rate, it takes a cell approximately 50 ms (T_2) to travel from the electrode to the constriction opening, and from there, another 200 ms to traverse through the entire constriction prior to exiting. T_2 can thus be used to approximate the cell's anticipated transit time in the constriction. When T_1 is less than T_2 in the case of fast flowing cells, the electroporation unit ignores the cell, registers it as an un-pulsed cell and return to system default state (Scan A). However when T_1 is greater or equal to T_2, then the electroporation unit will output a constant high frequency DC pulse train with a predetermined, initial strength and duration according to the cell type. Another comparator continuously evaluates changes in cell impedance (B) against a permeabilization threshold (C_i), i represents the percentage of impedance drop for the cell type under test. For instance, if a cell type has a predetermined maximal tolerable threshold of 40% for which beyond

this value, the cells will likely suffer irreversible damage. In this case, once the measured cell membrane impedance reaches 40%, the electroporation unit shuts off and returns to the default state (Scan A). However, if the initial pulse parameters fail to evoke a change in cell membrane impedance, then higher electric field strengths will be incrementally applied until C_i threshold is reached.

Chapter 8

Conclusion & Future Work

The major theme of this dissertation centers on single cell level electroporation and dynamic impedance analysis in an effort to establish a high throughput and fully automated microelectroporation platform to deliver diagnostic and therapeutic molecules into cells of various types without compromising cell viability. Our motivation arises from the need to develop effective electroporation protocols for improving the electroporation process by overcoming the trade-off between delivery efficiency and cell viability and extending its reliability to work with precious and hard-to-transfect cells. By recognizing cell membrane permeabilization signals indicative of cell viability and the importance of single cell level impedance monitoring, the goal is to develop a 'smart' microelectroporation device that delivers tailored dosage of electric pulses to single cells to maximize both intracellular delivery and cell viability at a high throughput. Microfabricated channel environment with nanofluid manipulation serves as the operation platform for interfacing with the single cells. Two main research thrusts of this dissertation are: (1) enhancing intracellular molecule delivery profile via controlled cell rotation and (2) cell viability assessment via cell membrane permeabilization measurement and control. The following sections summarize the specific approach involved in working towards the thesis goal.

8.1 Summary of Single Cell Manipulation

Hydrodynamic control of cell orientation in a micro-electroporation channel offers a new means to improve the delivery efficiency of molecules into single cells. Electroporation is fundamentally a polar phenomenon, whereby only cell surfaces perpendicular to the

electric field are permeabilized to allow the intracellular uptake of exogenous materials. By rotating the cell orientation during the application of an electric field, larger cell membrane surface is exposed for permeabilization, resulting in a more efficient and uniform transport of micro/macro molecules. Using a two-inlet microchannel geometry to introduce a sheath and cell carrier flow, cell flow path and rotational velocities can be precisely controlled by establishing higher flow rate ratios between the streams to pinch the cells against the channel sidewall. Depending on the flow rates and their ratios, cells rotating with slow or fast angular velocities in an electric field experience either partial or circumferential permeabilization of the cell membrane, respectively. The ability to control single cell orientation via differential flow rates in the microfluidic channel is beneficial in many flow-based single cell applications.

8.2 Summary of Single Cell Impedance Cytometry

Detection and measurement of single cell impedance in a microfluidic cytometry device is the basis for experimentally evaluating the electroporation-mediated cell membrane response and allowing control of the electroporation process for preserving cell viability. The complex impedance equation combined with the electrical circuit model for a cell suspended in buffer provided a comprehensive description of the overall impedance of this system, allowing the prediction of impedance variation due to parametric variations such as change in buffer conductivity. Experimental evaluation of single cell impedance detection sensitivity and reliability was performed using a straight rectangular microchannel, a Coulter Counter-inspired microfluidic channel, and a channel with a critically narrowed constriction that momentarily immobilized the cell. The results indicated that although there are advantages and disadvantages associated with each of

these three microfluidic channel configurations, the microfluidic Coulter Counter channel produces cell detection signals with reasonably high and sable SNR while enabling continuous single cell passage through the channel. The ability to extract cell membrane level impedance signals was accomplished via the implementation of a Lock-in amplifier sensor which is based on the principle of a phase sensitive detection mechanism to isolate the signal of interest.

8.3 Summary of Single Cell Membrane Permeabilization Detection & Control

Parametric analysis of the cell/electrolyte impedance model reveals that electroporation-mediated changes in cell membrane impedance are strongly influenced by the conductivity of the extracellular buffer and the cell volume fraction. It was determined from the model that 100 µS/cm conductivity buffer allows the determination of a frequency range between 1 and 10 kHz for cell membrane permeabilization detection while permitting the electrophoretic transport of charged molecules into cells according to our previous investigation. A constriction geometry was incorporated in the microchannel to amplify the applied electric field and increasing the cell volume fraction so that cell detection and membrane permeabilization with a high SNR can be achieved. Detection of cell membrane permeabilization was first verified with large stationary cell numbers ranging from a few to a few hundred cells. This allows the initial assessment of an aggregated cell membrane permeabilization response and detection feasibility during irreversible and reversible cell electroporation. Microfabricated structure was built to capture and immobilize single cells to better investigate membrane permeabilization response using: (1) frequency spectrum and time-domain signal analysis, and (2) optical quantification of PI fluorescence intensity in electroporated cells. Our accomplishment from this cell-immobilization enabled

impedance analysis platform fueled the translation of our electroporation and measurement strategy from a static domain to a continuous-flow micro-channel. By developing an automation algorithm in LabVIEW to govern the single cell detection, electroporation, and electrical and optical measurement process, the control of cell membrane permeabilization was demonstrated electrically through the characterization of permeabilization magnitude as a result of varying the electroporation pulse strengths and duration, and optically through quantification of electroporation-mediated PI fluorescence intensity in each cell under different pulsing conditions. Cell viability following different electroporation treatment conditions were assessed via live-dead staining after collection to demonstrate correlation to the applied pulse strengths.

8.4 Summary of Feedback-based Cell Membrane Permeabilization Control

The ultimate goal of the chapter is to create a 'smart' electroporation system that could detect the presence of a flowing single cell and triggers the application of a high frequency electroporation pulse according to the cell viability in real time. In an effort to accomplish this goal, cell membrane permeabilization magnitude is continuously being monitored and checked against a predetermined critical threshold, the electroporation unit either increases pulse amplitude to evoke a membrane permeabilization signal for cells that require additional energy to overcome the transmembrane potential or deactivate the pulse prior to reaching the critical threshold indicative of irreversible membrane damage for this particular type of cells. The main challenge associated with completing the development of this 'smart' system is the simultaneous sensing of cell membrane permeabilization and the application electroporation pulses. A high frequency 'sense-then-pulse' toggling strategy implemented by a carefully selected solid state switch has been proposed, and it is

currently being investigated to verify its ability to rapidly and fully transduce signals between the sensor input and the electroporator output. However, due to the extensive diversity of switch functionality and configuration available in the market, meeting all the requirements for our application is time consuming and labor intensive. Several potential switch candidates have been identified and currently being evaluated for undertaking the task of flawless signal relay.

8.5 Future Work

For the first time, a continuous-flow, automated single cell level electroporation system has been developed and demonstrated to detect, measure, and control cell membrane permeabilization at a high throughput. This electroporation system bridges the gap between cell immobilization-based cell impedance measurement and high throughput electroporation of cells in the microchannel, to enable control of cell membrane permeability via externally applied electric field strength. Ongoing efforts to bettering this system focuses on three aspects: (1) enabling simultaneous sensing and pulsing for un-interrupted tracking of cell membrane response as described above; (2) optimize the reliability of the microfluidic operation via channel redesign; (3) validate the 'smart' electroporator's ability to simultaneously optimize delivery efficiency and cell viability for different types of cells, including hard-to-transfect cells such as lymphocytes.

8.5.1 System Upgrade

The design, fabrication and testing of a new microfluidic channel to improve the system operation has already been underway (Figure 8.1). This new design permits the hydrodynamic focusing of cells through the constriction channel at much higher flow rates
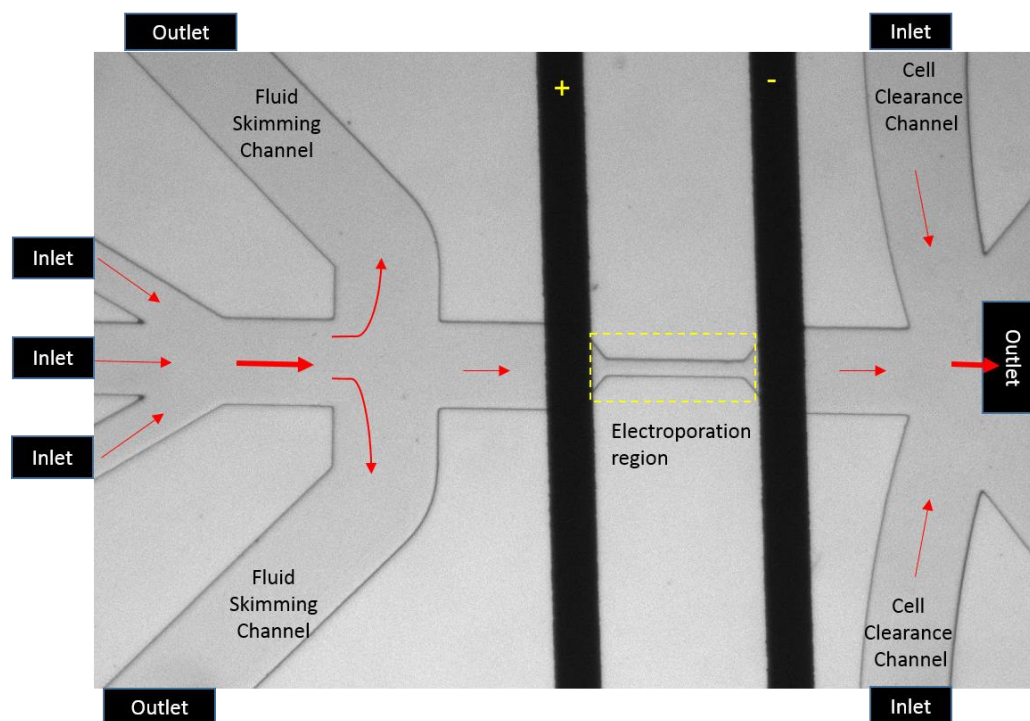
Figure 8.1. Bright field image of the next generation microfluidic device for automated electroporation. This device consists of three inlets to create a hydrodynamically-focused cell stream from the middle inlet, and a pair of fluid 'skimming' channel to reduce the cell stream flow rate entering into the electroporation zone (label by yellow dash line). A pair of cell clearance channel is also implemented to prevent cell adhesion and promote streamlining of cells after electroporation treatment into the collection chamber.

than before (> 0.1 µL/min) and still retains similar or longer cell residence time necessary for electrical and optical analysis. This capability was made possible by implementing a pair of fluid 'skimming' microfluidic channels upstream of the constriction region in order to reduce the total incoming flow rates entering the constriction. By calculating and balancing the hydrodynamic resistances of the microfluidic channel, the 'skimming'

channels are each designed to partition 45% of the total flow rate. Thus the total flow rate through the main channel after the skimming pair is reduced to 10%.

The motivation of this incorporation arises from the challenge in the previous microfluidic devices in which slow cell flow rate (1 µL/min) often yields small number of cells entering the constriction for electroporation. As a result, a longer waiting period is required to collect sufficient number of cells. This leads to a longer experiment time whereby cell viability deteriorates over long periods of incubation in a sub-optimal environment. In order to prevent cell death due to prolonged experiment time, we are forced to collect small number of cells or running multiple experiments which is time consuming and wasteful of reagents. These fluid 'skimming' channels also help to alleviate cell adhesion to the microchannel surfaces due to the slow flow rate. Although channel surfaces were treated with 10% BSA to reduce cell adhesion, this layer can deteriorate over time. With higher perfusion rates in regions prior to the channel constriction, the temporal window for cell adhesion is shortened, allowing continuous and smooth cell transit across the electroporation zone. Additionally, these fluid 'skimming' channels can potentially be connected with neighboring electroporation channels operating in parallel, allowing excess cells to act as sources for other devices, potentially forming a scaled-up, parallelly operated network to increase throughput.

Another feature incorporated in the new channel design is a pair of 'clearance' channels prior to the cell collection outlet. These channels allow for the perfusion of two sheath buffer solution at higher flow rates than the incoming cell stream, increasing the shear rate experienced by the cells, and carrying them to the collection reservoir. Typically, a flow rate of 2 µL/min is used for each clearance channel to clear out the cell stream.

The implementation of these 'clearance' channels also enables the potential downstream processing and further analysis of the electroporation treated cells by hydrodynamically transporting the cells. Instead of collection, the cells can be diverted into a buffer exchange microchannel where cells can be transported to a different buffer either through dielectrophoretic or hydrodynamic force. For instance, if on-chip cell incubation is desired for downstream processing, then cell medium would be used as the exchange buffer. The operability and sensitivity performance of this new microfluidic channel is currently being characterized by another group member to ensure the translatability from the previous device design, and better control of single cells through the electroporation zone.

8.5.2 System Validation with Different Cell Types

Optimization of the microfluidic platform will improve the overall operation of the device, and the translatability and feasibility of this high throughput operation on different cell types will then be verified. Intrinsic cell properties such as size, membrane rigidity, composition, etc. vary not simply among cells of the same type, but greatly among cells of different types. Cell sensitivity to electric fields is one of the major challenges behind electroporation-mediated transfections due to the cell's susceptibility to the degrees of membrane permeabilization. Heartier cells such as 3T3 fibroblast can withstand up to 50% of electroporation-mediated membrane permeabilization amplitude and still retain a high 70% viability, however the same condition may not applied to primary cells such as lymphocytes, which have been known as one of the most difficult cell types to transfect due to the low post-electroporation cell survival rate. This intelligent system will be used to electroporate these cells according to their ability to withstand the electric field prior to irreversible membrane damage.

8.5.3 System Validation with Transfection of GFP vectors

The ability to deliver diagnostic and therapeutic agents into cells using this intelligent electroporation system will also be investigated. So far, the molecules used for intracellular transport have been fluorescent probes such as Propidium iodide or fluoresceinated dextran for membrane permeabilization and delivery verification purposes. The ultimate goal of this electroporation system is to transfect hard-to-transfect cells, such as lymphoblasts. Instead of using fluorescent marker molecules, in which case the cells have to be sacrificed, green fluorescent protein DNA vectors will be substituted. Cells will be transfected and cultured post electroporation. After an incubation period, delivery of GFP will be validated through the expression of the fluorescent protein.

Appendix A

Microfluidic Channel & Electrode Fabrication

The fabrication procedures and post-conditioning of the micro-devices is described in this section. Schematic in Figure A.1 illustrates the photolithographic processes of making SU-8 photoresist-based channel master and Shipley S1818 photoresist-based substrates in the clean room. Chemical wet etching via 10:1 hydrofluoric acid (HF) is performed on the glass substrates patterned with desired features to create recess on the exposed features. The etching step is crucial in securing the metals, otherwise the sputtered metal can easily fall off due to surface shear or fluid contact. The metal deposition with hints and tips will be described. The master mold needs to be treated with a silanization agent prior to be bonded in order lengthen the lifetime of the mold. The operation of oxygen plasma to activate the PDMS and glass surfaces for irreversible bonding will then be discusses. The
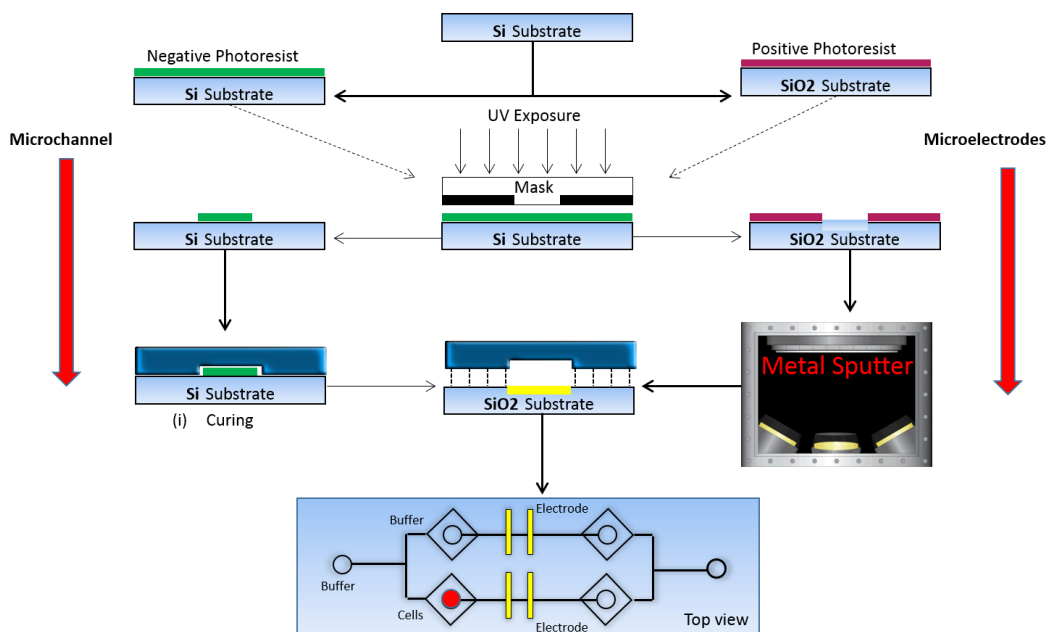
Figure A.1 Process steps of photolithography and physical vapor deposition of metals.

use of reverse casting method will be described as an alternative approach to preserve precious master molds and permit multiple replications. Two wire bonding techniques will be discussed to create electrical contact access to the bond pads of the micro-device.

Photolithographic Process

Fabricate Microfluidic Channels Using SU-8 Photoresists

Substrate Pretreatment:

1. Dip substrate into acetone solution for 10 minutes, then wash it with isopropanol.

2. Dip substrate in isopropanol solution for 10 minutes, then wash it with De-ionized water.

3. Dip substrate in DI water for 10 minutes, then air dry with nitrogen gas or filtered air.

4. Transfer substrates to oven ~150 $°C$ for 30 minutes, then allow it to cool in room temp.

Coating:

1. Make sure the spinner controller is on, turning it off is not advised.

2. Select the correct chuck for the substrate, layer the spinner bucket with aluminum foil and leave a hole in center of the foil so the rotor pieces through, do not allow aluminum foil or anything else to go into vacuum hole.

3. Insert the corresponding chuck, clean the chuck to clear off any liquid, debris when necessary as they will hinder the suction onto the substrate.

4. Align the substrate to center spinner chuck in all directions.

Photoresist	Thickness	Prebake Time	Softbake Time
SU-8 2010	10	1	3
SU-8 2010	13	1	3
SU-8 2010	20	1	4
SU-8 2025	25	1	4
SU-8 2025	41	2	7
SU-8 2025	75	3	12

5. Apply SU-8 photoresist: Start from the center, drip or pour the photoresist with either a syringe or small container to prevent overflowing.

6. Toggle the vacuum on to secure the substrate.

6. Select a spinner recipe from the MicroChem worksheet.

Press "Recipe" then the number

Photoresist	Thickness	Recipe	Spin Speed
SU-8 2010	10	0	3000
SU-8 2010	13	1	2000
SU-8 2010	20	2	1000
SU-8 2025	25	0	3000
SU-8 2025	41	1	2000
SU-8 2025	75	2	1000

Soft Bake:

1. Pre-bake the substrate on the hotplate at 65 ℃, then soft bake on the hotplate at 95 ℃, the chart below shows the recommended baking times. Ramping of the temperature is crucial in preventing thermal stress on the substrate and photoresists.

2. Allow it to cool.

Exposure:

1. Turn on EVG 620. Switch on the Main Switch (BIG & RED) on EVG 620, make sure the key switch is off. Toggle on the Lamp Power under the bench, then press Start switch to fire lamp, hold for 0.5 seconds before release for proper firing.

2. Allow Lamp to run for 10 minutes to reach the specified power (500 W) and 6-7 A of current before further action. Make a note of the lamp life before each use to ensure timely lamp bulb replacement. (Start considering lamp replacement when usage exceeds 500 hours).

3. Switch on key switch beneath the BIG and RED bubble.

4. Power on the PC. Navigate to EVG 620 icon Software on the desktop.

5. Login with the specified user name and password (i.e. Jean, pw: 750203). Try to avoid login failures since errors accumulate overtime that may lead to hardware failure someday, a firmware deficiency of EVG products we have come to peace with.

6. Click Open file and find the appropriate recipe. Create your own if necessary, do not change other people's recipe.

7. Press RUN, and wait for further on-screen instructions, do not click around.

8. To perform repetitive exposures, proceed with each on-screen instructions such as when "Load Substrate" is shown. When finished or any machine error warning, press exit to unload the mask.

Post Exposure Bake:

1. Pre-bake the substrate on the hotplate at 65 ℃, follow by soft baking it on the hotplate at 95 ℃. Recommend baking time is listed in the chart below. Follow the temperature ramping procedures to avoid thermal stress.

Photoresist	Thickness	Prebake Time	Postbake Time
SU-8 2010	10	1	2
SU-8 2010	13	1	2
SU-8 2010	20	1	2
SU-8 2025	25	1	3
SU-8 2025	41	1	3
SU-8 2025	75	1	7

Develop:

1. Soak the substrate in SU-8 Developer (filled to 15% of the overall volume of the beaker and replace and replenish regularly), rock the beaker gently to remove exposed SU-8 master.

2. Remove the substrate from developer and shower it with isopropanol solution.

3. Air dry it gently with filtered air. If substrate appears cloudy, Soak it in developer and gently shake it for another 15 seconds, and follow by Isopropanol solution rinse.

Inspection:

1. Carefully evaluate the quality of your first round of device fabrication to ensure accuracy and consistency of the procedure. Photoresists and luck varies from day to day, with temperature, air moisture, and other uncontrollable parameters, general protocol needs to be checked prior to mass production of the device.

2. Check your device under the stereo microscope provided in the clean room to ensure clean and high quality features are obtained.

Hard Baking:

Photoresist	Thickness	Develop Time
SU-8 20**10**	10	2
SU-8 20**10**	13	3
SU-8 20**10**	20	3
SU-8 20**25**	25	4
SU-8 20**25**	41	5
SU-8 20**25**	75	7

1. When the substrate pass inspection, transfer the substrate to $150\,^{\circ}C$ oven for 30 minutes.

2. The master mold is now been finalized for PDMS molding.

Completion:

1. Exit the EVG 620 software following the proper exit procedure.

2. Shutdown Windows.

3. Wait until the machine is off, then turn off Key Switch to shut off the electronics.

4. Power off the lamp switch toggle, THEN SWITCH THE LAMP POWER BACK ON, to allow proper cooling of the lamp. Wait 10 minutes before switch off the power again.

5. Switch off the Main Switch.

Fabricate Microelectrodes Using Shipley S1818 Photoresists

Substrate Pretreatment:

1. Dip substrate into acetone solution for 10 minutes, then wash it with isopropanol.

2. Dip substrate in isopropanol solution for 10 minutes, then wash it with De-ionized water.

3. Dip substrate in DI water for 10 minutes, then air dry with nitrogen gas or filtered air.

4. Transfer substrates to oven ~150$°C$ for 30 minutes, then allow it to cool in room temp.

Coating:

1. Insert the proper chuck for the substrate onto the spinner and cover the spinner bucket with aluminum foil to catch the photoresist spill.

2. Wash the chuck with acetone to remove debris and air dry to remove any liquid.

3. Center the substrate on the chuck and turn on the vacuum to secure the substrate.

4. Apply sufficient HDMS solution onto entirety of the substrate surface. It is a adhesion promotion agent. For making electrodes, no noticeable difference if HDMS is not used.

5. Spin at the proper Recipe, for Shipley: 3000 rpm, 500 rpm ramp up and down speed.

6. Apply sufficient Shipley to cover the entirety of the substrate surface.

7. Clean up after using the spinner by wiping it with acetone-soaked cleanroom wipe.

Soft Bake:

1. Bake the substrate on the hotplate at 120°C for 4 minutes. Check the color transition of the photoresist, it should be a uniform distributed pink color throughout the substrate. If not, you have temperature invariant, which is a common problem with hot plates. Attempt to place the substrate at the center of the hot plate.

2. Uniformity of photoresist is important in the final metal lift-off step, if the photoresist is too 'dry', it will be difficult to lift-off. If the photoresist is too 'wet', it may create 'bubbles' giving the illustration of over exposure.

2. Let substrate cool to room temperature.

Exposure:

1. Power on the EVG 620 machine. Switch on the main switch (red), make sure the key switch is in the "off" position. Toggle on the lamp power, beneath the bench. Then press "start" to fire lamp. The lamp must be heated ten minutes prior to usage. Turn on the key switch. Turn on the PC power, located under the bench in the cabinet.

2. Run EVG 620 Software and log in with user name and password. Use File-Open to find the appropriate recipe. Initial exposure can be set to 250 mJ/cm^2. Press "Run," then follow the instructions on the screen.

Develop:

1. Immerse substrate in MF- 319. Agitate so that the developer removes exposed Shipley. Developing time varies from 1-4 minutes.

2. Remove the substrate and rinse with DI water.

3. Air dry the substrate with filtered air.

Inspection:

1. Carefully evaluate the quality of your first round of device fabrication to ensure accuracy and consistency of the procedure. Photoresists and luck varies from day to day, with temperature, air moisture, and other uncontrollable parameters, general protocol needs to be checked prior to mass production of the device.

2. Check your device under the stereo microscope provided in the clean room to ensure clean and high quality features are obtained.

3. For making electrodes, make sure clear, transparent features are made without any signs of debris, which can appear in the forms of black dots, water marks, and hair.

Hard Bake:

1. Place the substrate in the oven at ~120˚C for 30 minutes. Cool to room temperature prior to collection.

Completion:

1. Exit the EVG Software following proper procedures. Shutdown Windows. Switch off the key switch. Cool lamp by turning off power and Turn it back. Wait for ten minutes then switch off the power. Turn off the main switch.

Hydrofluoric Acid Wet Etching

Setup and Preparation

1. Plan your process ahead of time, and always perform this process in pairs! Meaning you need to find a partner to assist you. You will be performing the main HF treatment, whereas your partner times the process, deliver the substrates, and warn others who get close to the hood. HF is extremely dangerous, and it is not to be kid around. If you are fatigued, DO NOT PERFORM HF etching!

2. The person who performs the HF etching should wear the provided plastic body covering (blue color), two layers of laboratory gloves plus the provided rubber gloves (yellow). Transparent face shield should also be worn.

3. The partner should also wear the same protective clothing, and must not be in contact with anything in the hood during the process. He/She should also prepared the HF neutralizing agents in case of emergency. The agents can be found on the shelf near the hood. The partner is to hold the timer and prepare the substrates to be treated, and also for moral support.

4. In an operable chemical hood, place a chemically inert tray covered with 2 layers of diapers for full surface coverage. Make sure a plastic bottle is available for HF waste collection.

5. Within the diaper-covered tray, place the "first-wash", "second-wash" plastic bowl filled with water. And a third glass dish for last round of dilution in water. Place the glass/wafer tweezer on it as well.

6. Place the substrates to be etched nearby the tray, 2 -3 substrates can be treated at once, however timing needs to be adjusted appropriately for each.

7. When the preparation is complete, you may go get the HF bottle from the Ante room cabinet while wearing all of your protective clothing.

Treatment

1. Start the etching process by tweezer your substrates into the 10:1 diluted HF solution for 1 minute. Try avoid contact with the solution as much as possible.

2. Anticipate the end of the minute, carefully (without splatter) tweezer up your substrate, and transfer it to the second wash bowl for dilution.

3. After another minute, transfer the substrate from the second to the third dilution bowl (glass beaker).

4. One minute later, submerge this substrate into a beaker/petri dish filled with water, exposing the treated substrate to air for prolonged period of time at this stage tends to form "cloudy" structure on the etched surfaces.

Finalization

1. Once the HF etching is complete, transfer all of your substrates to the sink.

2. Clear off the hood by dumping all the liquid waste into the plastic waste bottle using a funnel. And throwing away the diaper into the nearby white plastic bins. Wipe down the tray with acetone and isopropanol and place the bowls and tweezers into the secondary container in the hood.

3. Rinse the substrates one at a time, and air dry them to completion prior to storing them in a clean petri dish.

4. Wrap the petri dish with aluminum foil to shield from light, follow by storage in the $65\,^{\circ}C$ oven overnight. Do not stag the substrates on top of each other.

5. Prior to metal deposition, inspect all substrates for feature transparency and clarity. Pick your best candidates by throwing away the low quality substrates that you cannot rescue with water/air clearance.

6. By careful and smart arrangement, the PVD's metal chuck can hold up to 33 substrates (Record hold by Jack).

Metal Deposition Process

Things to know prior to start:

*Vacuum chamber is always under vacuum, the turbo and roughing pumps remains OFF.

* White text in the display interface represents user input dialog (activate by pressing on it).

* Green text in the display interface represents current machine operating values (not adjustable).

* Always check which metals are currently loaded (displayed on sputter door) and select accordingly.

* Typical exposure time for Titanium: 8 minutes @ 200 W (power).

*Typical exposure time for platinum: 10 minutes @ 200 W (power).

* Typical exposure time for gold: 10 minutes @ 200 W (power).

* Typical exposure time for Aluminum: 8 minutes @ 200 W (power).

1. Turn on Recirculating Chiller (temperature should be ~20 degree C)

2. Switch on the Air valve at the wall behind the machine (far left valve).

3. Login to computer as Admin if necessary, and start the "Cware" software.

    a. If you receive an initialization error (red bar), exit and restart program.

    b. Password is Admin.

4. Tab on the "Start PC Vent".

    a. This allows the chamber to be pressurized.

    b. You can open the chamber door once the "PC Vent process Complete" screen appears.

5. Take out platen and load substrate onto it with photo-tape.

    a. Make sure the substrate is facing downward.

    b. Tape two opposing corners of the substrate to provide a good hold.

    c. Wafers make 'tape rolls' and apply to back.

d. Ensure all substrates are secured.

e. Final air blow to remove any last minute dust particles.

6. Place the platen back into the vacuum chamber and properly secure it to the holder.

7. Shut off the chamber door tightly and start "Start PC pump".

8. Push on the door to avoid error messages.

a. Machines sometimes senses air leak and will stop operation.

b. You can stop pushing after the pressure on the indicator starts to change.

9. Wait by the machine until the "speed%" indicator reaches "95%" and 5×10^{-5} Torr.

10. At this point, the "Filament" icon would turn green (on). Tab it to turn it off.

a. The filament ion gauge always remains OFF only when checking for pressure less than $\sim 1 \times 10^{-5}$ Torr.

b. The filament ion gauge is NEVER to be turned on when the chamber is at higher pressures.

11. Then wait until the pressure goes down to $\sim 1 \times 10^{-5}$ Torr & "Pumping complete" screen is on.

a. Often times, the screen won't come on automatically (due to incorrect reading of pressure), so at ~10^{-5} or you've waited for >10 mins, turn on the filament momentarily.

12. Once the filament is turned off, wait for the pressure to research between 1×10^{-6} and 5×10^{-7} Torr.

a. This usually takes at least 4 hours.

b. During the wait, periodically check the screen for error messages, they occasionally appear as a certain level of pressure has been reached and you need to press the "ok" button for the machine to further pressurize the chamber.

c. The pressure reading displayed at the bottom of the screen isn't accurate when operating under low pressure (~1×10^{-5} Torr) to check the true pressure, but remember to turn it OFF right after!

13. Once the vacuum pressure is reached, go to "vacuum" tab and set "PC Pfeiffer turbo pump speed SP" to 50% by pressing on it.

14. Wait until it spins down to 80% or less before further action. This will lengthen the lifetime of the machine.

15. Then open the argon valve on the wall behind the machine (Argon gas is on the Right).

16. On the screen, select "Deposition Tab", set Velocity Set-point to 10 RPM and start platen motion (may be next step).

17. Select "Motion" tab turn on motor (platen motion on) and select FWD (should visually be able to see rotations).

18. On the screen, press the "Gas" tab to set the appropriate gas flow, PRESS on the gas valve cartoon ON the screen to open gas.

    a. The mass flow controller for argon is MFC1 and set it to 100 sccm.

19. Wait until the turbo pump reaches 50% and the pressure is stabilized.

    a. Make sure the filament is OFF since the pressure is too high.

20. Once the pressure is stabilized, on the screen, press "Deposition" tab to set power settings for the sputtering gun.

    a. Set Power Set-point to 200 W.

21. Now to turn on the sputter gun:

    a. Know the source number for your metal of interest (e.g. #1 is titanium, #2 is gold, etc.).

    b. (If depositing 1 metal) Press the appropriate "source switch" → press on the appropriate "power switch" → wait for 30 seconds (When the machine is working, there should be readings on the current.) → Press on the appropriate "shutter" for _____mins (depend on specification listed above) → after it is done, press "shutter" first to turn off → then "power" → then "source switch".

    c. (If depositing 2 metals) simply repeat part b with the correct source switch, power, and shutter number and depositing time.

22. Close the gas switch on screen (under "gas" tab).

23. Shut off the argon gas switch on the wall behind machine.

24. Leave the air valve on.

25. Stop platen motion by:

      a. Press "Stop All Motor" tap (in red).

      b. Uncheck the FWD motor tab.

      c. Uncheck platen motor's "on" tab.

26. Wait 5 minutes.

      a. To vent out the processed gas from the chamber.

27. Press on "PC vent".

28. Once the dialog window shows that the "PC vent" process is complete, then open the chamber door to remove platen.

29. Place platen back into the machine.

30. Set the Turbo pump speed back to 100 using screen tab.

31. Start PC Pump and press on the chamber door.

      a. Stop pushing on the door once the pressure value starts to change.

32. Wait for the Filament to automatically turn on, then turn it off after it turns on.

33. This process is complete once the dialog window shows "PC pump" complete message.

34. TURN THESE COMPONENTS OFF in this order: press on Turbo pump, valve, roughing pump.

35. Shut off the gas valves on the wall behind machine.

36. Turn off Recirculating pump.

37. Cross your fingers.

Metal Lift-off

The basic operation of the process can be illustrated in the figure below.
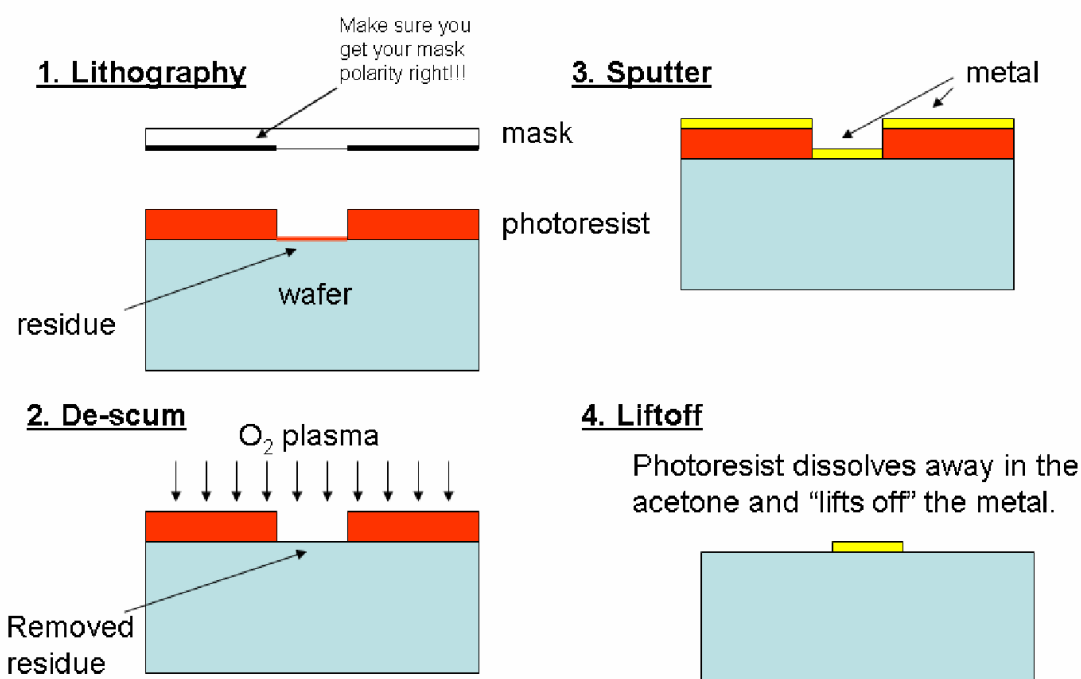
Figure A.2 Schematic illustrating the electrode fabrication process from lithography patterning of features to metal life-off.

1. Prepare the glass slide holder and filled with acetone solution.

2. Put in the substrates for full submersion.

3. Wait for 5 minutes and then gently shake the slide holder. Sonication can be used to assist this process by placing the glass slide holder half way into the sonication bath for about 15 seconds.

4. Take out the glass slides and manually spray away metal debris with bottle acetone if necessary.

5. Air dry the substrate and inspect under the microscope for signs of residue metal.

6. Store in 65 ℃ oven for an hour prior to bonding with PDMS.

Microfluidic Channel Silanization

1. Prepare the silanizing solution: Trichloro(1H,1H,2H,2H-perfluorooctyl)silane.

2. Go to a hood and pipette 25 µL of this solution around the petri dish, not on the master mold or on the same surface as the features.

3. Place the petri dish with the master mold in a dedicated desiccator and degas for 30 minutes.

4. You may see a slight oily film on the wafer surface, this is expected. Do not put too much of the silanizing solution or for too long, thick layer can interfere with PDMS's ability to bond to substrates. In which case, to eliminate this hindrance, you may soak the PDMS chunks in the acetone solution overnight, follow by oven incubation at 65 ℃ since acetone swells the PDMS in the process. This process may help.

5. Throw away the first mold as it contains residue of the silanizing solution.

Surface Activation via Oxygen Plasma

1. Warm up the oxygen plasma machine (chamber + vacuum pump) by pressing the big green knob on the chamber and the switch by the side of the vacuum pump. Flip down the sign to alert others not to shut down the machine while it is warming up.

2. Open the chamber door, and place your substrates into one of the three trays. Make sure the surfaces to be treated are facing upwards.

3. Latched the door closed, and turn on the oxygen tank and house air to enable gas flow.

4. Select the program for your surface activation treatment. For basic bonding between PDMS and glass, select program 5 with 100 W power for 60 seconds. And under gas flow tab, select gas 2 which has a flow set to 60%.

5. Press start to initiate the process. Depending on the working power of the vacuum pump, you may need to wait for up to 1-2 minutes for the chamber to reach 700 Torr pressure prior to RF activation.

6. The process is completed once a high pitched noise is heard (as a result of re-pressurization of the inner chamber) or after ~15 seconds from the moment of the ventilation.

7. For PDMS to glass bonding, timing is of the essence, the fast recovery of PDMS's hydrophobicity makes it crucial for irreversible bonding to take place. Make sure you secure the bond following the alignment if necessary under the nearby stereo microscope.

8. Methanol lubrication can be applied in between the PDMS and glass substrates if complex features demand in-contact alignment for precision. Blow off excess methanol after alignment is completed to facilitate the bonding.

Reverse Casting of Microfluidic Channels

One way to preserve the delicate wafer master features is through reverse casting of the first PDMS replica from the wafer master mold. This is done using:

1. Prepare a petri dish with a thin layer of cured PDMS in it.

2. Bond the back of the PDMS channel onto the thin layer inside the petri dish so that the channel feature is facing up.

3. Place this PDMS structure combo in the desiccator and degas with 50 µL of the silanizing solution for 30 minutes. Do not place the solution on the feature, but on the thin PDMS layer at the bottom.

4. Prepare about 5 ml of the reagent A and reagent B in two separate cups. Make sure the total solution does not exceed the maximal tolerable volume of 1 cup.

5. Place them in desiccator to degas.

6. Wrap aluminum foils around the petri dish that contains the PDMS structures, to form a vertical cylinder tall enough to contain any potential spills when placed in the oxygen plasma machine.

Appendix B

Basic Operations of Signal Acquisition Systems

This section describes the basic operations of various sensors that can be used to measure currents within a microfluidic device. The microfluidic device assumes the inclusion of a pair of Ti/Pt planar electrodes intersecting a straight channel as seen in Figure 3.8a. The measurement probe configuration uses in-series connection with the electrode wires of the device in order to obtain current measurement. Lock-in amplifier from Zurich Instruments is a very sensitive and powerful signal extraction sensor. ZiControl interface from this instrument provides the ability to perform basic current and impedance measurements, frequency sweeps, signal acquisition and analysis. Programming in LabVIEW language is required to expand the instrument's functionality and provide the users with control of the operation and process flow.

Zurich Instruments – Lock-in amplifier

ZiControl Interface

Figure B.1 HF2LI Lock-in amplifier by Zurich Instruments.

1. Connect the Lock-in amplifier's USB to the PC.

2. Turn on the switch at the back of the machine, and let it warm up for 30 minutes.

3. Start up the ZiControl Program.
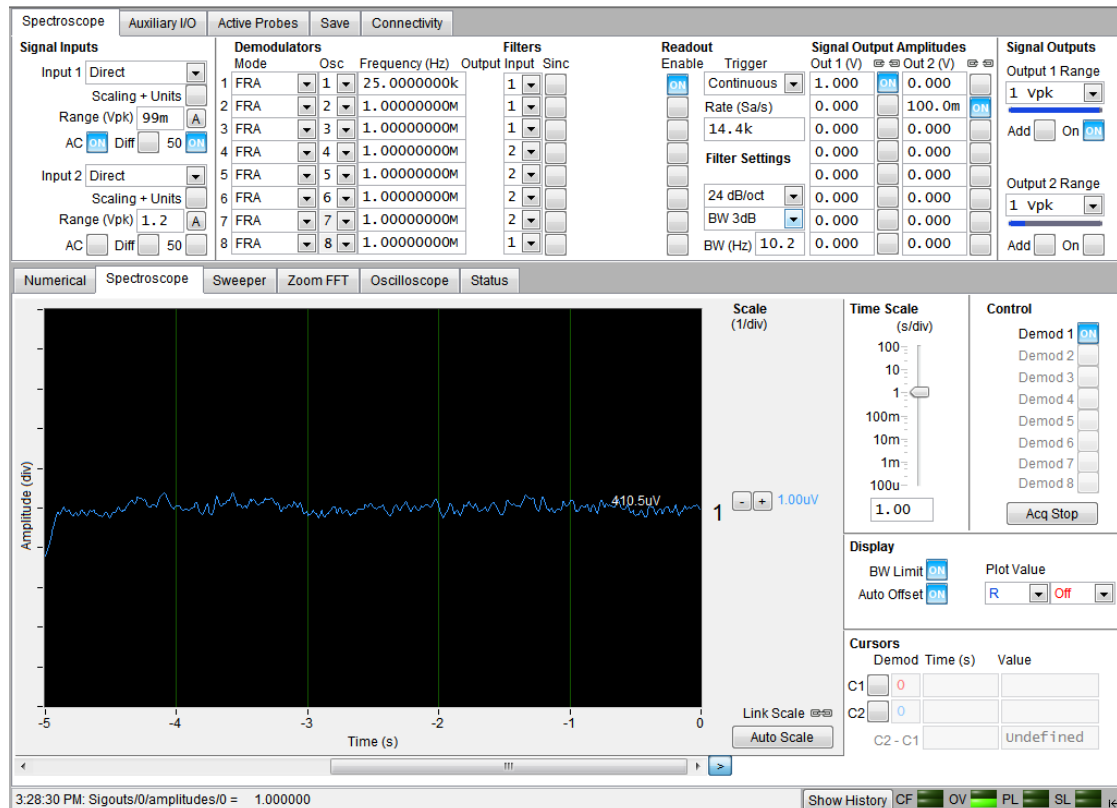
Figure B.2 ZiControl interface of the Lock-in amplifier by Zurich Instruments.

4. You should see the following interface.

5. Under the Spectroscope tab, you will find user adjustable parameters for the signal

    inputs.

    a. HF2LI has two input channels. Select the first channel input 1.

    b. If preamplifier is connected to the instrument, select HF2CA.

    c. The range specifies the range of signal input, i.e. if ±1V signal is expected,

        select 2.

    d. Press 'AC' if the signal is an AC signal, '50' represents signal comes from

        a signal source with a 50 Ω output resistance.

    e. Check the 'diff' mode when there is a differential signal (2 signals that will

        be subtracted) connected to the input.

6. There are eight demodulators in HF2LI for eight different demodulation (filtering) of the incoming signal.

    a. Select oscillator 1, and specify the frequency of interest for this demodulator.

7. Click enable readout button to activate the demodulator.

8. Set trigger to continuous for continuous acquisition of signal.

9. Set the demodulation rate. This specifies the number of samples used for calculation per second. This is different from the acquisition rate (in Hz), which always assumes a much higher sampling rate (up to 50 MHz) than the bandwidth of the incoming signal used in this lab.

10. Set the excitation output amplitude (i.e. 1 Volt)

11. The output range under the output tab is a voltage limiting step which prevents over-pulsing. Always set this value to be equal or higher than the amplitude of the excitation output.

12. Click the 'on' button to output the excitation sine wave.

13. If the device is correctly connected in series with the measurement probe, spectroscope should display the current/impedance reading.

14. If no display is shown on the oscilloscope, make sure the demodulator 1 is selected under the spectroscope tab. And the plot value shows 'R' for magnitude, 'X' for real value, 'Y' for quadrature value (commonly known as the imaginary value).

15. Pay attention to the 'OV' display LED at the bottom right hand corner, an overload is detected when the LED flashes. Immediately click on the 'A' button next to the input signal range to reset the sensor input range.

The Oscilloscope Function

1. The ZiControl interface also has a digital oscilloscope tool that can be used to measure digital signal at the signal inputs and outputs of the instrument.

2. It is useful for visualizing the signal to demodulate.

3. Select signal input 1 from the source for checking the frequency of input signal.

4. Click run to continuously scan or single to run 1 scan.

5. This tab also allows real time FFT and histogram analysis.
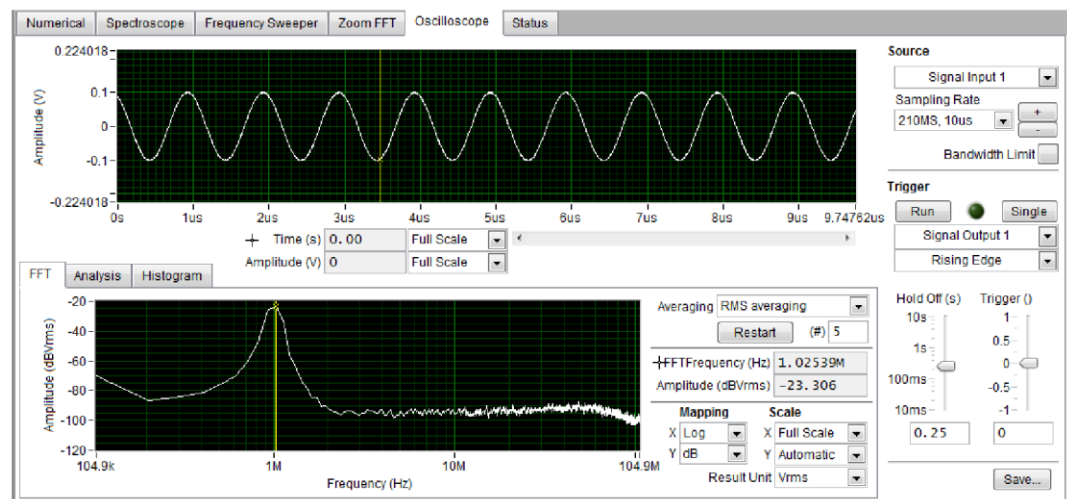
Figure B.3 Oscilloscope interface of Lock-in amplifier by Zurich Instruments.

The Frequency Sweep Function

1. Another powerful analytical tool within the ZiControl interface is the frequency sweep tool.

2. To enable a frequency sweep, first initiate the excitation voltage output from the signal output.

3. Then select range you would like to sweep, the number of points or resolution of the sweep. Larger the number, slower the sweep, and longer it will take to finish the sweep. The direction arrow indicates whether you would like to start

the sweep from low frequency or high frequency. The machine doesn't care either way.

4. User log sweep option to better display the signal, it is harder to see trends with linear scale.

5. Under sweep value drop down menu, you have the option to sweep as a function of frequency or lock-in time constant. 1 TC means a minimum settling to 90%, 3TC to 95% and 10TC to 99% of the total signal change.

6. Click Run/Stop to repeatedly perform the sweep or click single for one sweep.
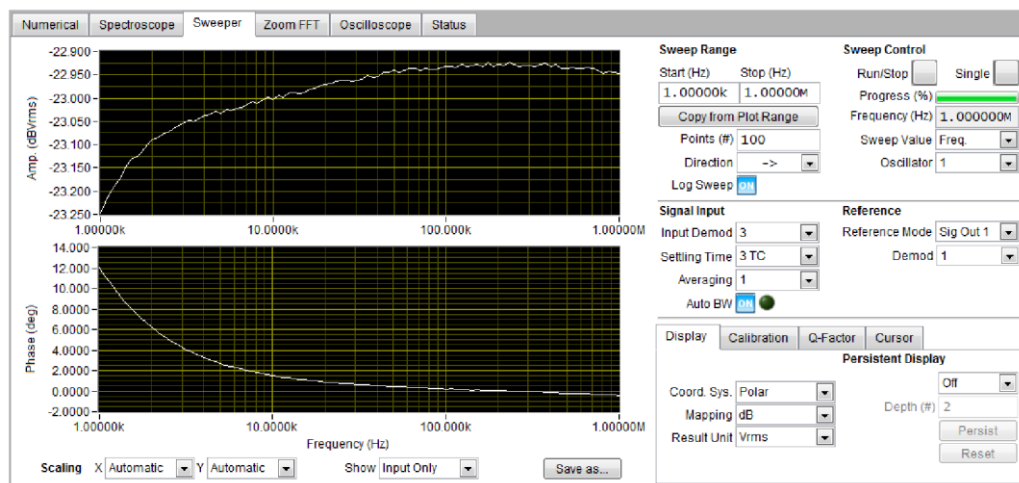
Figure B.4 Sweeper interface of Lock-in amplifier by Zurich Instruments.

Preamplifier Setting

1. The HF2CA preamplifier connected to the input of the Lock-in amplifier sensor can also be digitally controlled via the ZiControl interface.

2. This tab allows the adjustment of input gains up to 10 million folds.

3. Select the drop down menu next to 'R' symbol and click 1k for 1000 times of current to voltage gain.

a. The sensor reading is automatically changed from reading voltage to reading current after accounting for the amplification.

4. Click on the 'AC' tab if there is no DC coupling.

5. Additional gain stage can be selected by setting the 'G' drop down menu.

6. Set the input shield to be GND for reference.

Figure B.5 Preamplifier probe interface of Lock-in amplifier.

Data Storage

1. ZiControl interface provide a separate tab for storing data.

2. Because there are 8 demodulators, each is capable of producing desired data output. Therefore check on the appropriate demodulator box.

3. Specify the directory in which the file will be saved to, including the name of the test.

4. Click binary save if you wish to save the data in binary format, or leave it unchecked to save it as CSV file format.

5. Click prepend data so the saved data with the same name is not overwritten.

6. The saved demodulated data is arranged by column and each column contains different information regarding the data.
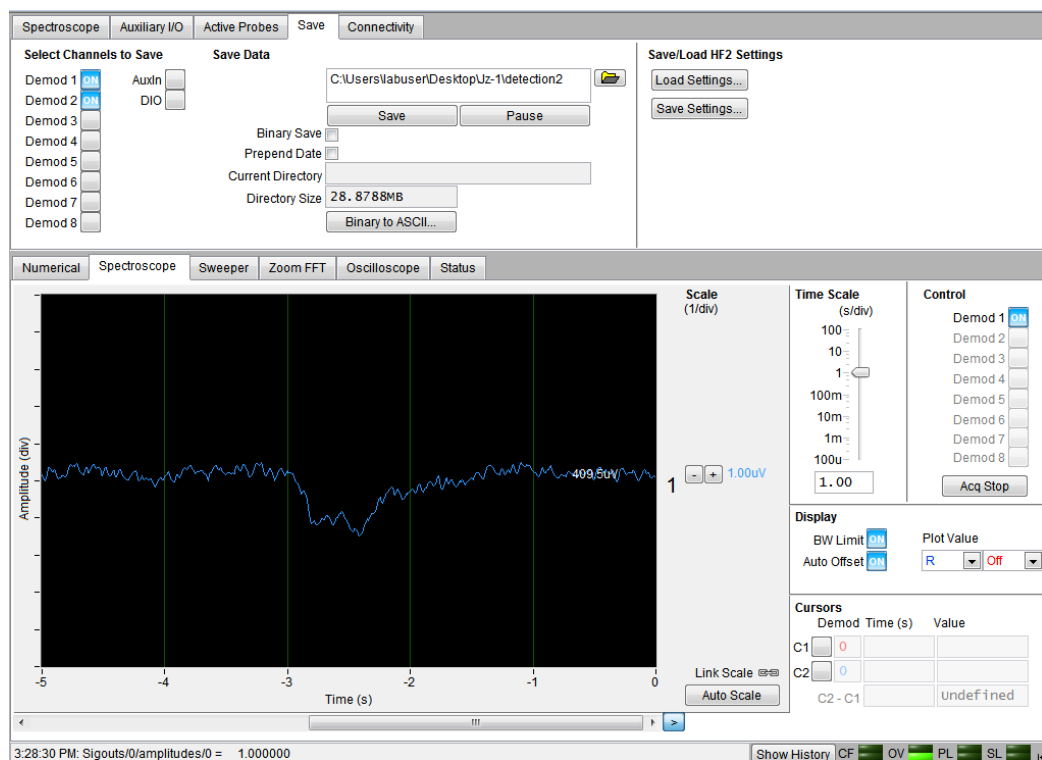
Figure B.6 Data storage interface of Lock-in amplifier by Zurich Instruments.

7. Arranging from left to right, column 1 contains time stamp in seconds, column 2 contains the 'X' value or real value, column 3 contains the 'Y' values or quadrature values, column 4 is frequency, column 5 is DIO value, column 6 is AUX in 1 or auxiliary input 1 voltages, and column 7 is AUX in 2, auxiliary input 2 voltages.

8. The magnitude of the signal is the square root of the sum of $X^2 + Y^2$.
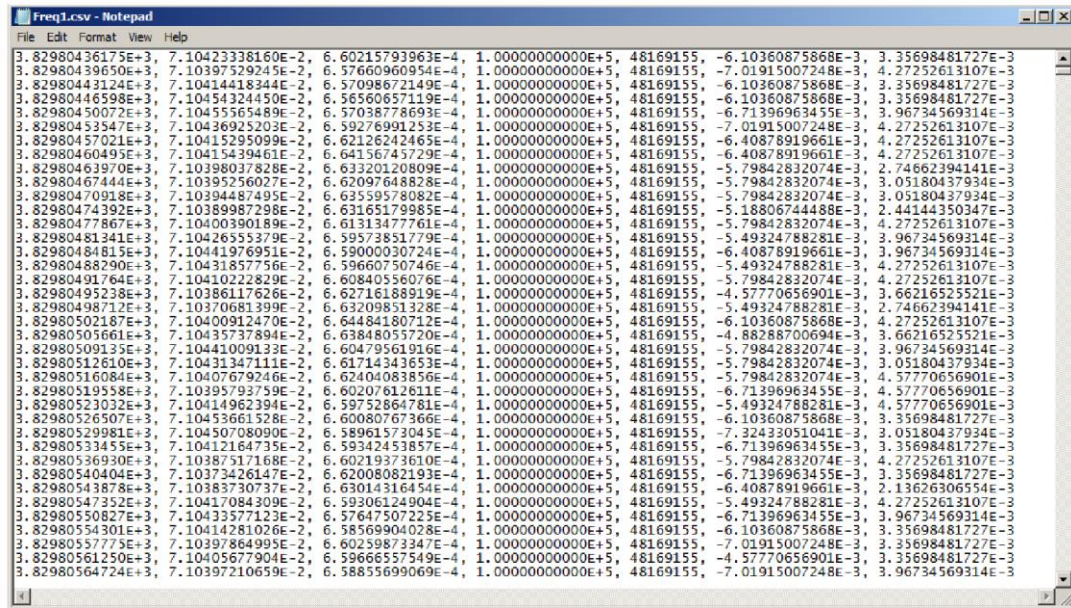
Figure B.7 An example of saved data set by Zurich Instruments Lock-in amplifier.

Application: Impedance Measurement Setup Schematics
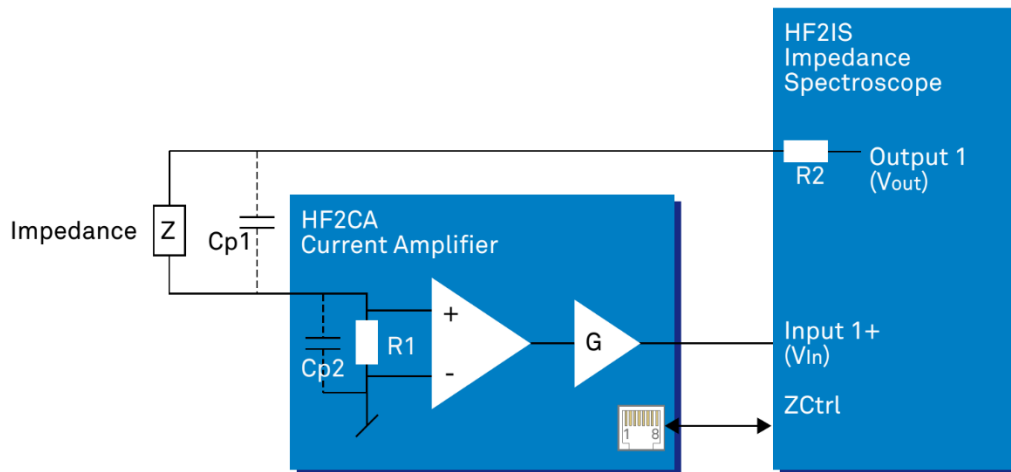
Figure B.8 An example application setup using Zurich Instruments Lock-in amplifier.

Application: Differential Signal Detection Setup Schematics
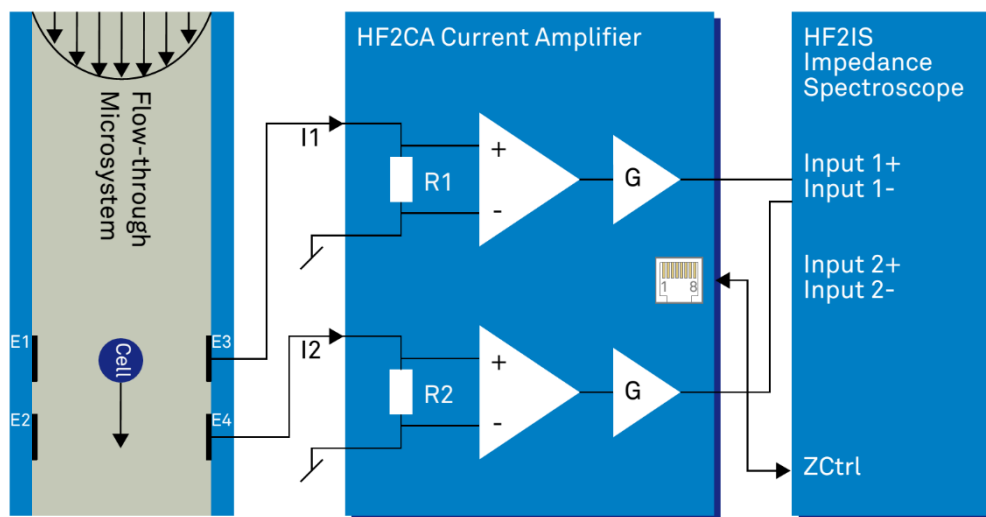
Figure B.9 An example application setup by Zurich Instruments Lock-in amplifier.

Using National Instruments DAQs for Signal Acquisition

National Instruments DAQ cards can be used to acquire analog signals when combined with a software driver and a simple signal acquisition and processing code written in LabVIEW. Software drivers are free for download from the National Instrument's software support website. SignalExpress is a built-in signal processing interface included in the LabVIEW program, make sure it is selected during the initial installation of the LabVIEW. Tutorials and examples on using the SignalExpress to perform basic signal filtering and processing can be found in the SignalExpress folder.

NI MAX

National Instrument Measurement & Automation Explorer (MAX) is a software-to-hardware portal which provides access to all NI hardware. When a new NI device
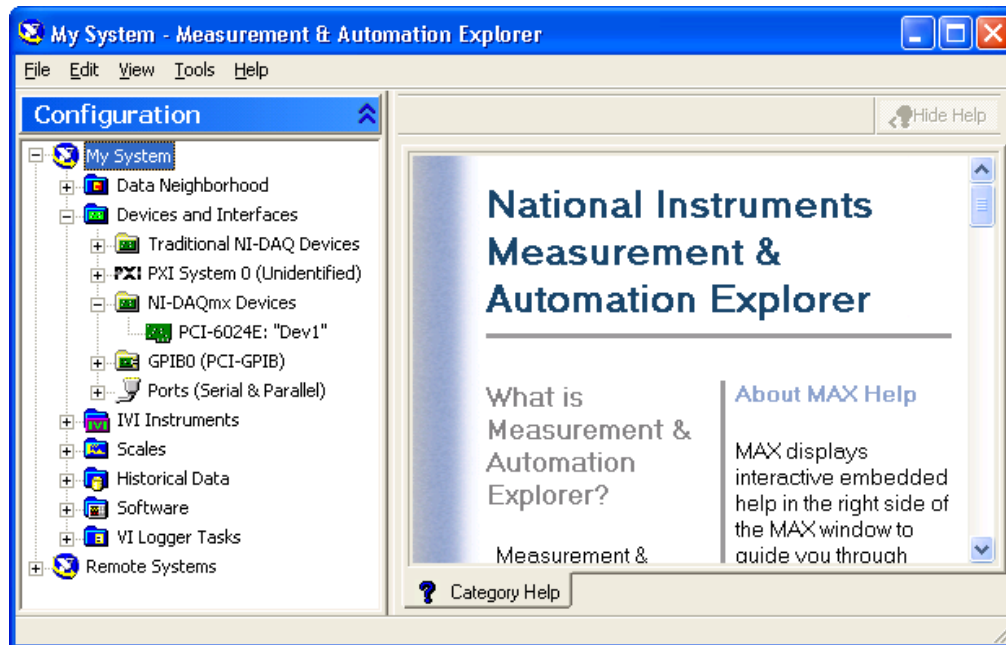
Figure B.10 Interface of National Instruments MAX device configuration panel.

(including DAQs) is connected to the PC and driver for the hardware is installed, it is encouraged to start up NI MAX and configure the device by activating the input and out channels, perform a hardware diagnostic test to inspect the condition of the device, update driver software, create and edit channels, tasks, interfaces, and virtual instruments. The following procedure will demonstrate the basic steps for connecting a Point Grey imaging camera as an example of using LabVIEW NI MAX and checking for its operation and basic functions.

1. Make sure both NI LabVIEW and Point Grey Camera driver is installed according to manufacture specificity.

2. Starting the testing the hardware.

    a. Turn on PC if needed. Open NI MAX from desktop.

    b. On the left panel, locate and expand "My System → Devices and Interfaces → NI-IMAQdx Devices → cam0: Point Grey Camera".

    c. Sometimes it takes a few seconds for the NI-IMAQdx icon to appear.

3. Click on "cam0: Point Grey Camera". You should see a grey display screen on right.

4. Click Grab to acquire an image.

5. Making adjustments with the camera settings in NI MAX:

    a. Go to the previously minimized **NI MAX** screen, click the "GRAB" tab.

    b. Make sure the "Camera Attributes" tab is selected at the bottom.

    c. Click **"Expand All".**

    d. Scroll down to **"Gain"**, change "**Auto**" to "**Manual**".

    e. Click on number next to "**Value**". A slider bar should appear. Adjust the slider accordingly.

NI USB DAQ for Multichannel Signal Acquisition

Figure B.2 is a NI USB 9162 DAQ, equipped with 8 analog signal inputs and 2 digital trigger pins. Analog signals such as electroporation pulse output can be fed into 2 of the analog channels (COM ground and 1 of the 8 channels) for signal extraction, filtering, and analysis.
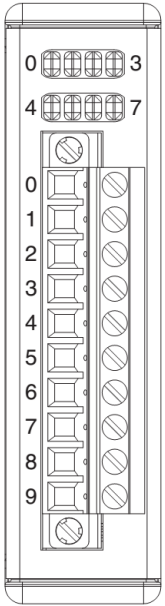
1. Prepare a few single threaded jumper cables.

2. Loosen the screw for the desired pin terminals.

    a. Two are typically used for a single channel measurement.

3. Insert the jumper cables lead into the slot provided by the loosened screws.

4. Connect the other ends of jumper cable to the output of a function generator.

   a. You may output any waveform to test the acquisition capability of the DAQ.

   b. Use a waveform with an amplitude of 1 V peak to peak to start, at 1 KHz.

5. Connect the USB to the PC if haven't done so already.

6. Activate the NI MAX to check and configure DAQ hardware.

7. Activate the SignalExpress software follow below example instructions.

Terminal Pin Diagram

Module	Terminal	Signal
	0	DI0
	1	DI1
	2	DI2
	3	DI3
	4	DI4
	5	DI5
	6	DI6
	7	DI7
	8	No connection
	9	Common (COM)

NI signal Express Image

1. Activate by double clicking on the Signal Express Icon found in the LabVIEW Toolbox folder.

2. You should see the interface shown in below figure.

3. Right click on the panel space bar to bring up the selection manual.

4. To acquire an incoming signal, select acquire signal → DAQmx acquire → Analog input → Voltage.

5. You should then see a device configuration panel on the right. Make sure the DAQ device signature here matches that shown in NI MAX.

6. Input the maximal and minimal tolerable signal range of the DAQ here.

   a. Look at the user manual of the DAQ card.
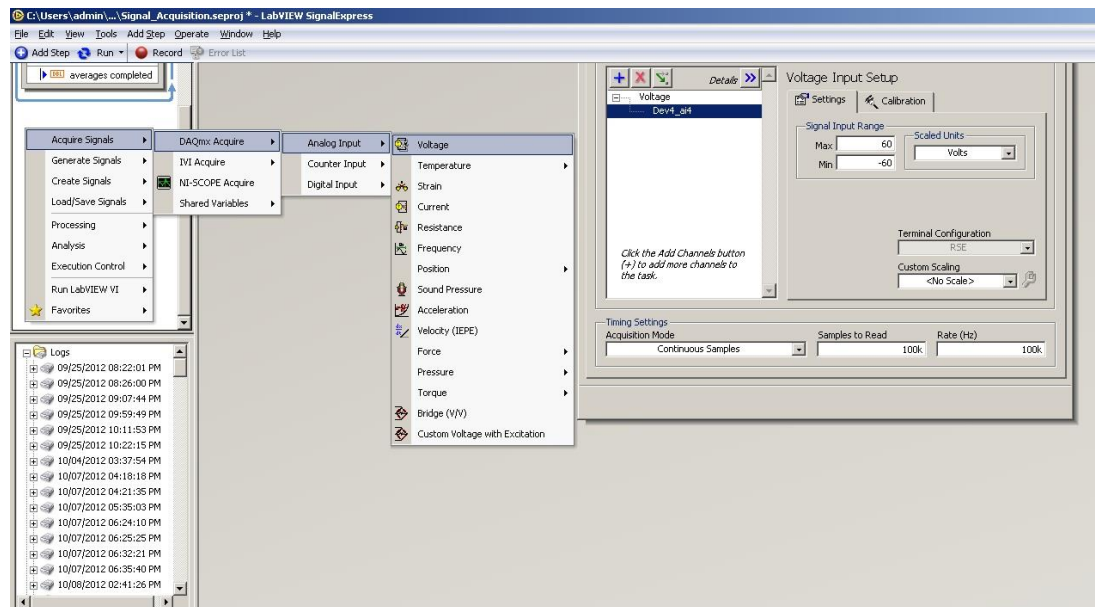
Figure B.11 Interface of voltage measurement using SignalExpress in LabVIEW 2015.

7. Under acquisition mode, select continuous sample to continuously acquire data.

8. The rate indicates the sample rate, make sure it is always more than twice the frequency of the input signal.

   a. In this case, greater than 2 kHz.

9. Under samples to read, it specifies the number of points that will be recorded from the 2 KHz of data it acquired.

10. Under the data view tab, right click on the display, and select add display → add

    signal → select the source of the signal which is also the channel of your DAQ.

11. You can add additional display to show different information such as spectrum

    analysis or signal from another channel on the DAQ. Use the figure below as a

    reference.
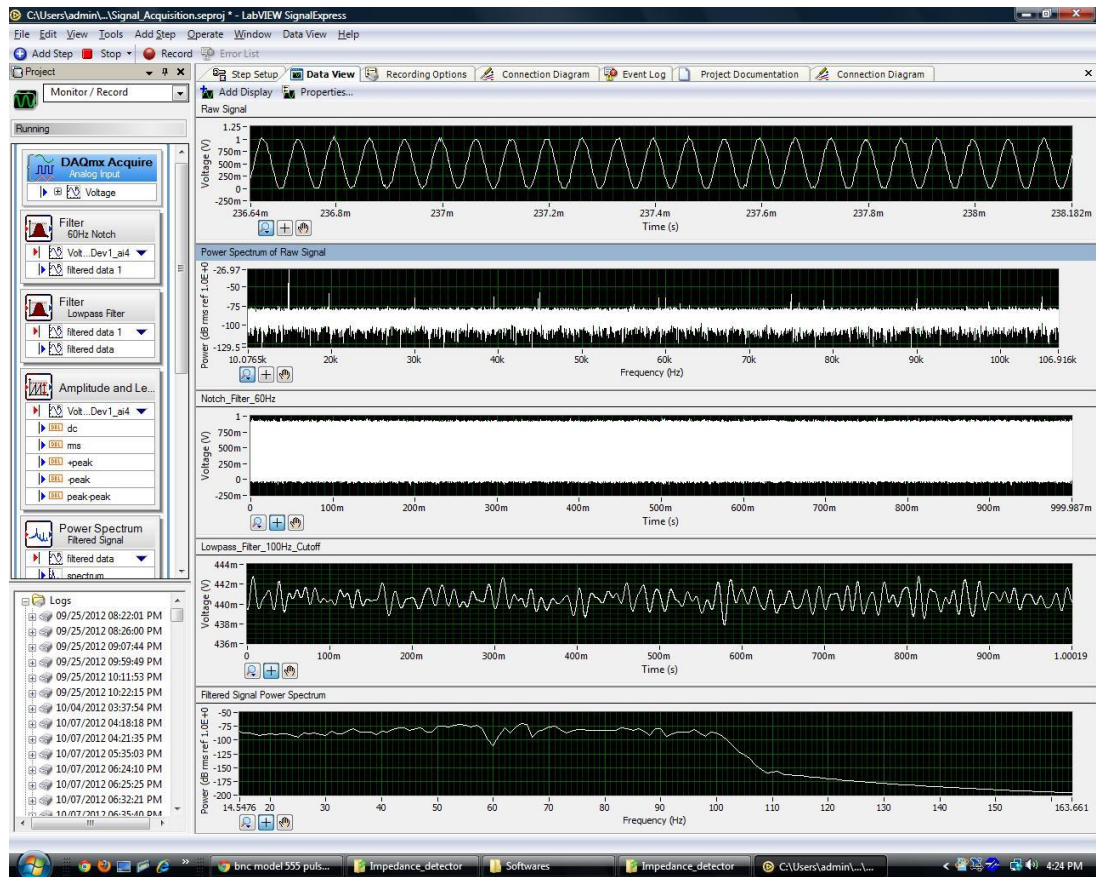
Figure B.12 Interface of SignalExpress panel with multiple displays using LabVIEW.

Recording Data
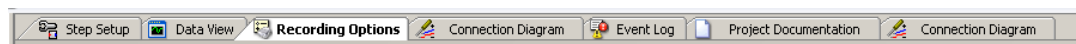
1. Click the recording options data and you should see the following save option.

2. Check the channel names or displays or signal processors that you wish to save the data.

3. Go back to the main manual and click on the record button.

4. You should see another dialog screen asking you to confirm the selection to record, click yes, and the recording starts. The recording does not start if the dialog is in place.
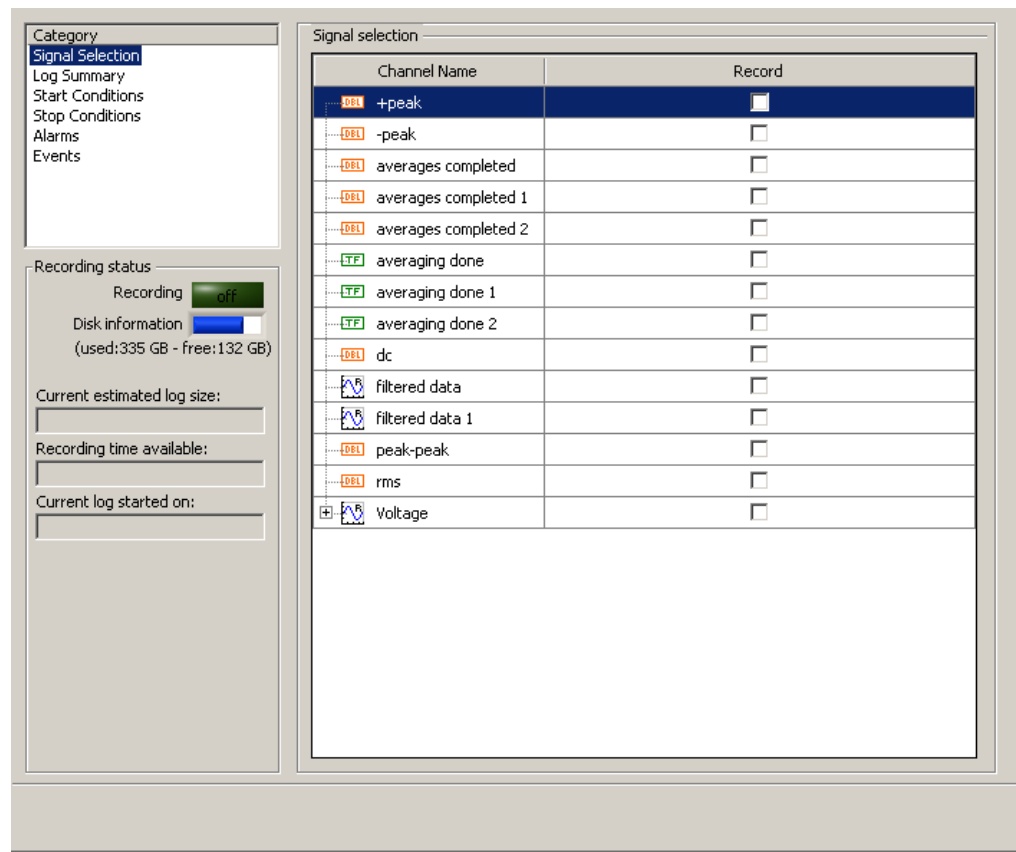
Figure B.13 Interface for device setup configuration in SignalExpress of LabVIEW.

Appendix C

COMSOL Simulation Basic Operations

Initialization (opening → geometry → physics selection)

1. Start Program

2. Select Dimensions

    a. 3D

3. Add Physics

    a. AC/DC—Electric Currents

    b. Fluid Flow—Single Phase Flow—Creeping Flow

4. Select Study Type

    a. Stationary or Time Dependent
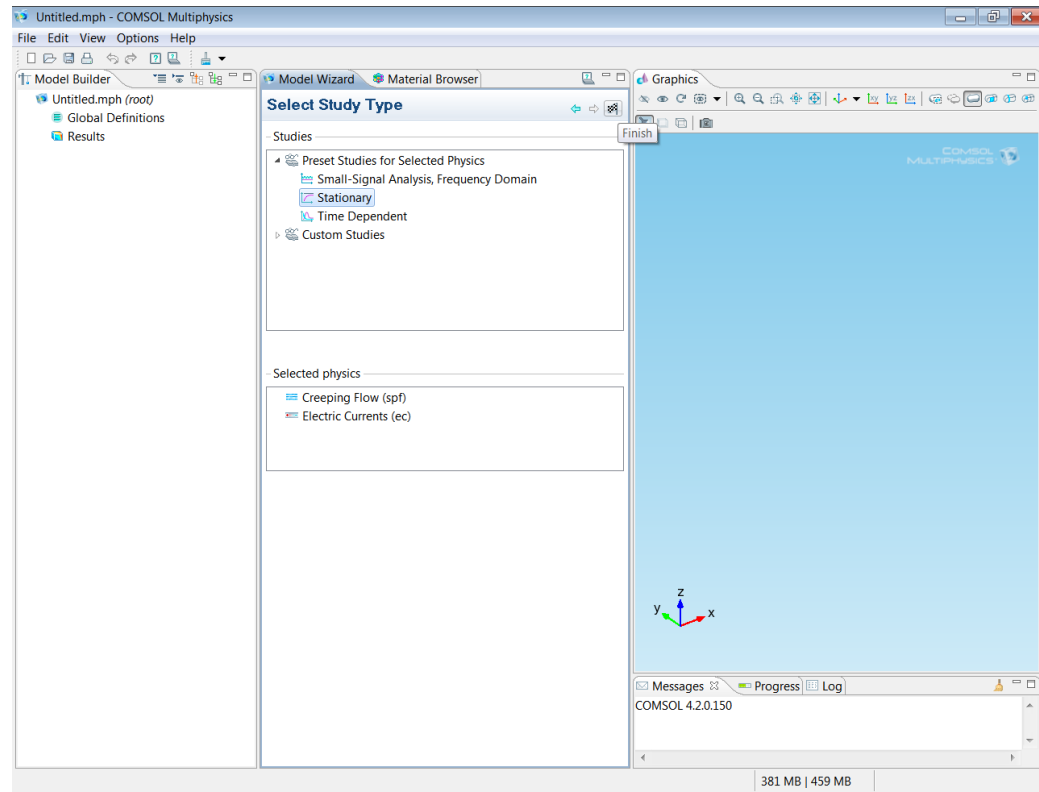
5. Click the Finish tab (Race Flag)

6. Geometry 1—Select Length Unit

    a. Micron

7. Right Click Geometry 1—Add Work Plane

    a. Define the plane (xy, z=0).

8. Under work plane, right click geometry—Bezier polygon

    a. Build the geometry (using coordinates)
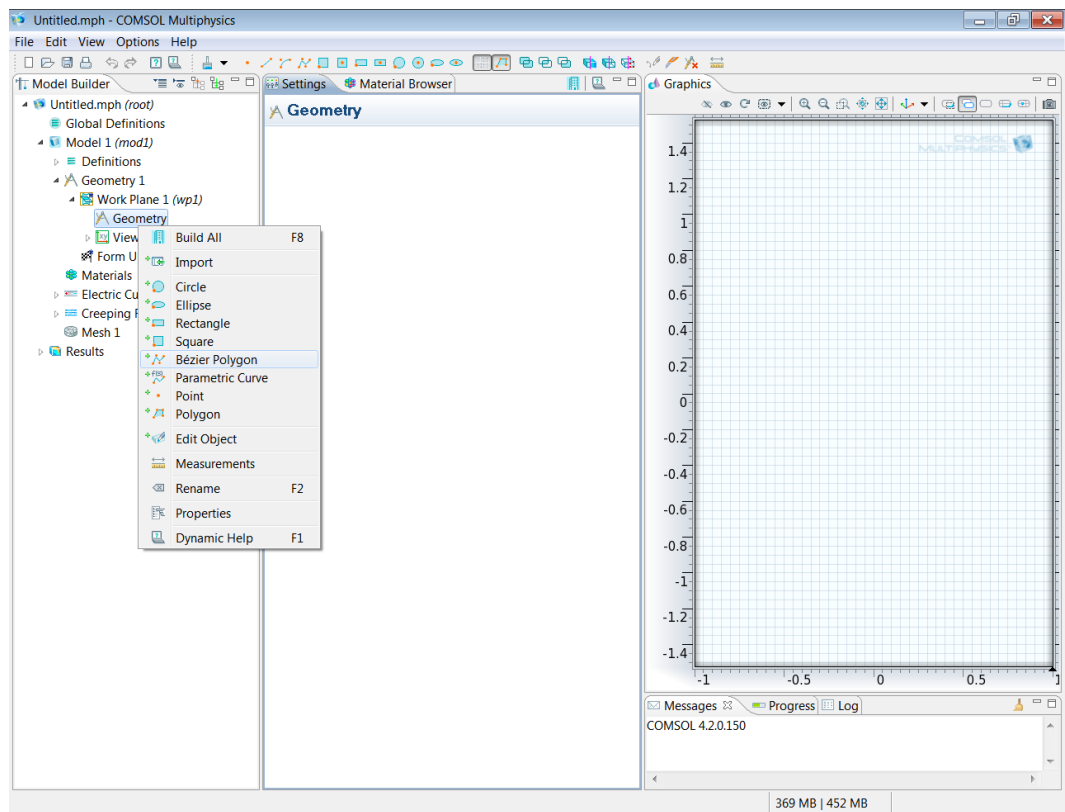
9. Repeat 7 and 8 for all geometries in the model

10. Select Build All.
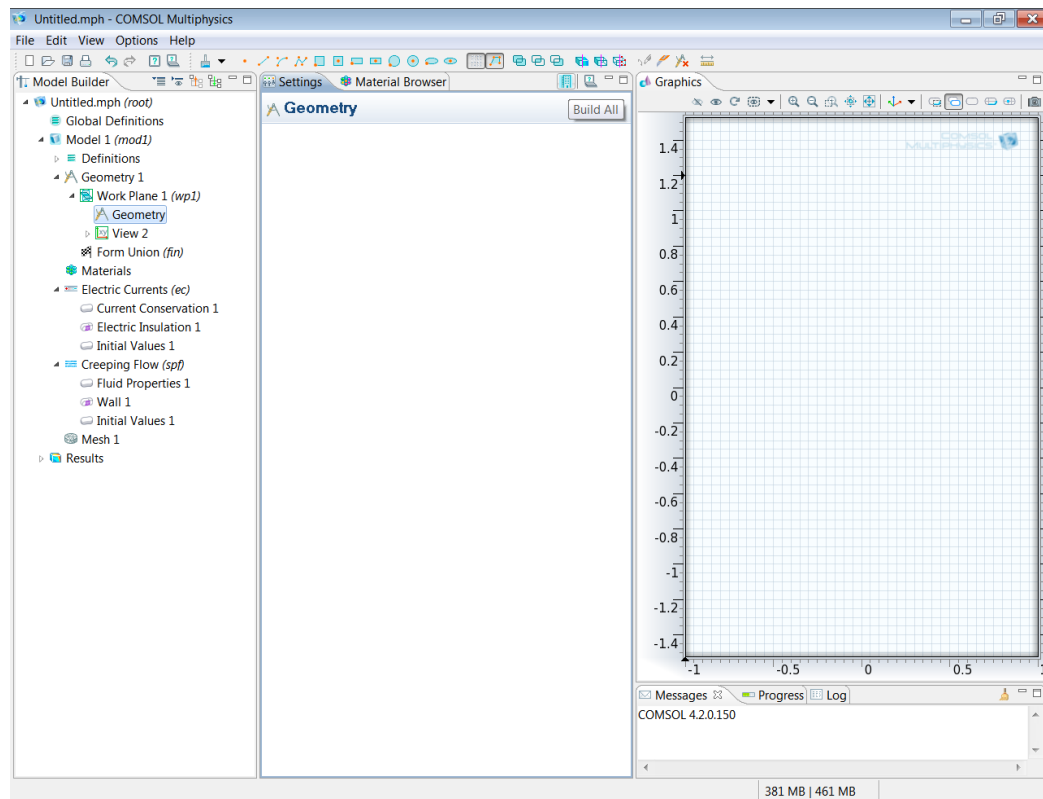
11. Add materials

    a. Right Click Materials—Open Material Browser—Add necessary materials

    b. Define the geometric domains to a specific material

    c. If necessary, alter material properties to fit model (i.e. conductivity)

Subdomain Setting for Physics I (Electric Currents)

1. Add domains to Electric Currents.

2. Current Conservation 1—Electrical Conductivity and Relative Permittivity—From Material

3. Initial Values 1—0 Volts

4. Right Click Electric Currents—Add Electric Potential

    a. Select and add all boundaries of the positive electrode

b. Set the initial Voltage
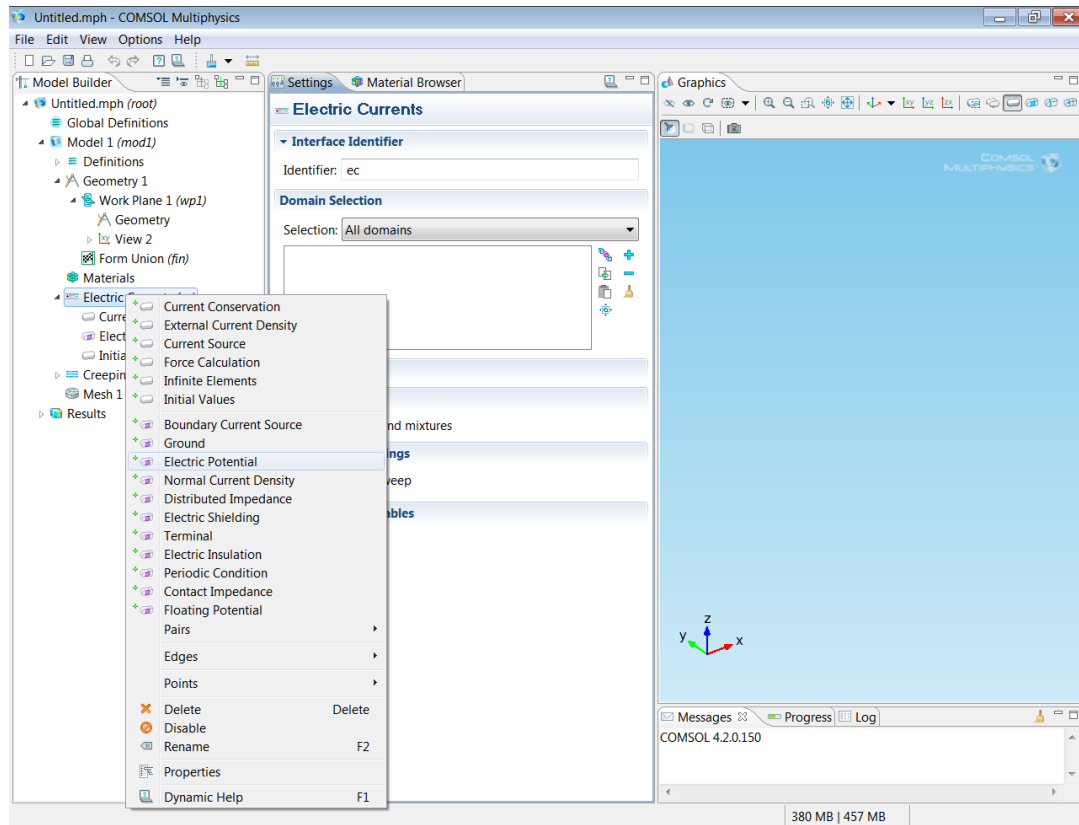
5. Right Click Electric Currents — Add Ground

    a. Select and add all boundaries of the grounded electrode.

Subdomain Setting for Physics II (Creeping Flow)

1. Add the fluid geometric domain to Creeping Flow

2. Compressibility—Incompressible (unless you are doing a gas)

3. Fluid Properties—From Material

4. Set Initial Values 1—0 Pressure

5. Right Click Creeping Flow—Add Inlet(s)

    a. Select the boundary of the inlet.

b. Set the initial condition (define the normal inflow velocity)
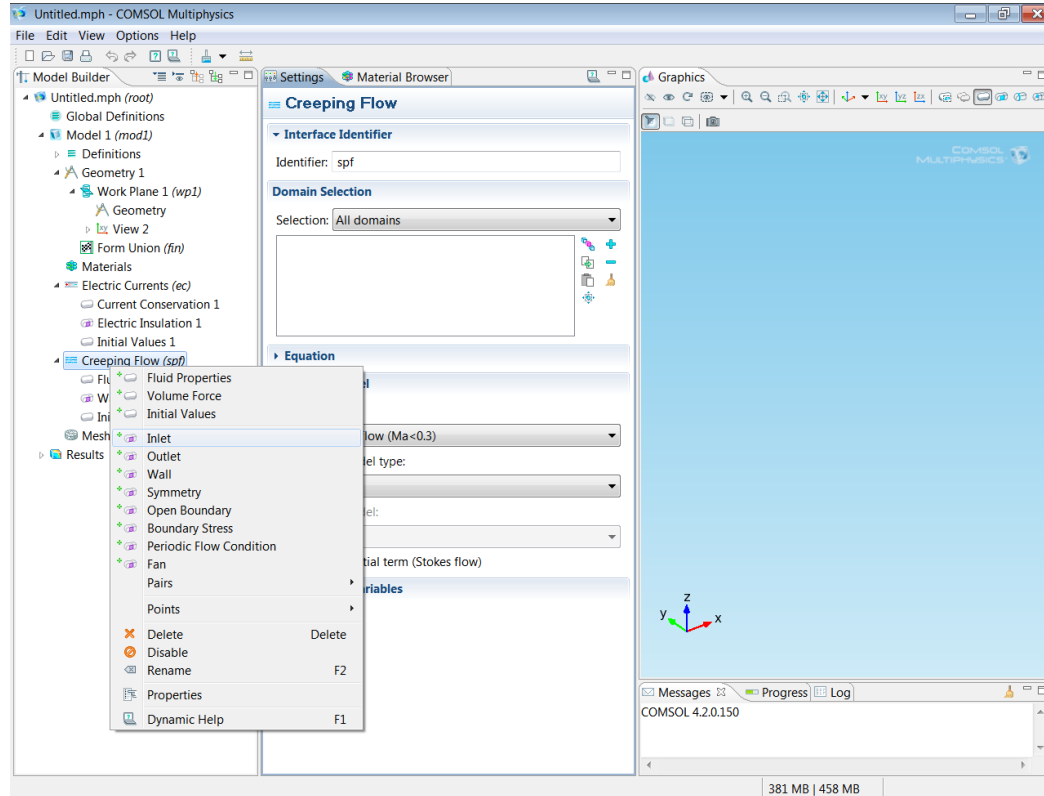
6. Right Click Creeping Flow—Add Outlet(s)

    a. Select the boundary of the outlet.

    b. Set the pressure to 0.

Model Tree and Mesh

1. Select Mesh 1

2. Select Physics Controlled Mesh

3. Element Size—Fine (you can change this, smaller elements, longer to solve)

Solver Parameters

1. Right Click Study 1—Compute
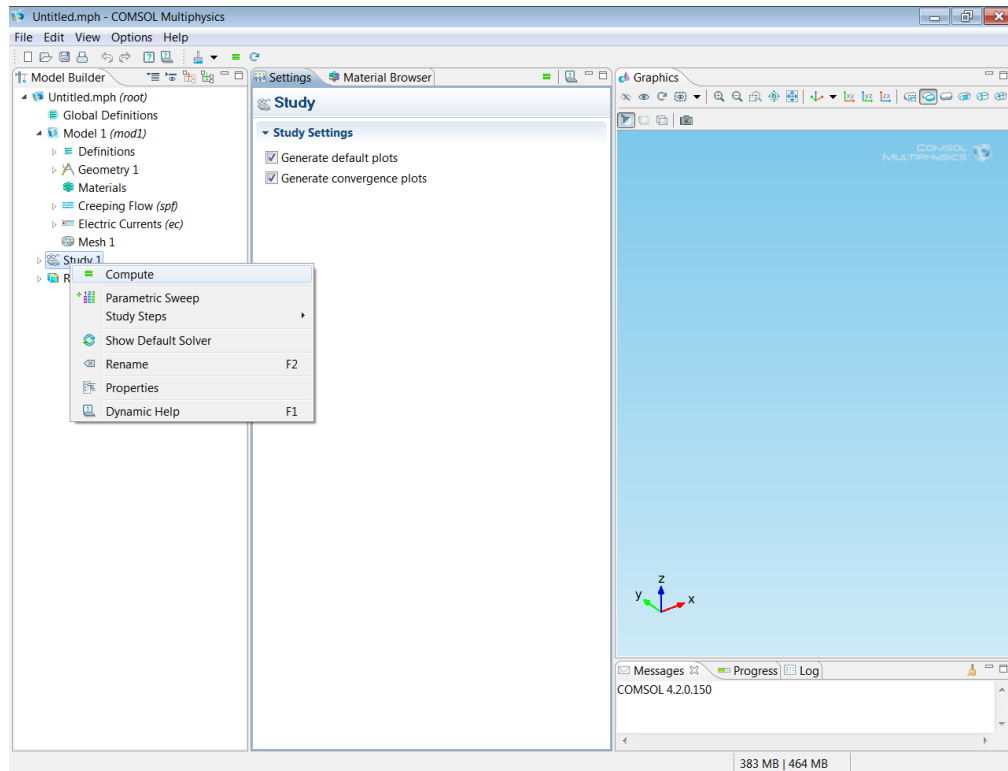
2. Results

    a. Right Click—Add Plot Group

    b. Define the result you would like to analyze

        i. Flow profile, electric field, etc.

Appendix D

Cell Passage/Culture

Preparation:

1. Thawed trypsin-EDTA tube in 37°C water bath.

2. Warm up the DMEM media in 37°C water bath.

3. Spray down your gloves with 70% ethanol prior to further action in the hood.

4. Spray down the hood area with 70% ethanol, use Kim wipe to wipe down the surface.

5. Prepare labeled centrifuge tubes and 2 ml (9.6 cm^2) or 7 ml well plates.

6. Obtain an empty flask (small-75cm^2, big – 125 cm^2 surface area) for cell culturing.

7. Check the density of cells (in flask) in the incubator.

8. Turn on hood light (second button, not UV).

9. Wash all tools that goes in the hood (pipetter, pipettes (3ml)) with 70% ethanol.

10. Get a tube rack to hold media tube and trypsin tube.

Renew the Cell Line in Flask Process:

1. Prep a new flask if necessary, then fill each with 5 ml media, then incubate them in the incubator.

2. Take the old batch (in flask) out of the incubator (cells attached to bottom surface).

3. Inspect the cells viability (has fibers stretching them sideways), not shrinking.

4. Within the hood, aspirate out the old media in the flask (75cm^2 surface area).

5. Add __3__ ml of trypsin to the flask (spread and swirl).

6. Incubate the flask in the incubator for __2__ minutes.

7. Take the flask out, add __6__ ml of media to neutralize the trypsin & wash the cells down.

8. Pipette up and down (__10__ml) the solution and transfer it to a centrifuge tube.

9. Centrifuge the tube for 2 minutes at 2000 RPM and 21C, 5 ACL/DEC.

10. Make sure it is balanced with another tube of solution (9ml).

11. Make sure you see the palates, then aspirate out the supernatant.

12. The next step determines your final cell density, so do a cell count on hemocytometer.

13. Add __1__ml of media to re-suspend the cell palates, pipette up and down to mix.

14. Add __60__ul of cell solution to the new flask with media.

15. Add __30__ul of cell solution into each well for next day experiments.

16. Label flask and wells with name and date, then put in incubator.

17. Clean up by putting trypsin back to the freezer, media (after labeling) back to the fridge, and everything else back (pipette tips, trash, etc.). Wipe down the hood with ethanol again, back to how it was before.

Cell Counting

1. Trypsinize the cells and centrifuge at 2000 RPM for 2 min.

2. Aspirate the supernatant without agitating the cell pellet at the bottom of the tube, use a transfer pipet and pipetter to do the job carefully.

3. Re-suspend cells in 2 ml DMEM medium.

4. Pipette in 50 µL medium/cell mixture into the microfuge tube.

5. Transfer 50 µL of trypan blue solution without dilution to the microfuge tube by using a dilution factor of 2.

6. Place the cells in hemocytometer and cover with coverslip.

7. Count cells under microscope with the following formula:

Total cell count = number count x 10,000 (hemocytometer factor) x 2 (dilution factor) x 2 ml (total volume).

General Microscale Electroporation Protocols

A) Prepare the Equipment

1. Set up the function generator to output a DC pulse with the following parameters:

    a. 350 mV$_{p-p}$ amplitude (use high level and level adjustment).

    b. 5 ms long pulse or 200 Hz frequency.

    c. 99.99% duty cycle (output a full pulse).

    d. Under Burst mode, set up the trigger to receive an external signal.

    e. Select the number of burst to set the number of pulses

2. Check the output of the function generator on the oscilloscope.

    a. Make sure to set the time scale on the oscilloscope to be in the range of at least 10 times of your pulse duration, so you may see it on the screen.

    b. Adjust the voltage per division so you can see the amplitude of the pulse.

3. Connect the function generator output to the DC amplifier for pulse amplification.

    a. This will multiple your pulse amplitude by 50, achieving 17.5 V$_{p-p.}$

4. Verify the output of the amplifier on the oscilloscope for pulse amplitude and width.

B) Prepare the Microfluidic Channel

1. Inspect the microfluidic channel for debris and leaks.

2. Turn on the viewing camera and set the device to center in the view screen.

3. Perfused 10% BSA solution into the channel and let it incubate for 0.5 – 1 hour.

4. Aspirate out the BSA solution with a syringe via negative pressure.

5. Inspect the channel for debris and clogs.

6. Turn on the syringe pumps and set up the operating parameters:

    a. Input syringe diameter

    b. Input desired perfusion rate in µL/min.

C) Prepare the 3T3 Cells

1. Follow the previously described procedures for setting up the hood.

2. Obtain cells from 2 of the 6 well plates (~ 1 million cells).

3. Trypsinize the cells and allow incubation for 2 minutes at 2000 RPM.

4. Neutralized the trypsin with 5 ml of media and centrifuge.

5. Aspirate out the supernatant and add 5 ml of 100 µS/cm buffer solution.

6. Centrifuge once more and aspirate out the supernatant.

7. Depending on the desired density, add 300 µL 100 µS/cm buffer to the cell pellet.

8. Pipette up and down gently to mix the mixture.

9. At this step, you may add fluorescence dye such as Propidium Iodide into the buffer.

    a. Typically 100 µM total concentration is used.

10. Transfer the mixture of cells and buffer to a 1.5 ml centrifuge tube.

11. Load the cells in buffer into a 1 ml glass syringe.

D) Electroporation

1. Perfuse the cells into the microfluidic channel.

2. Connect the output alligator clips onto the electrode wires of the device.

3. Press trigger on the function generator to output the electroporation pulse.

General Macroscale Electroporation Protocols

The Night before the Experiment

A) Prepare the Electroporator

1. Test electroporation voltages on oscilloscope to verify operation

2. Move the electroporator setup to Tissue culture Room to secure a hood

B) Prepare Test Tubes & Buffer Solutions

1. Locate & Label all required electroporation cuvettes.

2. Locate & Label all required flow cytometry tubes.

3. Locate & Label all required centrifuge tubes.

4. Add 5ml of PBS (NO calcium, NO magnesium) to all centrifuge tubes and put in fridge.

5. Add 200 µL of PBS and 20 µL of 7AAD (40 µg/ml) to flow cytometry tubes (mount on rack), without light!

Controls:	FD_Only	7AAD_Only	No-Pulse
	220 µL PBS	200 µL PBS + 20 µL 7AAD	200 µL PBS + 20 µL 7AAD

6. Leave all tubes covered in 4 ℃ fridge.

7. Fill 7AAD 1-ml tube with 220 µL of EP buffer & 7AAD (30 µL).

8. Filter the electroporation buffer needed for tomorrow – use syringe filters.

The Day of Experiment-Beforehand

A) Set up the hood

Under the Hood now

1. Centrifuge tube   2. Flow cytometry tubes   3. PBS

4. 2 Pipetters   5. Trypsin   6. Waste bucket   7. Buffer & Cell media + rack

        8. General tube rack   9. 2 Ice buckets   10.   Thawed/covered   2ml

Dextran solution

11. 7AAD-1ml tube with 220 µL of 7AAD

In fridge for later:

        1. Cuvettes   2. Centrifuge tubes   3. Flow cytometer tubes   4.   Disposable

pipettes

B) Prepare the Electroporator

        1. Tune the electroporator to generate 100 Volts, start P2 knob turned to right all

the way.

        2. Stabilize it.

C) Cell Preparation

        1. Trypsinize the cells in a T-75 flask for 2 minutes.

        2. Add media to neutralize the trypsinized cells.

        3. Centrifuge at 2000 RPM for 2 minutes.

4. Re-suspend with 5ml of 100 μS/cm buffer.

5. Centrifuge & aspirate out the supernatant.

6. Re-suspend with 2-ml of 100 μS/cm buffer.

7. Take 200 μL of this suspension and put into 1ml tube on ice (7AAD only control).

8. Add 3 ml of 100 μS/cm buffer.

9. Centrifuge & aspirate out the supernatant.

10. Add 2 ml of prepared fluorecinated Dextran solution to cells.

11. Put cells on ice for 5 minutes.

12. While waiting: clear off everything in hood except electroporation chambers, media, pipetter, timer and marker.

13. Turn the lights off to prevent photo bleaching.

The Day of Experiment-During

1. Condition 1: unplug second pulse BNC cable & check pulse parameter.

2. Add 90 μL cell suspension on ice to electroporation chamber.

3. ZAP and WAIT and UN-PRESS.

4. Take the cuvette out first.

5. Add 250 μL media to cuvette.

6. Put cuvette on covered ice igloo.

7. Start 15 minutes timer and record time.

8. Adjust timer on pulse generator.

9. Put next cuvette in place.

10. Repeat step 1 until finish.

Controls

7AAD_Only: unplug second BNC →change first pulse to **50 ms** →90 µL from 1ml Eppendorf tube.

Dextran_Only: unplug second BNC→ change first pulse to 10ms→ 90 µL from cell reservoir on ice.

No_Pulse: 90 µL from cell reservoir on ice → NO Pulse!

---

11. After 15 minutes, take out cuvette accordingly on the table.

12. Suck cell from cuvette to centrifuge tubes filled with 5 ml PBS using suckers.

13. Centrifuge   **(Return to TC for clean-up, except PBS + pipetters)**

14. Aspirate out the supernatant carefully.

15. Add 5 ml PBS again & centrifuge   **(Return to TC for clean-up)**

16. Aspirate out the supernatant.

17. Add 280 µL of PBS to cells.

18. Transfer 280 µL of previous stuff to flow cytometry tubes.

19. Cover them up and leave and Bring flash drive and notebook.

Cell Harvest - Prepare the cells for Electroporation & Flow Cytometry:

Set up equipment: Power supply cart, electroporation cuvettes, Ice bucket, and all the cell culture stuff.

1. Connect the cuvettes to the power supply leads in the hood.

2. Filter __10__ ml of (Dextran) into a centrifuge tube using syringe filter.

3. Store the filtrate in the fridge.

4. Get the cuvettes and label them all.

5. Get the centrifuge tubes and label them all.

6. Get the electroporation buffer (a combination of sucrose, magnesium, etc.).

7. Prepare the cells, the process is described previously.

8. Prepare the power supply, configure pulse (single shot, 3ms delay, 120 V_{p-p} over 1 mm equivalent to 1.2kV/cm).

9. Distribute cells into centrifuge tubes from the original source.

10. Add __90___ µl of cells into cuvette.

11. Apply the pulse.

12. Place the cuvette on ice and incubate for 15-20 minutes.

      After 1-2 minutes, add 2 ml of cell medium to each cuvette, put back on ice.

13. Turn off the voltage power supply, wait for the voltage to decrease.

14. Add 5 ml of PBS (1X) to each centrifuge tube.

15. Wait until time is up.

16. Add ETHD to stain the cells (only to selected cuvettes), 0.2-0.3 ml.

17. Incubate for 5 minutes.

18. Use small sucker to suck all of the fluid out of the cuvette into centrifuge tube with PBS.

19. Centrifuge the tube at 2000 RPM for 2 minutes.

20. Aspirate out the supernatant.

21. Add 5 ml of PBS (1X) to each.

22. Centrifuge and Aspirate again.

23. Prepare the flow cytometer tubes (label them).

24. Transfer 750 µL of PBS (1X) into the centrifuge tube with cell palates.

25. Pipette up and down the mixture, then transfer it to the flow cytometer tubes.

Basic Flow cytometry operations:

1. Machine Solution Check

- Open the lower compartment.

- Right bin: unscrew the cap, then empty all waste solutions.

- Flip the middle switch to un-pressurize the left bin (sheath fluid).

- Slide the metal plate up and lift it to uncover the bin (move the wires away).

- Unscrew the cap and fill the bin about half way with sheathing fluid.

• Place the bins, metal plate back and switch the pressure flip down.

2. Start the machine by pressing on the green button on the right side (Must be before PC starts)

3. Wait a few seconds before turning on the MAC PC.

4. Click on the Apple sign → Start Cellquest software → a window will pop up with blank space, next to it a toolbar with types of graphs and other options.

5. Click on Acquire → select "Connect to the Cytometer" → Acquisition control box will show up that starts your sampling.

6. Switch off the box on the acquisition control box because it is mainly for sorting.

7. Go to acquire and hit counter → tells you the total events (how many cells you will be counting, and duration).

8. Go to acquire and select "parameter description" → create a new folder/find your folder under Cellquest → click the file and name it something else in prefix: YourFileName.001.

9. Go to Acquire and select "acquisition and storage", and you can specify how many cells you want for each run (10000 is fine), once it counts all the cells the run will stop.

10. Go to cytometer and click Detectors/Amps → this allows you to control the power of the lasers. (It is similar to exposure time) (Ex: if signal is weak in FL3 channel, amplify signal by increasing the power which leads to increased signal).

11. Click the left side toolbar to select Histograms or scatter plots

    a. Traditional plot is Forward Scatter (FSC) versus Side Scatter (SSC)

i. Click on the dot plot

ii. Select "acquisition and analysis"

iii. Press ok

iv. Black plot will come up in the blank window

b. Histograms are used for quantifying fluorescence.

i. Click on histogram

ii. Select "acquisition and analysis"

iii. You can choose which parameters to plot

12. You can chose FSC, SSC.

13. FL1-H channel → green

14. FL3-H channel → TRITC

15. Manual has specific wavelengths of the channels.

16. Transfer the cells in the appropriate tube and vortex tube so that the cells get suspended.

17. Open lever arm and put the tube with cells.

18. When you ready to initiate the operation, click the run button (the light indicator will shift from Standby to Run then disappear), and then click acquire on the computer.

Appendix E

Note: Excepts of this appendix was adapted from the following publication:

M. Zheng. (2013). "A Theory-driven, Feedback-controlled Electroporation Microdevice for Efficient Molecular Delivery into Single Cells." A PhD dissertation proposal submitted to Rutgers University in partial fulfillment of requirements for doctoral candidacy. Thesis advisor: Professor Jeffrey D. Zahn. Submitted on May 31, 2013.

Multi-pulse Single Cell Electroporation & Analysis

1. Single Pulse Fluorescence Analysis on Static Cell

Because the PI fluorescence is directly associated with the amounts of delivery into the cell during electroporation, large accumulation was desired to better quantify delivery without severe background noise interference. Guided by the electrokinetics-dominated intracellular molecular transport theory, a buffer conductivity of 100 µS/cm was used. Previous macroscale electroporation studies have also suggested the initial use of 60,000 V/m to electroporate cells without significantly damaging them. A single pulse duration of 20 ms was applied, and the camera continued to record for a total of 250 ms. An additional image was also obtained 1-2 second post electroporation to inspect the long term status of PI inside and outside the cell. All of the images extracted from the recording camera were analyzed with MATLAB computing software version R2011b (MathWorks, Inc., Natick MA). In order to improve the quality of the fluorescence images, the background noise in the form of speckles was reduced by subtracting each image with an average background fluorescence intensity. This is a 20 pixel by 20 pixel region from the four corners of the

image where intensity remains to be most stable and uniform. The fluorescence intensity profile of the entire cell was summed for every image under the same condition. To better smooth the signal curves, a moving average filter was also used with a moving factor of 10 images.

Figure E.1 shows the summation of fluorescence intensity plotted as a function of 16 bit gray scale intensity value versus time in milliseconds (ms). The translucent red label shows the temporal region when the 20 ms pulse is applied. Two modes of transport mechanism can be unveiled, namely electrophoresis and diffusion mediated transport. During the

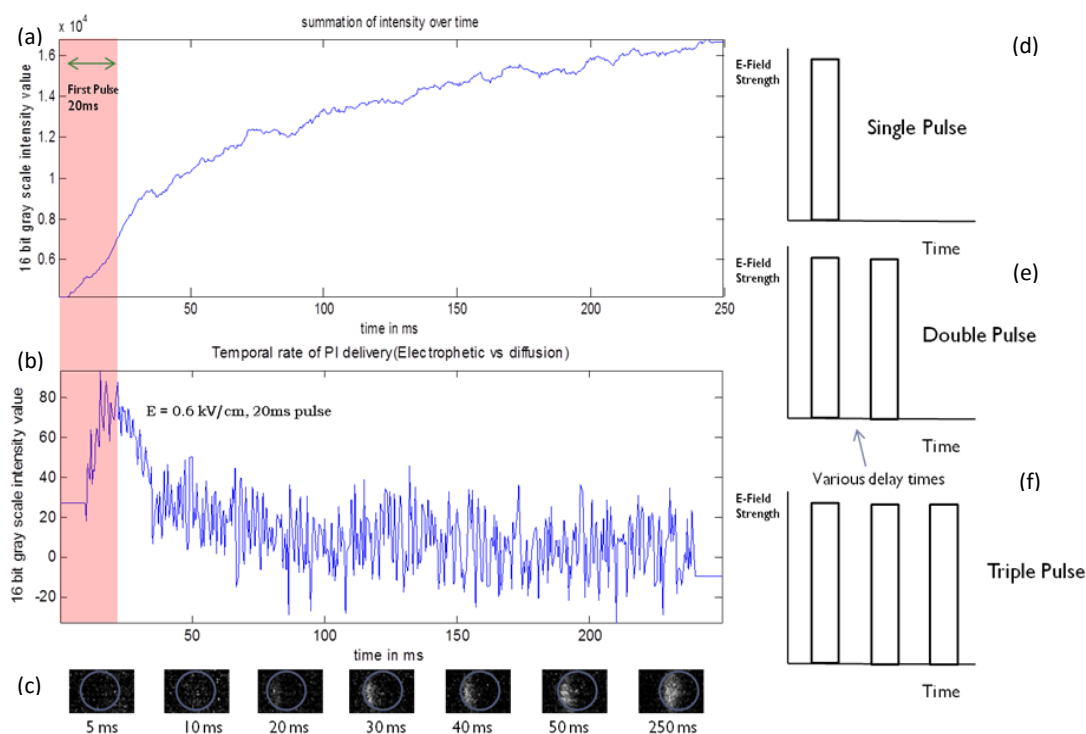**Figure E.1**. (a) Intracellular PI delivery fluorescence intensity summation over time for single pulse. Red translucent label indicates duration of electroporation pulse. (b) Temporal rate of PI delivery. (c) Optical visualization of PI delivery at 5 ms interval. (d) Schematics for single pulse applied (e) double pulse with various delay times in between (f) triple pulse with two delay intervals.

course of electroporation, electrophoretic mobility of the positively charged PI electromigrated along the direction of applied electric field (left to right) into the electropermeabilized cell at a much faster rate than diffusion mediated migration. Due to the occurrence of FASS at the intracellular buffer interface, PI accumulated and resulted in a stacked fluorescence signal. When the pulse ended, the electrophoretic force was no longer active; therefore transport of PI into the cell becomes dominated by diffusion which was a slow process. This can be seen from the intensity summation plot where the fluorescence curve slowly plateaus after a sharp rise in signal for the first 20 ms. To further verify the effect of electrokinetic-driven phenomenon at the first 20 ms of pulse application, Figure E.1b shows the temporal rate of PI delivery as a function relative intensity value and time. It can be clearly seen that the first 20 ms produces a very noticeable rise in the rate of PI delivery, and then the signal diminishes to a constant base-line value of roughly zero. This is mainly due to the resealing of the cell membrane. The strong difference between how fast the PI electromigrates before and after pulse application confirms the electrokinetic dominated transport duration electroporation. Figure Ac demonstrates the temporal and spatial progression of PI entry into the cell, the images shown here only represent every 5 ms of recording whereas in fact, the images were recorded and analyzed at a 0.5 ms temporal resolution. Analysis based simply on these visualizations clearly indicates that PI enters from the positive electrode as it should due to its positive charge, this is an aspect of the electrophoretic force driven theory where the active component is the charge of the species, not diffusivity.

2. Double Pulse Fluorescence Analysis on Static Cell

Optical evidence of electrokinetic driven transport can be re-enforced with the application of multiple pulses. Because the increased rate of PI delivery is dependent on the presence of an electric field, therefore a double pulse experiment with each pulse being 20 ms long and a short, 10ms delay in between and a long 70 ms in between can be carried out to show the consistency of our theory. Figure E.2a-b once again shows the fluorescence intensity summation as a function of delivery intensity and time. The translucent pink label indicates a 20 ms pulse application and the yellow label indicates a 10 ms and a 70 ms delay. Two distinct slopes can be observed from both plots as the pulse is applied, there is an increase in fluorescence signal in each delivery. Figure E.2b-d illustrates the temporal rate of delivery where the slopes of the applied pulses can be better distinguished from the slope
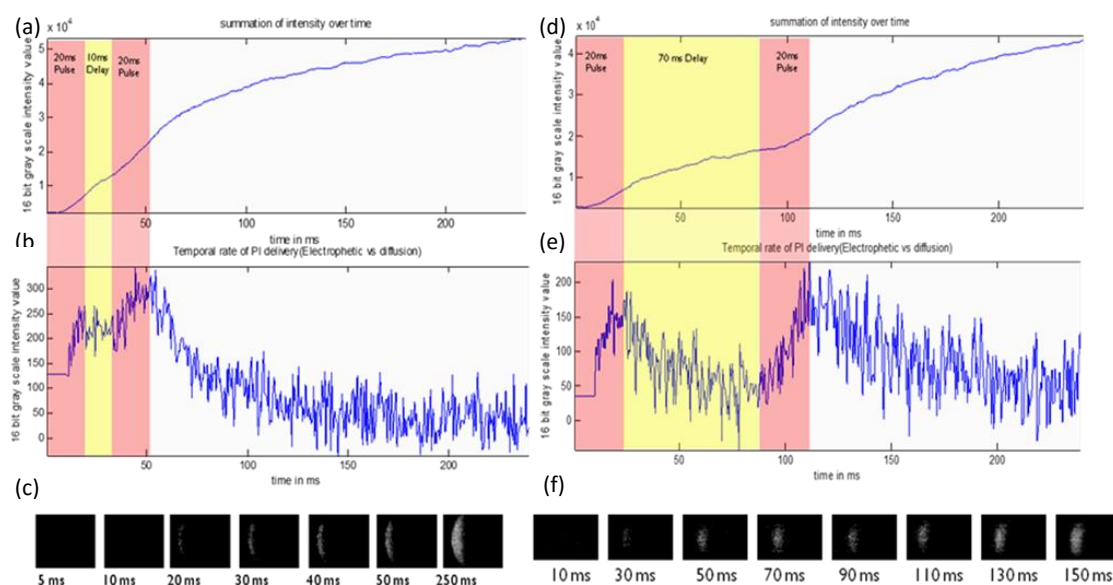

Figure E.2 (a & d) Intracellular PI delivery fluorescence intensity summation over time for double pulse. Red translucent label indicates duration of electroporation pulse and yellow label indicates time delay. (b & e) Temporal rate of PI delivery. (c & f) Optical visualization of PI delivery at 5 ms interval.

of the delay. This timely rise in intensity proves eletrokinetic driven forces is certainly behind electroporation mediated delivery. It is also interesting to note that during the 10 ms delay between the pulses, the rate of PI delivery decreases slightly, not falling off to zero as it would at the end of the second pulse or the end of first 70 ms delay in Figure E.2d. This can be explained by taking into account the cell membrane dynamics during electroporation. When the first pulse is applied, cell membrane pore opens up to a certain degree, and because the time between the first and second pulse is so short (10 ms), cell membrane does not have enough time to re-seal and neither can more PI be delivered into the cell, diffusion certainly is not fast enough for any delivery to take place. Therefore when the second pulse was applied, the cell membrane pore opened even bigger than before, resulting in an increase in delivery as seen from the magnitude of the second pulse. On the contrary, when the delay time is much longer (70ms) between the pulses, the cell membrane has ample time to re-seal, therefore by the time of second pulse application; the magnitude of delivery becomes roughly the same as the first pulse. This postulation of the cell membrane dynamics under multiple pulse electroporation still requires further investigation, because the rate of PI dissociation inside the cell can also be a factor that influences the accumulation of PI. For instance, if transported PI inside the cell dissociates slower than the delay time between the two pulses, as a result of high cytoplasmic density, then further delivery of PI under the second pulse may be partially hindered by the accumulated PI at the intracellular buffer interface where PI has been stacked due to FASS.

3. Triple Pulse Fluorescence Analysis on Static Cell

Similar fluorescence intensity curves as before can be observed through triple pulse application as well. In these experiments, two 30 milliseconds and 50 milliseconds delay were inserted between the applied pulses. Figure E.3a & d shows the fluorescence intensity plot where three regions of incremental delivery can be clearly identified which correspond to the three pulses (20ms each) applied. The total fluorescence at the end of the third pulse is the highest in comparison to the last pulse from the double and single pulse experiment. This is expected since resealing of the pores prevents additional PI entry as well as its escape. Sharp rises in the temporal rate of delivery which correspond to the application of electroporation pulses can once again be observed in Figure E.3b & e. The drastic drop of delivery rate at the end of each pulse supports the absence of electrophoretic driving forces as well as the resealing of the cell membrane pores.
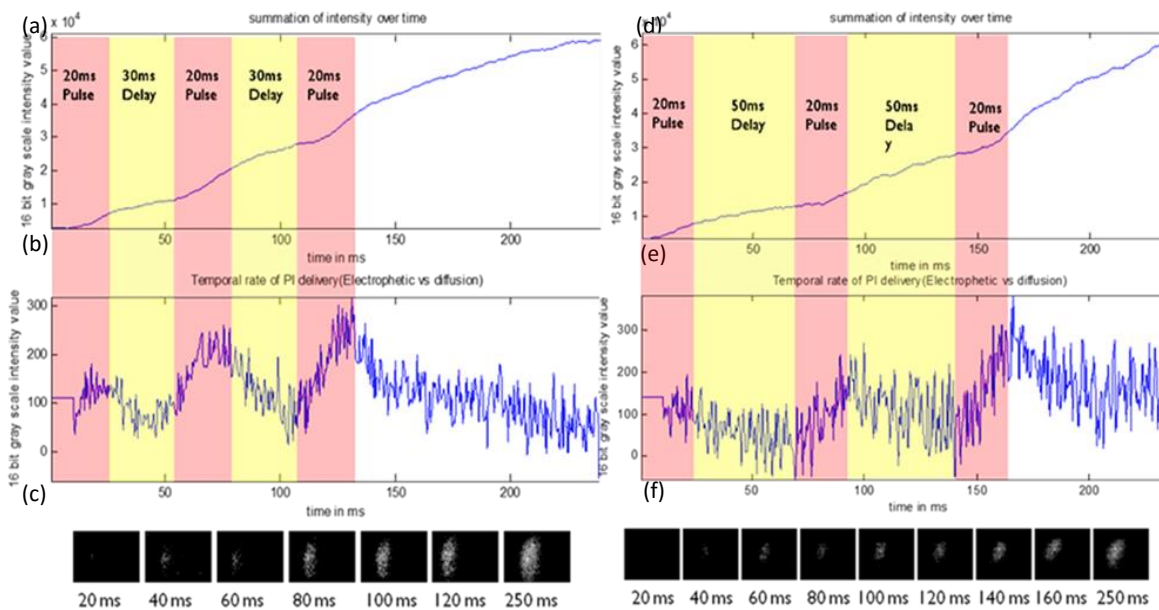

Figure E.3. (a & d) Intracellular PI delivery fluorescence intensity summation over time for triple pulse. Red translucent label indicates duration of electroporation pulse and yellow label indicates time delay. (b & e) Temporal rate of PI delivery. (c & f) Optical visualization of PI delivery at 20 ms interval.

Appendix F

Single Cell Trapping Device Designs

Four microfluidic channels have been designed, fabricated and tested for improving single cell level SNR (Figure F.1). A commonly feature among all four channel configuration is the physical 'trapping' of single cells through different geometrical designs. The "bowl" shaped single cell trapping design shown in Figure F1-1 has two vertical planar electrodes directed at the center of the 'bowl' with a 70 µm inter-electrode spacing. Low density of cells are perfused into the channel from the left inlet, they flew passed the center of the 'bowl' structure which is a small opening with a dimension of 10 µm in both width and depth, and they exit from either the right outlet, or through the center of the 'bowl' structure to two of the flow-pressure relieving outlets. This channel configuration allows the continuous flow of buffer and small cells over or through the 'bowl', rather than clogging the small opening. This architecture was specifically designed so that single cells with large radius (> 10 µm in diameter) could become passively immobilized at the small opening. After receiving electroporation treatment and permeabilization measurement, pulsatile fluidic flow pressure can be applied to dislodge the trapped cell to exit any one of the three channel outlets. This microfluidic channel configuration has proved to work well in our experiments. The second microchannel design is known as the "suction-cup" (Figure F1-2), similar to the design used by Khine and Rubinsky[4,5] in which a negative pressure was applied tangentially towards a stream of flowing cells through a narrow channel hole. Once trapped, electrodes across the suction hole performs the electroporation and measurement on the cell.
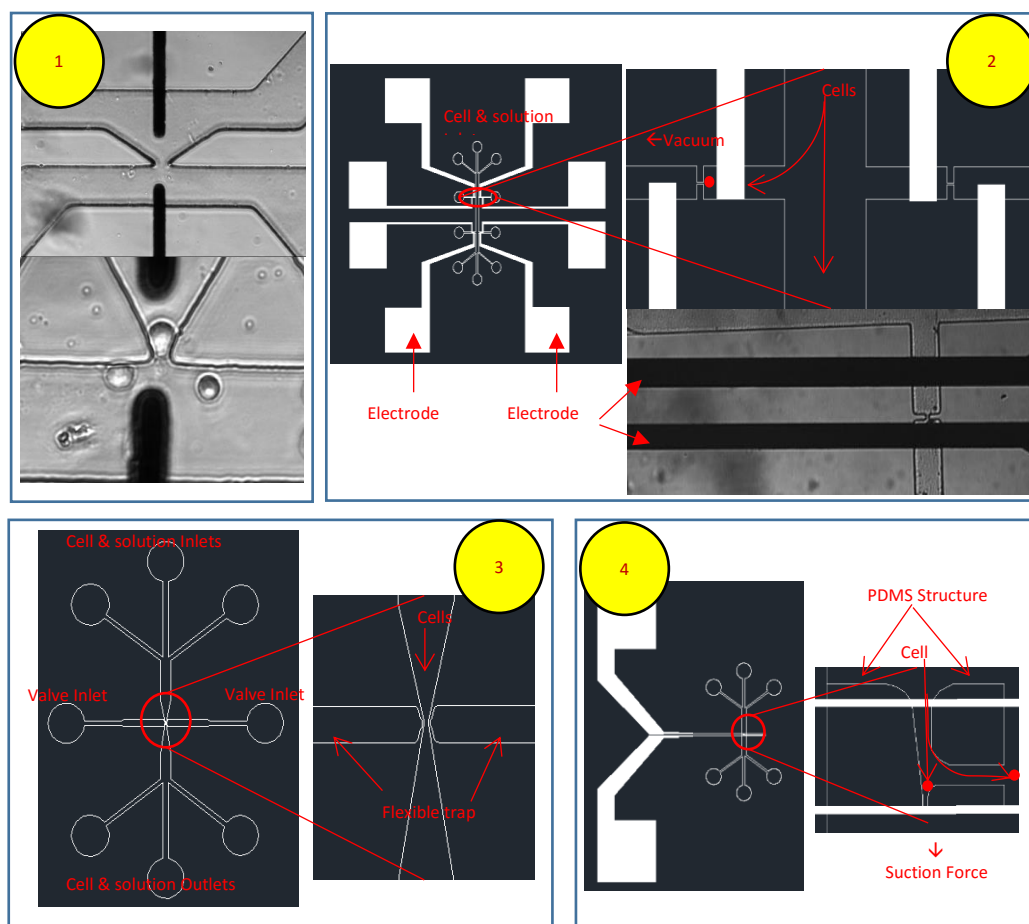
Figure F1. Microfluidic channel configurations designed to temporarily immobilize single cells for electroporation treatment and membrane permeabilization measurement study. Labelled by yellow circles, the first design is a pressure balanced "bowl" that holds the passing cell in place for measurement. The second design is the classic "suction-cup" which utilizes negative pressure to "suck" single cell to the hole. The third design used positive pressure applied through a pair of side channels to physically "pinch" the PDMS layers in order to compress the cell channel. A three-piece PDMS structure was used in the last design to passively contain the passing cells with a flow pressure relieving channel. First channel configuration was chosen for reliable single cell trapping.

One of the challenges associated with this design is the fabrication of a suction-channel dimension, which needs to be below the typical diameter of the 3T3 cells used here (< 10 - 15 µm) in order to establish successful immobilization.

Unwanted cell adhesion, aggregation, and debris often makes single cell immobilization very challenging and unreproducible. The third design takes advantage of the flexibility of PDMS membranes. By fabricating a constricted cell flow channel sandwiched by a pair of fluid-filled side channels separated by thin PDMS walls as shown in Figure F1-3. When the side channels are pressurized, the PDMS walls serve as closing valves 'pushing in' on the cell flow channel, resulting in the temporary immobilization of a cell. The device design requires a careful selection of PDMS thickness layer between the cell and side channel to effectively trap cells. However, one of the drawbacks is associated with the current measurement when the cell is trapped. Due to the incomplete closing of the PDMS walls during PDMS wall compression, a differential fluid pressure in the cell channel causes an inconsistent buffer flow through the compressed region, resulting in current drifts during the electrical measurement. In addition, the timing for applying the pressure to trap a flowing cell is difficult, many trial-and-error runs are required. The fourth channel design also relies on the passive settlement of cells in a channel to achieve arbitrary immobilization of a cell (Figure F1-4). Implemented in a wide microfluidic channel, a three-piece PDMS structure serves to direct the entry of single cells to an immobilization region while allowing excess fluid to exit from the side. This simple design does not require the exertion of positive or negative pressure, however a great deal of patience is required. In terms of fabrication, cell immobilization and measurement reliability and reproducibility,

the first design was selected to carry out the subsequent single cell membrane permeabilization investigation.